Universidade de São Paulo
Instituto de Astronomia, Geofísica e Ciências Atmosféricas
Departamento de Astronomia

Bruno Correia Mota

BeAtlas: A grid of synthetic spectra for Be stars

Bayesian inference of the physical properties of B and Be Stars

BeAtlas: Uma Grade de Espectros Sintéticos para estrelas Be

Inferência Bayesiana das propriedades físicas de estrelas B e Be

São Paulo

2019

Bruno Correia Mota

BeAtlas: A grid of synthetic spectra for Be stars

Bayesian inference of the physical properties of B and Be Stars

BeAtlas: Uma Grade de Espectros Sintéticos para estrelas Be

Inferência Bayesiana das propriedades físicas de estrelas B e Be

Tese apresentada ao Departamento de Astronomia do Instituto de Astronomia, Geofísica e Ciências Atmosféricas da Universidade de São Paulo como requisito parcial para a obtenção do título de Mestre/Doutor em Ciências.

Área de Concentração: Astronomia
Orientador(a): Prof. Dr. Alex Cavaliéri Carciofi
"Versão Corrigida. O original encontra-se disponível na Unidade."

São Paulo

2019

Acknowledgements

Se você está lendo os agradecimentos, muito provavelmente você deseja saber se me lembrei de você. Não se preocupe, pois saiba que, mesmo seu nome não estando listado aqui, eu sou muito grato por ter te conhecido. Não tenho como recompensar sua amizade, por isso deixo um singelo presente, uma música que gosto muito, espero que goste ;-)

TOCANDO EM FRENTE

Ando devagar
Porque já tive pressa
E levo esse sorriso
Porque já chorei demais
Hoje me sinto mais forte
Mais feliz, quem sabe
Só levo a certeza
De que muito pouco sei
Ou nada sei
Conhecer as manhas
E as manhãs
O sabor das massas
E das maçãs
É preciso amor
Pra poder pulsar
É preciso paz pra poder sorrir
É preciso a chuva para florir
Penso que cumprir a vida
Seja simplesmente
Compreender a marcha
E ir tocando em frente
Como um velho boiadeiro
Levando a boiada
Eu vou tocando os dias
Pela longa estrada, eu vou
Estrada eu sou
Conhecer as manhas
E as manhãs
O sabor das massas
E das maçãs
É preciso amor
Pra poder pulsar
É preciso paz pra poder sorrir
É preciso a chuva para florir
Todo mundo ama um dia
Todo mundo chora
Um dia a gente chega
E no outro vai embora
Cada um de nós compõe a sua história

Cada ser em si
Carrega o dom de ser capaz
E ser feliz
Conhecer as manhas
E as manhãs
O sabor das massas
E das maçãs
É preciso amor
Pra poder pulsar
É preciso paz pra poder sorrir
É preciso a chuva para florir
Ando devagar
Porque já tive pressa
E levo esse sorriso
Porque já chorei demais
Cada um de nós compõe a sua história
Cada ser em si
Carrega o dom de ser capaz
E ser feliz
Composição: Almir Sater / Renato Teixeira

"*... meu pai chegou lá, os médicos todos de branco, aí entraram os doidos com os carrinhos de mão que tinham sido adquiridos pelo Governo para iniciar a psicoterapia pelo trabalho. E um dos doidos estava com o carrinho de mão de cabeça para baixo. Aí papai chamou e disse,*

_Oh, não é assim não que se carrega, é assim!

_Eu sei doutor, mas se eu fizer assim, eles colocam pedra pra eu carregar. - Respondeu o doido."

Ariano Suassuna

"*Ardan: ...Vejam só a distância das estrelas! A estrela Vega e a estrela Sírius estão a bilhões e bilhões de quilômetros de distância! E ainda há quem me venha falar da distância que separa os planetas do Sol! E ainda há os que afirmam que essa distância existe! Isso é um erro! Sabem o que penso do mundo que começa no astro radioso e termina em Netuno? Querem conhecer minha teoria? Ela é bem simples! Para mim, o mundo solar é um corpo sólido, homogêneo; os planetas se tocam, se juntam e o espaço existe entre eles é como o espaço que separa as moléculas do metal mais compacto, seja ele prata ou ferro, ouro ou platina. Portanto, posso afirmar e repito com convicação: a distância é uma coisa vã, a distância não existe! ... E fez um movimento tão violento que quase caiu do estrado. Mas conseguiu recuperar o equilíbrio e evitar uma queda que lhe provaria, de forma brutal, que a distância não é uma coisa vã.*"

Julio Verne, Da Terra à Lua

Abstract

Classical Be stars are the only Main Sequence stars that possess Keplerian decretion circumstellar disks ruled by viscous processes. The physical properties of the disk can be studied by modeling its physical structure and solving the radiative transfer problem. At this point, the calculation of synthetic observables arises as a tool to investigate the physical quantities of these systems. Among the proposed models to explain Be star disks, the Viscous Decretion Disk model is the only one correctly explaining a large set of evidences that implies that viscous shear is the mechanism driving the disk outflow.

Modeling of observations requires elaborate procedures to achieve reliable results. In the case of Be stars, the system under study is very complex. The central star is affected by fast rotation and stellar pulsation. The disk structure varies in time, and depends in a complex way on several factors, e.g., disk feeding rate, viscosity, the presence of a binary companion, etc. Another source of complication is the complex interplay between stellar and disk parameters.

We present a new tool for modeling Be star observations that takes into consideration most of the relevant physical processes. Named BeAtlas, it consists of two parts. The first part is a grid of Be star models that cover all the relevant physical parameters of the star (mass, age, rotation rate, etc.) and the disk (size, density structure, density scale, etc.). BeAtlas was computed with the radiative transfer code Hdust. The stellar parameters were obtained from the Geneva stellar evolution models.

The second part is a set of computer tools to the fit of the observations with BeAtlas using Bayesian statistics to infer the posterior probabilities of each stellar and disk parameter. BeAtlas allows for using prior information, such as distance, $v \sin i$ and inclination, when available. Our main goal with BeAtlas is to provide means for studying B and Be stars observations into account all the relevant parameters and their cross correlations.

BeAtlas was first applied to study of 111 OBA stars. Using IUE data and prior information ($v \sin i$ and Hipparcos parallax) about these stars, we were able to derive their stellar and geometrical parameters, as well as the corresponding interstellar extinction. A comparison of our results of those from the literature yielded in general good results. Deviant cases must still be analyzed in more detail, but one possibility under investigation is that they due to fundamental differences between our approach and some of the ones used in the literature (e.g., rotating vs. non-rotating models) which limits the viability of a direct comparison.

A second application was on the Be Star β CMi, which was modelled by Klement et al. (2015) also using the Viscous Decretion Disk model. The results show the ability of BeAtlas to quickly recover the disk and stellar parameters. Furthermore, a detailed analysis of the results show that our procedure does indeed provide for more robust and realistic error estimates by properly considering the coupling between the parameters.

Finally, a third application was on the Be star α Arae. We present new observations (polarization, spectroscopy and sub-mm photometry) that, together with data obtained from the literature, show that α Arae had a stable disk for the last 50 years. We found a disk density slope ($n = 2.44^{+0.27}_{-0.16}$) that is inconsistent with the standard theory that predicts that isothermal steady-state disks should have $n = 3.5$. Two effects may be responsible for this: non-isothermal effects in the disk, or the effects of a binary companion. Our results provide evidence that α Arae is a binary system. In our case, evidence came for the change of the SED slope in the sub-mm domain, here interpreted as being caused by an unseen binary companion that truncates the disk of the primary.

List of Figures

List of Tables

Contents

Chapter 1

Introduction: The Be phenomenon

1.1 Chapter Summary

This Chapter presents a synopsis of the scientific problem and its astrophysical relevance (Sec. 1.2), followed by a discussion about the stellar rotation (Sec. 1.3). Thereafter, in Sect. 1.4, we introduce additional classes of stars that were studied alongside the Be stars. A detailed description of the circumstellar disks of Be stars and its current paradigm is given in Section 1.5. We summarize our objectives in Sect. 1.6.

1.2 Classical Be Stars

This thesis will deal mostly with stars in the mass range of 3 to 20 $M_{\odot}$. During their Hydrogen burning phase known as the Main Sequence (hereafter MS), these stars have spectral types between B9 and B0. Table 1.1 summarizes the stellar parameters of the B stars for each subtype.

A sizeable fraction of these stars present spectroscopic peculiarities (e.g. emission lines) in their spectra (e.g. Smith, 1996). The reason for these emission lines is always the presence of circumstellar material around the star. For some objects, e.g., magnetic B stars, magnetic fields are the underlying cause for the presence of circumstellar material (e.g. Wade G. A., Wade). This thesis focus on another class, the Classical Be Stars (hereafter, CBe; see Jaschek et al., 1981; Collins, 1987, for proposed spectroscopic definitions). They are recognized by their outwardly diffusing gaseous, dust-free Keplerian circumstellar disk that arises in active phases (Rivinius et al., 2013) and by showing the highest rotation rates among MS stars (e.g. Townsend et al. 2004; Frémat et al. 2005; Granada and Haemmerlé 2014).

Since the discovery of CBes (Secchi, 1866), many efforts have been made to understand their distinguishing characteristics. For instance, progressing observational techniques seen in the last

Table 1.1 - Stellar parameters of MS Be stars obtained from Townsend et al. (2004).

Sp. Subtype	$M_\star$ [$M_\odot$]	R_{pole} [$R_\odot$]	v_{crit} [km s^{-1}]	log $L_\star$ [dex $L_\odot$]
B0	17.5	7.7	538	4.64
B0.5	14.6	6.9	519	4.41
B1	12.5	6.3	502	4.21
B1.5	10.8	5.7	491	4.01
B2	9.6	5.4	475	3.85
B2.5	8.6	5.0	468	3.68
B3	7.7	4.7	456	3.52
B4	6.4	4.2	440	3.24
B5	5.5	3.8	429	3.00
B6	4.8	3.5	418	2.78
B7	4.2	3.2	408	2.56
B8	3.8	3.0	401	2.39
B9	3.4	2.8	393	2.20

decades, such as space-based photometry, long-term monitoring campaigns, polarimetry, high-angular resolution interferometry, etc. have provided invaluable data to study these objects in detail (Rivinius et al., 2013). Adding this to the advances in our understanding of Be star physics (both of the star itself and its disk) and of our computational ability, such that our knowledge of Be stars has reached an unprecedented level (Sect. 3.2). The so-called *Be phenomenon* itself (the origin of their observational features) is now much better understood, but progress must still be made if we are to uncover the origin of the circumstellar disk. The interested reader is invited to read the following review papers on CBes: Underhill and Doazan (1982); Slettebak (1988); Porter and Rivinius (2003); Rivinius et al. (2013). They provide an interesting panorama of how our knowledge on CBes has evolved over time.

The study of CBes is important for several reasons. For instance, even the range in spectral type of the Be phenomenon is still uncertain, which demands a careful investigation of the neighboring spectral types, i.e. O and A spectral types, Golden-Marx et al. (2016), for instance, report the discovery of a few Oe stars in the Magellanic Clouds. Furthermore, despite the paucity of massive stars[1], they play a crucial role in the evolution of the Universe, being regarded as one of the main sources of heavy elements and UV radiation (Massey, 2003). The earliest B-type stars

[1] The terms massive star and high-mass star denote OB stars sufficiently massive to produce type II supernovae ($M_\star$ / $M_\odot$ > 8).

provide a crucial test bed for the role of rotation for the evolution of both massive and intermediate mass stars (Huang et al., 2010). Moreover, massive stars are not born isolated (Sect. 1.2.2), in which case the combined effects of winds, massive outflows of nearby companions, gravitational interaction, and supernova explosions of these objects provide energy that can trigger processes of mixing and formation of turbulence into the interstellar medium (Martins et al., 2005), as well as affect their global evolution (Zinnecker and Yorke, 2007). Additionally, the CBe fraction among B stars as a function of age, metallicity, and rotation is not well known yet, ranging from 3 to ~ 50 % (e.g. Wisniewski and Bjorkman 2006; McSwain and Gies 2005; Zorec and Briot 1997; Keller et al. 1999; Maeder et al. 1999; Marco and Negueruela 2013; Bastian et al. 2017). Approximately 10% of the MS B stars in the Galaxy are CBes (Rivinius et al., 2013).

One of the most challenging problems involving the study of CBe, Bn (Lamers et al., 1980), B normal, Oe (e.g. Conti and Leep 1974; Negueruela et al. 2004) and Ae stars (Bohlender, 2016) is the inference of their fundamental parameters (i.e., mass, temperature, rotation rate, radius, inclination, etc). This task becomes more complex in our case due to two complicating factors: the rapid stellar rotation (Sect. 1.3) and the fact that CBe stars have disks that partially veil the star, making the problem more complex. We have, then, a coupled problem: the apparent stellar parameters are changed by the disk, while the disk structure depends on the stellar characteristics. Still in Be context, the currently accepted model (the Viscous Decretion Disk model) was tested only for a handful of CBes to-date (Sect. 3.2). As such, more detailed studies of individual Be stars are necessary to provide further validation of the model and an improvement of our knowledge about the Be phenomenon.

1.2.1 Variability of Be Stars

Be stars are also subject to different sources of variability, which are manifested in several observables and cover various time-scales. For instance, the *short-term variations* (~ hours-days), observed in emission lines, are associated with non-radial stellar pulsations (NRP) (Baade et al., 2016). On longer timescales, there are *intermediate-term variations* (~ days-months) seen in the V/R variations of emission lines and associated with global disk oscillations (e.g. Okazaki 1997; Carciofi et al. 2009). Recently, Labadie-Bartz et al. (2017) provided evidences that photometric outbursts correspond to incomplete disk build-up events. What triggers these disk events is still not clear, but mounting evidence points to NRP as the fundamental cause of mass loss in Be stars (Baade et al., 2016). Intermediate-term variability has also been traced back

Table 1.2 - Typical types of variability observed in CBe. NRP: Non-rotational pulsations. O: Outburst. QPO: Outbursts and quasi-periodic oscillations.

Type	Timescale	Cause
Shorter	Hours to days (0.1 to 2 days)	NRP
Intermediate	Days to months (2 and 200 days)	O or QPO
Long	Occasionally have duration of decades	O

to the effects of a binary companion (Sect. 1.2.2). Finally, *longer term variabilities* (~ years-decades) represent the complete process of formation and dissipation of the disk (e.g. Bjorkman et al. 2002; Rímulo et al. 2018). We summarize this variability in Table 1.2.

1.2.2 Binarity and Disk Truncation

Most of the massive O stars are binaries (~ 75%), or were at some moment of their life (Sana et al., 2012). For B stars, the binary fraction can reach up to ~ 40% (Chini et al., 2012) or 29 ± 8 % (Oudmaijer and Parr, 2010). It is also high among Be stars, ranging from 27 (Sterken et al., 1996) to 30 ± 8 % (Oudmaijer and Parr, 2010). Hence, binary effects might be a common component in massive star evolution, and is associated with a variety of astrophysical processes and objects such as γ-ray bursts, X-ray binaries, pulsars and double-neutron stars (Chini et al., 2012). In this context, a close companion can significantly influence the massive star evolution (e.g. Langer et al. 2008). The mass transfer in such a system is also an ingredient that must be considered (Dunstall et al., 2015). All these relevant aspects lead to an increase in the search for binary companions in the last decades (e.g. Chini et al. 2012). As a result, the conclusion is now that most massive stars may be born as part of multiple systems (Sana et al., 2012).

The possibility that Be stars and supergiant sgB[e] might be binary evolutionary products was explored in the past, and gained new momentum recently (e.g., Baade 1992; Vanbeveren and Mennekens 2017). Currently, there exists about 20 known binary CBe + sdO/B systems, which are believed to be a direct result of binary stellar evolution (e.g., Wang et al. 2018; Peters et al. 2016). In brief, it is believed that the larger mass component, as it evolves and expands after the end of the MS, fills its Roche Lobe and dumps material and angular momentum on the secondary that, in turn, spins up and acquires the necessary rotational velocity to become a Be star (Gies, 2000). The primary eventually has its outer layers striped off, and what remains is its exposed core.

Furthermore, some observational evidence points out to the possibility that gravitational interactions between a Be star and a companion could induce periodic variability and ellipsoidal precession of the disk (Panoglou et al. 2018; Cyr et al. 2017). In addition, the companion might act on the disk by tidal effects or in its thermal properties, e.g., by irradiating the outer part of the disk (Peters et al., 2016). A list of some known binary Be stars is shown in Table A.1.

Long-baseline interferometry is the most powerful technique to detect companions (Meilland et al., 2012). Despite this, the detection of very close companions ($\lesssim$ 100 mas) has an observational limit (Sana et al., 2014). To investigate this issue, Chini et al. (2012), using another technique, performed a high-resolution radial velocity study of a spectroscopic survey containing $\sim$ 250 O stars and $\sim$ 540 B stars in the southern Milky Way. They found that $>$ 82% with $M > 16\,M_\odot$ form close binary systems; this fraction drops to only 20% for $M \sim 3\,M_\odot$. The smallest orbital period found in their study was only a few days, corresponding to critical separations of $\sim$ 0.2 AU. This is the limit in which the system could merge into a single object. In summary, the multiplicity fraction seems to decrease with decreasing stellar mass.

A peculiar phenomenon in binary Be systems is that the secondary could truncate the disk to a radius dependent on the orbital parameters (eccentricity, semi-major axis, etc.) (e.g. Okazaki et al. 2002). Observational detection of disk truncation is difficult due to the fact that the outer disk emits very little flux in the visible and infrared. Recently, Klement et al. (2017) proposed that the observed drop in the SED slope in the radio domain, observed in several Be stars and dubbed SED turndown, might be associated with disk truncation. Since that paper, many more cases of SED turndown were found (Robert Klement, priv. comm.). It must be emphasized, however, that an alternate explanation for the SED turndown exists. It involves a transonic transition in the disk, which is defined by the locus pressure forces are larger than the viscous torque, resulting in a sudden drop in the gas density profile (Okazaki et al., 2002). Nevertheless, as mentioned by Klement et al. (2017), this photoevaporation transition is expected to occur much farther away than the putative truncation radii estimated from the SED turndown.

The hypothesis that the SED turndown is caused by binary truncation, requires an independent identification and characterization of the binary orbit, e.g., by means of radial velocity measurements. Of the stars studied by Klement et al. (2017), γ Cas and ζ Tau were previously known as binaries, and the truncation radius inferred from the SED turndown agreed with the orbital parameters. Another example is β CMi, which was suggested to be a binary by Klement et al. (2015) and later identified as such by Dulaney et al. (2017).

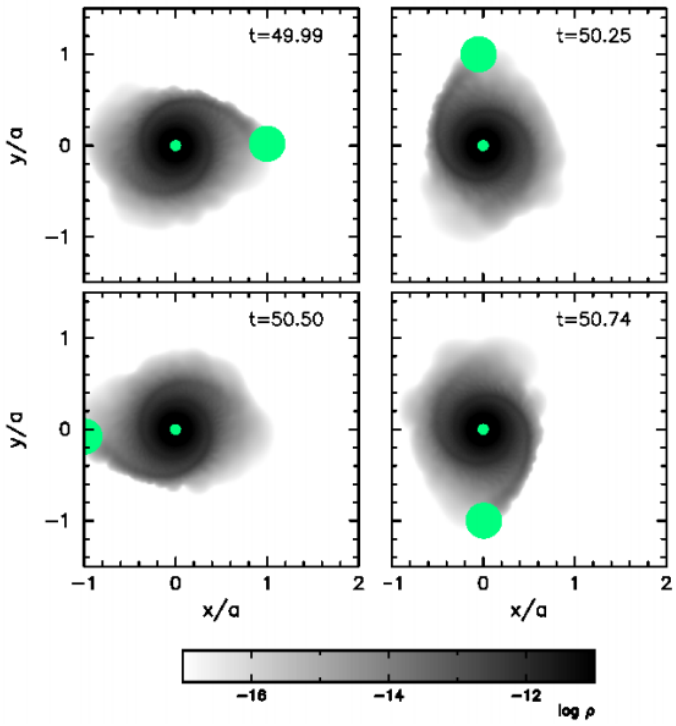

Figure 1.1: Snapshots of a complete cycle of the reference binary system at quasi-steady state simulated by Panoglou et al. (2016). The distances are given in semi-major axis, a, units. Green dots: position occupied by each companion.

The truncation problem was explored by Panoglou et al. (2016). They examined theoretically the cases of circular and eccentric coplanar orbits, both prograde and retrograde, using the same 3D SPH code adopted by Okazaki et al. (2002)[2]. Their main conclusions were:

1. In near circular binaries, the disk maintains a near-steady state structure composed of two-opposing spiral arms that rotate in phase with the orbital motion of the companion (see Fig. 1.1). In such cases, the truncation region might be independent of the orbital phase;

2. A small disk could be present even for very close binaries, for instance, a companion with $P_{\rm orb} = 5$ days could have an observable disk with truncation radius, $R_{\rm t} = 2.5\,R_{\star}$. Such small disks have indeed been observed in short-period Be X-ray binaries;

3. From circular to moderately eccentric ($\epsilon \sim 0.6$) orbits, the inner disk preserves its structure, but the outer disk has a truncation region that varies with the orbital phase. These effects are maximized for highly eccentric orbits;

[2] The case of non-coplanar orbits was investigated by Cyr et al. (2017).

4. The binarity induces an accumulation of material in the inner disk (as effect dubbed as accumulation effect) that generates an inner density exponent lower than the steady-state value for isolated Be disks;

5. For non-coplanar orbits, the disk can become warped, i.e., it no longer lies in the equatorial plane of the primary.

1.3 Stellar Rotation

A star may acquire angular momentum during the pre-MS phase, from its parent cloud angular momentum is conserved or through interactions with other protostars (e.g. Huang and Struve, 1954). In this phase, the accreting protostar can break up due to the centrifugal force. When a star enters the MS, it is believed that its magnetic field can interact with the stellar wind, carrying away its primordial angular momentum. Over time this gradually slows the stellar rotation rate (e.g. Ferreira et al., 2000).

The breaking mechanism discussed above does not apply to CBe. Actually, this is an important ingredient to differentiate magnetic stars from CBe, since large-scale magnetic fields have not been detected in any CBe star, which strongly indicates that the Be phenomenon could be independent of magnetism or suppressed by magnetism (Grunhut et al., 2012). As an example, we show the mean intensity of the magnetic field along the line of sight, $< B_z >$, of several MS stars in Figure 1.2. This figure shows that the stronger magnetic fields appears around the A spectral types decreasing towards the early spectral types B and O. When we plot the $< B_z >$ field versus $v \sin i$ (Right panel of the Fig. 1.2) there is no clear evidence of correlation between these physical quantities.

The equatorial rotational velocity, $v_{\rm eq}$, is frequently used to describe the rotation, but is usually difficult to measure directly. Actually, what is measured is the projected rotational velocity, $v_{\rm eq} \sin i$, which depends on the inclination of the stellar rotation axis with respect to the line of sight, i. Among the usual techniques to determine the $v \sin i$, there are: (i) Doppler broadening of photospheric lines caused by the stellar rotation (Shajn and Struve, 1929). Townsend et al. (2004); (ii) direct measurement of the shape of the star by interferometric techniques (see below; e.g. Domiciano de Souza et al. 2014).

The break-up or critical velocity of a star is used to describe when the centrifugal force at the equator is equal to the gravitational force. While the equatorial rotational velocity is below this

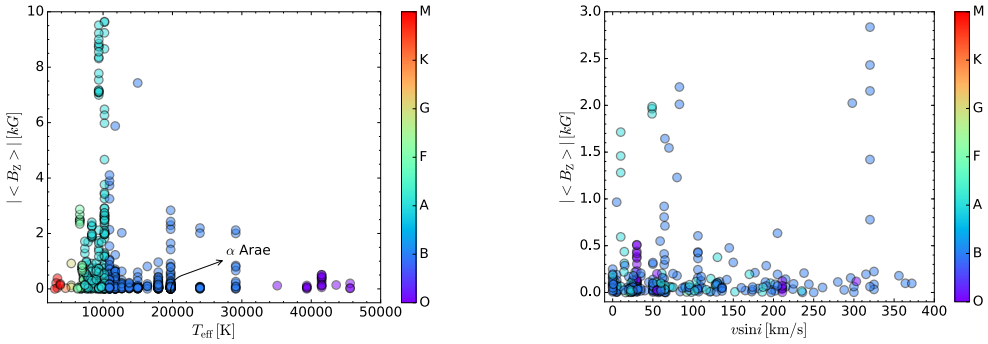

(a) *(b)*

Figure 1.2: Left: Magnetic field versus effective temperature for main sequence stars taken from Bagnulo et al., 2015. B_z refers to mean intensity of the magnetic field along the line of sight. Right: Magnetic field versus projected rotational velocity for main sequence stars taken from Bagnulo et al., 2015.

value, the star remains stable (Hardorp and Strittmatter, 1970). The critical velocity is given by,

$$V_{\rm crit} = \sqrt{\frac{2\,G\,M_\star}{3\,R_{\rm pole}}} = \sqrt{\frac{G\,M_\star}{R_{\rm eq}}}, \tag{1.1}$$

where $M_\star$ is the stellar mass, $R_{\rm pole}$ and $R_{\rm eq}$ are the polar and equatorial radii, respectively. The term $3/2$ above comes for the Roche equipotential approximation for a critically rotating star in solid rotation (Roche, 1859). In this approximation, a critically rotating stars has an equatorial radius $3/2$ larger than the polar radius (see below for more details).

In our work, we employed the stellar rotation rate definition,

$$W = \frac{v_{\rm rot}}{v_{\rm orb}}, \tag{1.2}$$

where $v_{\rm orb}$ is the Keplerian circular orbital velocity at the equator, and $v_{\rm rot}$ is the rotational velocity at the equator (Rivinius et al., 2013). Rivinius et al. (2013) argue that W is the physically most meaningful quantity to describe rotation because it is model independent (e.g., it does not depend on the particular structure assumed for the star as the Roche approximation does). Physically, it "defines what velocity boost is required for a given star to launch material into the closest possible orbit, i.e., just above the photosphere at the equator." (Rivinius et al., 2013).

1.3.1 Fast Rotation in Stars

Rotation is an important ingredient for understanding the formation and evolution of stars (e.g. Cranmer 2005; Ekström et al. 2008; Granada et al. 2013), being the main cause of several physical effects observed in stars. This is especially relevant in our case, since high-rotation rates are expected to be more common among early spectral types (Cranmer, 2005). As pointed out by Ekström et al. (2011), the effects of fast rotation on the stellar structure during its evolution are several: oblateness (e.g. Collins and Harrington 1966; Maeder 2009), mixing, transport of angular momentum from the core to the surface, and gravity darkening (Collins, 1963) which changes its surface brightness distribution (von Zeipel, 1924). For these reasons the gravity darkening and oblateness must be considered in any modeling effort, as its effects produce significant changes to the disk thermal structure of Be stars (e.g. McGill et al. 2011), as well as the SED and line profiles (Townsend et al., 2004). In addition, the evolutionary tracks (Ekström et al., 2012) show that rotating hot stars and non-rotating models have non-negligible evolutionary differences. For instance, models show that fast rotation can substantially increase the MS lifetimes.

In the Roche approximation (rotating solid body equipotentials, Cranmer 1996), the oblateness of the star is related to the rotation rate by

$$W = \left(2\frac{R_{\rm eq}}{R_{\rm pole}} - 2\right)^{1/2}, \tag{1.3}$$

where $R_{\rm eq}$ and $R_{\rm pole}$ are the equatorial and polar radius, respectively. Therefore, as W approaches 1, $R_{\rm eq}/R_{\rm pole}$ goes to 1.5.

Figure 1.3 shows the estimated oblateness versus v sin i for several spectral types and luminosity classes. Some relevant aspects are: i) most of the MS early-type stars (circles) occupy high-velocity regions ($\gtrsim$ 200 km/s), while the late-type stars are more concentrated in low-velocity regions; ii) giant, subgiant, and MS early-type stars have larger oblateness. These results strengthen the view the fast rotation is important to understand the formation and evolution of stars, being more common among early-type O, B and A stars (Cranmer, 2005).

The large rotation rates associated with Be stars play an instrumental role in the formation of the disk, allowing photospheric material to be ejected into orbit and so triggering the Be phenomenon (Struve, 1931). These high rotation rates require spin up mechanisms, to enable the Be star to reach nearly critical rotation rates as they evolve (Grudzinska et al., 2015). Among these mechanisms is the *spin up during the* MS evolution (Ekström et al., 2008), associated with

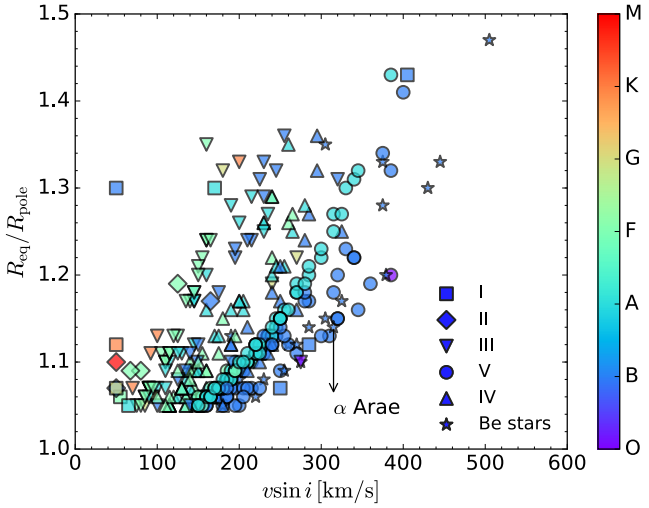

Figure 1.3: Oblateness versus projected velocity for several spectral types. The different colors represents the spectral types and the different symbols the luminosity classes (data from van Belle, 2012). The position occupied by α Arae is indicated for later comparison.

the second half of the MS lifetime of the B stars (McSwain and Gies, 2005). Besides, Huang et al. (2010) concluded from V_{eq}/V_{crit} distributions that low-mass B stars are born with a larger proportion of rapid rotators than high-mass B stars. Their results suggest that high-mass B stars experience angular momentum losses across the pre-MS and during the MS phase. In this context, statistical studies (e.g. Cranmer 2005) present evidence that cooler Be stars are more likely to be critical rotators. Furthermore, according to Massey (2003) the rotation might also be responsible for transporting stellar material from the core to the photosphere (Meynet and Maeder, 2000). This could exert a profound effect on the stellar mass loss rates (Maeder, 2009).

Another spin up mechanism is the binary spin up in a mass exchange binary, already described above. One current topic of interesting in CBe research is to identify the relative role of each process (evolutionary spin up vs. binary evolution) in determining the observed CBe population.

It has been understood long ago that fast rotation is not the only mechanism behind the Be phenomenon. The existence of Be stars rotating at somewhat lower rates (as low as $W \sim 0.6$), mainly among the earliest spectral subtypes (Huang et al., 2010), suggests that rotation alone can not trigger the Be phenomenon. Therefore, additional mechanisms to push the photospheric material to form the disk are needed (Sect. 1.5.1).

1.3.2 Gravity Darkening

Gravity Darkening (GD) is another effect caused by rotation. It causes flux to be redirected towards the pole, thus making the poles hotter than the equator (von Zeipel, 1924). McGill et al. (2011) studied the effect of the GD upon the thermal structure of Be star disks for models covering a wide range of spectral types and rotation rates. They showed that the GD produces changes in the temperature structure of Be disks.

GD increases the relative weight of the polar regions in the integrated flux, causing the photospheric line profiles to appear narrower (Townsend et al., 2004; Cranmer, 2005). This later effect is quite important, as it leads to a systematic underestimate of the $v \sin i$ (Townsend et al., 2004). Therefore, there are systematic errors in the determination of rotational rates and inclination angles, depending on whether GD is adopted (Frémat et al., 2005).

1.4 Other Peculiar Hot Stars

Besides CBe, there are several other stellar groups classified as peculiar stars (see summary by Rivinius et al., 2013) that, sometimes have their properties associated with the presence of non-negligible magnetic fields. This constitutes an important ingredient to differentiate them from the CBe, since large-scale magnetic fields have not been detected in any CBe star to date.

Below we describe the broad characteristics of some other emission line stars.

1.4.1 Classical Oe Stars

A few stars hotter than B0 can present signs of decretion disks; this is the case of Oe stars. Oe stars are rapidly rotating O stars with narrow Balmer and helium emission lines along with broad absorption lines, but not having the characteristic emission features of Of stars, such as HeII λ4686 and NIII λ4634-40-42, associated with strong stellar winds (Conti and Leep, 1974). They also present V/R and Balmer line variability (e.g. Rauw et al., 2007) and can present HeI emission lines (e.g., Frost and Conti, 1976). In the context of the VDD model, Golden-Marx et al. (2016) suggests that Oe stars are the high-mass extension of the Be phenomenon. Oe stars have stronger radiative forces, reducing their disk lifetime to order of days[3]. This can explain the rarity of the Be phenomenon among O-type stars. From Figure 1.4, adapted from Kee et al.

[3] Johnston et al. (2015) published the discovery of a keplerian-like disk around the forming O-type star AFGL 4176 from ALMA data in 1.2 mm.

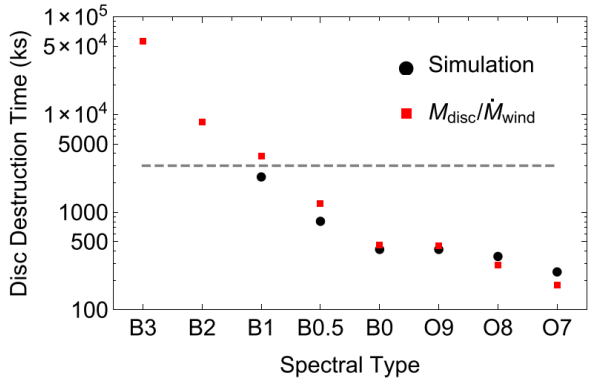

Figure 1.4: Time to destroy an optically thin disk as predicted by $M_{\rm disc}/\bar{M}_{\rm wind}$ (red squares) compared with the time from simulations (black circles) made by Kee et al. (2016).

(2016), it is possible to note that the lifetime of a disk decreases by a factor of ~ 250 when we compare B3 to O7 spectral types. It must be emphasized, however, that the role of ablation in the disk mass budget is still uncertain.

For the purpose of studying the presence of the Be phenomenon in late-type O stars, we made use of a new calibration of the stellar parameters of O stars given by Martins et al. (2005). In their work, contrary to previous works (e.g. Vacca et al. 1996), new ingredients such as metallicity, wind, and line-blanketing effects were considered (they did not consider the oblateness). Their results are shown in two types of effective temperature scales: a) an *observational scale* derived from a compilation based on spectroscopic studies; b) a *theoretical scale*: calculated directly from interpolations of a `CMFGEN` (Hillier and Miller, 1998) grid of `NLTE` spherically extended line-blanketed models. They obtained a good agreement between the theoretical and observational scales for dwarfs and super-giants stars. Table 1.3 shows their stellar parameters for the *observational scale*.

1.4.2 Bn Stars

The spectroscopic appearance of Bn stars is virtually identical to CBes when the later are in a disk-less phase (Kolb and Baade, 1994). They are a non-negligible subgroup of the B stars. For instance, Baade (1992) pointed that there is for every Be star listed in the Bright Star Catalogue (Hoffleit and Jaschek, 1982) a similar Bn star with the same spectral type and projected velocity, $v \sin i$.

Table 1.3 - Stellar parameters of late MS O stars obtained from Martins et al. (2005). Spec: results obtained from spectroscopic analyses.

Spectral Class	$T_{\rm eff}$ [K]	$\log g_{\rm spec}$ [cm s^{-2}]	$M_{\rm V}$	BC	$\log L$ [$L_\odot$]	$R_\star$ [$R_\odot$]	$M_{\rm spec}$ [$M_\odot$]
5	40,862	3.92	5.21	3.77	5.49	11.20	38.08
6	38,867	3.92	4.92	3.62	5.32	10.11	30.98
7	36,872	3.92	4.63	3.47	5.14	9.15	25.29
7.5	35,874	3.92	4.48	3.39	5.05	8.70	22.90
8	34,877	3.92	4.34	3.30	4.96	8.29	20.76
8.5	33,879	3.92	4.19	3.22	4.86	7.90	18.80
9	32,882	3.92	4.05	3.13	4.77	7.53	17.08
9.5	31,884	3.92	3.90	3.04	4.68	7.18	15.55

Interestingly, the occurrence of Be/Bn transitions appears to be absent. In summary, there are two main characteristics that differentiate Be and Bn stellar types and point to independent evolutionary paths: (i) no record of Bn stars observations displaying any circumstellar emission; (ii) the absence of non-radial pulsation in Bn stars, in contrast with the relatively high incidence among Be stars (Baade, 1992).

1.4.3 Ae and A Shell Stars

The A spectral class has two peculiar spectral types: Ae and A shell stars. They might present emission in the Balmer lines and strong IR excess. Bohlender (2016) found an increase in the frequency of Hα emission and shell phenomena in the most rapidly-rotating A-type stars and a decrease as the $T_{\rm eff}$ decreases. These trends are also seen in CBe and might be ascribed to the presence of a disk. This evidence suggest that the Ae stars are regarded as the late-type extension of Be stars, although they are likely confused with β Pictoris objects, in which case their disks would be pre-MS primordial disks (Rivinius et al., 2013). We show their stellar parameters in Table 1.4.

1.5 The Circumstellar Disk of Be Stars

Disks are natural consequences of accretion systems, being present in the formation of Young Stellar Objects and in close binary systems with mass exchange (Owocki, 2006). In this context, Be stars are too old to have kept a protostellar disk, and today it is firmly established that their

Table 1.4 - Stellar parameters of early MS A stars obtained from Adelman (2004).

Stellar Class	$M_\star$ [$M_\odot$]	$R_\star$ [$R_\odot$]	$T_{\rm eff}$ [K]
A0V	2.40	1.87	9,727
A2V	2.19	1.78	8,820
A5V	1.86	1.69	7,880
A6V	1.80	1.66	7,672
A7V	1.74	1.63	7,483
A8V	1.66	1.60	7,305
A9V	1.62	1.55	7,112

disks are not primordial. The disk of Be stars becomes apparent at optical wavelengths mainly by the presence of hydrogen (e.g. Balmer lines) and metallic emission lines (stronger HeI and FeII lines) (Lamers et al., 1980), and by the polarization of the stellar light by the disk (e.g., Yudin, 2001; Kjurkchieva et al., 2016). The IR domain is characterized by an excess emission due to continuum bound-free and free-free thermal emission (e.g. Cote and Waters 1987).

The geometry of Be star disks is well known. For instance, the confirmation that the disk shape was not spherically symmetric came from polarimetric and optical interferometric observations (e.g. McLean and Brown, 1978; Porter, 1996; Quirrenbach et al., 1997). These facts have been recently strengthened by the measurements of opening half-angles of disks of CBe (Cyr et al., 2015). The values range from 0.15° to 4.0° in thin disks, being able to reach larger values (3.7° to 14°) in thicker disks, which agrees with the current theory (Sect. 1.5.1).

The current theory used to explain the workings of the CBe disks is the viscous decretion disk model (VDD, Sect. 1.5.1). The life cycle of a Be disk is quite complex, since the vast majority of Be stars show variability in different temporal scales (Okazaki 1997; Carciofi et al. 2009; Rivinius et al., 2013). Conceptually, the disk formation starts from material ejected from the star through some still unknown process (Sect. 1.5.1). After being ejected, the material diffuses outwards under the action of viscous torques resulting in the formation of a decretion disk. The disk continues to build-up as long as the mass injection goes on. If this phase lasts for a sufficiently long time, the disk will eventually reach a near steady-state. After mass injection ceases, the disk begins to dissipate inside-out, with the inner disk (partially) reaccreting quite quickly, followed by the slow dissipation of the outer disk. Haubois et al. (2012) explored several mass injection scenarios (e.g., long formation followed by long dissipation; cyclic on and off behavior, etc.), and showed that the density profile of Be stars disks can be quite complex. Several recent stud-

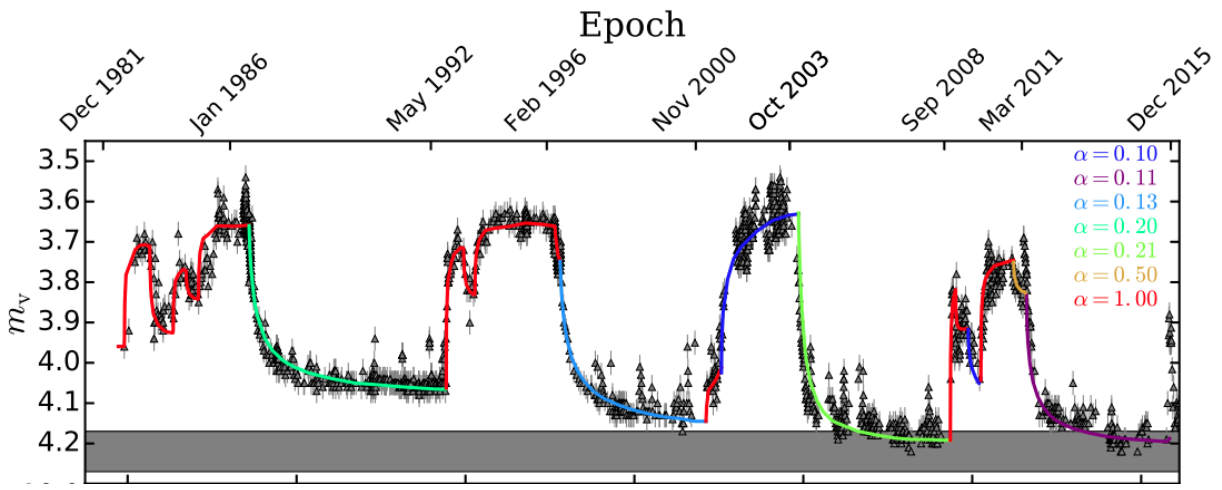

Figure 1.5: Model fit of the full light curve of ω CMa (Ghoreyshi et al., 2018).

ies (Carciofi et al. 2012; Ghoreyshi et al. 2018; Rímulo et al. 2018) successfully fitted detailed disk hydrodynamical calculations with observations. One example is shown in Fig. 1.5, what fits long-term observations of the CBe ω CMa with `VDD` models (Ghoreyshi et al., 2018). The star went through four complete cycles of disk formation and (partial) dissipation in the past 30 years, and the `VDD` model was able to reproduce this complex behavior.

The disk physical parameters were investigated by many authors. For instance, Vieira et al. (2017) inferred the disk density parameters (Fig. 1.6), the density at the base of the disk, ρ_0, and the slope of the density profile, n, for a sample of 80 Be stars in the `VDD` context. They found that $1.5 < n < 3.5$ with the most frequent values spanning from 2.0 to 2.5 for all spectral types. In addition they found that $10^{-12} < \rho_0 < 10^{-10}$ [g cm^{-3}], which agrees with Arcos et al. (2017b). Both studies established that the disks are denser around early-type than in late-type stars. According to the results of Haubois et al. (2012) and Panoglou et al. (2016), the disk density slope is a proxy of the dynamical state of the disk. In short, a disk with $n \geq 3.5$ is probably still in the build-up phase; if n is in the 3.0-3.5 range, the disk is likely in a steady-state phase, while disk with low values of n can either be dissipating (Haubois et al., 2012) or showing signs of matter accumulation owing to a nearby binary companion (Panoglou et al., 2016).

According to Huang et al. (2010), the low-mass stars ($M < 4\,M_\odot$) need a higher rotation rate ($V_{\rm eq}\,/\,V_{\rm crit} > 0.96$) to become a Be star, while that for high-mass cases ($M > 8.6\,M_\odot$) this lower limit decreases to $V_{\rm eq}\,/\,V_{\rm crit} > 0.64$. Earlier statistical studies endorse this hypothesis. For example, Yudin (2001) identified that larger values of polarization and `IR` excesses are more present among early spectral types. Moreover, they found that about 95% of the Be stars in their

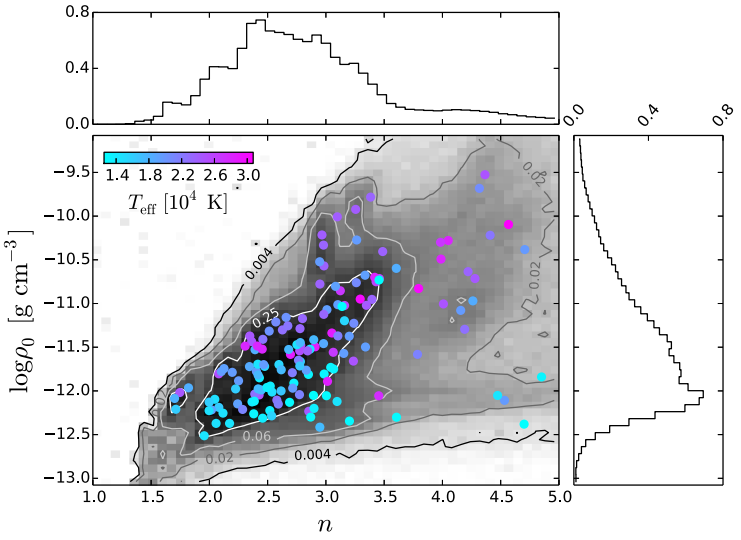

Figure 1.6: Distribution of $< n >$ and $< \log \rho_0 >$ for Be stars with emission line profiles. $< n >$ is a measure of the density slope of the disk and $< \rho_0 >$ is the mass density at its base. Reproduced from Vieira et al. (2017).

sample exhibit intrinsic polarization on the level $0\% < p_\star < 1.5\%$ (Fig. 1.7a). The behaviour of the polarization and the near IR excesses of the Be stars revealed a maximum mean value between B1-B2 spectral types, decreasing toward late spectral types (1.7b).

1.5.1 Viscous Decretion Disk Model

In the last decade, a consensus emerged of how Be disks are structured thanks to observational and theoretical advances. Undoubtedly, the only theory capable of explaining the global picture presented by observations of Be disks is the Viscous Decretion Disk model, proposed by Lee (1991) and developed by several other authors (Porter 1999; Okazaki 2001; Bjorkman and Carciofi 2005b, Krtička et al. 2011). The VDD model is similar to that employed for protostellar disks (Pringle, 1981), the difference being that Be disks switch between *outflowing* and *inflowing*, while pre-MS disks are *inflowing*. In the VDD model, it is supposed that an unknown mechanism injects material at the base of the disk at Keplerian orbital velocity. It is nowadays commonly suggested that the underlying mechanism behind the actual mass loss involves some combination of the following: non-radial pulsation, a combination of frequencies of different pulsation modes (Baade et al., 2016), binarity (Sect. 1.2.2) or small scale magnetic fields (Rivinius et al., 2013). Once the material was ejected, turbulent viscosity transports mass and angular momentum from the inner to the outer disk. Therefore, the density rises faster in the inner disk regions during its growth, with the outer parts filling up much more slowly.

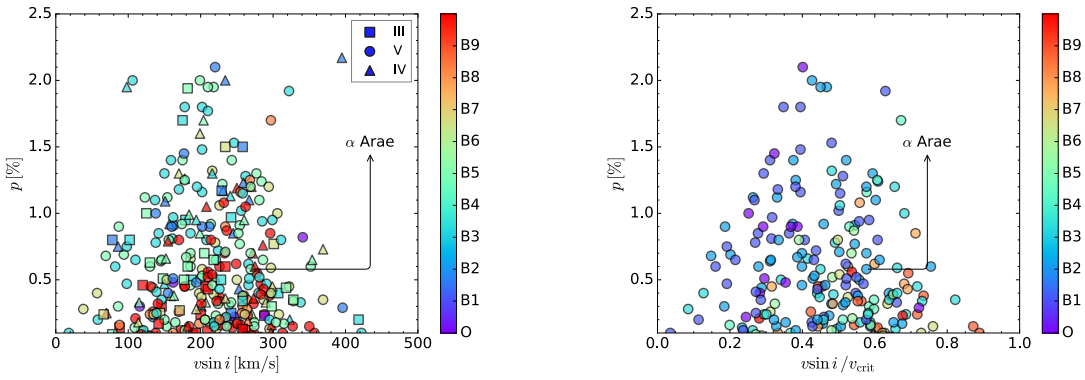

(a) *(b)*

Figure 1.7: Left: Linear polarization level versus projected velocity for luminosity classes III, IV, and V. Right: Linear polarization level versus projected velocity over critical velocity for MS stars. Data from Yudin, 2001.

The VDD model has been employed in the study of individual Be stars (e.g. Carciofi et al. 2006; Carciofi et al. 2009; Tycner et al. 2008; Wheelwright et al. 2012; Carciofi et al. 2012; Wheelwright et al. 2012; Sigut et al. 2015; Faes et al. 2015; Escolano et al. 2015; Klement et al. 2015; Silaj et al. 2016; Ghoreyshi et al. 2018) and samples of Be stars (e.g. Jones et al. 2008; Haubois et al. 2012; Haubois et al. 2014; Touhami et al. 2014; Vieira et al. 2015; Panoglou et al. 2016; Vieira et al. 2017; Klement et al. 2017; Arcos et al. 2017a; Rímulo et al. 2018).

1.6 Aims of this PhD Thesis

The introduction presented above provides a quick summary of the state-of-the-art in Be star research. Much has been learned about the central star characteristics, with some Be stars having their intrinsic properties measured with great precision by means of interferometric observations (e.g., Achernar; Domiciano de Souza et al. 2014). However, for the vast majority of Be stars their fundamental parameters are still poorly known, with estimates in the literature sometimes differing by several spectral sub-types. This is issue number one.

Their disks have also been subject of an unheard of level of scrutiny. Only a handful of Be stars were carefully modeled in detail, while samples were modeled using more simplified approaches. This is issue number two: detailed modeling of large samples are needed in order to form a clear picture of Be stars as a population.

Detailed modeling of one star is a very time-consuming endeavor, since what is usually done is a manual search in the parameter space (e.g., the model of β CMi of Klement et al., 2015 that to

date remains the most detailed model of a Be Star disk). This approach has a fundamental flaw: since a Be + disk system has many free parameters, *without exploring all the parameter space one cannot be confident of the results of manual searches especially when there are degeneracies is the parameters*. Furthermore, all studies so far usually fix a set of parameters (e.g., the central star properties), and let only a few vary. This is problematic as the results usually do not include the usually large uncertainties and their correlations in the parameter values. This is issue number three.

A final issue is that most studies so far approach the star and disk independently. A set of observations (say, photospheric line profiles) is used for pinpointing the central star properties, while another set (say, polarization) is used to investigate the disk. The system, however, is coupled: the star affects the disk by its irradiation, while the disk may affects how a star is seen by the observer. *Therefore, a proper approach to the problem is to explore all observables simultaneously*. This is issue number four.

The goal of this thesis is to address the four issues above. This was done by developing a large and complete grid of CBe models that include all the relevant stellar and disk parameters. The grid, dubbed BeAtlas, is then used in conjunction with advanced Bayesian statistical methods for multi-parametric fitting to allow for a seamless analysis of arbitrary sets of observations. The analysis is done simultaneously for all observables and all parameters, resulting in a set of posterior probabilities for each parameter. These posterior probabilities show how well a parameter was constrained (or not), allow for robust error estimates and, more importantly, allow the exploration of the interdependence of the parameters.

BeAtlas was tested initially for the well-known and well-studied star β CMi and for a set of 111 B, Bn, Oe, Ae stars that had precise `UV` spectra from the `IUE` satellite. It was then applied to the CBe α Arae.

The thesis is organized as follows. The statistical tools and BeAtlas are shown in Chapters 2 and 3, respectively. In Chapter 4, we describe the adopted methodology. Chapter 5 is devoted to the study of the sample of B, Bn, Oe and Ae stars, and Chapters 6 and 7 describes the results for β CMi and α Arae, respectively. We summarize our conclusions in Chapter 8. In Chapter 9, we show the future prospectives. The published articles, tutorials, and tables are presented in the appendices.

Chapter 2

Statistical Tools

2.1 Chapter Summary

This Chapter describes the statistical tools adopted in our study. A discussion on the statistical theory is presented, followed by a description of the Emcee code used in the inference procedure. The visualization tools are shown in Section 2.4. We end this chapter by showing an example application (Sect. 2.5).

2.2 Astrostatistics

The history of Astrostatistics can be traced back as far as the ancient studies developed by Thales of Miletus (624 - 546 BC); (Hilbe et al., 2017). Notoriously, he predicted a total solar eclipse in central Lydia in May 585 BC. Similarly, Hipparchus (190-120 BC) also applied primitive statistics in his analysis. It looks that, at least from these examples, statistics somehow or another accompanied the developments in Astronomy, being essential for the development of our knowledge. In principle, we can say statistics refers to a science designed to summarize[1] a set of collected finite raw data, providing useful information that allows us make decisions based on the data while allowing for the imperfection in the data.

2.2.1 Machine Learning and Data Mining

The term Machine Learning refers to a set of techniques for interpreting data. These techniques essentially work by comparing data with models through several inference methods, for

[1] Here, it is implicit the process of analyzing the data for "the purpose of classification, prediction, and of attempting to quantify and understand the uncertainty inherent in phenomena underlying data" J. M. Hilbe 2014.

instance: regression, supervised classification, maximum likelihood estimators, or Bayesian inference (Ishak, 2017). In the Machine Learning context, there is a set of techniques for analyzing and describing structured data called *Data mining* which is used, for example, to find patterns in large data sets.

Next, we will revisit essential statistics concepts to draw an overview didactic picture of our inference problem.

2.2.2 Probability Distributions

Wall and Jenkins (2012) argue that the concept of probability is the keystone in statistics, providing crucial information to make a decision. For our purposes, i.e. the Data Mining and parameter inference context, it poses the problem of how to estimate the distribution $h(x)$ from which the values of a continuous random variable x are drawn. The distribution $h(x)$, also called the probability density function (PDF), simply quantifies the probability, $h(x)dx$, of a value of x to be between x and $x + dx$. The PDF has the following properties, that apply in the case x is a continuous quantity with allowed values between $-\infty$ and $+\infty$

(i) $p(a < x < b) = \int_a^b h(x)dx$;

(ii) $\int_{-\infty}^{\infty} h(x)dx = 1$;

(iii) $h(x)$ is a single-valued non-negative number for all real x.

The integral of the PDF from minus infinity to x, in the case of a continuous distribution,

$$H(x) = \int_{-\infty}^{x} h(x')dx' \,, \tag{2.1}$$

is called the "cumulative distribution function", CDF. For a random variable Y, $H(Y)$ is the probability that Y will be less than or equal to x.

The *quantile function*, which specifies the value of a random variable being less than or equal a given probability, is the inverse of the CDF. In other words, the quantiles are values that limit a certain percentage of the observations of a given variable. The notation for a quantile is q_d, where d indicates the defined percentage. For instance, $q_{12\%}$ is the quantile that delimits 12% of the lower values of the data.

2.2.3 Bayes' Theorem

Thomas Bayes (1702 - 1761) was an English vicar, mathematician, and statistician. His work as a statistician, probably published posthumously, is the *Essay Towards Solving a Problem in the Doctrine of Chances*. Bayes' theorem allows us to make inferences from data, by considering what is known about each free explored parameter. Therefore, Bayesian method yields optimum results assuming that all the supplied information is correct.

Nowadays Bayes' inference is often applied to estimate parameters and their uncertainties from a set of model parameters when the shape and scale of their probability density distribution are unknown (Astrobites - "Your Gateway to the Bayesian Realm"[2]). Opposite to descriptive (also called frequentist) statistics, in the Bayesian context, we have a probability distribution $f(\text{data}|\Theta)$[3], and we wish to know the parameter vector Θ. The Bayesian route is clear: it proposes using Bayes' theorem to compute the posterior distribution of Θ

$$p(\Theta|x) = \frac{p(x|\Theta)p(\Theta)}{p(x)} \,. \tag{2.2}$$

The posterior probability $p(\Theta|x)$ is the probability of our model parameters Θ given the data x. To compute this we multiply the prior $p(\Theta)$ (what we know about Θ before we have seen any data) and the likelihood $p(x|\Theta)$, i.e. how we believe our data is distributed. $p(x)$ is the probabilities of observing x independently of θ, also known as the *marginal probability*.

Likelihood function

We can rewrite the Bayes' theorem as

$$p(M, \Theta|D, I) = \frac{p(D|M, \Theta, I)p(M, \Theta|I)}{p(D|I)} \,, \tag{2.3}$$

where D represents the experimental data, M the set of models, $\Theta = \Theta_1, ..., \Theta_k$ the model parameters and I additional information.

The term $p(D|M, \Theta, I)$ is the distribution that is used to explain the predictor (i.e. independent variable) and parameter data called likelihood, defined by some model $M(\Theta)$ and all prior information I.

[2] astrobites.org/2011/11/26/your-gateway-to-the-bayesian-realm;

[3] The conditional probability of A, given that we know B is given by, $p(A|B)$.

As an example of likelihood, let's consider the well-known χ^2 function

$$p(D|\Theta) = \sum \frac{(f_\mathrm{i} - f_{\Theta,i})^2}{\sigma_\mathrm{i}^2}. \tag{2.4}$$

This function represents the probability of getting a set of N observations of the quantity f_i with an error of σ_i given a theoretical model $f_{\Theta,i}$. Therefore, the likelihood is a function of the model parameters, Θ.

Priors

The term $p(M, \Theta|I)$ in Eq. 2.3 is called *prior* or "initial belief". It is a *a priori* information that summarizes the probability about a particular model parameter or a set of model parameters. Therefore, a prior is essentially used to constrain model parameters. Although the term "prior" suggests "before the inference process" actually it summarizes what it is known about the data.

Posterior

The product of the prior and likelihood distributions defines the posterior ($p(M, \Theta|D, I)$), the probability of our "improved belief". In particular, we can quantify the uncertainty in our model parameters using this posterior probability distribution. A common approach is to apply some numerical technique to draw samples from the posterior, so we can characterize the shape of its distribution. This is where Markov Chain Monte Carlo (`MCMC`) comes in.

2.3 Markov Chain Monte Carlo

`MCMC` methods were developed for sampling `PDF`s. The most common `MCMC` implementation is a random-walk algorithm that estimates the posterior distribution thus allowing us to obtain the uncertainties for each of our model parameters.

In essence, the random walk starts with one random set of model parameters (a "initial state"), which is then perturbed and moves (walks) in the parameter space[4]. A "chain" of states is created through this process. Note that the next step only depends on the current step. This is a fundamental requirement since it guarantees the Markov Chain will be able to explore all of the parameter space. Through this process, we build a "chain" of states that can be used to generate the `PDF`s of each parameter.

[4] The step size should be controlled according to the acceptance fraction (Foreman-Mackey et al., 2013).

In summary, the typical procedure is:

1. Initially, identify an acceptable starting model. From here, we gauge how the model parameters are constrained and use this information to assign a list of "walkers", and the scale length to perturb each parameter value;

2. Calculate the posterior probability of this state, $p(\Theta_{\rm old}|D)$;

3. Next, apply a random step to our current state, and calculate the posterior probability for this new trial state $p(\Theta_{\rm new}|D)$;

4. Compare the two posteriors. If $p(\Theta_{\rm new}|D)$ is better than $p(\Theta_{\rm old}|D)$, accept it as a new state. If it is worse, there is no change otherwise the new state is accepted. Note that because we are taking the ratio between the two probabilities for the same physical model, it is not necessary to compute again the evidence term, $p(D)$;

5. Go back to step 3. Keep repeating until a "chain" of $N_{\rm step}$ states is assembled. The whole chain, or part of it, can be used to estimate the posterior distribution of each parameter.

2.3.1 Metropolis-Hastings `MCMC`

The Metropolis-Hastings algorithm (Metropolis et al., 1953) constitutes the simplest `MCMC` algorithm. It depends on two inputs: (i) a set of model parameters to be sampled, $f(\Theta)$; (ii) a proposal function $q(\Theta'|\Theta)$ that delivers samples. By using these two inputs, the algorithm is able to evaluate $f(\Theta)$[5] for any set of the parameters Θ. Then, the algorithm proceeds drawing a new position Θ' in the parameter space starting from a previous position Θ. This procedure allows us to random-walk around the parameter space.

In summary, the algorithm is:

1. Initialization: choose an arbitrary point Θ_0;

2. For each iteration k, given a probability function $f(x) \propto p(x)$:

   (a) For the next sample, generate a candidate Θ' from the distribution $g(\Theta'|\Theta_{\rm k})$. $g(\Theta'|\Theta_{\rm k})$ is an arbitrary probability density function that suggests a candidate for the next sample value Θ' given the previous sample value $\Theta_{\rm k}$;

[5] In our context, this function would be the posterior function evaluated at the observed data D.

(b) Calculate the fraction: $\alpha = f(\Theta')/f(\Theta_k) = p(\Theta')/p(\Theta_k)$. This allows us to decide if we accept or reject the current candidate;

(c) Accept or Reject:

i. Generate a random number u between 0 and 1;

ii. If $u \leq \alpha$ the candidate is accepted ($\Theta_{k+1} = \Theta'$);

iii. If $u > \alpha$ the candidate is rejected ($\Theta_{k+1} = \Theta_k$).

2.3.2 Emcee

The code Emcee is a high-performance open source Python module[6]. It uses variations of a MCMC method developed by Goodman and Weare (2010) where multiple "walkers" are used to propagate multiple Markov chains simultaneously for the parameter determination, their correlations and error estimates. The algorithm has several advantages with relation to traditional MCMC sampling methods (Foreman-Mackey et al., 2013), as well as the Metropolis-Hastings (Sect. 2.3.1), being more efficient even in parameter spaces with many dimensions. Another advantage of the algorithm is that it requires hand-tuning of only 1 or 2 parameters compared to $\sim N^2$ for a traditional algorithm in an N-dimensional parameter space. What is used as input to the code are i) a function to generate a new random model; such function can be based on a previously computed model grid; ii) the observational values to be fitted; iii) whatever prior information available.

The Emcee code uses the following definition for the posterior probability

$$p(\Theta, \alpha|D) = \frac{1}{Z} p(\Theta, \alpha) p(D|\Theta, \alpha) \tag{2.5}$$

where $p(\Theta, \alpha)$ is the *a priori* distribution, $p(\Theta, \alpha|D)$ is the likelihood, and $Z = p(D)$ is a normalization factor.

Therefore, having defined the likelihood and prior functions, together with the models and the observations, the MCMC generates a *random walk* in the parameter space and uses these chains to draw samples $\{\Theta_i\}$ to estimate the posterior probability density.

[6] It is available online: http://dan.iel.fm/emcee under the MIT License.

Estimator of performance and reliability

Usually, many (N_{chains}) chains are independently computed. The end result is the combination of all chains, unless there is a reason to discard some chains. In summary, a MCMC simulation is composed of a total of $N_{\text{step}} \cdot N_{\text{chains}}$ samples of $(\Theta, \alpha|D)$.

The quality of each simulation done with the Emcee code is accessed by an important measurement: the acceptance fraction, a_{f}. It corresponds to the number of accepted steps over the total number of steps of each walker. Hence, each walker, after finishing the chain, will carry its own acceptance fraction. As a rule of thumb, the mean acceptance fraction, $\bar{a}_{\text{f}}$, must be between 0.2-0.5 (Foreman-Mackey et al., 2013). If $\bar{a}_{\text{f}} \sim 0$, then nearly all proposed steps are rejected, so the chain will have few independent samples and the sampling will not represent the target PDF. Typically, a low mean acceptance fraction means that the posterior probability is multi-modal, with the modes separated by wide, low probability "valleys". Conversely, if $\bar{a}_{\text{f}} \sim 1$ then nearly all steps are accepted and the chain will not produce representative samples. One possible case with $a_{\text{f}} \sim 1$ is when all the parameter space is narrowly confined within a minimum in the PDF for all parameters.

2.4 Visualization Tools

In this section we show some useful visualization tools used to display the results of MCMC simulations.

2.4.1 Box Plots

A box plot is a graphical representation involving quantiles. It allows the visualization of position, variability, asymmetry and the occurrence of atypical values of distributions.

To build a box plot, we define a rectangle ("box") in which the lower edge coincides with the first quartile (Q_1)[7] and the superior edge coincides with the third quartile (Q_3)[8]. The interquartile range is defined as $IQR = Q_3 - Q_1$ and comprises 50% of the data. The median is represented by a horizontal trace positioned between Q_1 and Q_3. Outside the box we include the "whiskers" that indicates the data between $[Q_1 - 1.5IQR; Q_3 + 1.5IQR]$. Values outside this range are called "outliers". The above definitions are graphically represented in Fig. 2.1.

[7] 25% of the numbers in the dataset lie below Q_1;
[8] 75% of the numbers in the dataset lie below Q_3;

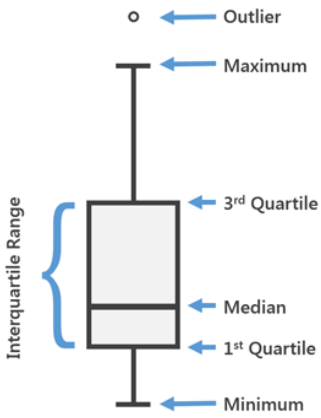

Figure 2.1: Box plot example. Source: ArcGIS - Box Plot[9].

2.4.2 Corner Plots, Chord Plots, and Convergence Diagrams

A corner plot is an illustrative representation to visualize the probability density of the samples in the multidimensional parameter space. The projected probability of the samples is for each pair of parameters plotted to reveal their covariances. In Figure 2.2, we show an example of a corner plot where the distributions of three parameters: x, y and $\log \alpha$ is shown. The dashed lines in the diagonal subplots correspond to the 16th, 50th, and 84th percentiles of the distributions. The subplots under the diagonal panels show the probability density cross-correlations between the pairs of parameters. The path traveled by the walkers in the parameter space is also shown by smoothed black points in the `2D` corner plots.

A chord diagram is a graphical method used to display the inter-relationships between data in a matrix. The data are arranged along the circumference with the relationships between the data drawn as arcs connecting the data (Fig. 2.3). The wider the arc, the stronger the correlation between a pair of parameters.

Figure 2.4 shows the convergence of a `MCMC` simulation for one fitted parameter. This representation constitutes a simple way to verify if the walkers converged to a value. In the same Figure is the "burn-in" phase containing the initial irrelevant steps also shown. In general, the data obtained during the "burn-in" phase over-sample regions with very low probabilities. Due to this, the data obtained during this phase is removed. The remaining region, called the "posterior chain", is used during the statistical analysis to obtain the `PDF`s of the parameters of interest.

[9] https://pro.arcgis.com/en/pro-app/help/analysis/geoprocessing/charts/.
[10] https://corner.readthedocs.io/en/latest/;
[11] https://datavizcatalogue.com/methods/chord_diagram.html;
[12] https://events.mpifr-bonn.mpg.de/indico/event/30/material/slides/12.pdf.

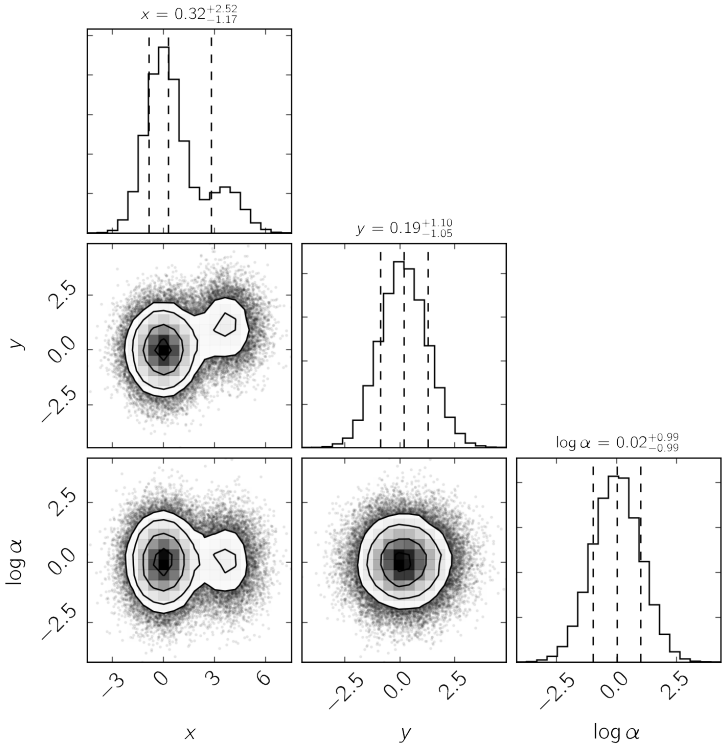

Figure 2.2: Corner plot example. Source: Readthedocs: Corner[10].

2.5 Example of Application

2.5.1 Bayesian Approach

To illustrate the Bayesian inference using the EMCEE code, we choose a set of models and some observational data. For the models, we adopted the KURUCZ (Castelli and Kurucz, 2003) atlas of model atmospheres [13]. This atlas contains about 7 600 models of stellar spectra for a large range of metallicities, effective temperatures (3 500 K $\leq T_{\rm eff} \leq$ 50 000 K), surface gravities ($0.0 \leq \log g \leq 5.0$) and stellar radius ($1\,R_\odot \leq R_\star \leq 2\,500\,R_\odot$).

The observational data were gathered from the INES Archive Data Center[14] for the star Vega (HD172167), which is a star that has been studied in an other project (see Appendix L). The data is from the IUE satellite (see Section 5.2), covering the wavelength range 1 000 to 3 000 Å. Few details are given here about the data and model for simplicity, but the reader is referred to Chapters 5, 6 and 7 for more detailed examples of the usage of the UV data.

[13] Available at http://kurucz.harvard.edu/grids.html;
[14] http://sdc.cab.inta-csic.es/cgi-ines/IUEdbsMY.

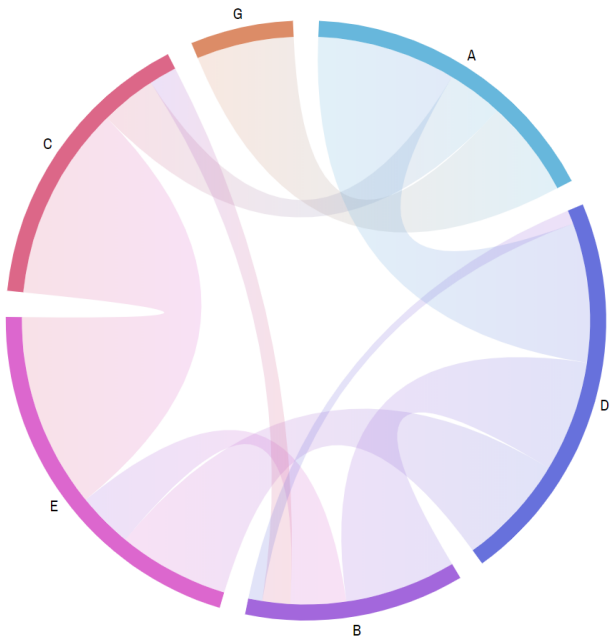

Figure 2.3: Chord plot example. Source: Datavizcatalogue[11].

2.5.2 Likelihood

Given a pair of stellar parameter $T_{\rm eff}$ and $\log\ g$, the observed flux at Earth is

$$F_{\oplus} = F(T_{\rm eff}, \log\ g) \times \left(\frac{R_\star}{d}\right)^2 \times f_{\rm red}, \tag{2.6}$$

where $F(T_{\rm eff}, \log\ g)$ is the interpolated model flux for the free parameters ($T_{\rm eff}$ and $\log\ g$), $(R_\star/d)^2$ is the flux normalization factor[15], which takes into account the stellar radius, $R_\star$, and the distance to the star, d, and $f_{\rm red}$ is the reddening correction law used.

The reddening correction is fundamental since it affects significantly the determination of the stellar parameters. We adopted the correction suggested by Fitzpatrick (1999). This correction is valid for a large wavelength range, going from the far-UV (0.1 μm) up to the IR (3.5 μm). See Sect. 4.2 for more details about interstellar extinction.

The term $f_{\rm red}$ has, as free parameters, the object's color excess $E(B-V)$ and the optical total-to-selective extinction ratio $R_{\rm V}$, given by

[15] The term $(R/D)^2$ comes from the ratio $F_{\oplus}/F_\star$. It is usually called angular radius.

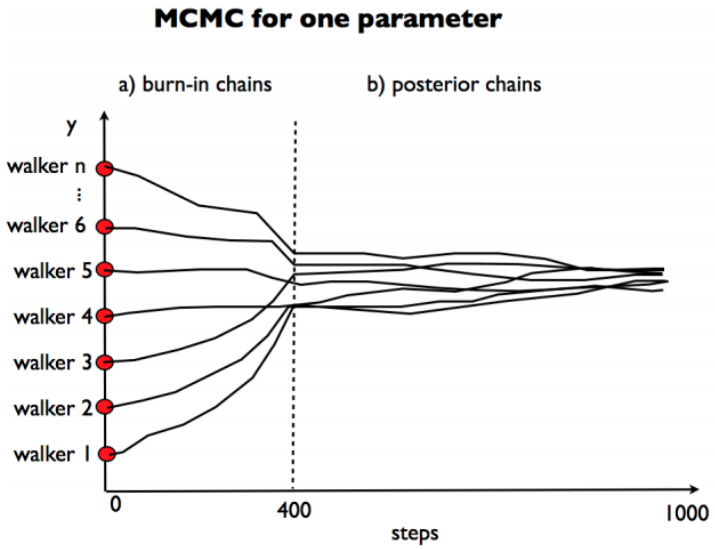

Figure 2.4: Convergence plot example. Source: IMPRS-2017[12].

$$E(B-V) = (B-V)_{\text{observed}} - (B-V)_{\text{intrinsic}}; \tag{2.7}$$

$$R_{\text{V}} = \frac{A(V)}{E(B-V)}. \tag{2.8}$$

Eq. 2.6 reflects a choice made in the modeling procedure: the model is reddened to match the data, not the contrary. In summary,

$$F_{\odot} = F_{\odot}(\lambda, T_{\text{eff}}, \log\, g, E(B-V), R_{\text{V}}, \pi, R_{\star})\,. \tag{2.9}$$

In the last equation, the distance to the star, d is replaced by the astrometric parallax, π (see below). Therefore, the interstellar extinction is evaluated inside each step of each chain.

From the above assumptions, we define the log of our likelihood functions as,

$$\log p(D|\Theta, \alpha) = -0.5 \left[\frac{\log(F_{\odot}/F_{\text{mod}})}{\sigma_{F_{\odot}}/F_{\odot}} \right]^2. \tag{2.10}$$

In short, we have a 6-dimensional parameter space: T_{eff}, $\log\, g$, $R_{\star}$, π, $E(B-V)$ and R_{V}. In terms of code, the likelihood was written as,

```
def lnlike(params, lbd, flux, dflux):
    # Model Parameters
    Teff, logg, Rstar, dist, ebmv, rv = params[0], params[1], params[2],\
        params[3], params[4], params[5]
```

```
    # Corresponding model
    wave_mod, flux_mod = kurucz_models_interp(10**Teff, logg, 10**Rstar,
                                              10**dist, np.min(lbd),
                                              np.max(lbd))
    # Reading observational data
    lbd1, dlogF, logF, logF_mod = log_flux(lbd, dflux, flux,
                                           wave_mod, flux_mod)
    # Reddening the model
    flux_mod = pyasl.unred(1e4 * lbd1, 10**logF_mod, ebv=-1 * ebmv, R_V=rv)
    logF_mod = np.log10(flux_mod)
    chi2 = np.sum(((logF - logF_mod)**2 / (dlogF)**2.))
    return -0.5 * chi2
```

2.5.3 *Prior Assumption*

For this example, we used as prior the Hipparcos parallax (van Leeuwen, 2007). A Gaussian prior was assumed

$$\log p_\pi(\Theta, \alpha) = -0.5 \left(\frac{\pi - \pi_{\rm mod}}{\sigma_\pi} \right)^2 , \tag{2.11}$$

where $\pi_{\rm mod}$ is the random parallax generated in each step of the inference; π and σ_π are the observed parallax and its uncertainty, respectively.

In addition to the prior on the distance, all the parameters were fixed to lie within a given range. This effectively is also a prior, whose functional form is a uniform probability distribution, which is a constant function. The adopted ranges are:

- $3\,500 < T_{\rm eff} < 50\,000$ K;
- $0 < \log g < 5$;
- $0 < E(B-V) < 20$;
- $0 < R_{\rm v} < 6$;
- $1 < R_\star < 2\,500\,{\rm R}_\odot$.

Table 2.1 - Best-fit parameters of Vega. Simulation parameters: 50 walkers, 300 steps and $a_f = 22\%$. [a]: The polar temperature is around $\sim 2\,000$ K higher than the equatorial temperature (Kinman and Castelli, 2002). [b]: IRSA-DUST Webpage [16].

	Values		
Parameter	Inferred	Literature	Ref.
$T_{\rm eff}$ [K]	$3.99^{+0.03}_{-0.01}$	3.982 ± 0.002 [a]	Kinman and Castelli (2002)
$\log g$ [cgs]	4.0 ± 0.5	4.1 ± 0.1	Aufdenberg et al. (2006)
$\log R_\star$ [$R_\odot$]	$0.43^{+0.14}_{-0.04}$	0.41 ± 0.01	Yoon et al. (2010)
$\log d$ [pc]	0.89	0.885 ± 0.001	van Leeuwen (2007)
$E(B-V)$ [mag]	$0.06^{+0.13}_{-0.02}$	0.058 ± 0.001	IRSA[b]
R_V	$3.97^{+0.89}_{-0.91}$	-	-

Once having defined the fluxes, the best-fitting model, in a first stage, is obtained by sampling equation 2.5 with the Emcee `MCMC sampler`, with the likelihood and the prior functions given by Eq. 2.10 and Eq. 2.11, respectively, for all set of parameters simultaneously. The `MCMC` simulation produces samples of the posterior probability density for each free parameter.

In Python the prior can be written as

```
def lnprior(params, dist_pc, sig_dist_pc):
    # Read distance free parameter
    dist = params[3]
    # Determine prior from the observed distance
    chi2_prior = ((dist_pc - dist) / sig_dist_pc)**2
    return -0.5 * chi2_prior
```

The following is an example function for the posterior in Python:

```
def lnprob(params, lbd, flux_obs, dflux_obs, dist_pc, sig_dist_pc, ranges):
    lp = lnprior(params, dist_pc, sig_dist_pc)     # Prior
    lk = lnlike(params, lbd, flux_obs, dflux_obs) # Likelihood
    lpost = lp + lk                                # Posterior
    return lpost
```

[16] https://irsa.ipac.caltech.edu/applications/DUST/.

2.5.4 Results

We tested the method described in the previous sections in a well-known star, Vega. The inferred results are shown in Table 2.1. In the same table, for comparison purposes, we list literature values. These results are only illustrative of the Bayesian inference process, and an analysis of the results for this particular star is not presented in this thesis. Nevertheless, it is striking the inference accuracy when we compare our results with the literature. Noteworthy is the fact that *only the UV spectrum was used in the inference,* nothing else.

Figure 2.5 shows the corner plot, where we can see the resulting PDFs, their correlation, and the best fit in the inset. Figure 2.6 shows the corresponding chord diagram. The chord diagram, for instance, that the extinction parameter $R_{\rm V}$ is strongly linked with the $E(B-V)$ parameter, as expected. There is also a strong correlation between the stellar radius, $R_\star$, and the parallax, p, which simply reflects the fact that a larger (brighter) and more distant star is (somewhat) equivalent to a smaller (dimmer) and closer star. In Fig. 2.7 the convergence diagram is shown. Note a clear convergence for some of the free parameters ($\log g$, $R_\star$, $E_{\rm B-V}$, $R_{\rm V}$). For d, however, the convergence diagram reflects the prior. It is seen that its PDF distribution obeys the range of values (observational parallax and its statistical error) given as prior.

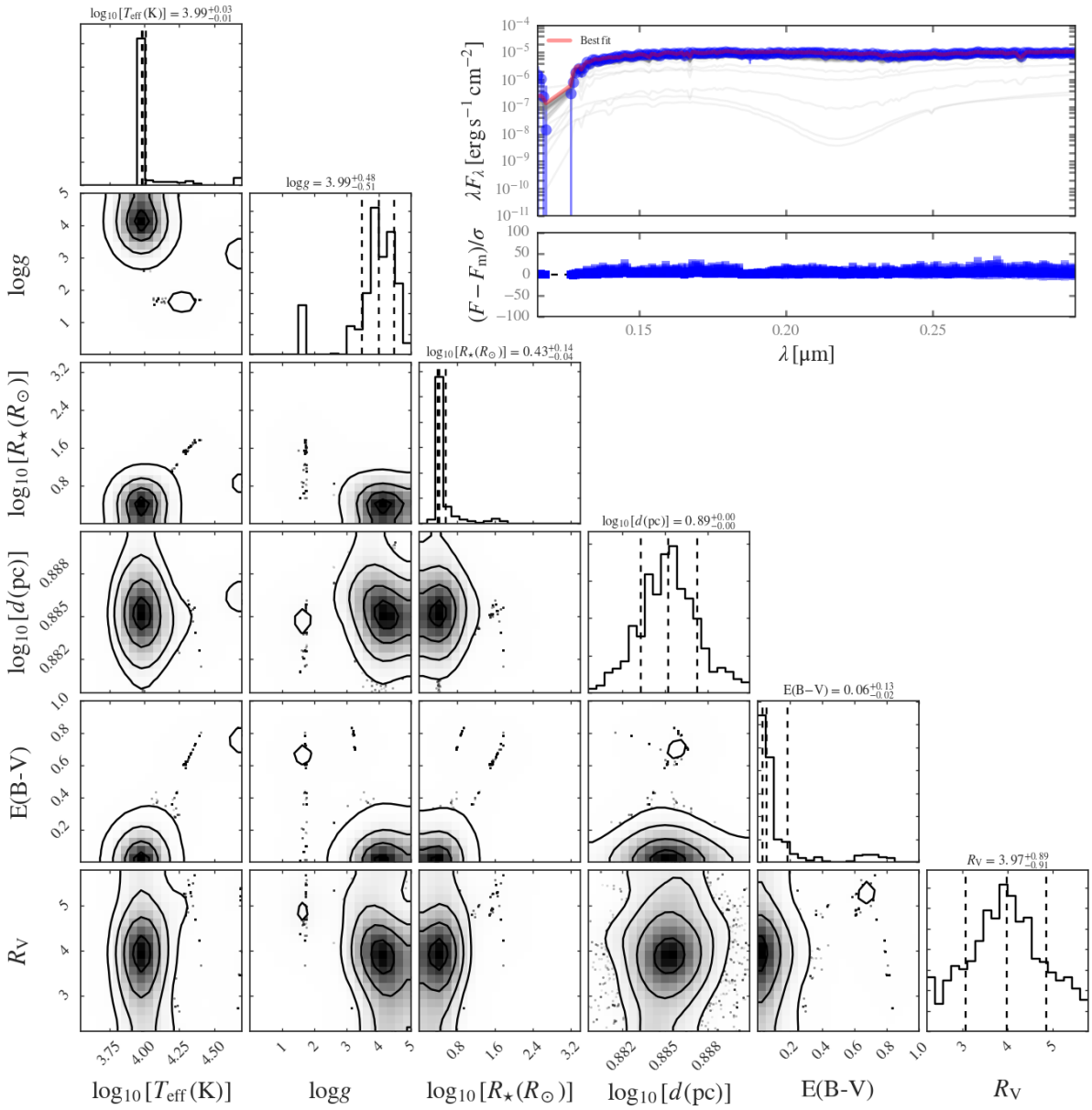

Figure 2.5: Corner plot for the Vega modeling using Kurucz spectra (see text). An explanation of a corner plot can be found in Fig. 2.2. Top right, upper plot: Observed data (blue points) and a random set of sampled models (red curves). Top right, lower plot: residuals of the fit.

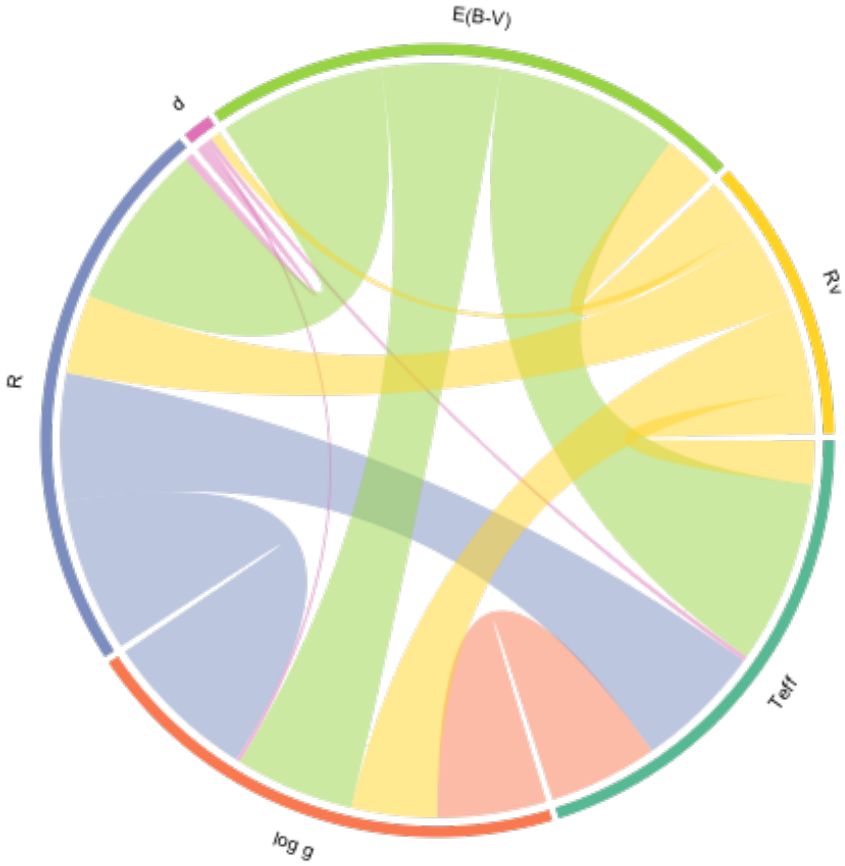

Figure 2.6: Chord diagram for the Vega modeling using Kurucz spectra (see text).

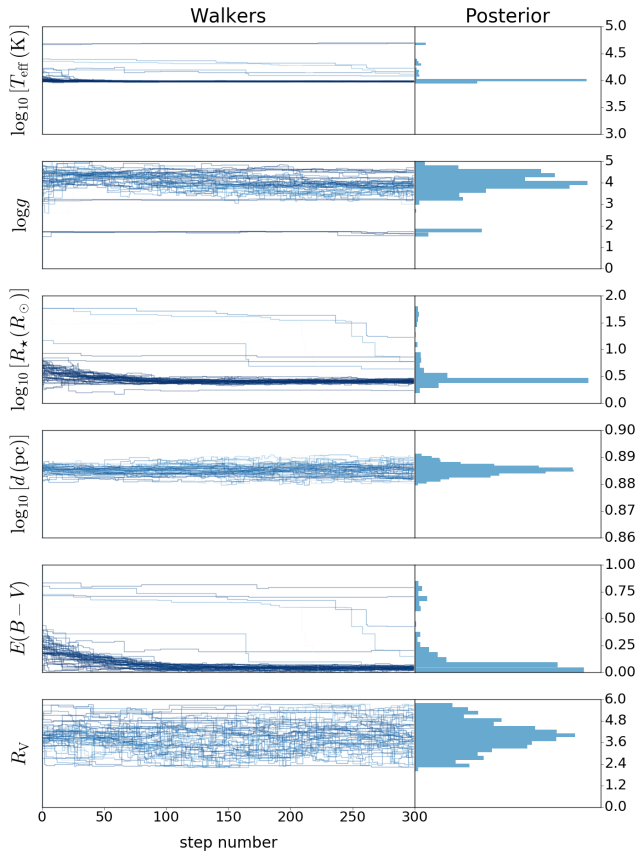

Figure 2.7: Convergence plot for the Vega modeling using Kurucz spectra (see text).

Chapter 3

Model Description: The BeAtlas Grid

3.1 Chapter Summary

This Chapter presents the BeAtlas grid of models (Section 3.2). The radiative transfer code used to compute the models is briefly described in Sect. 3.2.1. The central star is described in detail in Sect. 3.3). The purely photospheric grid is described in Sect. 3.3.1. The disk models and the adopted range in the model parameters are discussed in Sect. 3.4. We discuss the selected observables in Sect. 3.5.

3.2 The BeAtlas Grid of Models

The BeAtlas project arises in the context of grid-based modelling, routinely applied to the determination of physical model parameters (e.g. Hekker et al., 2013; Serenelli et al., 2017). The BeAtlas comprises two systematic grids of models: a photospheric-only (i.e., diskless) grid, and a star plus disk grid (hereafter referred to as "disk grid"), computed according to the `VDD` formulation (Sect. 1.5.1) and covering the typical range of stellar and disk parameters associated with the Be phenomenon.

Some aims of the BeAtlas project are: (i) interpreting the observations of large samples of B and Be stars; (ii) detailed modelling of individual objects; (iii) theoretical studies on the physical properties of disks (e.g., disk thermal structure, effects of the parameters on the observables, etc.); and (iv) planning of new observations. We naturally expect that many other applications will arise from such a comprehensive project.

In the next section we detail the radiative transfer calculations (Sect. 3.2.1). Next, we give an introduction to the Geneva stellar evolution models (Sect. 3.2.2), from which we derived the range of stellar parameters adopted in the BeAtlas grid.

3.2.1 Radiative Transfer Calculations

The models were calculated with the Monte Carlo radiative transfer code Hdust (Carciofi and Bjorkman, 2006, 2008). This code has been successfully applied in several previous studies to interpret multi-technique observations. Some recent examples are: the interferometric study of Achernar (Dalla Vedova et al., 2017), the computation of line profiles of binary CBes, for which the tidal interaction with the secondary excites $m = 2$ spiral density waves in the disk (Panoglou et al., 2018), and the interpretation of optical light curves of CBes using the `VDD` model (Rímulo et al., 2018; Ghoreyshi et al., 2018).

Hdust uses the Monte Carlo method to solve the radiative transfer of polarized radiation in moving media. As such, it can be applied to gaseous disks, winds, etc. Furthermore, it simultaneously solves the radiative and statistical equilibrium problems, thus providing `NLTE` (non-local thermodynamic equilibrium, see Carciofi and Bjorkman 2006) atomic level populations and ionization fractions, as well as the gas kinetic temperature.

The code accepts arbitrary `3D` geometry and kinematics. The circumstellar chemistry comprises atomic hydrogen and/or dust grains, and the inclusion of other atomic species is currently under development (Carciofi et al., 2017). The implemented gas opacity sources are: Thomson scattering, bound-bound, bound-free and free-free absorptions, while the dust grains opacity is computed using Mie theory (e.g. Carciofi et al., 2004). The code also offers a realistic description of the star, which includes limb darkening, gravity darkening, and rotational flattening according to the Roche model (see details in Sect. 3.3). Hdust computes the emergent spectrum (both continuum and emission lines), the polarized spectrum, and synthetic images (Fig. 3.1).

3.2.2 Geneva Grids of Stellar Evolution Models

One very important tool for this work is the Geneva code for stellar evolution of fast-rotating stars (Ekström et al., 2008 and references therein). The code computes the stellar structure and evolution from the `MS` up to the end of carbon burning for massive stars, the early asymptotic giant branch phase for intermediate-mass stars, or core helium flash for low-mass stars. Predictions regarding the spectral evolution of massive stars can also be obtained.

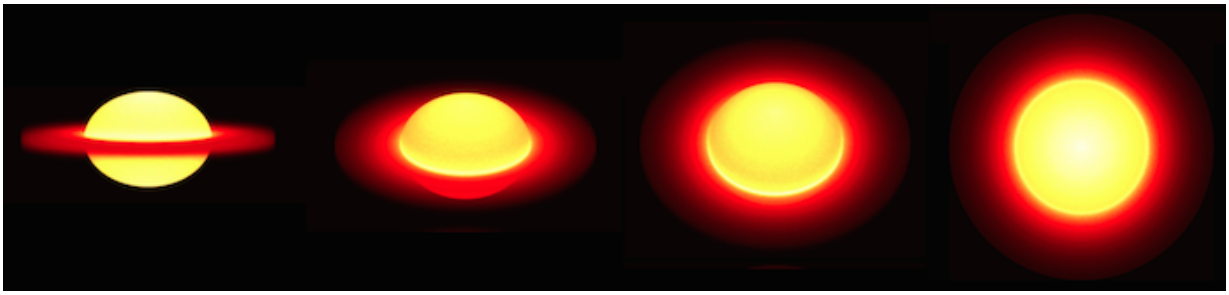

Figure 3.1: Hdust simulation of the Be star Achernar for different inclination angles. The colors are associated with the emitted flux in logarithm scale (brighter regions in light yellow and coldest in dark red). The effects of the stellar rotation can be clearly seen in the central star. (Image courtesy of D. M. Faes).

B-type stars are known to rotate at various velocities, including very fast rotators near the critical velocity such as CBes (Sect. 1.2). Hence, any analysis should take into account these rotational effects. To satisfy this condition, we have chosen the rotating models described by Georgy et al. (2013) and Granada et al. (2013). We selected their models with solar metallicity (i.e., $Z = 0.014$), according to Grevesse and Sauval (1998). The models cover the mass range from 1.7 to 15 $M_\odot$ and $\Omega/\Omega_{\rm crit}$ encompassing from 0 to 1. Specifically for this project, our collaborator Cyril Georgy (Observatoire de Genève) computed evolutionary models for 20 $M_\odot$. This was very important because the old model grid of Georgy et al. (2013) missed the high-mass end of the Be phenomenon. The new mass range now includes typical masses of known Be stars as well as the transition from massive and energetic late-O stars, with strong stellar winds, to the less massive early-A stars in the regime of negligible winds (Georgy et al., 2013).

To illustrate the importance of the rotation for the models, Figure 3.2a shows the evolution of the angular rotation rate ($\omega = \Omega/\Omega_{\rm crit}$) for a `MS` star with 9 $M_\odot$ starting on the Zero Age Main Sequence (`ZAMS`) with different rotation rates. This figure exemplifies the so-called evolutionary spin-up, where angular momentum from the core of the star is transported outwards, causing the outer layers to spin up in evolutionary timescales (see Sect. 1.3.1). The figure also illustrates one of the main shortcomings of the models of Georgy et al. (2013): in their calculations, the star enters the `ZAMS` as a solid-body rotator, and only after `MS` starts does the star relaxes to its differently rotating structure. This is the cause of the fast initial drop of ω for all models. This issue was partially addressed by another publication of the group (Granada and Haemmerlé, 2014), but unfortunately a grid of such models is not available yet.

In Figure 3.2b, the `HR` Diagram is shown for stars with 5, 7 and 9 $M_\odot$ for different values of ω. These figures show basically two aspects of these models: (i) the high influence of rotation

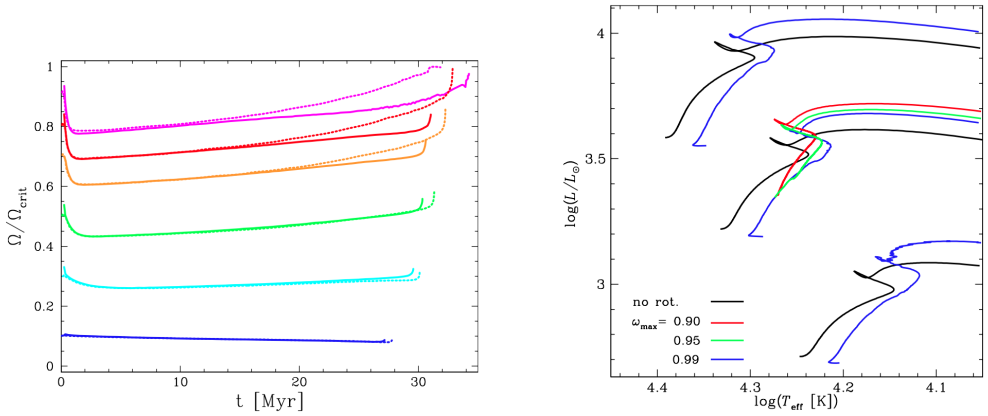

(a) (b)

Figure 3.2: (a) Evolution of rotation rate for a 9 $M_\odot$ stars with $Z = 0.002$, during the MS phase. The solid lines show the Georgy et al. (2013) models, the dotted lines the models by Ekström et al. (2008). (b) HR diagram for 5, 7, 9 $M_\odot$ models at solar metallicity (blue: $\omega = 0.99$, green: $\omega = 0.95$, and red: $\omega = 0.90$).

for the stellar evolution, and (ii) the effects of the rotation on the stellar parameters throughout their evolution. These characteristics motivated us to adopt the grid of Geneva in our study to assess the multiple stellar parameters in a consistent way.

3.3 The Central Star

As discussed in the previous section and in the Chapter 1, CBes rotates much faster than typical B stars, which causes important effects on these stars (Sect. 1.3.1).

Two possibilities were considered to define the parameters of the stellar grids employed by BeAtlas: an empirical grid or a theoretically-oriented grid. An empirical grid may be specified by the following four parameters, all of which are necessary to define a stellar model in Hdust: stellar mass ($M_\star$), polar radius ($R_{\rm pole}$), stellar luminosity (L) and the rotation rate (W, Eq. 1.3). The choice of these parameters rely in principle on the ranges typically found in the literature for B stars on the MS or close to it (e.g. Schmidt-Kaler, 1982; Harmanec, 1988). Consequently, the correlation between $M_\star$, $R_{\rm pole}$ and L are taken into account implicitly. On the other hand, the theoretically-oriented grid is defined to be constrained by stellar evolution models. The advantages of such an approach are both reducing the number of parameters necessary to specify a given model, and associating a specific evolutionary stage to it.

For this work, we adopted the theoretically-oriented option. In particular, we chose the parameters $M_\star$, W, and $t/t_{\rm MS}$ to completely describe each model, where $t/t_{\rm MS}$ represents the time

fraction spent in the MS. The remaining parameters necessary for the radiative transfer calculations, $R_{\rm pole}$ and L, can be subsequently determined from Geneva evolutionary models.

The Roche equipotential formalism (e.g. Cranmer, 1996 and references therein) is frequently used to describe the rotating stellar geometry. In HDUST this is approximated by an ellipsoid shape, for which the ratio between the large and small axis are given by the Roche theory (Eq. 1.3), see Carciofi and Bjorkman (2008) for more details. The effects of this approximation on the emergent spectrum are very small (Faes, 2015). The limb darkening follows the prescription given by Claret (2000), and the gravity darkening effect is described by the modified von Zeipel law (see Cranmer, 1996):

$$T_{\rm eff}(\theta) = \left(\frac{L/\sigma_{\rm B}}{\oint g^{4b} {\rm d}A} \right)^{1/4} g^{\beta_{\rm GD}}(\theta), \tag{3.1}$$

where θ is the polar angle (spherical coordinates), $\sigma_{\rm B}$ is the Stefan-Boltzmann constant, and $\beta_{\rm GD}$ is the gravity darkening exponent.

To constrain the gravity darkening exponent, we adopted the model presented by Espinosa Lara and Rieutord (2011), where $\beta_{\rm GD}$ is function of the rotation rate. This model has provided a successful description for many cases in the literature (e.g., Domiciano de Souza et al., 2014).

For BEATLAS, we devised two grids of stellar parameters to serve different purposes. The first grid aims at calculating the detailed emergent spectrum of purely-photospheric (i.e., diskless) models. This grid can be used to model observations of, e.g., normal B stars, Bn stars, or CBes observed in diskless phases. The second grid will serve as the set of stellar parameters for models with a disk (Sect. 3.3.1). The reason two grids were necessary is that the purely photospheric models are much simpler and faster to run and, for this reason, a much finer grid could be made.

3.3.1 *Grid of Stellar Parameters for Purely Photospheric Models*

The range of model parameters, as well as their individual values, used in the purely photospheric grid is shown in Table 3.1. This grid is comprised of 7 700 models photospheric models (11 M × 10 W × 7 $t/t_{\rm MS}$ × 10 i). Each model belonging to this grid is determined by four parameters (M, W, $t/t_{\rm MS}$ and i). The range of masses covers the spectral types of interest (see Sect. 1.4). Additionally, the grid encompasses the full range of rotation rates in the MS.

Table 3.1 - BeAtlas stellar parameters of the purely-photospheric model grid. The steps follows $W_{\rm i} = 0.99\sqrt{0, \frac{i}{N}, \frac{2i}{N}, ..., \frac{N-1}{N}, 1}$. The spectral types are based on Martins et al. (2005), Townsend et al. (2004), and Adelman (2004), for O, B and A spectral types, respectively.

	Parameters	Ranges	Values
ST	Spec. Type	O8 - A7	A7, A2, A2, B9.5, B7, B6, B3, B2.5, B1, B0, O8
$M_\star$	Mass ($M_\odot$)	1.7 - 20	1.7, 2, 2.5, 3, 4, 5, 7, 9, 12, 15, 20
W	Rotation Rate	0.00 - 0.99	0.00, 0.33, 0.47, 0.57, 0.66, 0.74, 0.81, 0.87, 0.93, 0.99
$t/t_{\rm ms}$	Stellar Age	0 - 1.02	0, 0.25, 0.5, 0.75, 1, 1.01, 1.02
$\cos i$	Inclination angle (^{o})	0.0 - 90.0	0, 0.11, 0.22, 0.33, 0.44, 0.55, 0.67, 0.78, 0.89, 1

Table 3.2 - BeAtlas stellar parameters for disk models.

	Parameters	Ranges	Values/Step
ST	Spec. Type	O8 - B9	B9, B7, B6, B4, B2.5, B1, B0.5, O8
$M_\star$	Mass ($M_\odot$)	3 - 20	3, 4, 5, 7, 9, 12, 15, 20
W	Rotation Rate	0.5 - 0.99	0.5, 0.75, 0.85, 0.92, 0.99
$t/t_{\rm ms}$	Stellar Age	0 - 1	0, 0.5, 1, 1.02

3.3.2 Grid of Stellar Parameters for Disk Models

Because the disk grid of BeAtlas takes a very large amount of computing time to be completed (see below), we had to reduce the number of grid points to an acceptable minimum. One of the ways of doing that was by reducing the range and number of values of the stellar grid.

The adopted stellar grid for the disk models is shown in Table 3.2. With the exception of the stellar mass and the rotation rate, the adopted ranges for the stellar parameters are the same as the photospheric models; however, the number of values explored in the grid was reduced. This reduction was necessary to keep the number of models realistic, in view of the large computer requirements of the disk grid.

We set the mass range lower limit at 3 $M_\odot$, due to convergence difficulties of Hdust for lower masses. Also, we decided to restrict the disk models to $W \geq 0.5$, since no Be star disk has ever been detected around slow rotators (see the compilation presented in Rivinius et al., 2013).

In the next section, we describe our assumptions for the `VDD` model and the ensuing choice for the disk parameters.

Table 3.3 - BeAtlas disk model parameters.

	Parameters	Ranges	Values/Step
Σ_0	Surface density at the base of the disk (cm^{-2})	1.5 - 4.5	0.5
R_D	Disk radius (R_{eq})	10 - 100	30
n	Mass density radial exponent	1.5 - 4.5	0.5

3.4 Disk Models

The parameter set of the grid of disk models has two components: the central star (Sect. 3.3.2) and the circumstellar disk.

3.4.1 Disk Density Profile

Several papers and recent PhD thesis and dissertations of the Beacon group (Mota 2013; Faes 2015; Rímulo 2017; Ghoreyshi 2018; Figueiredo 2018) have used some variant of the `VDD` model. In order to avoid unnecessary repetition of definitions, derivations, etc., we just mention here four important aspects of the `VDD` theory, relevant for our work. A good reference for the discussion below is Vieira et al. (2017).

1. A star that loses mass at a constant rate for a long time forms a disk that initially grows in density such that initially the density profile is very steep and with time the profile approaches an inverse power-law with index 3.5. This *steady-state configuration* is only valid if the disk material is assumed to be isothermal (Bjorkman and Carciofi, 2005a);

2. Young, forming disks that have not yet reached steady-state have density profiles that can be approximated to a power-law of index $n < 3.5$ (Haubois et al., 2012);

3. Disks that are in a dissipative state, where the star has ceased mass loss, have a density profile associated with $n > 3.5$ (Haubois et al., 2012);

4. Both binary effects (Panoglou et al., 2016) and radiative transfer effects (Carciofi and Bjorkman, 2008) may act together to change the density profile in CBes.

Therefore, despite being a simple approximation to the `VDD` model, a power law parametrization of the disk radial density profile represents a useful description, which is easily compared to several results in the literature. Besides, part of the dynamical information contained in the

time dependent solutions of the VDD model can be extracted from this particular formulation, as explained in items 2 and 3 above. The adopted parametric expression for the mass density is:

$$\rho(r,z) = \frac{\Sigma_0}{H\sqrt{2\pi}}\left(\frac{r}{R_{\rm eq}}\right)^{-n}\exp\left[-\frac{z^2}{2\,H^2}\right], \tag{3.2}$$

where Σ_0 is the disk base surface density, $R_{\rm eq}$ is the equatorial stellar radius, r and z are respectively the radial and vertical cylindrical coordinates in the stellar frame of reference, and H is the disk scaleheight. In particular, H is a function of the radius given by:

$$H(r) = H_0\left(\frac{r}{R_{\rm eq}}\right)^{\beta}, \tag{3.3}$$

where $H_0 = (c_{\rm s}/V_{\rm crit})\,R_{\rm eq}$, $c_{\rm s} = (k\,T_{\rm d}/\mu\,m_{\rm H})^{1/2}$ is the isothermal sound speed, $V_{\rm crit} = (G\,M_\star/R_{\rm eq})^{1/2}$ is the critical velocity, k is the Boltzmann constant, μ is the molecular weight of the gas, $m_{\rm H}$ is the hydrogen atom mass, $T_{\rm d}$ is the disk temperature (assumed constant throughout the disk), and β is the disk flaring exponent. We adopt $T_{\rm d} = 0.72\,T_{\rm pole}$ as an estimate of the average value of $T_{\rm d}$ to compute H_0 (Carciofi and Bjorkman, 2006). Additionally, β is fixed at 1.5, which corresponds to the VDD model isothermal solution (e.g., Bjorkman and Carciofi, 2005a). Future grid versions are planned to have self-consistent scaleheights (Carciofi and Bjorkman, 2008). Note that the current version of the grip employs what Carciofi and Bjorkman (2008) called mixed models, in which, albeit the density is fixed, the gas state variables (temperature and level populations) are calculated by Hdust.

3.4.2 Disk Density Scale

The adopted upper and lower limits of the disk surface base density were defined as functions of the stellar mass, written as,

$$\Sigma_0^{\rm upper}(M) = \begin{cases} \exp(-aM^2 + bM + c), & M \le 8.6\,{\rm M}_\odot, \\ \exp(dM + e), & M > 8.6\,{\rm M}_\odot, \end{cases} \tag{3.4}$$

and

$$\Sigma_0^{\rm lower}(M) = \exp(-fM^2 + gM + h). \tag{3.5}$$

The upper limits correspond to the Hdust convergence limits[1], and were estimated from previous experiences with the code (see Fig. 3.3), while the lower limits roughly correspond

[1] Because Hdust is based on the MC method, it requires that, everywhere in the disk, a sufficiently large number

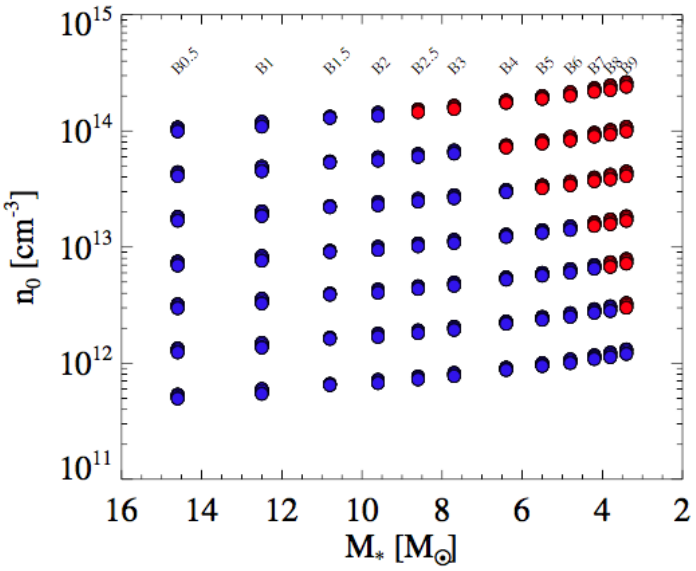

Figure 3.3: Convergence in BeAtlas. Blue symbols represent the converged Hdust models, while red symbols the non-converged models.

to the detection limit of an emission feature (however weak) in the Hα line. Notice that the convergence limitation does not impose a severe restriction to the grid, since a similar trend of increasing Σ_0 upper limit with stellar mass is also observed in nature (Vieira et al., 2017).

3.4.3 Disk Radius

The disk radius range was set from 10 to 100 $R_{\rm eq}$. The lower value corresponds to an estimate for the disk radius of the Be star *o* Pup, which has the shortest period (hence smallest orbital separation) among all known binary CBes. This value was calculated through its orbital period ($\sim$ 30 days) and semi-major axis ($\sim$ 11.5 $R_{\rm eq}$); (see Tab. A.1). We can use these values to estimate the disk radius as $R_{\rm D} \simeq 0.8 \times 11.5\, R_{\rm eq}$ (the 0.8 factor comes from Panoglou et al. 2016). On the other hand, the upper limit, 100 $R_{\rm eq}$, corresponds to a disk size for which the disk emission starts to be negligible at all wavelengths considered in the simulation (see Section 3.5); (Vieira et al., 2015). The grid values are, therefore, $R_{\rm D} = 10, 40, 70, 100\, R_{\rm eq}$.

of photons crosses a given grid cell, in order to sample quantities such as photoionization rates, etc. (see Carciofi and Bjorkman, 2006 for details of the model). This is particularly important for UV photons. The convergence limits of Hdust are reached when the density becomes so large, and the inner disk so optically thick, that not enough UV photons are available to properly sample the necessary rates.

3.4.4 Mass Density Radial Exponent

The n exponent range (Eq. 3.2) was defined according to Vieira and Carciofi (2017), ranging from 1.5 to 4.5. This range is in broad agreement with other studies from the literature about this parameter (e.g. Waters et al., 1989, Silaj et al., 2014, Touhami et al., 2014). As discussed in Section 1.5, this range could represent different evolutionary disk phases.

3.4.5 Summary of the Disk Model Grid

The parameters described above are all listed in Table 3.3. The atlas of disk models comprises a total of 358 400 models (8 masses × 5 rotation rates × 4 ages × 7 slope densities × 4 disk sizes × 10 inclination angles).

It must be emphasized that the final grid could not be completed for this thesis, unfortunately. The purely-photospheric grid was computed in full, but only parts of the disk grid were computed, aiming at bracketing the parameter space needed to study β CMi and α Arae (Chap. 6 and 7, respectively).

The full grid needs about 6 months of computation time using the full resources of LAi[2]. As such, BeAtlas is an ongoing computational effort, that is still being carried on.

3.5 Observables

To finish the specification of BeAtlas, we must provide a list of "observables" (e.g., continuum bands, spectral lines, images, etc.) and "observers", which basically is the specification of the viewing angles for which the models are computed. The latter follow the same specifications of i as in Tables 3.4, adopted a continuum ranging from 1 000 Å (UV domain) up to 75 cm (radio wavelength) for both photospheric-only and disk models (Fig. 3.4). The most efficient way to run Hdust is to compute individual runs for each spectral range of interest. To make optimal usage of this feature, we specified 22 spectral bands (first part of Table 3.4) covering all the way from the UV up to the radio. Each band is defined by a minimum and maximum wavelength, the number of spectral bins (i.e., its spectral resolution), their spacing (linear or logarithm), and the number of photons. This latter quantity is very important: if too low, the model will carry too much Monte Carlo noise; if too large, the simulation will take more time to run than necessary. Much effort was dedicated to find the optimum value of $N_{\rm phot}$. Other quantities affected by $N_{\rm phot}$

[2] https://lai.iag.usp.br/projects/lai;

is the accuracy of the polarization calculation (important for the UV and visible, and that is the reason why these bands have 10 times more photons than most of the other ones), and the need or not to calculate model images, in which case more photons are also necessary to properly sample the spatial surface brightness of the disk.

We are also interested in spectral lines (both in emission and in absorption) in the optical in IR domains. These lines were selected among the most commonly used in the literature (second part of Table 3.4). Although inteferometric observables were not yet computed, special emphasis was given to the inclusion of interferometric observables in our selection. These observables are based on future decommissioned interferometers (e.g. AMBER[3] and MIDI[4]) and now interferometers already in operation at ESO (e.g. GRAVITY[5] and MATISSE[6]). Figure 3.5 summarizes the coverage of each interferometer used to define the interferometric observables.

[3] https://www.eso.org/sci/facilities/paranal/instruments/amber/overview.html;
[4] https://www.eso.org/sci/facilities/paranal/decommissioned/midi.html;
[5] https://www.eso.org/sci/facilities/paranal/instruments/gravity.html;
[6] https://www.eso.org/sci/facilities/develop/instruments/matisse.html.

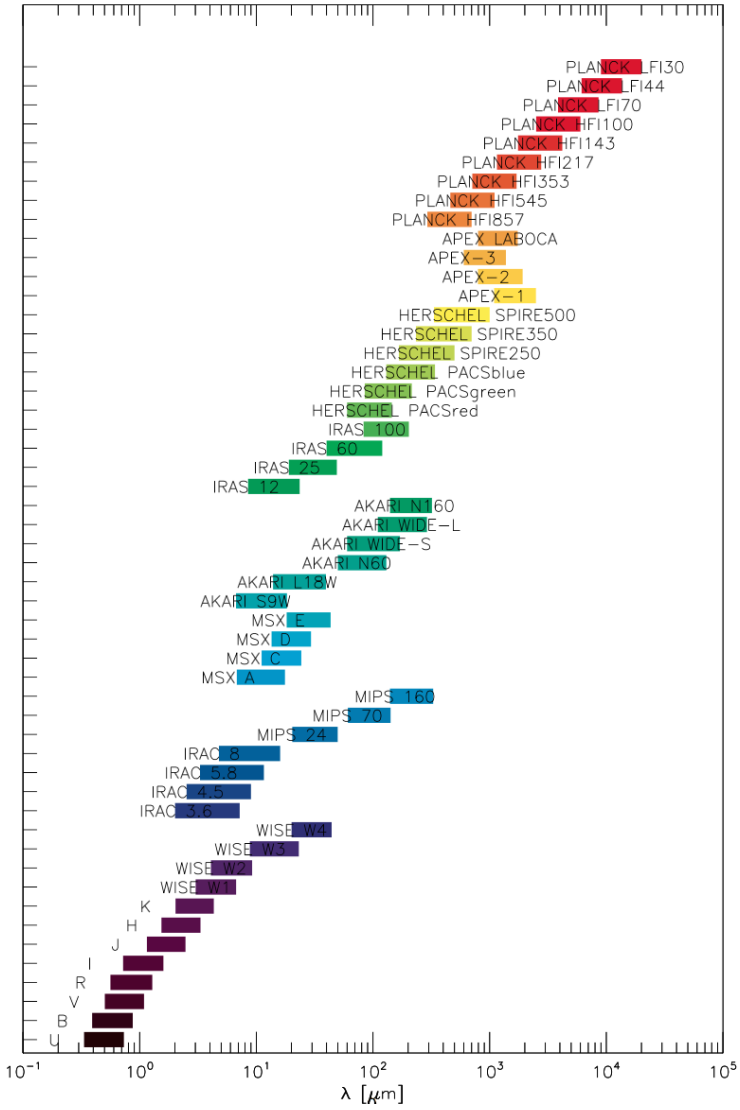

Figure 3.4: Broad bandpasses collected in the literature for the most common sources of data available for stars. This figure was used as a guide for making Table 3.4.

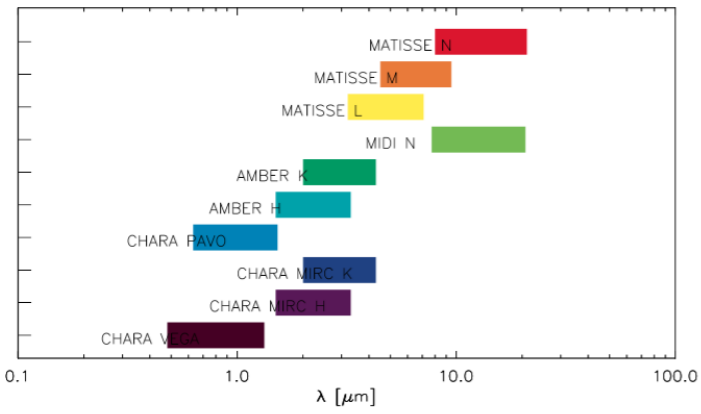

Figure 3.5: Wavelength coverage of interferometers. This figure was used as a guide for making Table 3.4.

Table 3.4 - Definition of observables.

Observable	λ_{min} [μm]	λ_{max} [μm]	N_{bins}	Spacing	N_{phot}	Image	Comments
UV	0.1	0.35	225	linear	2e8	No	Kurucz resolution
SED	0.35	1	50	log	2e8	No	–
J	1	1.4	30	linear	2e7	No	–
H	1.4	1.85	80	linear	1e8	Yes	PIONIER, MIRC, R~300
K	1.85	2.45	1000	linear	1e8	Yes	GRAVITY, R~4,000
L	2.45	3.9	450	linear	1e8	Yes	MATISSE, R~1,000
M	3.9	8	380	linear	1e8	Yes	MATISSE, R~550
N	8	13	120	linear	1e8	Yes	MATISSE, R~250
Q1	13	18	30	linear	2e7	No	–
Q2	18	25	30	linear	2e7	No	–
IR35	25	45	30	log	2e7	No	–
IR65	45	85	30	log	2e7	No	–
IR100	85	120	30	log	2e7	No	–
IR160	120	200	30	log	2e7	No	–
IR300	200	400	30	log	2e7	No	–
IR600	400	800	30	log	2e7	No	–
MM	800	1200	30	log	2e7	No	LABOCA, JCMT1/2, IRAM
CM07	6000	7500	10	log	2e7	No	VLA/Q
CM13	11300	16700	10	log	2e7	No	VLA/K
CM20	16700	25000	10	log	2e7	No	VLA/Ku
CM30	25000	37500	10	log	2e7	No	VLA/X
CM60	37500	75000	10	log	2e7	No	VLA/C
Observable	λ_c [Å]		R	Spacing	N_{phot}	Image	Comments
Halpha	6564.61		20,000	linear	2e8	Yes	CHARA/VEGA 100 bins image/R~10,000
Hbeta	4862.71		10,000	linear	1e8	No	–
Hdelta	4102.89		10,000	linear	1e8	No	–
Hgamma	4341.69		10,000	linear	1e8	No	–
Brgamma	21661.2		10,000	linear	2e8	Yes	AMBER
Br11	16811.1		27,000	linear	1e8	No	APOGEE
Br13	16113.7		27,000	linear	1e8	No	APOGEE
Pfgamma	37405.6		10,000	linear	1e8	No	Sabogal et al. (2017)
Hu14	40208.7		10,000	linear	1e8	No	Sabogal et al. (2017)
Bralpha	40522.6		10,000	linear	1e8	No	Sabogal et al. (2017)

Chapter 4

Methodology

4.1 Chapter Summary

Recent efforts by our group (e.g. Vieira and Carciofi, 2017; Rímulo et al., 2018) showed that a grid, no matter how much science has been put to it, is useless without a statistical engine that allows exploring all the likely solutions.

In Sections 4.2 and 4.3 we define the essential functions (likelihood and priors) adopted in our Bayesian approach, according to the statistical tools and theoretical background given in Chapter 2. We summarize the BeAtlas pipeline in Sect. 4.4 together with other developed tools. Finally, we show an alternative method to infer stellar parameters in Section 4.5.

4.2 Definition of the Likelihood Function

The likelihood is an essential factor in the convergence of any `MCMC` method (see Sect. 2.3). Although the Metropolis-Hastings algorithm will converge for different likelihood functions, the most commonly used one is the χ^2 distribution. After some convergence tests with different variations of this function, we decided to adopt as the likelihood the following function,

$$\log p(D|\Theta,\alpha) = -0.5 \left[\frac{\log(F_{\rm obs}/F_{\rm mod})}{\sigma_{F_{\rm obs}}/F_{\rm obs}}\right]^2 \tag{4.1}$$

where $F_{\rm obs}$ and $F_{\rm mod}(\Theta)$ are the observed and model fluxes. In our case, the latter represents the grid of models described in Chap. 3. The usage of logarithm versions of the χ^2 function can be found in the literature (e.g. Bouffanais and Porter, 2018). It offers better performance when the data being modelled has a large dynamic range (e.g., the `SED` of a CBe from the `UV` to the radio can vary 6 orders of magnitude in wavelength and 17 orders of magnitude in flux; e.g. Fig. 6.8).

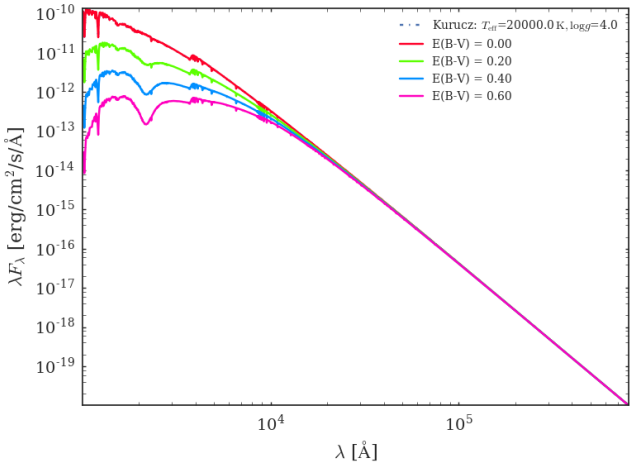

Figure 4.1: Effects of the interstellar reddening on the spectrum of a $T_{\rm eff}$ = 20 000 K, log g = 4 star. The $R_{\rm V}$ is fixed at 3.1.

The fitting procedure is performed with the grid of models and the observed fluxes ($F_{\rm obs}$) in Eq. 4.1. The synthetic fluxes can be converted to the fluxes received on Earth by

$$F_{\rm mod} = F_0(\Theta)\,(\lambda) \times \left(\frac{10}{d}\right)^2 \times f_{\rm red}, \tag{4.2}$$

where $F(\Theta)_0\,(\lambda)$ is the emergent stellar flux, d is the distance to the star (in parsecs), and $f_{\rm red}$ is the correction of the total extinction along the line of sight.

The reddening correction, represented by the function $f_{\rm red}$, is fundamental since it affects significantly the determination of the stellar parameters. Recent articles attest the complexity of the extinction determination of CBes using spectral lines (McEvoy et al., 2015). To date, arguably the most precise method for determining the interstellar extinction (hereafter $E(B-V)$, see Sect. 2.5) is via the absorption feature centered at 2 175Å the so-called "UV bump". This feature has been long used as an $E(B-V)$ proxy (e.g. Dougherty et al., 1994). Even the UV bump, however, has its issues. For instance, Zagury (2013) showed that there are $E(B-V)$ extinction curves without the UV bump, i.e., linear (see his Fig. 1). In this work, we adopted the most widely used prescription for the interstellar extinction, which is the one of Fitzpatrick (1999). As an example, Figure 4.1 shows the effects of interstellar extinction upon the spectrum of a Kurucz photosphere model with $T_{\rm eff}$ = 20 000 K and log g = 4.0. This result illustrates that as the extinction increases, the original spectrum becomes fainter in the UV domain. The extinction can be a large source of uncertainties in the determination of fundamental parameters of stars (see next chapters).

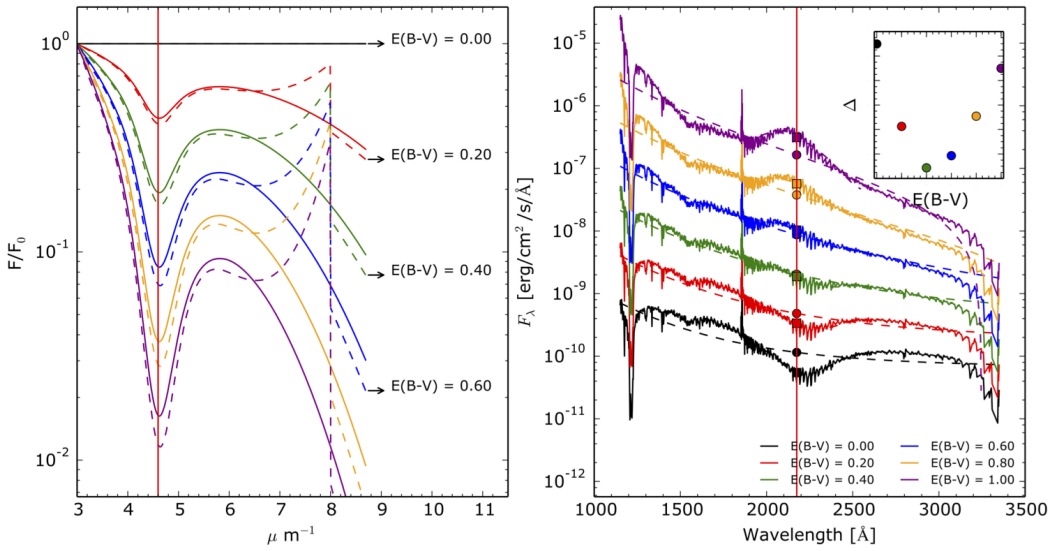

Figure 4.2: Left: Comparison of the Fitzpatrick (1999)'s (dashed lines) and Cardelli et al. (1989)'s (solid lines). Right: Correction of the original UV spectrum (black line) of the star ρ Ophiuchi by using the Fitzpatrick (1999)'s law.

In the left panel of the Figure 4.2, we show a comparison between Fitzpatrick (1999) and Cardelli et al. (1989), showing that both laws roughly agree in their description of the UV bump. In the right panel, we show the result of a manual search of the $E(B-V)$ parameter for the star ρ Ophiuchi. What was done was to choose different values of $E(B-V)$ and select the one for which the UV bump vanishes (green curve in the left panel of the Fig. 4.2). This procedure allowed us to obtain a reasonable estimate for the $E(B-V)$ which agrees with literature values (Wegner, 2003, $E(B-V) = 0.47$). What is done in the Emcee sampler is different: we used Fitzpatrick's law to *redden* the theoretical model (see Eq. 4.2), in order to best match the observations. Furthermore, we fixed the parameter R_V (see Eq. 2.8) at a typical value, 3.1, for all studied objects (Schultz and Wiemer, 1975).

4.3 Prior Choice Description

One of the reasons for choosing the Bayesian approach is its capacity to combine the data with prior knowledge (Sect. 2.3). In our study, we adopted two priors, a prior to the parallax (Sect. 4.3.1) and the other to the $v \sin i$ (Sect. 4.3.2).

4.3.1 Parallax Prior

The chosen prior for the parallax was,

$$\log p_{\pi}(\Theta, \alpha) = -0.5 \left(\frac{\pi_{\rm obs} - \pi_{\rm mod}}{\sigma_{\pi_{\rm obs}}} \right)^2 , \tag{4.3}$$

where $\pi_{\rm mod}$ is the random parallax generated in each step of the inference; $\pi_{\rm obs}$ and $\sigma_{\pi_{\rm obs}}$ are the observed parallax and its uncertainty, respectively.

In order to select the observed parallaxes, $\pi_{\rm obs} \pm \sigma_{\pi_{\rm obs}}$, we compared the latest Hipparcos (van Leeuwen, 2007) and Gaia dr2 (Gaia Collaboration, 2018) data for all stars studied in this thesis. The general agreement of both measurements is evident in Fig. 4.3; however, for a number of individual cases Gaia dr2 and Hipparcos disagree well above the nominal uncertainties.

We realized that there is no global agreement among the parallaxes, which is indicated by the high dispersion of the measurements around the dashed line in Fig. 4.3.

Gaia dr2 already indicates limitations in the published data (Gaia Collaboration et al., 2018). This release is still intermediate, being based on: i) a limited amount of input data ($\sim$ 22 months), ii) simplifications in the data processing. This probably introduced shortcomings in the calibrations that could have propagated systematic errors.

An additional parameter, the *duplicated source* quality field, present in Gaia dr2, indicates that the source was identified as duplicated during data processing. It may indicate: observational cross-matching, processing problems, stellar multiplicity (nearby companions), astrometric or photometric problems. Hence, Gaia dr2 may have provided incorrect parallaxes for multiple systems. This may explain the incompatibility among Gaia dr2 and Hipparcos parallaxes for many cases (e.g. α Arae, α Col).

Given the above, we decided to use the Hipparcos data for all objects studied in our work.

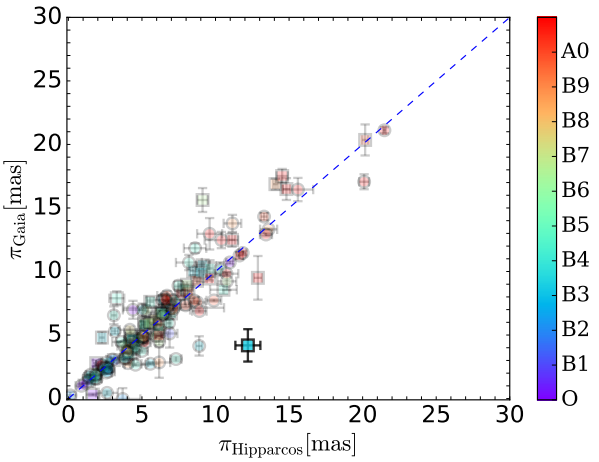

Figure 4.3: Comparison of Hipparcos and Gaia dr2 parallaxes for our sample of stars. Circles: Non-duplicated source according to Gaia. Squares: Duplicated source according to Gaia.

4.3.2 $v \sin i$ Prior

The prior function used for $v \sin i$ was

$$\log p_{\rm v\,sin\,i}(\Theta, \alpha) = -0.5 \left(\frac{v \sin i_{\rm obs} - v \sin i_{\rm mod}}{\sigma_{v \sin i_{\rm obs}}} \right)^2 , \tag{4.4}$$

where $v \sin i_{\rm mod}$ is the random $v \sin i$ generated in each step of the inference; $v \sin i_{\rm obs}$ and $\sigma_{v \sin i_{\rm obs}}$ are the observed $v \sin i$ and its uncertainty, respectively. The measurements of $v \sin i$ were taken from several sources that are indicated below. A total of $\sim 20\%$ of our targets had measurements with uncertainties. For the remaining stars, we assumed a $\sigma_{v \sin i_{\rm obs}} = 0.10\, v \sin i_{\rm obs}$.

By providing $v \sin i$ values, we can constrain the values of the likely inclinations, masses and oblateness, i.e. physical quantities directly related with this parameter. To implement such a prior, it was calculated for each iteration a $v \sin i(\Theta)$. For the stars with $v \sin i(\Theta)$ without uncertainty, we fixed the errors as 10 % of the measurement. Here, it is important to highlight the fact pointed by Townsend et al. (2004), i.e. that the old $v \sin i$ measurements, which did not consider the gravity darkening effect, could be underestimated by 9 to 33% at $W = 0.75$ for B0 to B9-type stars. In these cases, inaccurate values of $v \sin i$ could propagate systematic errors in the inference of the studied parameters. In the next Chapter we present a study of how the inclusion of the $v \sin i$ prior may change the inferred parameters.

4.3.3 Posterior Function

Given the expression for the the theoretical model as observed from Earth (Eq. 4.2), the best-fitting model is obtained by using the Eq. 2.5 with the likelihood given by the Eq. 4.1 together with the prior functions (Eq. 4.4 and 4.3) for all set of parameters simultaneously. This is done with the EMCEE sampler that returns samples from the posterior probability density for each free parameter.

The posterior probability defines, for a set of parameters (Θ), their probability of being the true parameters. Therefore, once the samples produced by EMCEE are available, the marginalized constraints on Θ can be approximated by the histogram of the samples projected into the parameter subspace spanned by Θ. The uncertainties on each parameter were defined as the ranges containing the percentiles of 16 and 84 % on the marginalized PDFs, and the best-fit value as the median of the distribution.

4.4 BEMCEE - *The* BEATLAS *pipeline: a quick summary*

The BEMCEE open-source code comprises all modules developed during this PhD thesis. It is a community effort, for which many members of the BEACON group contributed, to develop a common core package for the inference of Be stars parameters in PYTHON. It is available online in the GITHUB[1] repository at this address[2]. We wrote a comprehensive manual and tutorial on how to use BEMCEE, which is provided as an appendix to this text (Appendix C). In Figure 4.4, we show the workflow that comprises:

1. The preparation of the BEATLAS Grid (see Chap. 3):
   - Based on modern stellar evolution models and a prescription for the VDD model, we solve the radiative transport with the HDUST code (Chap. 3);
   - The results are two grids of models: i) purely photospheric models (Sect. 3.3.1), ii) Disk models (Sect. 3.4);
2. The selection and pre-processing of the observations:
   - Starting from catalogues and some conditions (e.g. spectral and luminosity classes), the BEFAVOR WEB code (see details in Sect. 4.4.1) selects from the available facilities

[1] It support collaborative development of software and the tracking of changes to software source code over time.
[2] https://github.com/tangodaum/bemcee.

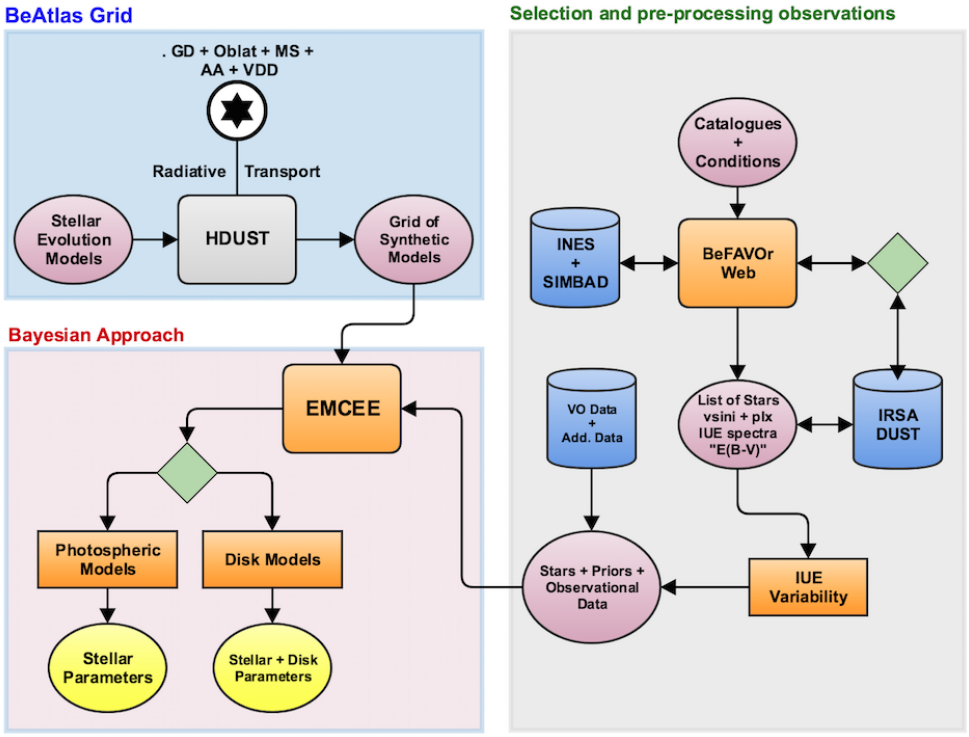

Figure 4.4: Workflow of the developed routines. `GD`: gravity darkening. Oblat: oblateness. `MS`: multiple scattering. `AA`: auto-absorption by the disk. `Ines`: http://sdc.cab.inta-csic.es/cgi-ines/IUEdbsMY. `IRSA Dust` is a service that gives the galactic dust reddening for a line os sight, it is available at https://irsa.ipac.caltech.edu/applications/DUST/. `Simbad`: http://simbad.u-strasbg.fr/simbad/sim-fbasic. The green rhombus represent decision made by the user or by the pipeline.

(e.g. INES, SIMBAD, IRSA-DUST, and VO tools) a list of stars together with their $v \sin i$, parallax and observational data (`IUE` and photometry data);

3. With the appropriate BEATLAS grid (photospheric vs. disk), priors, and observational data, EMCEE returns the stellar and (if appropriate) the disk parameters.

4.4.1 BEFAVOR *Tools*

This tool started with a "Iniciação Científica" project with the student Artur Alegre (Appendix J). It uses "Web Service" PYTHON routines to get data and a list of stars given some conditions. The routines are available at the GITHUB link[3]. A detailed description is given in Appendix K.

[3] https://github.com/tangodaum/BeFaVOr-WEB.

4.5 BCD *System*

The BCD System is a consolidated method for obtaining the photospheric parameters of "normal" stars, i.e. objects whose atmospheres can be studied in the framework of hydrostatic and radiative equilibrium approximations. However, since both circumstellar and photospheric components of the Balmer Discontinuity are spectroscopically distinct, the BCD System is usually applied to "peculiar" stars as the Be stars (e.g. Divan et al. 1982; Zorec and Briot 1991; Shokry et al. 2018).

It is based on measurable quantities that are sensitive to the ionization balance and gas pressure in stellar photospheres. This makes the method ideal as proxies for $T_{\rm eff}$ and $\log g$. In summary, the method is based in four quantities taken from the spectrum around the Balmer Discontinuity (see Fig. 4.5):

1. D: the Balmer jump at $\lambda 3\,700$ Å given in dex; this parameter is a strong function of $T_{\rm eff}$;
2. λ_1: the mean spectral position of the Balmer Discontinuity (BD), usually defined as $\lambda_1 = 3\,700$ Å; this parameter is very sensitive to $\log g$;
3. $\Phi_{\rm UV}$: the gradient of the Balmer energy distribution in the near-UV from $\lambda 3\,100$ to $\lambda 3\,700$ Å in μm;
4. $\Phi_{\rm rb}$: the gradient of the Paschen energy distribution in the range $\lambda\lambda 4\,000 - 6\,200$ Å in μm.

The BCD parameters (λ_1, D) can be measured even in spectra of low resolution and in cases of high ISM extinction, which makes the method applicable also for distant objects.

During this PhD, we worked with this method, developing a Python Code (PharaUS) to apply the BCD method. The code is available at the GitHub link[4]. This contribution helped in the work published by Shokry et al. (2018). This article is in Appendix E.

[4] https://github.com/tangodaum/pyxshooter.

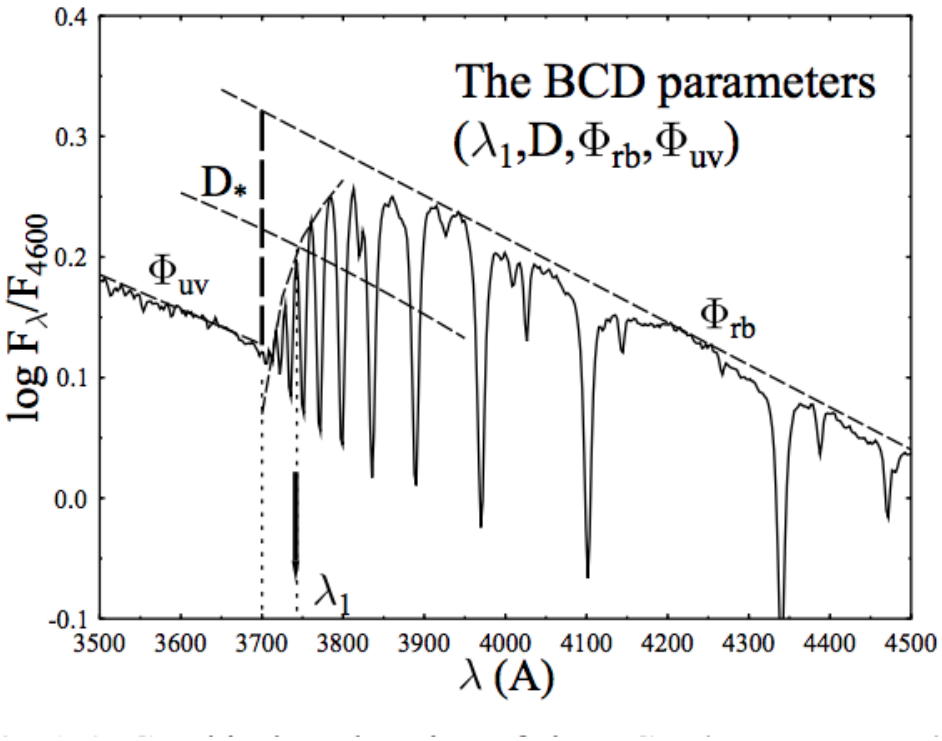

Figure 4.5: Graphical representation of the BCD parameters (Zorec et al., 2009).

Chapter 5

A UV Study of O, B, and A Main-Sequence Stars

5.1 Chapter Summary

In this Chapter we present the first application of the current version of the BeAtlas, namely the systematical study of a sample of O, B, and A stars.

Initially, we offer a general motivation for this work and outline the criteria used to form our sample of stars (Sect 5.2). We present a theoretical study of the effects of the disk in the UV spectrum of CBes in Section 5.3, and in Section 5.4 we investigate the effects of the usage of priors in the Bayesian inference. The results of the BeAtlas modeling are shown in Sect. 5.6.

5.2 Motivation and Sample Selection

The main motivation for this study is to address issue number 2 discussed in Sect. 1.6: Detailed, self-consistent modeling of CBes are still rare, and studies of large samples are even rarer. The results presented in this Section are also important to assess the ability of BeAtlas to infer reliable parameters of the studied star. To this end, a careful comparison between our results and those of the literature was made. However, one issue that presented itself from the beginning was that the lack of studies of large samples that apply a reliable procedure to the data (more details below) imply that a comparison with reference values must be done with some caution.

Our sample of stars comprises O, B and A stars, including the peculiar classes Be, Bn, Ae, and Oe stars. Each selected peculiar class was detailed in Section 1.4. Basically, we selected stars from the Bright Star Catalogue (Hoffleit and Jaschek, 1982, BSC) and from the Catalogue of Be-Stars (Jaschek and Egret, 1982). Another criterium was to restrain our sample to stars in the MS and the post-MS (sub-giants); for this reason, only stars with luminosity classes V and IV (MS and subgiants) were selected. Naturally, stars without UV data were discarded.

There were several missions covering the UV domain: EUVE (Malina et al., 1982) (70−760 Å), CHIPS (Hurwitz and Sholl, 1999) (90 – 260 Å), ORFEUS (Kraemer et al., 1988) (400 – 1 250 Å), Astro 2 (Stecher and UIT Science Team, 1994) (425 – 3 200 Å), FUSE (Cash, 1984) (905 – 1 187 Å), IUE (Macchetto, 1976) (1 145 – 3 300 Å), and GALEX (Bianchi et al., 1997) (1 300 – 3 000 Å). Among these missions, we adopted data from the International Ultraviolet Explorer spatial mission - IUE - because this mission offered the largest sample, with a well-known and tested reduction pipeline, as well as, for many objects, several observations at different dates, which allowed us to look for variability in the data (see below).

The IUE had two cameras: the SWP camera (1 145 – 1 975 Å) and the long-wavelength LWP/LWR cameras (1 850 – 3 300 Å)[1]. Following Freire Ferrero et al. (2012), we only selected high-dispersion large-aperture observations, because they can be flux calibrated. A proper flux calibration is absolutely essential to our work. The IUE fits files were obtained from the INES Archive Data Center[2], maintained by ESA.

Another criterium used was to avoid stars with large intrinsic variability of the data. A similar criterium was to discard wildly discrepant observations. As a measure of the variability, we calculated the flux level, F_0, and its slope, m, for each spectrum by fitting a power-law function

$$f = F_0 \left(\frac{\lambda}{\lambda_0} \right)^m . \tag{5.1}$$

Both F_0 and m can be used as a proxy of data variability. For each selected star, we discarded the spectra that were more than $3\,\sigma$ away from the mean values obtained for the inclination and level, respectively. The final spectrum of each star was the average of all remaining spectra, and the error of each data point was taken as the standard deviation of the mean. This procedure ensures that intrinsic flux variability, if present, is properly considered in the estimates for the parameter confidence levels.

As an example, the fitted parameters F_0 and m obtained from each IUE spectra of α Arae are shown in Fig. 5.1. These results show that α Arae can be considered stable in the UV domain. We see that only two spectra were more than $3\,\sigma$ away from the average (dashed lines) in the dates 1994-03-30 and 1986-04-06 (points with black error bars). These spectra were removed from the analysis. Following the so-called $3\,\sigma$ *rule of thumb* (Kazmier, 2004).

In summary, our selection criteria were:

[1] https://nssdc.gsfc.nasa.gov/astro/astrolist.html;
[2] http://sdc.cab.inta-csic.es/cgi-ines/IUEdbsMY.

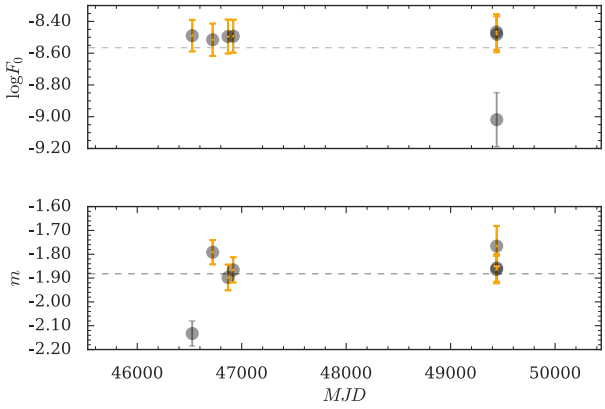

Figure 5.1: Parameters F_0 and m found to α Arae. Modified Julian Date (MJD) are in abscissas and F_0 and m parameters in ordinates. The dashed lines represent the mean values.

1. Nearby stars, members of BSC or the Catalogue of Be-Stars;

2. Availability of at least one IUE spectrum taken in the high-dispersion, large-aperture mode;

3. Deviant spectra, in the criteria described above, were discarded.

The final sample is listed in Table A.8. It is composed of 111 stars, out of which:

- 2 (1.8 %) are O stars and 2 (1.8 %) are Ae stars;

- 67 (60.4 %) are normal B stars, 30 (27 %) are CBes, 10 (9 %) are Bn stars.

5.3 The Effects of the Disk in the UV Spectrum

As explained previously our goal is to investigate a sample of OBA stars from UV observations. The choice of the UV domain appears to be a natural one, because: (i) B stars emit most of their energy (over 70%) in the UV (e.g. Bless and Percival 1997; Fitzpatrick and Massa 1999); (ii) for CBes, the contribution of the disk to the far UV spectrum is in general small (e.g. see Fig. 2 of Klement et al. 2015 and Fig. 1 of Briot 1978). Therefore, regarding the study of the stellar properties, the UV domain should provide one of the best observables to develop a first application of BeAtlas.

Despite these previous results already pointing to a weak influence of the disk in the UV domain, we revisited this problem by using BeAtlas, exploring different scenarios. In order to do that, we define the *disk effect* function as the following average taken in the UV domain,

$$\left\langle \frac{\Delta F}{F_\star} \right\rangle_{\rm UV} = \frac{1}{\Delta\lambda} \int_{\lambda_{\rm min}}^{\lambda_{\rm max}} \frac{|F_\lambda - F_\lambda^\star|}{F_\lambda^\star}\, d\lambda\,, \tag{5.2}$$

where $\lambda_{\rm min} = 1000\,$Å, $\lambda_{\rm max} = 3000\,$Å, $F_\lambda^\star$ is the flux of a purely photospheric model and F_λ the total flux. The choice of $\lambda_{\rm min}$ and $\lambda_{\rm max}$ is somewhat arbitrary, but reflects the range for which more abundant UV data was available (e.g., the IUE data).

Figure 5.2 shows the disk effect function for a few representative cases of CBe disks. For instance, the first row shows the disk effects for a low-mass case ($4\,M_\odot$) seen at two inclinations. In this case, the disk effects in the UV domain increases with the inclination angle substantially for $n \gtrsim 3.5$, reaching the maximum of ~ 0.0175, for pole-on orientation, and ~ 0.070 for edge-on cases. This happens because i) the smaller the n the larger the mass of the disk and the larger the disk effect, and ii) the disk emission in the UV is very small (Vieira and Carciofi, 2017), but the optical depth is rather large; therefore, the effects are larger for edge-on disks due to disk obscuration of the central star.

In the second row we look at a typical early-type star ($9\,M_\odot$). An interesting result in this case is that the disk effects do not strongly depend of the density slope n, except for the edge-on case. Because disks around early-type CBes can have much large densities, the values of the disk effect function are much larger than the for the low-mass case. The maximum value attained by this function is ~ 0.70 for edge-on orientation and ~ 0.20 for pole-on. As expected, we see that in general either large Σ_0 or small n values are associated to strong disk effects.

In a nutshell, the disk effects in the UV become stronger towards early-spectral types and edge-on orientations, showing a complex dependence on n. For low mass stars, the maximum effects do not exceed $\sim 2\%$ in the range $0^{\rm o} \leq i \leq 70^{\rm o}$, reaching $\sim 7\%$ for edge-on orientation. For early-type cases, the maximum effects are between $\sim 10 - 24\%$ in the range $0^{\rm o} \leq i \leq 70^{\rm o}$, reaching $\sim 70\%$ for edge-on disk.

These results demonstrate that the disk effects in the UV are, for the most part, relatively small, except at early spectral with dense disks and frequently even negligible. This is an important realization, since it allows one to use UV observations to independently constrain the photospheric parameters, as long as care is taken to avoid objects with quite dense disks.

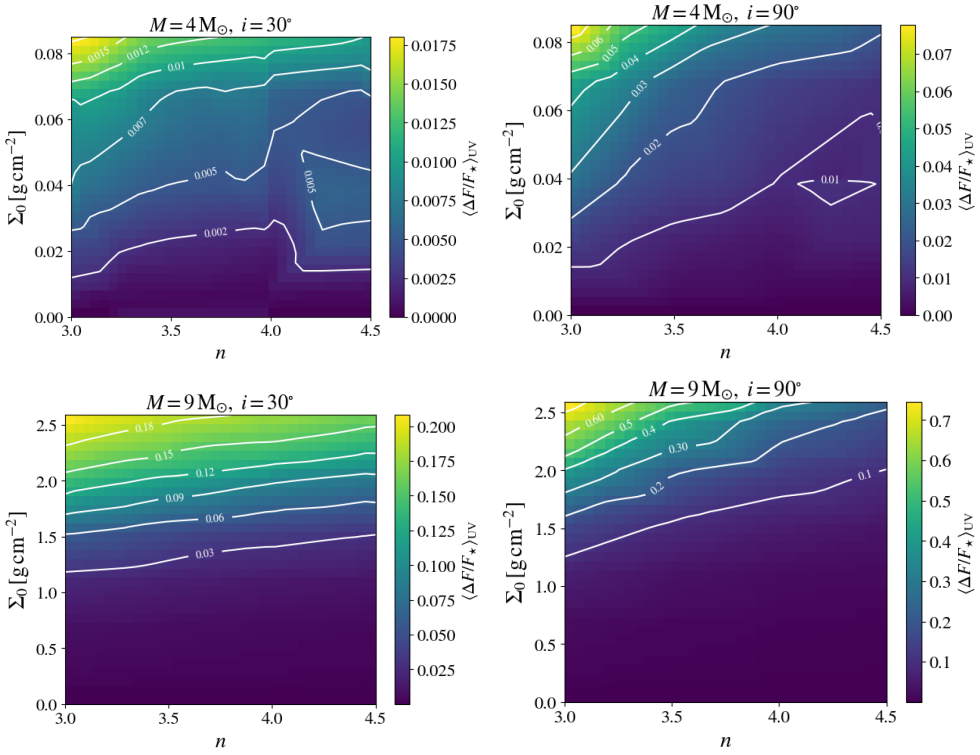

Figure 5.2: Top: UV disk effect function of a typical late-type Be star ($M = 4\,M_\odot$) at different orientations. Left: $i = 30°$. Right: $i = 90°$. Bottom: UV disk effect function of a typical early-type Be star ($M = 9\,M_\odot$) at different orientations. Left: $i = 30°$. Right: $i = 90°$.

5.4 The Influence of the $v \sin i$ Prior

Before moving on to the main goal of this chapter, which is to apply BeAtlas to a sample of OBA stars with UV observations, we use the photospheric grid of BeAtlas (Sect. 3.3.1) to model IUE observations of the CBe α Arae.

Initially, and mostly as a didactic exercise, we compute the stellar, (M, t/t_{MS}, W), geometrical and interstellar extinction ($E(B-V)$) parameters of α Arae using only the IUE data and the distance prior (Eq. 4.3). Figure 5.3 shows the corner plot obtained. The posterior probability distributions indicate that all the parameters were well constrained. As a second step, we redo the procedure, but now considering the $v \sin i$ prior of Eq. 4.4, using $v \sin i = 305 \pm 15\,km\,s^{-1}$ (see Chapter 7 for more details about the choice of $v \sin i$). The results are shown in Figure 5.4. At first sight, the posterior probability distributions appear narrower when compared with the distributions shown in Fig. 5.3. This can also be seen by the (usually) narrower confidence intervals listed on top of each diagonal subplot. This indicates that the $v \sin i$ prior, in fact, improves the ability of BeAtlas to determine the stellar parameters from the fit of the UV spectrum. This happens because the $v \sin i$ prior effectively narrows down the range of stellar models by associ-

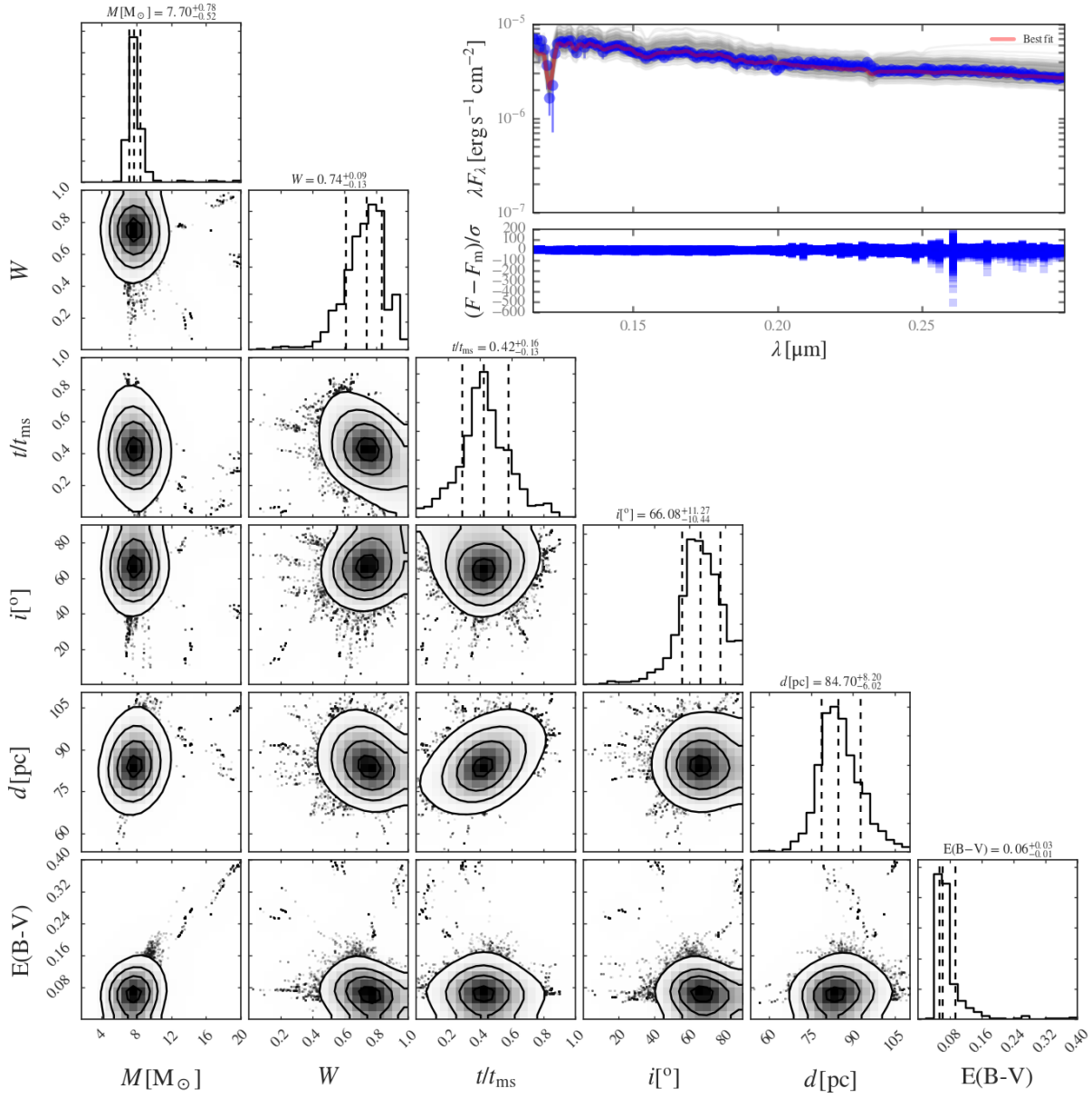

Figure 5.3: Cornet plot of a BeAtlas simulation of IUE observations of α Arae. The inset shows the fitted SED (blue points) in the upper panel and the residuals of the fit in the lower one. The red line shows the best fit. The dashed lines in the diagonal subplots correspond to the 16th, 50th, and 84th percentiles of the distributions. The subplots under the diagonal subplots show the probability densities correlations between all pairs of parameters.

ating lower posterior probabilities to sets of parameters with $v \sin i$ values far from the published ones. This comparative work led us to adopt the v sin i prior, when available, for all studied stars.

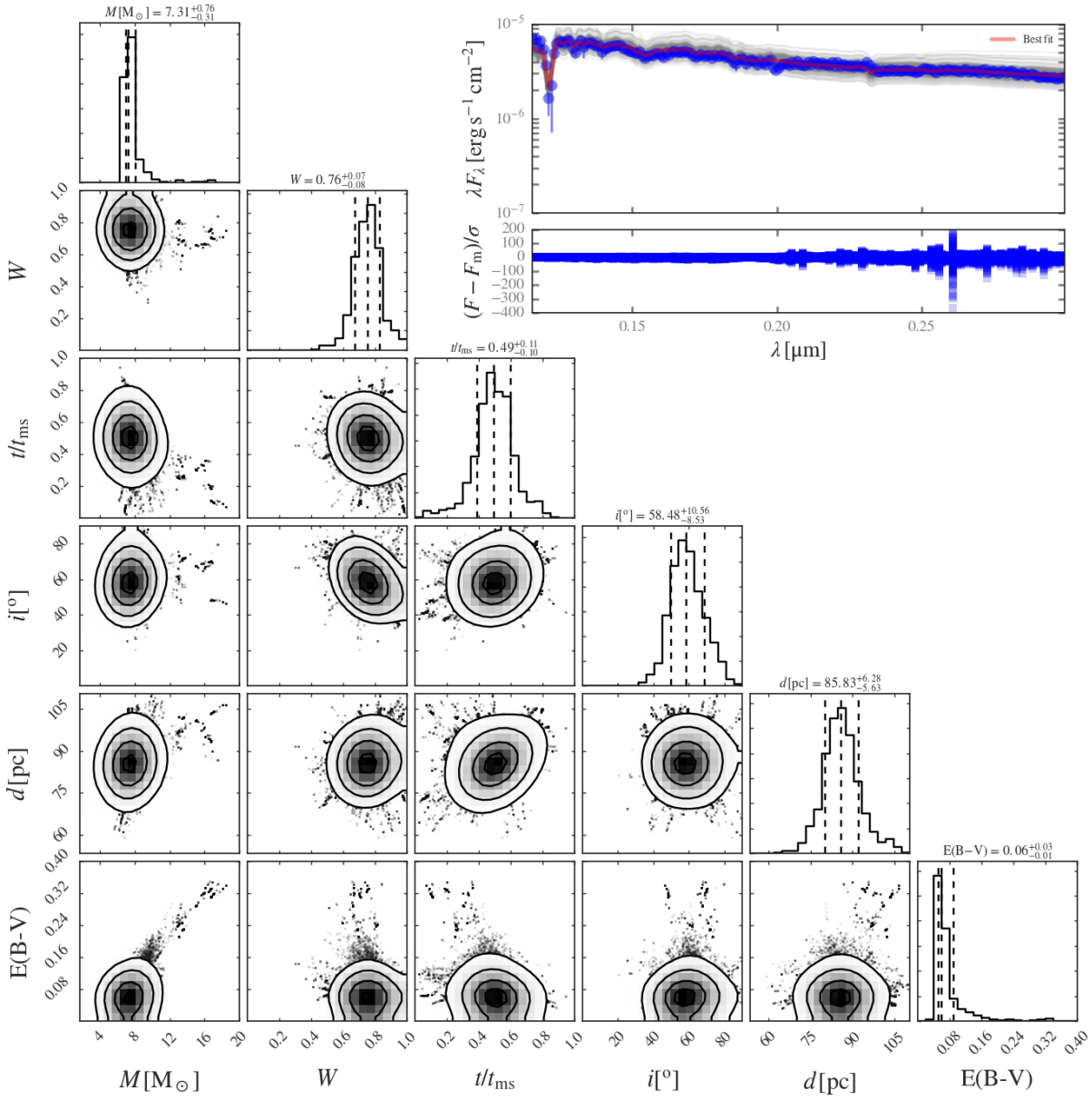

Figure 5.4: Same as Fig. 5.3, using the prior of $v \sin i$ (see text for details).

5.5 Results

The steps followed in this section were directed to explore the spectral limits of the Be phenomenon, possible evolutionary links among peculiar stars (Bn, Be, Ae and Oe stars), and to have a global overview of stellar properties of these stars, including rotational rates. We proceeded with the inference of the stellar parameters of the sample of stars shown in Section 5.2 following the procedure outlined in Sect. 4.4. The individual corner plots of each target, as well as a plot of the UV spectrum and the best fit, are available in the Appendix M.

Our results are compared to those of the literature from many sources. The main sources are three papers: Frémat et al. (2005), Levenhagen and Leister (2006) and Zorec et al. (2016). Frémat et al. (2005) used the input spectra of Chauville et al. (2001) for 130 Be stars, and applied their own code, FastRot, to obtain their photospheric parameters. However, it should be pointed out that the results of Frémat et al. (2005) have been questioned in the literature. For instance, Rivinius et al. (2013) argue that their determination for the inclination angle have obvious issues. According to the authors: "Unfortunately, a close inspection of the data reveals some potential problems, e.g., in a histogram of the derived inclination the bin $i > 80^{o}$ is almost empty, even known shell stars being assigned partly much lower inclinations". Shell stars are Be stars seen edge-on, and Fremat et al. failed to identify several stars as such in their study.

Furthermore, some comments are in order about the work of Levenhagen and Leister (2006). They performed spectroscopic analyses of southern Be stars using non-rotating models. This can result in inaccurate determinations of surface parameters such as $T_{\rm eff}$ and $\log\, g$ (Townsend et al., 2004). In addition, the derivation of parameters such as age, the old calibrations for non-rotating stars of Schaller et al. (1992) were used. Therefore, a direct comparison between our results and those of Levenhagen and Leister (2006) should be done with caution.

The results presented here are somewhat preliminary, as some of the most deviant cases, for which our results and the reference values are very discrepant, still must be individually analyzed before publication. In any case, the following can be regarded as a decisive test of the BeAtlas and an assessment of its ability as an analysis tool.

5.5.1 Effective Temperature and Surface Gravity

The effective temperature derived from BeAtlas is compared with the reference values in the literature in Fig. 5.5. The three reference papers (see caption of the figure) all used spectroscopic analyses of photospheric line profiles. Although some deviant cases do exist, the agreement is generally good. The situation is different for the $\log\, g$ (Fig. 5.6). Even though most reference values do not agree with our inferences, our values are inside the typical range for B-type stars ($3.7 \lesssim \log g \lesssim 4.2$) (e.g. Silaj et al. 2014). We suspect that we may have made some mistake in the $\log\, g$ calculation, because our error bars are way too small (Tab. A.9). Another issue is that our values are systematically larger than the reference ones. Before the completion of this text we did not find the reason for the small error or for the systematic shift in $\log\, g$.

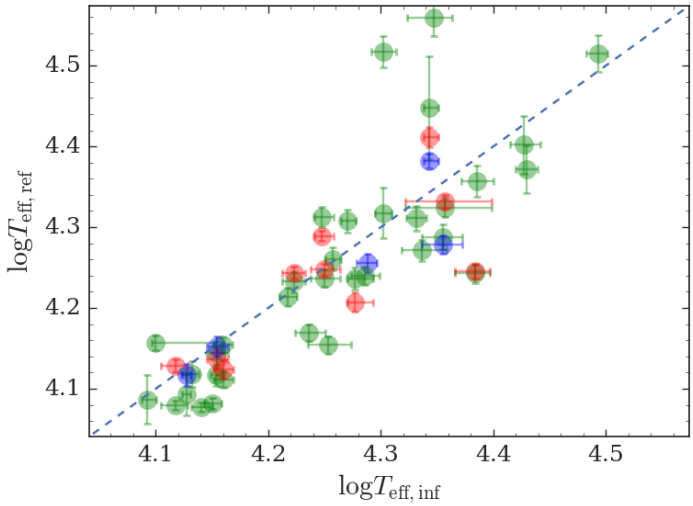

Figure 5.5: A comparison of the values of $T_{\rm eff}$ inferred for our sample ($T_{\rm eff,inf}$) with those of the literature ($T_{\rm eff,ref}$). Blue: data from Levenhagen and Leister (2006). Red: data from Frémat et al. (2005). Green: data from Zorec et al. (2016).

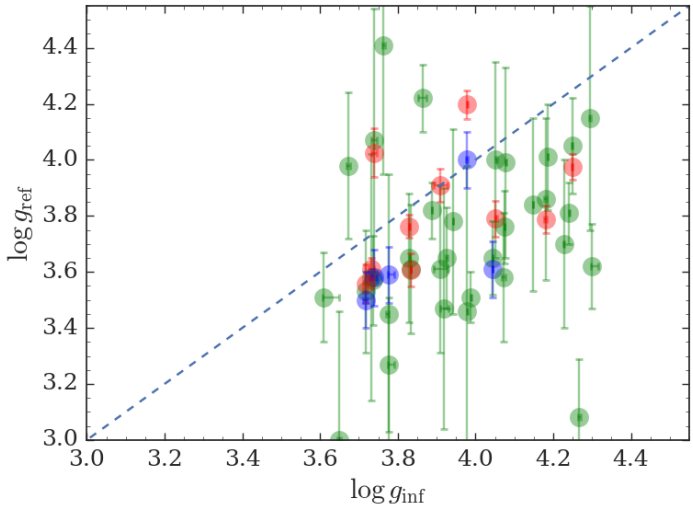

Figure 5.6: Same as Fig. 5.5 for the surface gravity.

5.5.2 *Luminosity and Age*

In Figures 5.7 and 5.8, we show the comparison of the inferred luminosities and ages compared with the literature. For the luminosity, we did find a good agreement between the results, but the same is not true for the age, for which about 1/4 of the estimates are farther then 3 σ from each other. This latter discrepancy must still be better investigated.

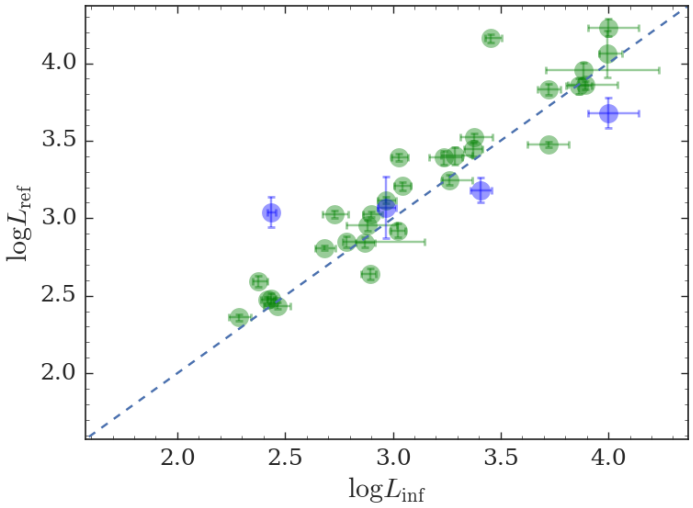

Figure 5.7: Same as Fig. 5.5 for the luminosity.

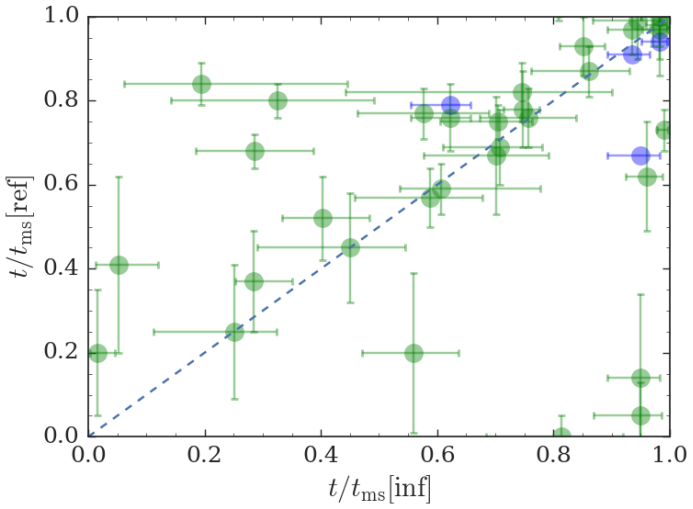

Figure 5.8: Same as Fig. 5.5 for fraction of the time spent in the MS.

5.5.3 Inclination Angles

The inclination angle determination is very important, mainly for fast rotators. It is justified by the degeneracy between the inclination and the luminosity. In principle, a fast-rotating star with $i \sim 0^{\rm o}$ and late spectral type could have a similar UV spectrum to that of a star of early spectral type with $i \sim 90^{\rm o}$. Therefore, the inference of the i might influence substantially the determination of the effective temperature, as surface temperatures which can vary over the stellar surface by 50% between the pole and equator (Vinicius et al., 2007). In Fig. 5.9, we present a comparison between the inclination angles inferred with the values found in the literature. Al-

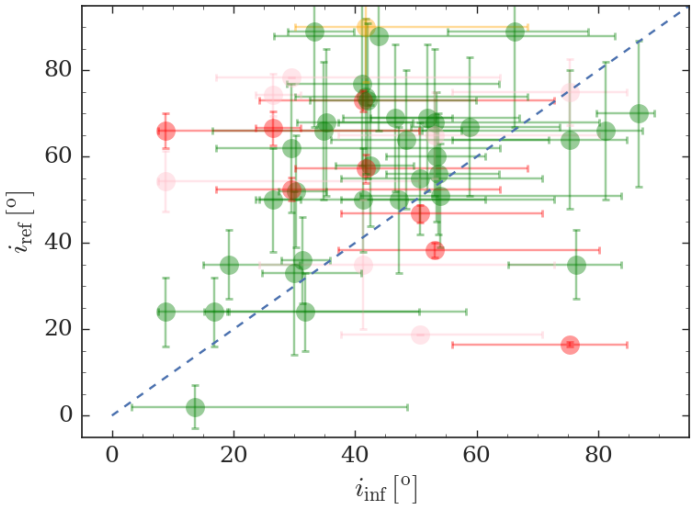

Figure 5.9: Plot of the i calculated and from the references for each star. Red: data from Frémat et al. (2005). Green: data from Zorec et al. (2016). Yellow: data from Tycner et al. (2006). Pink: data from Meilland et al. (2012).

though, our error bars are large, since we only used the SED for estimating i. However, there is a trend to lower inferred values, masked by the error bars.

5.5.4 Interstellar Extinction

Some inferred $E(B-V)$ values are shown in Figure 5.10 together with their respective reference values (e.g. Dougherty et al. 1994; di Benedetto 1998; Hunter et al. 2006; Zorec et al. 2016). There is a trend for the reference values to be lower than the inferred, but they agree when we consider the error bars.

5.5.5 Evolution of the Rotation Rate

Examining the relationship between the rotation rate and the stellar mass, we see no clear dependence between them as shown in Fig. 5.11. This figure also shows that all selected Be have $W \gtrsim 0.4$, consistent with results from the literature (Huang et al., 2010). Furthermore, the selected stars cover the entire MS strip (Fig. 5.12). Our results support well-known results, e.g. the presence of few Be stars with masses $M \leq 7\,M_{\odot}$, $\sim 14\%$ of the studied Be stars in the first half of the MS phase (Frémat et al., 2005). Actually, most of our Be stars (~ 76 %) belong to the second half of the MS phase. This is in agreement with the general belief that B stars spin up during their MS evolution (Ekström et al., 2008); therefore, the Be/(B+Be) ratio increases with age (McSwain and Gies, 2005). The evolutionary spin-up is quite clear in Fig. 5.13.

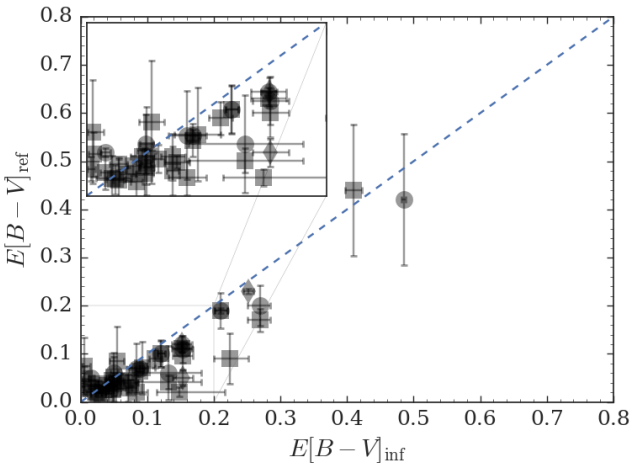

Figure 5.10: Plot of the $E(B-V)$ calculated and from the references for each star (♦: Hunter et al. (2006), •: Dougherty et al. (1994) calculated using the 2 200 bump; ■: Zorec et al. (2016)).

Our results also indicate that low-mass B stars are born with a larger proportion of rapid rotators than high-mass B stars (Huang et al., 2010). Moreover, our results point out to a wide age range ($0.0 \lesssim t/t_{\rm MS} \lesssim 0.95$) occupied by Bn stars. This result disagrees with earlier studies that discuss the occurrence of Bn stars in the first MS evolutionary phases (Zorec et al., 2007). higher rotational rates than high-mass B stars

Figure 5.13 shows the correlation between rotation rate and age. The results corroborate the conclusion of Martayan et al. (2007), that the Be phenomenon appears earlier ($t/t_{\rm MS} \sim 0.05$) in the MS for early B-types than for their late counterparts ($t/t_{\rm MS} \sim 0.30$).

5.6 Discussion

As a preliminary study, the results shown in this section demonstrate that our method, even dealing with a large set of parameters and few observables (UV spectrum, parallax and $v \sin i$), has the capability of reproducing fundamental stellar parameters and the $E(B-V)$ from an random sample, with usually consistent errors. This was already expected for slow rotators, since there is a clear unicity among them and their correspondent UV spectra. On the other hand, initially it was not obvious that the UV alone could lift the degeneracy introduced by fast rotation and viewing angle. The results show that it does. Furthermore, the usage of priors such as $v \sin i$ can improve the inference. We could reproduce important trends previously known in the literature such as the spin up during the MS and the evidence that cooler Be stars are more likely to be critical rotators (e.g. Cranmer 2005).

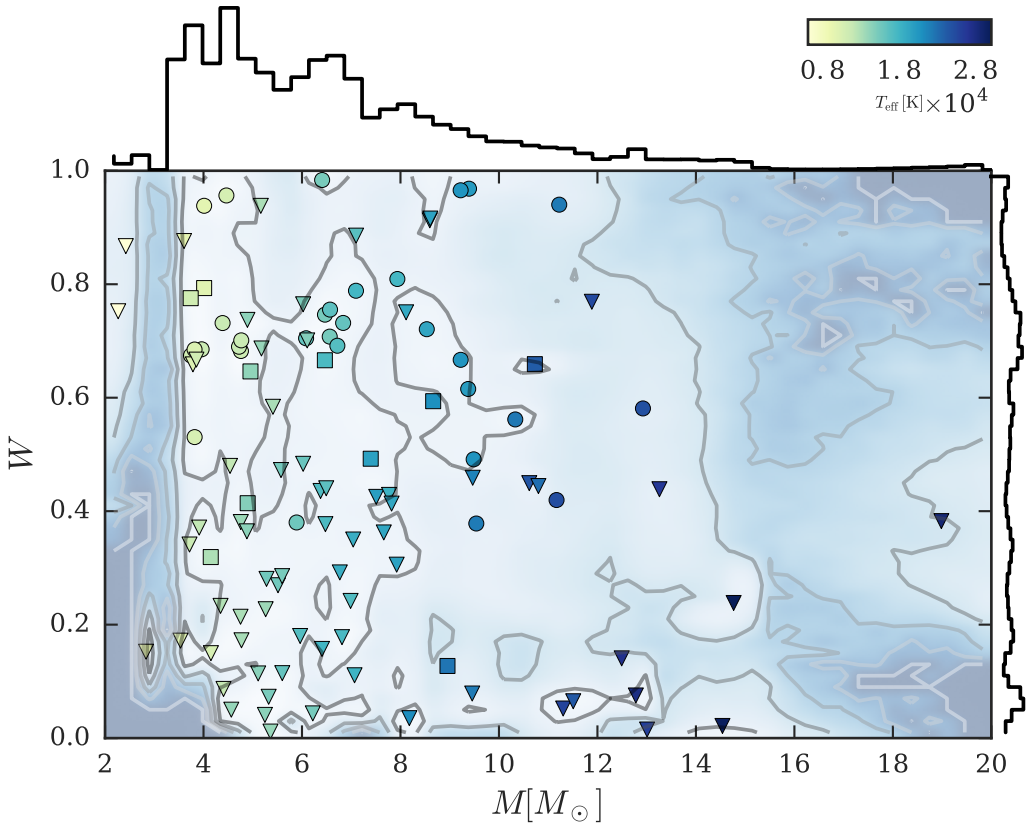

Figure 5.11: Mass versus rotation rate, W. ▼: B stars , •: CBe, Oe and Ae stars. ■: Bn stars.

As pointed out above, more work will be done before publishing the results of this chapter. A careful, one by one analysis of each star must still be done. However, the results are largely positive. Even though nothing new was discovered with this study in regards to the nature of the stars and the properties of the sample, the results points to the usefulness of BeAtlas as an analysis tool.

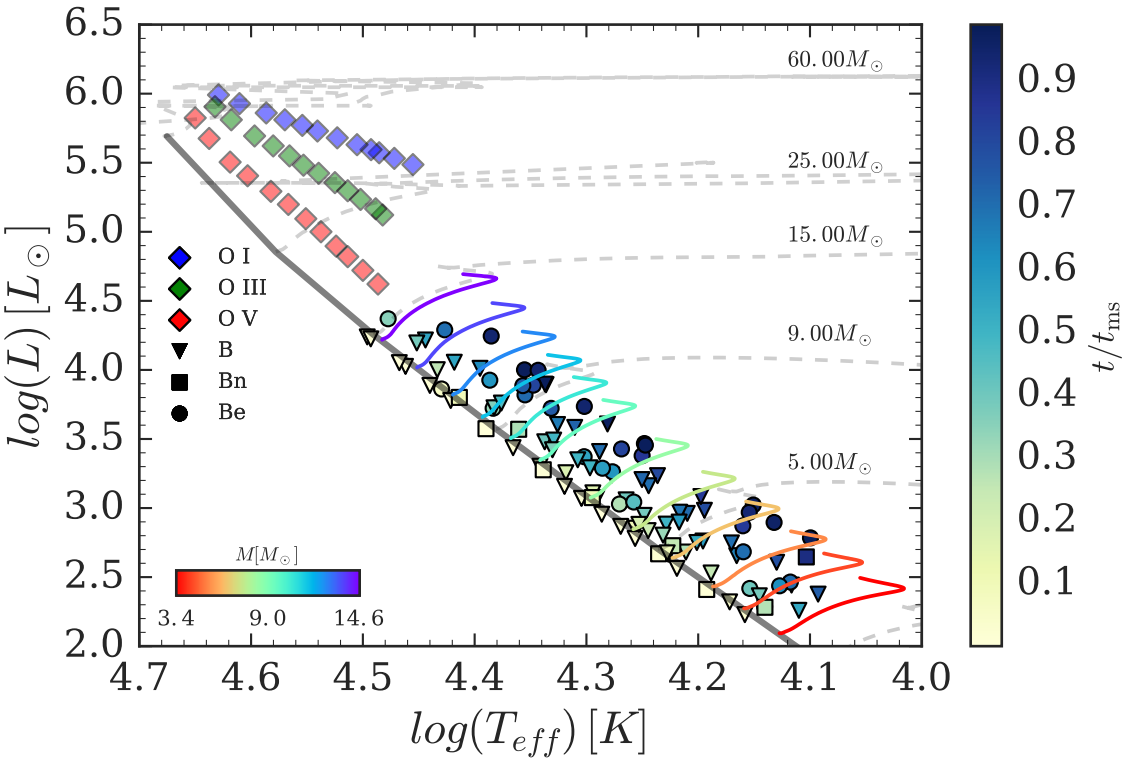

Figure 5.12: HR Diagram constructed using the data shown in Table A.9. The gray curve indicates the zero age main sequence ZAMS. Each evolutionary track (grey dashed curves labeled with different masses; data from Georgy et al. (2013) extends from ZAMS through to terminal age TAMS, defined by the cessation of core hydrogen burning. The vertical colorbar at the right represent the MS lifetime fraction. The colorbar at the left lower corner represents the stellar mass. The different symbols are representative of the object type as indicated in the figure. The O-type stars are put just for comparison group of points in red (OV), green (OIII) and blue (OI) with $\log(T_{\rm eff}) > 4.5$, (data from Martins et al. 2005).

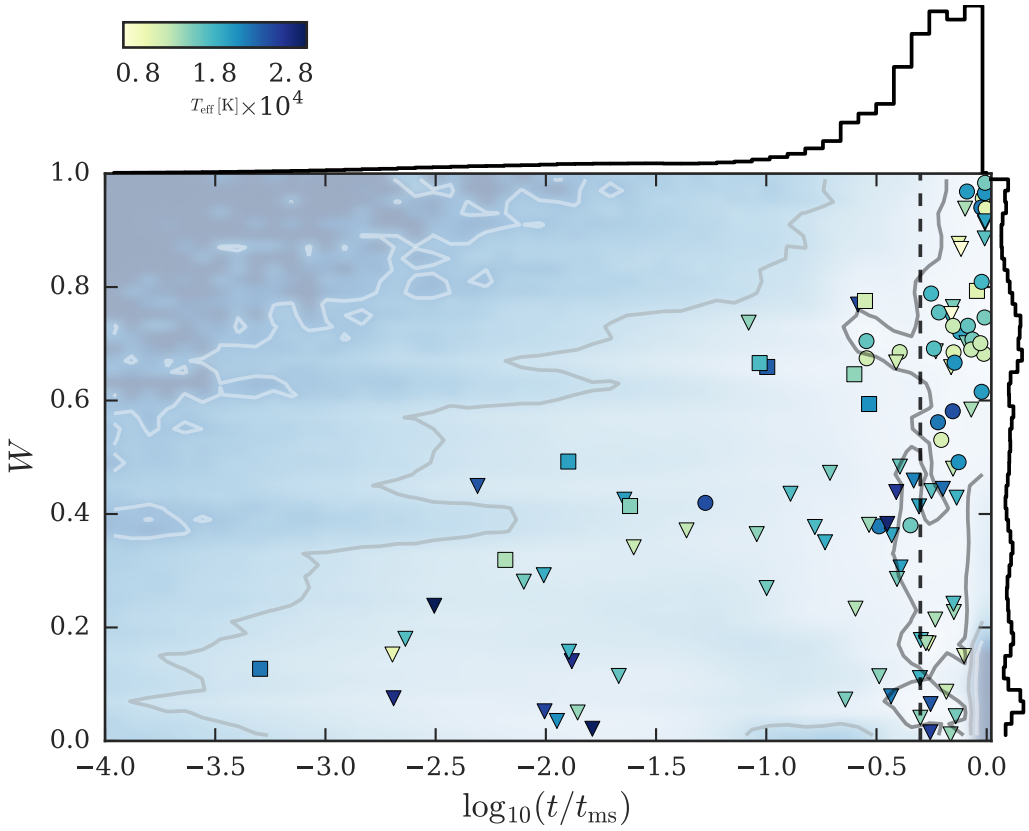

Figure 5.13: Rotation rate, W, versus MS lifetime, $t/t_{\rm MS}$. ▼: B stars , •: CBe, Oe and Ae stars. ■: Bn stars. Vertical dashed line: half of the Main Sequence lifetime.

Chapter 6

The Case of β CMi

6.1 Chapter Summary

There are different physical processes operating in Be disks, each of them being associated with distinct observables. Therefore, the multiplicity of observations could, in principle, yield complementary results, providing support for the modeling process. In this Chapter, we study the SED and polarization of the CBe β CMi. The general properties of the star are reviewed in Section 6.2. Next, the data and their reduction are shown (Sect. 6.3). The modeling of the observations with BeAtlas is done in Section 6.4. In Section 6.5, we discuss and analyse our results.

6.2 β CMi

In Chapter 1 we presented a summary of CBe variability (Sect. 1.2.1), with an emphasis on disk variability. Early-type CBes are usually quite variable, and variability decreases towards later spectral subtypes (Rímulo et al., 2018).

The CBe β CMi is a good example of this feature. It has been extensively observed in the past few decades, and its disk has remained remarkably stable (see, e.g., Klement et al., 2015 for a thorough review of this star). As such, this star is a gift from Nature, as it provides the perfect opportunity to study a stable disk.

β CMi was the target of pioneer interferometric studies. For instance, Quirrenbach et al., 1997 published the disk and stellar diameters from interferometric measurements. They also estimated the equatorial radius, $R_{\rm eq} = 3.6\,{\rm R}_\odot$, and a lower limit for the disk size, $R_{\rm D} = 13\,{\rm R}_\odot$. Later, Tycner et al. (2005), also through long-baseline interferometric data, determined the rotation rate ($W = 0.85 \pm 0.21$) and the equatorial radius, $R_{\rm eq} = 3.6 \pm 0.3\,{\rm R}_\odot$, obtained from H$\alpha$ channels.

Table 6.1 - Disk and stellar parameters of β CMi obtained from the literature.

Parameter	Klement et al., 2015	Klement et al., 2017
$R_{\rm pole}[R_\odot]$	2.8	2.8 ± 0.2
$M\,[M_\odot]$	3.5	3.5
$L\,[L_\odot]$	185	185 ± 5
W	0.98	1.0
β	$0.1367^{+0.0025}_{-0.0013}$	-
$\log_{10}\rho_0[\mathrm{g\cdot cm^{-3}}]$	-11.70	$-11.78^{+0.18}_{-0.30}$
$R_{\rm D}[R_{\rm eq}]$	35^{+10}_{-5}	40^{+10}_{-5}
$i\,[^{\rm o}]$	43^{+3}_{-2}	-
d [pc]	49.6	-
$E(B-V)$[mag]	-	$0.01^{+0.02}_{-0.01}$
n	-	2.9 ± 0.1

Recently, multi-technique analyses were applied to β CMi (Klement et al., 2015; Klement et al., 2017). Both studies shared the same stellar parameters. Table 6.1 shows the best-fit parameters of each study. For comparison, we adopted the results from Klement et al., 2017 since it resulted from a improved version of the HDUST code and from additional Very Large Array (VLA)[1] measurements.

The model of Klement et al. (2015) and its revision in 2017 represents a landmark in the Be literature, as it is still the most comprehensive model of a Be Star to date. One of the most remarkable results was that a single model (a fast-spinning Be star surrounded by a steady-state VDD) could explain a very large and diverse dataset, that included a SED from the UV to the radio, optical polarimetry, spectroscopy, interferometry and spectrointerferometry.

One interesting result was the detection of a SED turndown in the radio that was successfully modeled by a truncated disk (see Table 6.1). Under the assumption that the truncation was due to an orbiting companion, the authors used the results of Panoglou et al. (2016) to predict the semi-major axis and the orbital period of the secondary, which was later found by Dulaney et al. (2017) by means of radial velocity measurements. We will come back to this point later on.

6.3 Observational Data Overview

A diversity of data is important to explore different system parameters because each spectral domains reflects different physical mechanisms. The disk of Be stars are perhaps most conspicu-

[1] http://www.vla.nrao.edu/;

ous at optical wavelengths by the presence of hydrogen Balmer and metallic emission lines (e.g. HI and FeII lines) in their spectrum (Lamers et al., 1980). In the IR range, a strong emission excess, of disk origin, arises from continuum bound-free and free-free thermal emission (e.g. Cote and Waters, 1987). Besides these processes, the polarization of starlight by the disk is also present (e.g., Yudin, 2001; Kjurkchieva et al., 2016).

Most of the observations used here are the same as the ones used by Klement et al. (2015), but not all. We combined data from the literature, including photometric, polarimetric and spectroscopic data. Most data were accessed through online Virtual Observatory Tools (VO): Bess[2], VO SED Analyzer (VOSA, Bayo et al. 2008), Spectral Analysis Tool (VOSpec; Arviset et al. 2008), MAST[3], VAO[4], SDSS[5], AAVSO[6], ESO archive[7], US Virtual Astronomical Observatory[8], and from VizieR Photometry viewer (Ochsenbein et al., 2000). All the routines used to read and plot the observational data are available in the GitHub Repository Link[9].

6.3.1 *Photometric Data*

VO Tools can provide the SED of an object by searching in several catalogues. Our photometric data comprises results of several observers and missions: Ducati (2002), Hipparcos (ESA, 1997), Mermilliod (1994), IUE, 2MASS, TYCHO (Hog et al., 2000) in the visual domain, DENIS, IRAS, WISE (Cutri and et al., 2014) in the IR domain, AKARI (AKARI/IRC mid-IR all-sky Survey; Ishihara et al. 2010), MSX (MSX6C Infrared Point Source Catalog; Egan et al. 2003), SDSS, and from the Catalogue of Homogeneous Means in the UBV System (Mermilliod, 1994).

Klement et al. (2015) presented the model of the radio SED of a CBe. They used new radio data from APEX, as well as VLA data from the literature. In the 2017 revision of the model (Klement et al., 2017), new VLA data was made available. Recently, they obtained the first 5 cm and 10 cm measurements of a CBe disk, and these were kindly made available for this thesis. The radio data is summarized in table 6.2.

[2] http://basebe.obspm.fr;
[3] http://archive.stsci.edu;
[4] http://vao.stsci.edu;
[5] http://www.sdss.org;
[6] http://www.aavso.org;
[7] http://archive.eso.org;
[8] http://vao.stsci.edu;
[9] https://github.com/tangodaum/AstroPLOT.

Table 6.2 - Recent radio data of β CMi.

Band	λ [cm]	Flux [erg/s/cm^2/Å]	Flux Error [erg/s/cm^2/Å]	Reference
K	1.36	2.24×10^{-24}	2.76×10^{-25}	R. Klement, priv. comm.
X	3	1.56×10^{-25}	1.33×10^{-26}	R. Klement, priv. comm.
C	5	2.90×10^{-26}	2.64×10^{-27}	R. Klement, priv. comm.
S	10	2.28×10^{-27}	6.00×10^{-28}	R. Klement, priv. comm.
	0.087	1.53×10^{-20}	1.23×10^{-21}	APEX/LABOCA

6.3.2 Linear Polarization Data

Linear polarization of starlight can be intrinsic to the star and its immediate environment or due to interstellar contribution. This measurement is one the most sensitive quantities to detect circumstellar activity (Carciofi et al., 2007). The interstellar polarization results from dust particles partially aligned to the Galactic fossil magnetic field (Cotton et al., 2016). In contrast, the intrinsic polarization arises from scattering of starlight by circumstellar material. In CBe disks, the polarigenic mechanism is Thompson scattering by free electrons present in the disk (see, e.g., Wood et al. 1997). This polarization is strongly connected with the stellar subspectral type, the density scale and with the inclination angle (Haubois et al., 2014).

We made use of polarimetric data from the Pico dos Dias Observatory (`OPD-LNA`) (Tab. A.6), and from the `HPOL` Spectropolarimeter at the University of Wisconsin-Madison Pine Bluff Observatory (`PBO`) (Tab. A.7). The `OPD-LNA` data was reduced with packages developed by the Beacon group[10], and described in Magalhaes et al. (1984, 1996) and Carciofi et al. (2007). We obtained the `HPOL` data from the `MAST` Archive[11].

6.4 Modelling with Be Atlas

6.4.1 Modeling of the Entire SED

We applied the method described in Sect. 4.4 for the photometric data of β CMi. We define two priors: 1) for the $v \sin i$ (Eq. 4.4), using the values of Becker et al., 2015, i.e. 248 ± 13 km s^{-1}, which is in agreement with previous studies (e.g Yudin, 2005; Frémat et al., 2005); 2) a prior on the distance (Eq. 4.3), for which we used the Hipparcos parallax (van Leeuwen, 2007).

[10] http://beacon.iag.usp.br/;
[11] https://archive.stsci.edu/hpol/.

Table 6.3 - Correlation matrix of the parameter correlations of β CMi. Red: strong correlation. Orange: medium correlation. Green: weak correlation. Purple: no correlation.

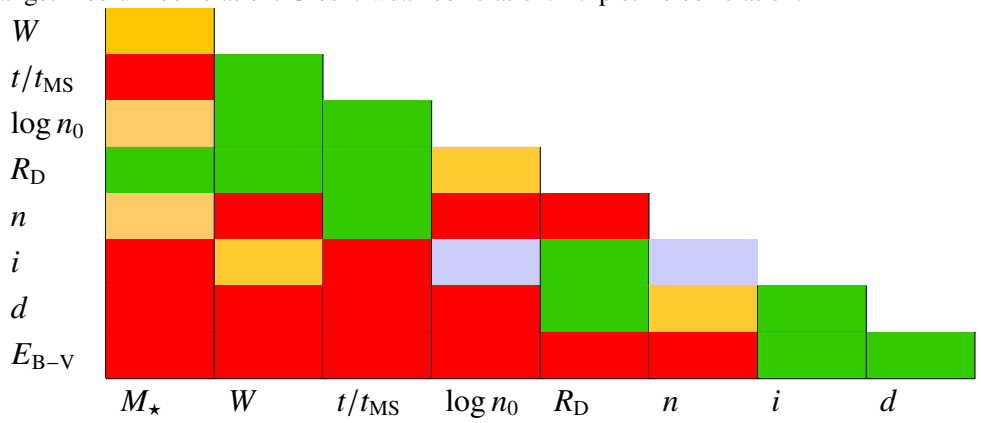

For the BeAtlas simulation shown in Fig. 6.2 we used 500 walkers and 300 steps. The acceptance fraction of the simulation was 0.22. The chord diagram of the simulation is shown in Fig. 6.3 and the convergence plot is shown in Fig. B.1.

The results of the SED fit with BeAtlas reveal several interesting points:

- The PDFs of all the parameters (diagonal row in Fig. 6.2) are well-defined, and tend to zero towards the limits of the plots. Those are the characteristics of a well-converged simulation, in which all parameters were sufficiently constrained;

- Most PDFs are single-peaked, with the exception of n, i, and $E(B-V)$ that are double-peaked. This reveals other possible solutions; however, the separation of the peaks are probably not large enough to warrant this conclusion;

- We postpone a detailed comparison of our results with those of Klement et al. (2015, 2017) for later. For the moment we notice that our derived mass $M = 4.13 \pm 0.15\,\mathrm{M}_\odot$ is $0.6\,\mathrm{M}_\odot$ larger than their value, but this is due to the fact that our self-consistent $E(B-V)$ is larger than their assumed value;

- The error in the mass is small ($\sim 0.2\,\mathrm{M}_\odot$), and this deserves some careful consideration. Typical spectroscopic determinations of the mass have usually much larger uncertainties, so why are our results for the mass so precise? We believe this has to do with a combination of two factors: 1) the UV spectrum is quite sensitive to the temperature (and mass) of the star (see previous Chapter). 2) The $E(B-V)$ is essentially zero for β CMi.

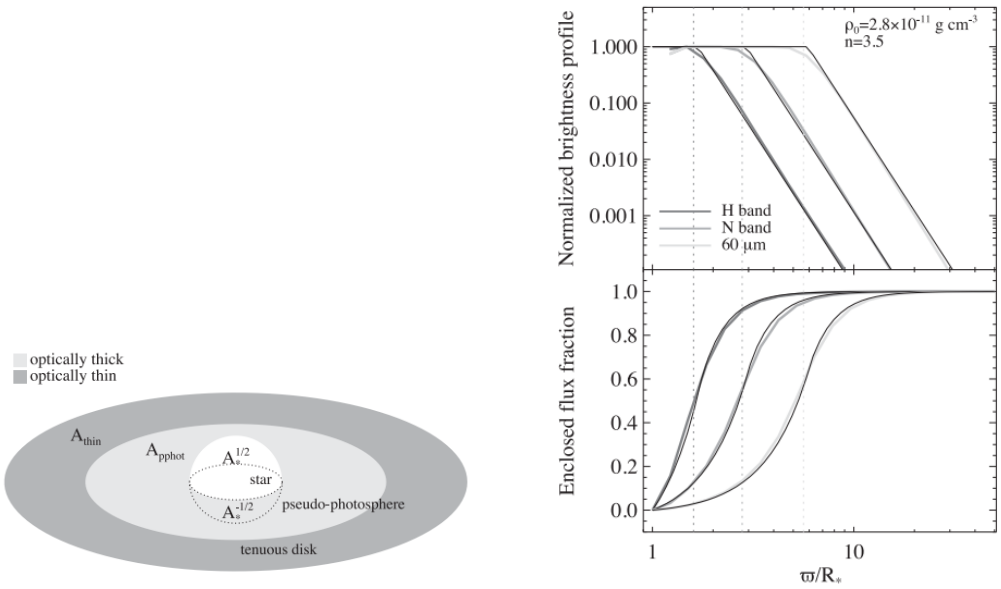

(a) (b)

Figure 6.1: (a) Schematic representation of disc components (Modified Figure 6 from Vieira et al. (2015)). (b) Normalized brightness profiles at three spectral bands (top), and respective formation loci curves (bottom) (Figure 13 of Vieira et al. (2015)).

The correlation matrix shown in Figure 6.3 reveals some interesting correlations between the model parameters. Similar information is shown in Table 6.3 where we illustrate the degree of dependence for each pair of parameters. To simplify this discussion, we selected some of the most important correlations and grouped them into categories:

Stellar Mass

- There is a strong correlation between $t/t_{\rm MS}$ and M. This is expected because the stellar luminosity is proportional to $R_\star^2$ (which is a function of age) and $T_{\rm eff}^4$ (which is a strong function of mass). For similar reason, a correlation between M and d is expected;
- The correlation between M and W appears because low-mass models with large rotation rates may appear similar to high-mass models with small rotation rates;
- M and i are also correlated. Low-mass stars seen at low-inclination angles (pole-on) may be similar to a high-mass star seen at high-inclination angles (edge-on). This is explained because a less massive star seen pole-on will show a larger luminosity than when it is seen from the equatorial region. Equivalently, a high-mass star seen at its equatorial region will have a lower luminosity;

- The $E(B-V)$, as well as the mass, strongly affects the UV domain, which explains their strong correlation.

Rotation Rate

- W and $t/t_{\rm MS}$ with d: W affects the projected size of the star on the Sky, depending on the inclination, thus affecting the observed flux. $t/t_{\rm MS}$ is related to the stellar radius. For this reason, these two pairs of parameters show some correlation.

Disk base density

- The density level (n_0) and slope n are also correlated. To understand this it is useful to recall the concept of pseudo-photosphere (Vieira et al., 2015). These authors showed that the disk emission can be approximated as the sum of two disk components: an inner, optically thick pseudo-photosphere and an outer, optically thin (Fig. 6.1a). The radius of the pseudo-photosphere is a function of mainly n and n_0 (e.g., Eq. 8 of Vieira et al. 2015): a dense disk with a steeper density slope may have a pseudo-photosphere of similar size to a more tenuous disk with a shallower density slope;

- The concept of pseudo-photosphere may also explain some weaker correlations observed, for instance, $t/t_{\rm MS}$ and log n_0, W and n, etc;

- Interestingly, the density level n_0 is strongly correlated with many parameters such as mass, distance and inclination. These correlation arise again because the measured IR excess requires a given size of the pseudo-photosphere (basically an emitting area) which depends in complicated ways on all these parameters;

- log n_0 and i are anti-correlated. Thinking in terms of projected area of the pseudo-photosphere, a low i and low log n_0 model may have a similar emitting area as a high i and high log n_0 model;

- One correlation that is surprising at first sight is n_0 and $E(B-V)$. Why is a parameter that only affects the blue part of the SED ($E(B-V)$) correlated with a parameter that controls the disk emission (n_0) and affects only the IR SED? We believe the answer is the strong correlation between $E(B-V)$ and M, which in turn also correlates with n_0. This is

an example of how complex the interdependence of the parameters can be, a complexity revealed by the present analysis for the first time.

6.4.2 Modeling Different Sections of the SED

The concept of pseudo-photosphere outlined above suggests another approach to the data. As seen in Fig. 6.1b, the pseudo-photosphere radius depends strongly on the wavelength: short wavelength emission comes mostly from the inner disk while emission at long wavelengths comes from the entire disk (Carciofi, 2011).

To investigate how much information each section of the SED carries about different model parameter, we split the SED in different parts and performed the BeAtlas simulation in each part and for several combinations of these parts. The results are displayed in the box plot of Fig. 6.4. The abscissa indicates the SED section (or combination of sections) used. Each plot corresponds to a given parameter, as indicated. For instance, the upper plot in the first column represents the inference of the stellar mass for each spectral domain analyzed. In general, we verify that shorter wavelengths (UV, visible and NIR) better constrain the stellar parameters: M, W, and $t/t_{\rm MS}$. On the other hand, the disk parameters (mainly $R_{\rm D}$) are poorly constrained by these spectral domains. When we include the MIR domain is a global improvement of the fit is seen, especially in the disk parameters, $\log n_0$, $R_{\rm D}$ and n, and in the inclination angle. The stellar parameters are much worse constrained when we remove the short wavelengths from the analysis. Overall, the best results were obtained when the full SED was used (SED label in Fig. 6.4). This is easily understood by the strong correlation seen among most of the parameters (Fig. 6.3): the removal of part of the data may result in a worse determination of one or more parameters that, in turn, propagates to all others.

6.4.3 Optical Polarization

The linear polarization is strongly dependent on the number of scatterers (free electrons) and their geometry. It also depends a lot on the inclination angle (Haubois et al. 2014; Halonen and Jones 2013). Therefore, one expects that polarization will provide useful constraints on n, n_0, and i. The results of a BeAtlas fit of the polarization data alone is shown in Fig. 6.5. The convergence plot is shown in Fig. B.2. This is an example of a completely non-converged simulation, that basically does not provide any useful constraint on any parameter. The reason the polarization could not constrain the disk parameters and the inclination, as naively expected,

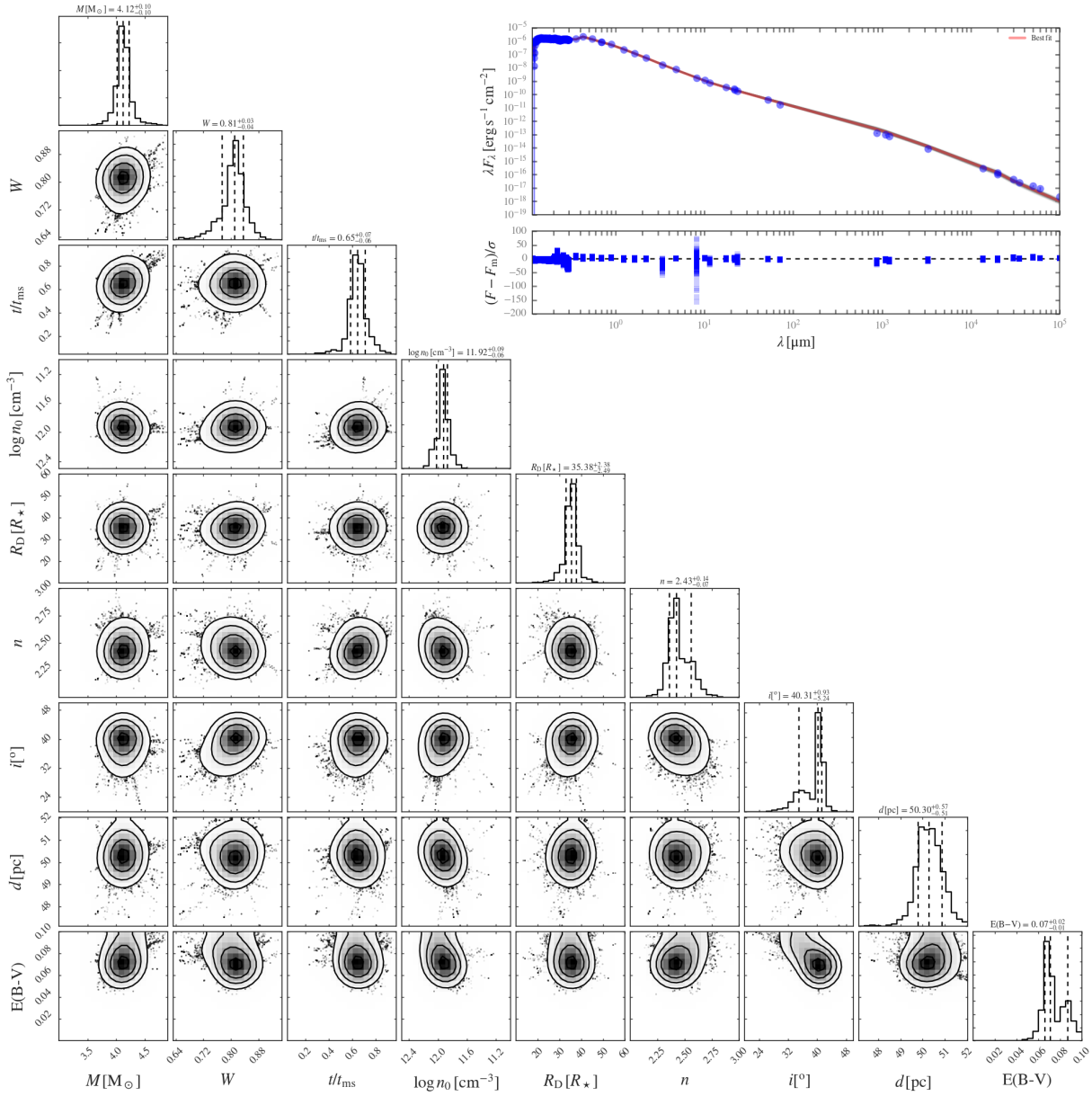

Figure 6.2: Corner plot for a BeAtlas simulation of β CMi. See text for details. The inset shows the SED in the upper part and the residuals of the fit in the lower part. Blue points: observed data. Red line: the best fit.

is that the polarization is also strongly dependent on the stellar characteristics. For instance, the number of scatterers in a CBe disk is given by

$$N_e = 2\pi \int_{R_{eq}}^{R_D} r\Sigma(r)dr = f(R_{eq}, n, n_0, R_0). \tag{6.1}$$

Therefore, N_e depends on the radius of the star. Because polarization alone cannot provide any constraints on the stellar properties, this negatively impacts the inference power for the disk parameters.

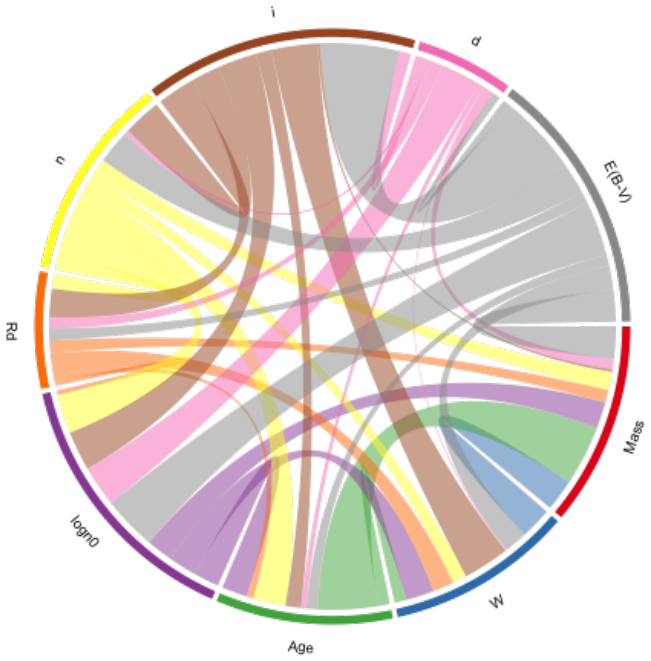

Figure 6.3: Chord diagram of the Figure 6.2.

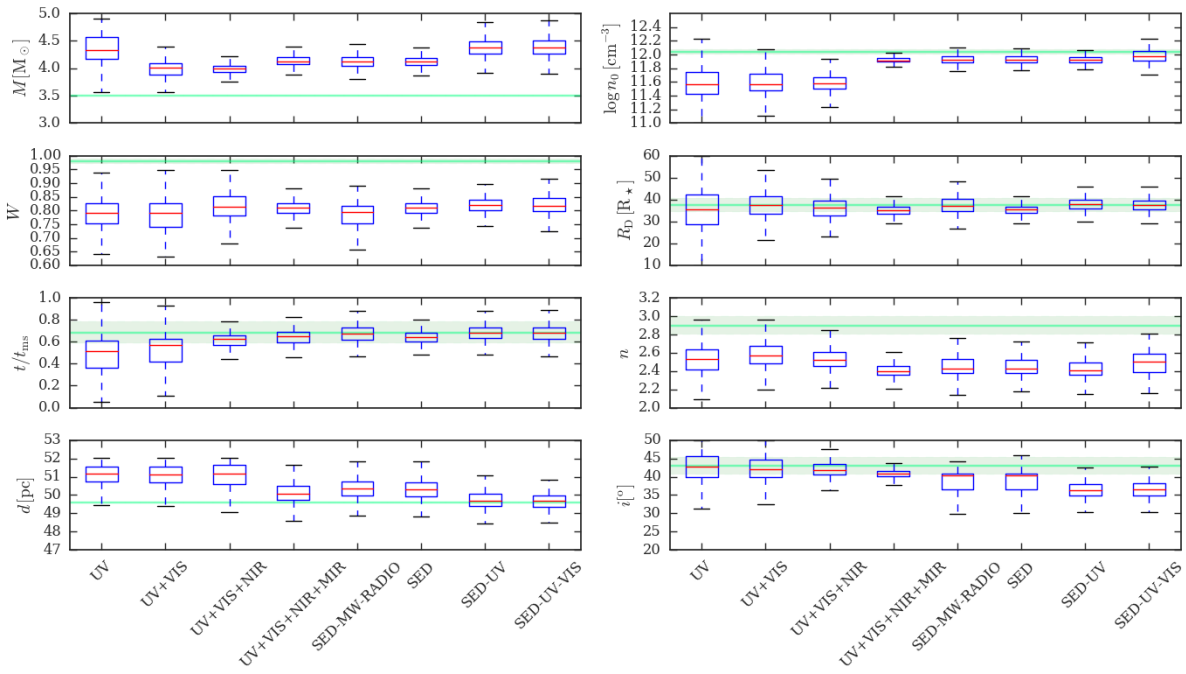

Figure 6.4: Box plot of the PDFs of different spectral domains for all parameters. The abscissa indicates the SED section (or combination of sections) used. Each plot corresponds to a given parameter, as indicated. The green horizontal bands are the best fit parameters of Klement et al. (2015, 2017).

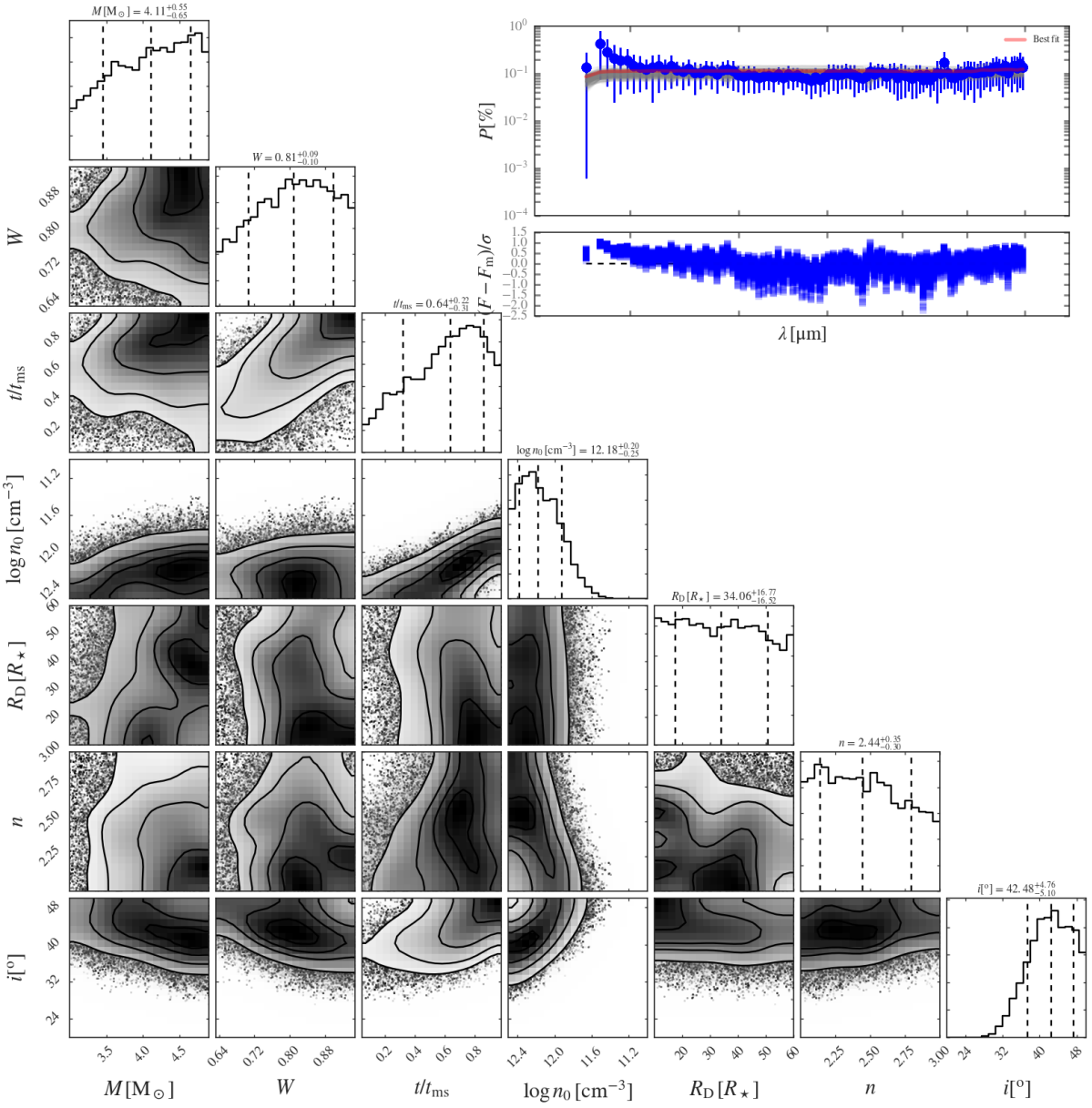

Figure 6.5: Same as Fig. 6.2 for the linear polarization.

Interestingly, we can use additional priors based on the previous results obtained from the entire SED. We can adopt a Gaussian kernel density estimator (KDE)[12] for the PDF of each stellar parameter (M, W and $t/t_{\rm MS}$) constrained previously from the full SED. This additional prior function becomes,

$$\log p_\star(\Theta, \alpha) = -0.5 \left[\hat{f}_{\rm M}(M) + \hat{f}_{\rm W}(W) + \hat{f}_{\rm t/t_{MS}}({\rm t/t_{MS}})\right]^2, \tag{6.2}$$

where $\hat{f}_{\rm M}$, $\hat{f}_{\rm W}$ and $\hat{f}_{\rm t/t_{MS}}$ are the inverse of the KDE distributions.

[12] https://jakevdp.github.io/blog/2013/12/01/kernel-density-estimation/.

Table 6.4 - Best fit parameters of β CMi. Free parameters: M, W, $t/t_{\rm MS}$, $\log n_0$, $R_{\rm D}$, n, i, d, $E(B-V)$. Derived parameters: $\log g$, $R_{\rm pole}$, L, $T_{\rm eff}$, $\beta_{\rm GD}$.

Parameter	Value	Parameter	Value
M [$M_\odot$]	$4.13^{+0.15}_{-0.15}$	$\log n_0$	$11.99^{+0.21}_{-0.10}$
$\log g$	$4.047^{+0.001}_{-0.001}$	$R_{\rm D}$ [$R_\star$]	$35.20^{+9.50}_{-11.90}$
$R_{\rm pole}$ [$R_\odot$]	$3.20^{+0.04}_{-0.03}$	n	$2.44^{+0.27}_{-0.16}$
L [$L_\odot$]	$365.3^{+31.2}_{-28.2}$	i [°]	$41.50^{+5.30}_{-3.50}$
$T_{\rm eff}$ [K]	14080^{200}_{-215}	d [pc]	$50.3^{+0.6}_{-0.5}$
W	$0.81^{+0.04}_{-0.05}$	$\beta_{\rm GD}$	$0.21^{+0.04}_{-0.04}$
$t/t_{\rm MS}$	$0.64^{+0.09}_{-0.09}$	$E(B-V)$ [mag]	$0.07^{+0.02}_{-0.01}$

Using the above priors, another simulation was run to fit the polarization. The result is shown in Figure 6.6, and the convergence plots is in Fig. B.3. Using the KDE priors of the stellar parameters allowed for inferring the disk density scale and the inclination. Most importantly, the values of these parameters agree with the previous determination. This is relevant because these two independent observations (SED and polarization) probe different disk regions and are due to different physical processes in the disk (free-bound and free emission vs. polarization).

6.4.4 *Combining the Polarization and the SED*

In the above we obtained two determinations of some of the model parameters using the full SED (Fig. 6.2) and the polarization (Fig. 6.6). To combine both PDFs, one must simply multiply them, thus obtaining a new PDF that takes both dataset into consideration. From the combined PDFs (Fig. 6.7) we obtained the best-fitting parameters for β CMi, shown in Table 6.4.

6.5 *Discussion*

A comparison of our best-fit parameters with those of Klement et al. (2015, 2017) (Tab. 6.1) shows an agreement for some parameters but a discrepancy for others. From now on, we refer to the results of Klement et al. as the *reference model*.

Curiously, our estimate of the $R_{\rm eq}$ and W match previous studies of Quirrenbach et al. (1997, $R_{\rm eq} = 3.6\,R_\odot$) and Tycner et al. (2005, $W = 0.85 \pm 0.21$; $R_{\rm eq} = 3.6 \pm 0.3\,R_\odot$) but differ from the reference model. This is likely due to the discrepancy in mass. We believe our inferred mass is larger than the reference model because our $E(B-V)$ is larger. It is worth noting that our results are in agreement with those of Catanzaro (2013, $3.8\,M_\odot$) and Frémat et al. (2005, $3.5 \pm 0.2\,M_\odot$).

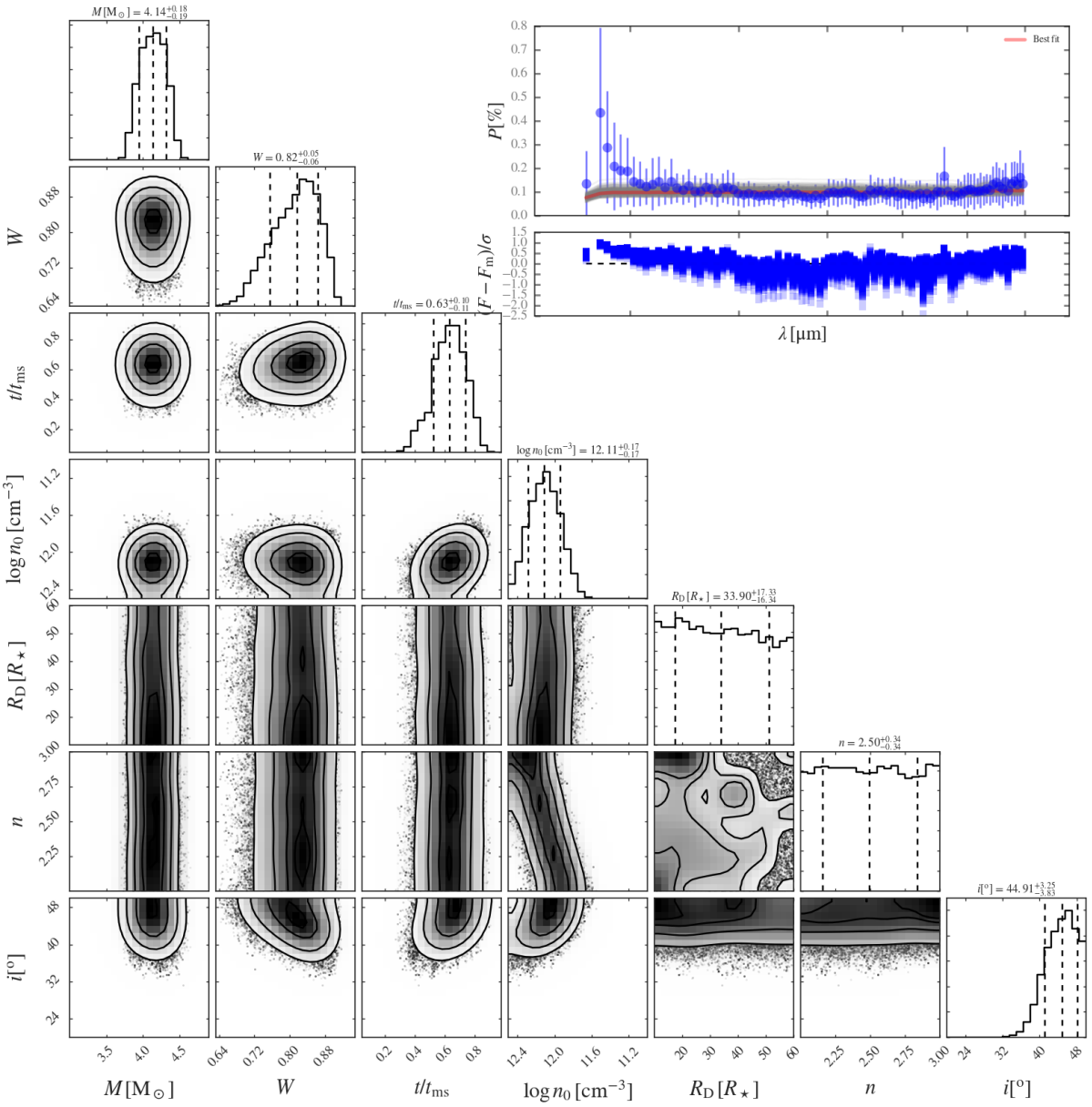

Figure 6.6: BeAtlas simulation of β CMi's polarization data using the KDE priors on the stellar parameters (see text).

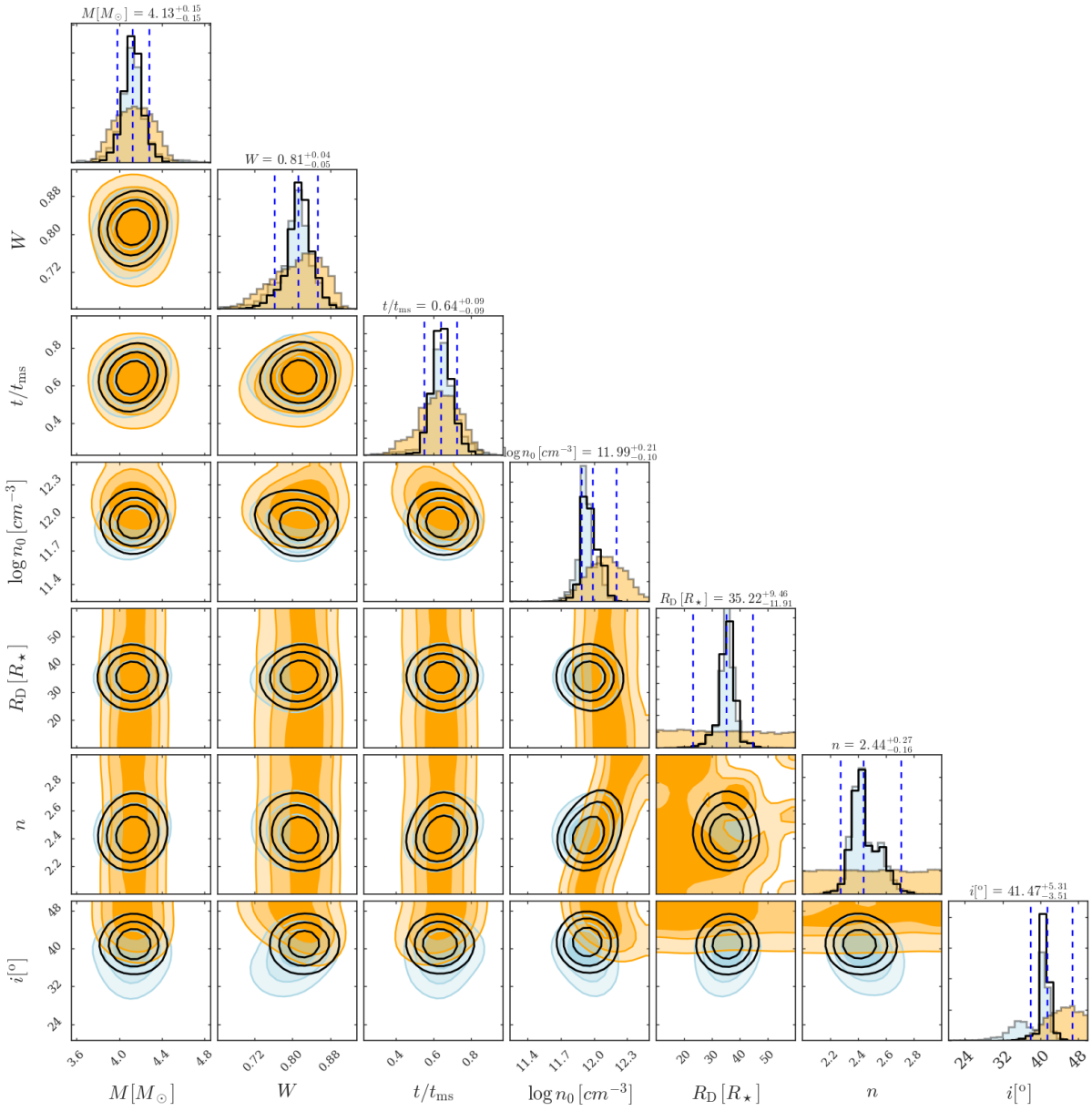

Figure 6.7: PDFs (black lines) of the SED (blue shades) and polarization (orange shades).

The inclination angle is in good agreement with the reference model, as well as with the values determined by Frémat et al. (2005, 54.5 ± 2.9^{o}) and Kraus et al. (2012, 38.5 ± 1.0^{o}). The close match of our value of i and those of Kraus et al. and the reference model is a quite significant result, since our model used only the SED and the polarization, while the other determinations relied on interferometric measurements, which is quite sensitive to i. Finally, our estimate for the age in the MS is in agreement with previous determinations (e.g. Zorec et al., 2005; Levenhagen and Leister, 2006) suggesting that β CMi is in the second half of its MS lifetime.

As for disk, we found $n = 2.44^{+0.27}_{-0.16}$ and $\log n_0 = 11.99^{+0.21}_{-0.10}$ in good agreement with the reference model. According to Vieira et al. (2017), these are typical values for Galactic late-type CBes (see their Fig. 7). The relatively low value of n deserves some further comments. Since β CMi has a stable disk, and because isothermal steady-state disks have a density slope of $n = 3.5$ (Bjorkman and Carciofi, 2005b), we speculate two possible causes for the low n: 1) Accumulation effect caused by a binary companion (see Chapter 1 and Panoglou et al. 2016); 2) Non-isothermal effects in the disk, that may indeed cause a shallower profile (Carciofi and Bjorkman, 2008). Further studies are necessary to clarify this issue.

Figure 6.8 shows the full SED of β CMi, together with our best-fit model and the reference model. The SED turndown is easily seen around the wavelength 1 mm, and both models seem to reproduce it well, which is expected given the rough agreement between the inferred values of the disk radius, $R_{\rm D}$, for both cases.

A comparison between the residuals shows some interesting features. The BeAtlas model clearly performs better in the UV up to the FIR regions. The residuals of the reference model are systematically offset to positive values. Furthermore, they have a negative slope. Both these facts indicate that the stellar mass may have been underestimated by the reference model. This further corroborates the larger mass found in our study. On the other hand, the reference model performed much better in the microwave region of the SED. One possible reason for this lies in the modeling procedure adopted by Klement et al. (op. cit.), which focused on the long-wavelength SED when manually searching for the best parameters.

Overall, the BeAtlas fit ($\chi^2 = 0.80$) is significantly better than the reference model ($\chi^2 = 6.2$). We recall here the issues raised in Section 1.6, when we outlined the goals of this work. The BeAtlas model fitted the entire SED and the optical polarization, providing a self-consistent determination of the stellar (issue 1) and disk parameters (issue 4). The usage of MCMC techniques ensures that the errors of each parameter are properly propagated to all others (issue 3). A final

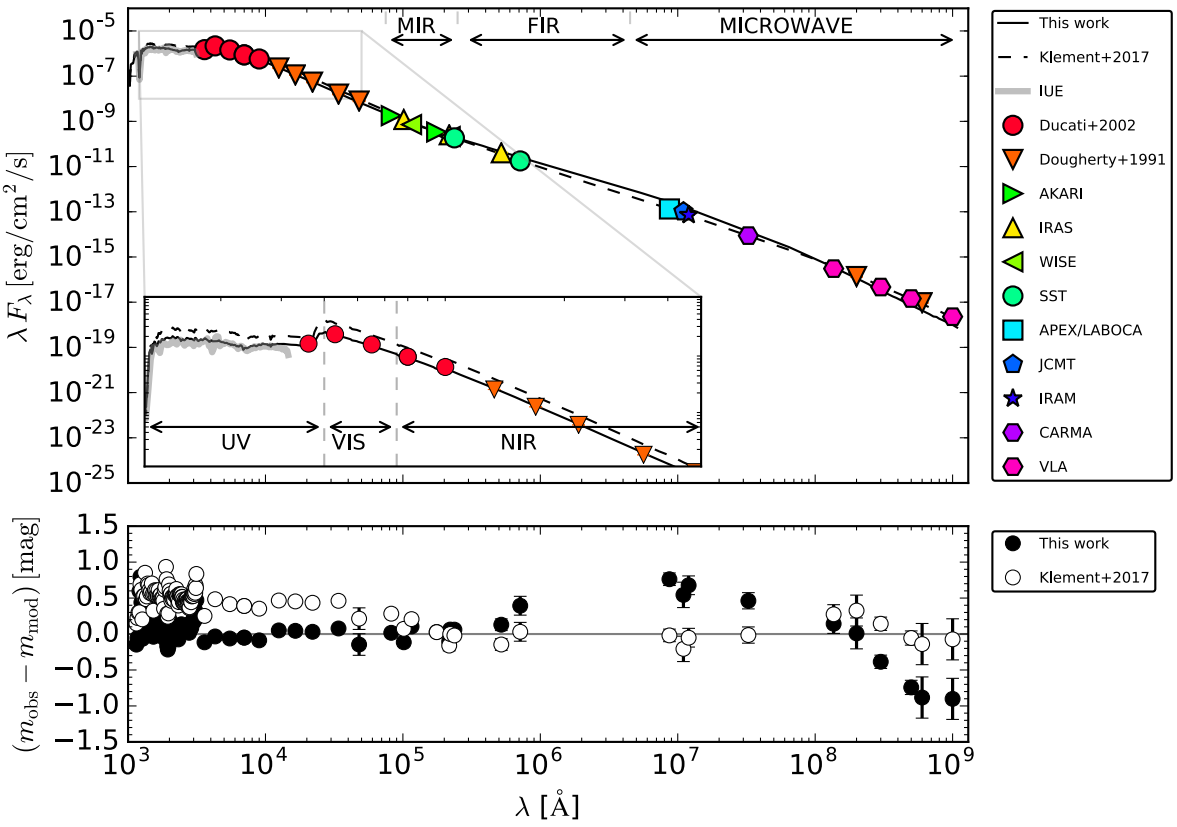

Figure 6.8: Upper panel: SED of β CMi showing the best-fit BeAtlas model (black solid line) and the reference model of Klement et al. (2017). The spectral regions are highlighted in order to facilitate the identification of the adopted spectral regions. Inset: A zoom to the UV up to the NIR region. Lower panel: residuals of the best-fit BeAtlas models (black dots) and of the reference model (white dots).

remark is that the BeAtlas model, once the grid was ready and all the routines written and tested, was produced in a matter of hours, instead of the months taken by R. Klement for this manual search of the parameter space. This demonstrates that BeAtlas offers an ideal solution for the quick analysis of a large number of CBes (issue 2).

Chapter 7

The Case of α Arae

7.1 Chapter Summary

This Chapter shows the application of our method for the study of the disk and stellar proprieties of the early-type Be star α Arae (Sect. 7.2). The observational data used is described in Sect. 7.3 and a variability study of some of the data is presented in Section 7.4. In Section 7.5, the results obtained from our method are shown. We finish with a discussion (Sect. 7.6).

7.2 α Arae

The southern star α Arae (HD 158427, HR 6510) is a `MS` star of spectral type `B2Vne` according to Levenhagen and Leister (2006); however, it is a good example of a star that has been classified very differently in the literature (see below). Its proximity (74.3 pc, van Leeuwen 2007) and brightness ($m_V = 2.93$) allowed for the constitution of a rich observational dataset, offering unique opportunities to perform a detailed study of the process that governs the dynamic of CBes and their disks. Furthermore, the Arae region in the sky is suitable for such studies, since dark clouds are not as important there (Vega et al., 1980), which results in lower extinction levels.

Recently, Bagnulo et al., 2015, using the `FORS1` instrument on `ESO`'s Very Large Telescope (`VLT`), measured the mean longitudinal magnetic field from low-resolution circular polarised spectra of nearly a thousand different stars. In Figure 1.2, we show the `MS` stars studied by them and the position occupied by α Arae ($< B_z > (G) = -27 \pm 38$, $MJD = 53869.353$) , which indicates that α Arae shares the same characteristic of a non-detectable global magnetic field as seen in other Be stars. α Arae has also shown a relatively stable behavior over the years, in contrast with most early-type Be stars that have quite variable disks (Labadie-Bartz et al. 2018; Rímulo et al. 2018). This property of α Arae is quite important and will be reviewed later on

Table 7.1 - α Arae's stellar parameters determined previously.

Source	M [$M_\odot$]	$T_{\rm eff}$ [K]	R [$R_\odot$]	L [$L_\odot$]	i[°]	d[pc]	$v \sin i$[km s^{-1}]	ST
Dachs et al., 1988	9.5	18 000	5.1	-	-	-	-	-
Dachs et al., 1990	-	18 000	-	-	-	-	-	-
Chauville et al., 2001	-	18 000	-	-	-	-	-	-
Chesneau et al., 2005	-	19 010	4.8	2.2×10^3	45 ± 5	105	-	-
Zorec et al., 2005	6.2	17 360	3.94	-	-	-	-	-
Frémat et al., 2005	-	18 044	-	-	51.3 ±3.2	-	-	-
Levenhagen and Leister, 2006	11.9	22 150	9.60	22908	-	-	270 ± 25	B2Vne
Meilland and Stee, 2006	9.6	18 000	4.8	5.8×10^3	-	105	-	B3Ve
Meilland et al., 2007	9.6	18 000	4.8	5.8×10^3	55	105	375	-
Meilland et al., 2009	7.2	18 044	4.5	-	-	81	-	-
Hamed and Sigut, 2013[1]	9.6	18 044	4.8	2.2×10^3	55, 45, 75	-	-	B3Ve

Table 7.2 - Disk parameters determined by previous works. $R_{\rm D}$ represents the size of the emitting region at 2, 8, and 12 μm. ρ_0: [1] From Meilland et al., 2007.

Source	$R_{\rm D}$ [$R_\star$]	$R_{\rm D}$ [mas] ($2\,\mu$m)	($8\,\mu$m)	($12\,\mu$m)	n	ρ_0 [10^{-10} g cm^{-3}]
Meilland et al., 2009	-	7.3 ± 2 [1]	5.5 ± 0.3	8.1 ± 0.6	-	-
Hamed and Sigut, 2013	5.0	7.6 ± 1.4	4.0 ± 1.8	5.9 ± 2.98	2 and 3	0.75 to 1.0

(Sect. 7.4). α Arae has been the subject of several studies in the literature, targeting both the central star and its disk. A summary of the results in the literature can be found in Tables 7.1 (stellar properties) and 7.2 (disk properties). Below, we discuss some of these results.

The stellar properties found in the literature vary widely (Tab. 7.1; issue 1 of Sect. 1.6). For instance, masses are reported in the range 6.2 - 9.5 $M_\odot$, and the polar radius varies by a factor of more than two (between 3.94 and 9.6), with corresponding discrepancies in the luminosity.

Possible binarity of α Arae was first suggested from studies performed with the `MIDI` and `AMBER` interferometers (Meilland and Stee, 2006). `MIDI` was a two-beam combiner that worked in the `MIR` (rough between 8 and 13 μm) and `AMBER` was a three-beam spectro-interferometer, capable of high spectral resolution ($R \sim 12\,000$) observations around the Br-γ hydrogen line. The interpretation of these results, obtained using an outflowing disk model, suggested a *dense polar wind* along its rotational axis and a geometrically thin disk truncated by an unseen binary. These previous models suggested a period of $\sim$ 74 days and a semi-major axis of 32 $R_\star$ for the companion ($M_\star < 2\,M_\odot$) (e.g. Chesneau et al. 2005, Vinicius et al. 2007, Meilland et al. 2007).

Recently, Meilland et al. (2012) concluded that the size of the emitting region does not differ in the range 8 - 12 μm from `MIDI` measurements (see Table 7.2). Their results are supported by

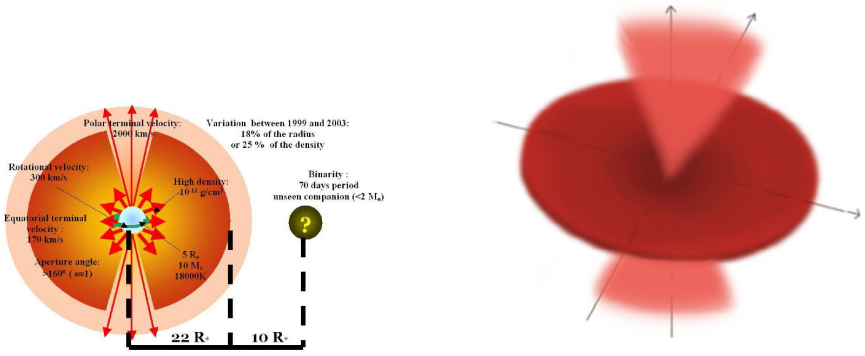

(a) *(b)*

Figure 7.1: Left: Model with a polar dense wind proposed by Chesneau et al. (2005). Right: 3D artistic view of the best model achieved by Meilland and Stee (2006).

Hamed and Sigut (2013). These authors found that α Arae's disk, between 2.1 and 12 μm, does not change considerably and, according to them, this corroborates the hypothesis of a truncated disk by an unseen companion. In passing, it is worth clarifying some misconceptions found in the above papers. The authors sometimes confuse *disk size* with *size of emitting region*. These are different things. An interferometric observation, for instance, can measure the size of the emitting region, but not the disk size. The only exception is when these quantities are the same, e.g., for a truncated disk.

About the suggestion that α Arae has a dense polar wind (Fig. 7.1), the recent review of Rivinius et al. (2013) argues that the evidence proposed by Chesneau et al. (2005) is weak, as it was based on a single interferometric measurement. Here, a simple calibration bias in the interferometric measurement could cause fluctuation in the derived size along the direction of the baseline of observations in the Sky. Apparently, the only case of wind in CBes that deserves to be considered is Achernar (Kervella and Domiciano de Souza, 2006) (see discussion in Rivinius et al. 2013, page 43). Despite this, the interplay between winds and rotation should be better investigated. For instance, the combination of these effects could affect the stellar evolution and the mass injection to the circumstellar environment (Georgy et al., 2013).

7.3 Observational Data Overview

7.3.1 Photometric Data

The selection of the photometric data of α Arae followed the same procedure described in Section 6.3.1. The selected photometric data is in Table A.3.

Of particular importance for this project is the APEX/LABOCA measurement made at 870 μm in the context of a radio survey of CBes conducted by R. Klement and A. Carciofi. In addition to these, we found measurements at 3.5 and 6.3 m by Clark et al. (1998). Unfortunately these authors could not measure the flux, but still were able to set upper limits of 0.06 and 0.2 mJy, respectively. This new radio data gives us opportunity to investigate the claims of a binary companion reported above, using the SED turndown method employed for β CMi (see Chap. 6).

Additional light curves were obtained from the tools AAVSO[1], VSX[2] and from the Hipparcos mission (Hipparcos VizieR Table[3]).

7.3.2 Linear Polarization Data

Cotton et al. (2016) reported the linear polarization of 50 nearby ($d \lesssim 100$ pc) southern stars without correcting for the interstellar polarization. One of the main results of their study is illustrated in Figure 7.2. Notably, the most highly polarized stars were four CBes: α Eri, α Col, η Cen and α Arae. Thereafter, they showed the trend of the polarization with spectral type, highlighting the remarkable polarization levels among CBes and a clear separation between A and B-type stars that suggests a peculiar mechanism in B stars (the presence of disk).

For α Arae's case, we estimated the interstellar polarization in its line of sight by measuring a set of field stars (Tab. A.2). The selected field stars showed that the average interstellar polarization does not exceed 0.05%, which is consistent with previous studies of McLean and Clarke (1979) ($p_{\max} \sim 0.03\%$) and Dachs et al. (1988) ($E_{\rm IS}(B-V) = 0.0$). Due to this small amount of interstellar contribution, we did not perform any interstellar polarization correction.

We made a complete search in the literature for published values of polarization. We obtained historical polarimetric data from and McLean (1979). The polarimetric data of α Arae are summarized in Table 7.3. The observations made by our research group at OPD-LNA polarimeter

[1] https://www.aavso.org/lcg;
[2] https://www.aavso.org/vsx/;
[3] http://vizier.cfa.harvard.edu/viz-bin/VizieR-3?-source=I/239/hip_main.

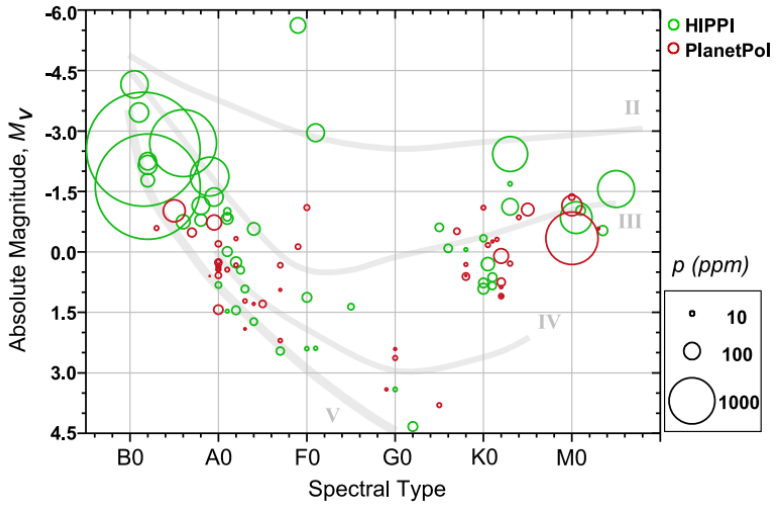

Figure 7.2: H-R Diagram of Cotton et al., 2016. The gray lines represent the main sequence (V), sub-giant (IV), giant (III), and bright giant (II) branches. The diameter of the bubbles represents the degree of polarization for HIPPI and PlanePol surveys.

Table 7.3 - Full polarimetric datased available for α Arae. The table lists the average of all data and the standard deviation. Notes: [a]: Intrinsic values. [b]: The respective error is 0, according to Cotton et al. (2016). [1] Yudin (2001). [2] Cotton et al. (2016). [3] OPD-LNA. [4] McLean (1979).

MJD	P_U [%]	P_B [%]	P_V [%]	P_R [%]	P_I [%]	PA_{int} [°]	Ref.
-	-	-	0.58[a]	-	-	174[a]	[1]
56996	-	-	0.62400(34)	-	-	172[b]	[2]
54260 to 57624	0.39 ± 0.02	0.61 ± 0.05	0.59 ± 0.04	0.48 ± 0.01	0.45 ± 0.01	142.2 ± 2.6	[3]
40085 to 42877	0.33 ± 0.01	0.67 ± 0.01	0.60 ± 0.01	-	-	172	[4]

and McLean (1979) are detailed in Table A.4. One interesting feature of the data is the absence of large-scale variations in the polarization. We come back to this important point later on.

7.3.3 *Spectroscopic Data*

Historically, emission lines have provided fundamental information about the disk. For instance, evidence of variability in emission line profiles of CBes are quite common. Curious cases are the V/R variations ($V/R = F(\lambda_V)/F(\lambda_R)$), in which the peak intensities change in relation to each other in timescales of weeks to months. These variations can be understood in terms of a disk whose axial symmetry is modified, e.g., by a density wave. In such a scenario, when the over-density region approaches the observer, the violet peak (V) is enhanced, but when it is moving away from the observer the red peak (R) becomes prominent. One example of a well-studied case of V/R variations is the Be star ζ Tau, which cyclic V/R behavior (with a quasi-period of about 4 years, Štefl et al. 2009) was modelled by Carciofi et al. (2009), who demonstrated that

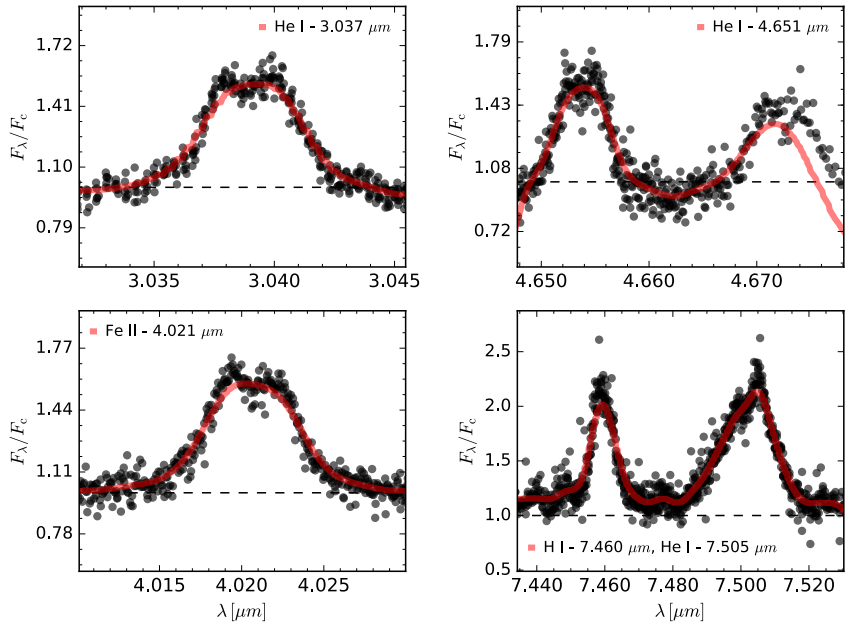

Figure 7.3: Infrared Space Observatory (ISO) spectra of α Arae (1996-02-17). We selected some lines (He I, Fe II and H I) found in the spectrum. Red curves are the smoothed lines.

they are caused by one-armed spiral density waves formed in the disk. The hydrogen lines are the most prominent ones and constitute one of the best diagnostic-lines. The most important are: Hα (6562.8 Å), Hβ (4861.3 Å), Hγ (4340.5 Å). Hδ (4101.7 Å), Hϵ (3970.1 Å). During the active state (i.e., with a disk), the typical Hα line profile of an edge-on CBe comprise a central reversal core and two emission peaks (red and violet) displaced almost symmetrically around the central reversal. In the B state (i.e, diskless), the profiles are purely in absorption. Neutral helium HeI can also be seen in emission at, e.g., 4009.3, 4026.2, 4143.7, 4387.9, 4437.5, 4471.5, 4713.1, 4921.9, 5875.6 and 6678.2 Å. Besides these lines, another large group of lines are observed, such as: CII (3920, 4267, 4738, 4745, 6578, 6583 Å), NII (3995, 4630 Å), OII (4119, 4367, 4415, 4642, 4649, 4662 Å), MgII (4481 Å), SiIII (4552, 4568 and 4575 Å triplet; several lines around 3800; also at 3924, 4338, 4813, 4829 and 5740 Å), SiII (3856, 3863, 4128, 4131, 5041, 5056, 6347, 6371 Å), and sometimes FeII lines[4]. In addition, many important lines are also observed in the IR domain, as exemplified in Figure 7.3.

In our study, we focused basically on Hα lines. The spectroscopic data of α Arae were gathered from VO tools, observatories and papers, in addition to new data taken at the Pico dos Dias Observatory (OPD-LNA).

[4] https://www.shelyak.com/be-stars/?lang=en.

All sources are listed below:

- ECass, a long slit Cassegrain spectrograph, and the MUSICOS (Multi-SIte Continuous Spectroscopy)[5], both installed at OPD-LNA. These data were reduced using standard procedures found in the IRAF[6] package;
- Reduced Flash and Heros data, covering from 3 500 Å to 9 000 Å, where accessed through the German VO tool GAVO[7];
- Our compilation also includes historical digitalized hydrogen lines (Hα and Hβ) published by Dachs et al. (1981) (1978-11-02 to 1977-07-08), Hanuschik et al. (1996) (1982-08-30 to 1993-09-09), Banerjee et al. (2000) (1999-04-13) and by Dachs et al. (1986) (1982-02-27 to 1983-03-17);
- From the ESO facility[8], we obtained UVES data. This echelle spectrograph covers from 3 000-5 000 Å (blue arm) to 4 200-11 000 Å (red arm). Its spectral resolution can reaches up to 80 000 (blue arm) or 110 000 (red arm) (Dekker et al., 2000). We reduced the data using the UVES pipeline described in UVES-Tutorial[9](version 5.7.0);
- CRIRES[10] instrument provided high-resolution data from 1 to 5 μm (Kaeufl et al., 2004). These data were reduced by the EsoRex platform (201, 2015) as described in CRIRES-Tutorial[11] (see Tab. A.5). An example is shown in Fig. 7.4;
- Harps and Feros reduced data were downloaded from ESO archive.

All the data listed above is listed on Table A.5.

[5] http://www.lna.br/opd/instrum/instr.html;
[6] Available at http://ast.noao.edu/data/software;
[7] http://dc.zah.uni-heidelberg.de/;
[8] The reduction chain used for all instruments of the ESO followed the sequence: 1) classify/organize the data, a process called "data association", which uses, in principle, FITS headers information present in "association keywords". 2) Next, the instrument pipeline is called by a standard ESO application, i.e. Gasgano (ESO, 2012), Reflex or Esorex (Freudling et al., 2013);
[9] ftp://ftp.eso.org/pub/dfs/pipelines/uves/uves-pipeline-manual-22.12.pdf;
[10] CRyogenic high-resolution InfraRed Echelle Spectrograph;
[11] https://www.eso.org/public/teles-instr/paranal-observatory/vlt/vlt-instr/crires/.

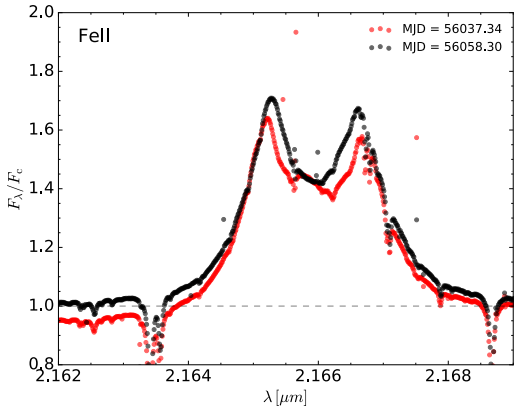

Figure 7.4: α Arae Fe II lines from CRIRES spectrograph from 2012-04-20 to 2012-07-05.

7.4 Temporal Evolution of the Observables

The CBe α Arae was reported to be stable on long time-scales by Dachs et al. (1981) and, in the words of Hanuschik et al. (1988), "still seems to represent an active Be star in a well-balanced equilibrium state". Its stability was reported by the study of V/R variability and global oscillations by Hanuschik et al. (1995), showing almost no variability in the line profiles over 7 years (see Fig. 12 in Hanuschik et al. 1995) and an equivalent width (EW, see below) of about 20-30 Å over the same period. Earlier, Mennickent and Vogt (1991) detected rapid V/R variations from high time-resolution observations ($\sim$ 7 days) between 1984 and 1989, having detected a quasi-period of 0.13 yr ($\sim$ 47.5 days) using data from Hanuschik et al. (1988). In another study, Mennickent (1991) showed that α Arae had a relatively constant and moderate Hβ emission (see their Fig. 12) with V/R variations of small amplitude, only slight changes in strength of emission and mean EW relatively constant between 1977-87, except for a rapid decrease in 1982. In summary, these previous studies concluded that α Arae might have had variations in timescales of months, however without showing a clear, organized long-term pattern.

To confirm the long-term stability of α Arae's disk and, more importantly, the *recent* stability, we plot in Fig. 7.5 the temporal evolution of the linear polarization measurements of the star α Arae (data from Table A.4). The center of the grey bands marks the median of the data and the width the standard deviation of the mean. The UBV data is spread over about 50 years, with a gap of $\approx$ 30 years starting in 1976. Data for the RI bands is available only since 2007. The polarization levels are remarkably stable for all bands. More remarkable is the lack of variability between the seventies and the years 2000, which may suggest that the disk has remained stable

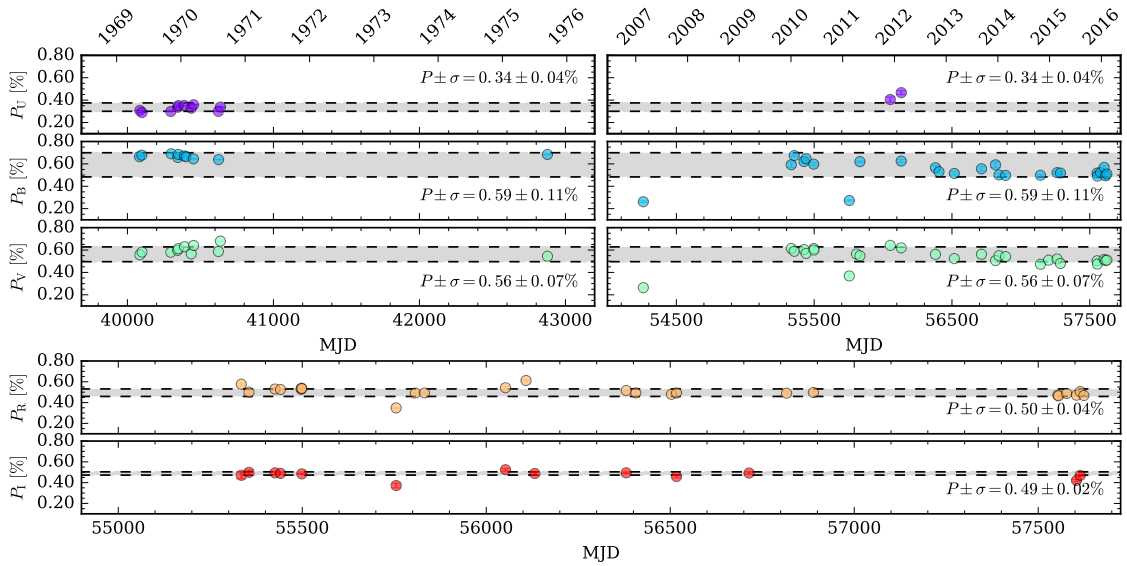

Figure 7.5: Temporal evolution of the polarimetric measurements. Upper panels: U, B and V filters. Lower panels: R and I filters. The center of the grey bands marks the median of the data and the width the standard deviation of the mean.

for 5 decades. As discussed above, several short-term variations were observed in the literature (e.g., the 1982 drop in the Hβ emission seen by Mennickent 1991). A similar feature is seen in the polarization data. There is one drop in early 2007 (seen only in B and V) and another, smaller one seen in early 2011 in all filters, except U for which no data is available.

The spectroscopic data confirms the conclusions drawn from polarimetry. We plot in Figure 7.6 the following spectroscopic quantities derived from the spectral lines:

- Peak separation, defined as the distance, in km s^{-1}, between the red and violet peaks. The position of the peaks were measured by fitting a Gaussian to each one;
- Equivalent width (EW), defined as

$$EW = \int \left(1 - \frac{F_\lambda}{F_0}\right) d\lambda \,, \tag{7.1}$$

  where, F_0 represents the continuum and F_λ represents the intensity across the wavelength range of interest;
- Emission over the continuum ratio (E/C), which is the ratio between the highest value of the emission profile over the adjacent continuum;
- V/R ratio, already defined above.

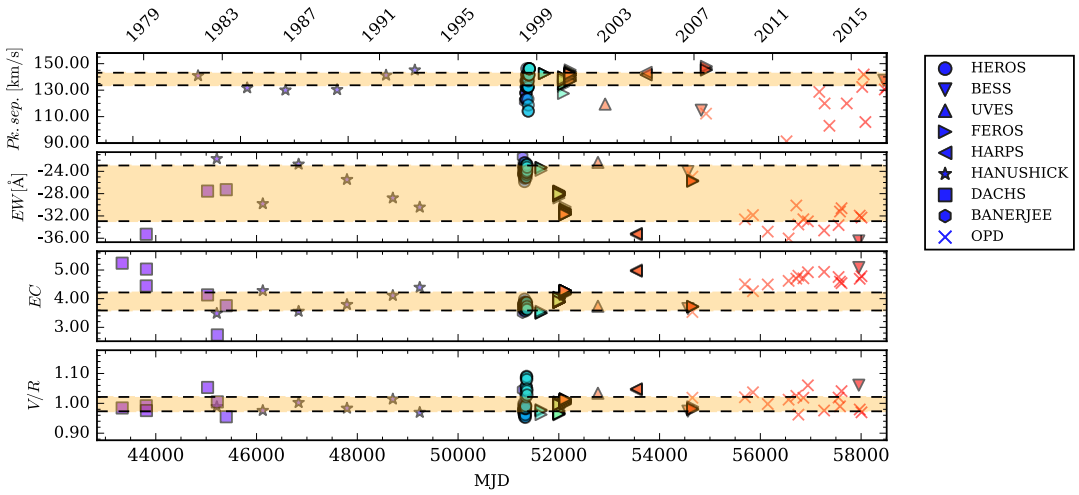

Figure 7.6: Temporal evolution of the spectroscopic quantities obtained from the Hα line. Top panel: peak separation ($\Delta v_{\rm peak} = v_{\rm P_V} - v_{\rm P_R}$). Second panel: Equivalent width. Third panel: E/C ratio. Bottom panel: V/R ratio. The center of the orange band is given by the median of all the data and the with is the standard deviation of the mean.

As before, the orange band in each panel of Fig. 7.6 marks the median and the standard deviation of the mean. The properties of the Hα emission lines have remained roughly constant since 1978, in line with the results from the literature search reported above. However, the latest data (since 2012 or so) shows a deviation of this behavior: one can see the EW becomes larger in modulus (more negative), the E/C ratio rises and the peak separation becomes smaller than the average value. One possible explanation for this behavior is that the adjacent continuum of the line became suppressed, e.g., by a partial dissipation of the inner disk, thus causing both the E/C and the modulus of the EW to increase. Some hints indicating this partial dissipation of the inner disk may also be seen in Figure 7.5, mainly at the B and V bands. It will be interesting to see how the disk around α Arae evolves in the coming years.

Having analyzed the long-term trend of the data, we take advantage of the wealth of data gathered from the literature to perform a period analysis, in order to identify possible periods.

We performed the period analysis on the photometric, polarization and spectroscopic data. Initially, we applied the Lomb-Scargle (`LS`) method (VanderPlas, 2017), which assumes a sinusoidal variability pattern, but without success. Next, we applied two methods that are independent of the signal shape, the `PMD`[12] (e.g. Stellingwerf 1978; Rivinius et al. 1998) and the Supersmoother method (e.g. VanderPlas and Ivezić 2015; Reimann 1994). Neither the Supersmoother algorithm nor the `PDM` method requires a *a priori* knowledge of the light curve shape.

[12] Period determination using phase dispersion minimization.

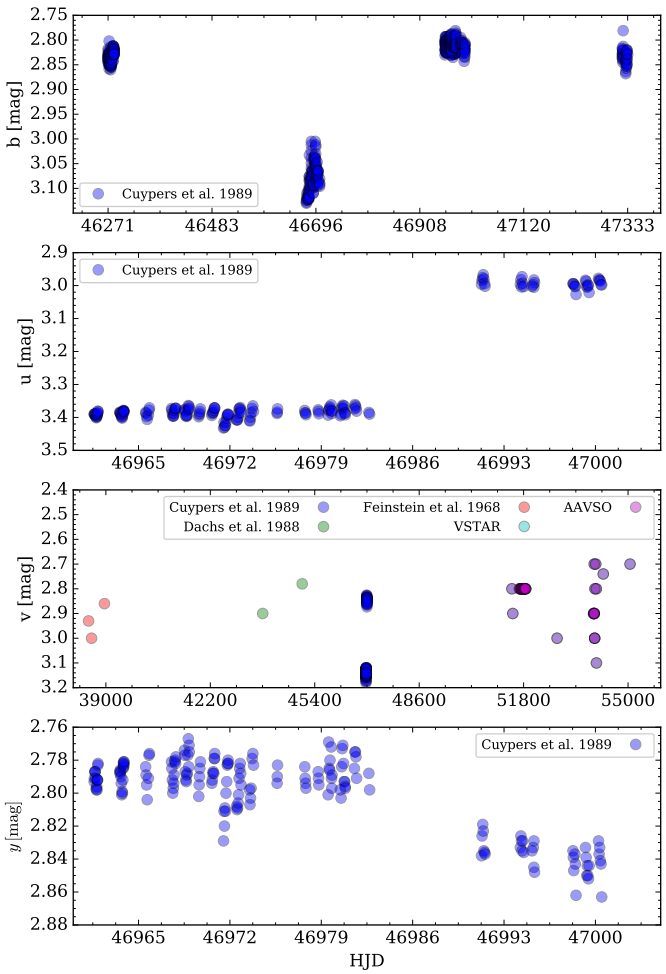

Figure 7.7: Compilation of the light curves of α Arae. From top to bottom: b filter, u filter, v filter and y filter. Data from Cuypers et al. (1989), Feinstein (1968) and Dachs et al. (1988).

In Figure 7.7, we show the temporal evolution of the apparent magnitudes of four filters taken from various sources, covering $\sim$ 1 000 days, $\sim$ 40 days, $\sim$ 1 600 days, and $\sim$ 40 days respectively. The LS analysis applied to these data did not produce any significant period.

Next, we applied a method of determination of periods through the analysis of multi-band Lomb-Scargle (VanderPlas and Ivezić, 2015) using only the filters with longer coverage, which are the b and v filters. The power spectrum is shown if Fig. 7.8. Unfortunately, as before, even this more refined method yielded a null result, with no significant period found. All the methods above were also tried in the polarization and spectroscopic data, but again no significant period was found.

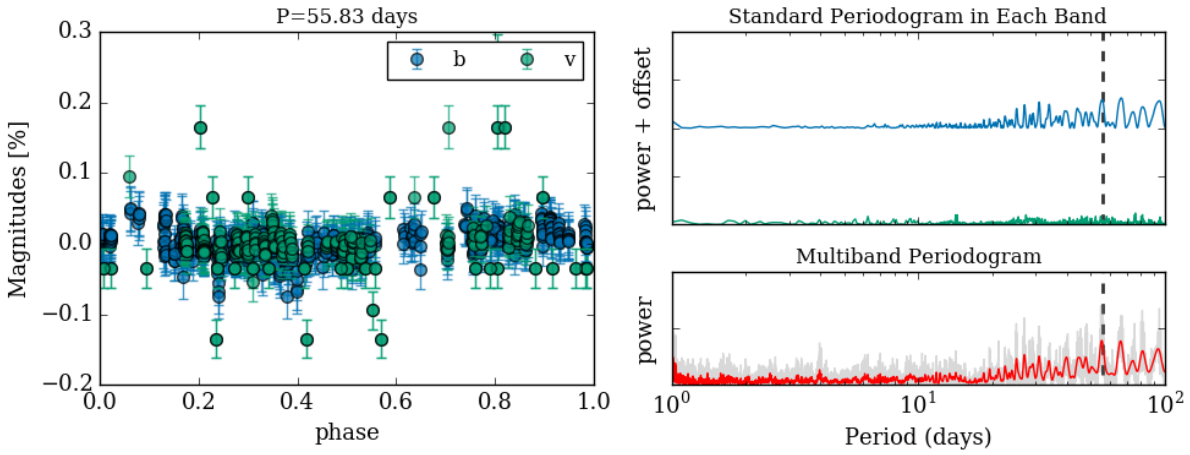

Figure 7.8: Lomb-Scargle Multi-band power spectrum made using the b and v filters. No significant period was found.

7.5 *Modelling with* BeAtlas

In this section, we show the results of modeling α Arae with BeAtlas. We applied the same procedure described in Sect. 6.4 for the SED and the polarimetric data presented in Sect. 7.3. Because the disk did not show any significant variability we bundle together all the photometric observations for all bands in a single SED. For the polarization we took the median of all the data, using the standard deviation of the mean as a measure of the uncertainties.

7.5.1 *Initial Estimates from the SED and from the Polarimetric Data*

Figure 7.9 shows the results obtained by considering the full SED. We see that all the parameters are well constrained. In addition, we show the results obtained from the polarimetric data (Tab. 7.3) combined with the KDE stellar prior in Figure 7.10.

The box plot for all parameters and for each section of the SED, or combination of sections, analyzed is shown in Fig. 7.11. As was the case for β CMi, we verify that shorter wavelengths (UV and visible) sample better the stellar parameters. By removing the UV from the complete SED, we lose precision in the inference of the M; curiously, the precision in W, $t/t_{\rm MS}$ and $R_{\rm D}$ are improved. Now, removing the UV and the visible causes a precision loss in the inference of all parameters. The precision becomes worst as we continue to remove shorter wavelengths. When just the long wavelength remain, the discriminating power of BeAtlas is rather poor. These results show that when the central star is not well-constrained, all the other parameters also become less constrained, given their strong interdependence (see discussion in Sect. 6.5).

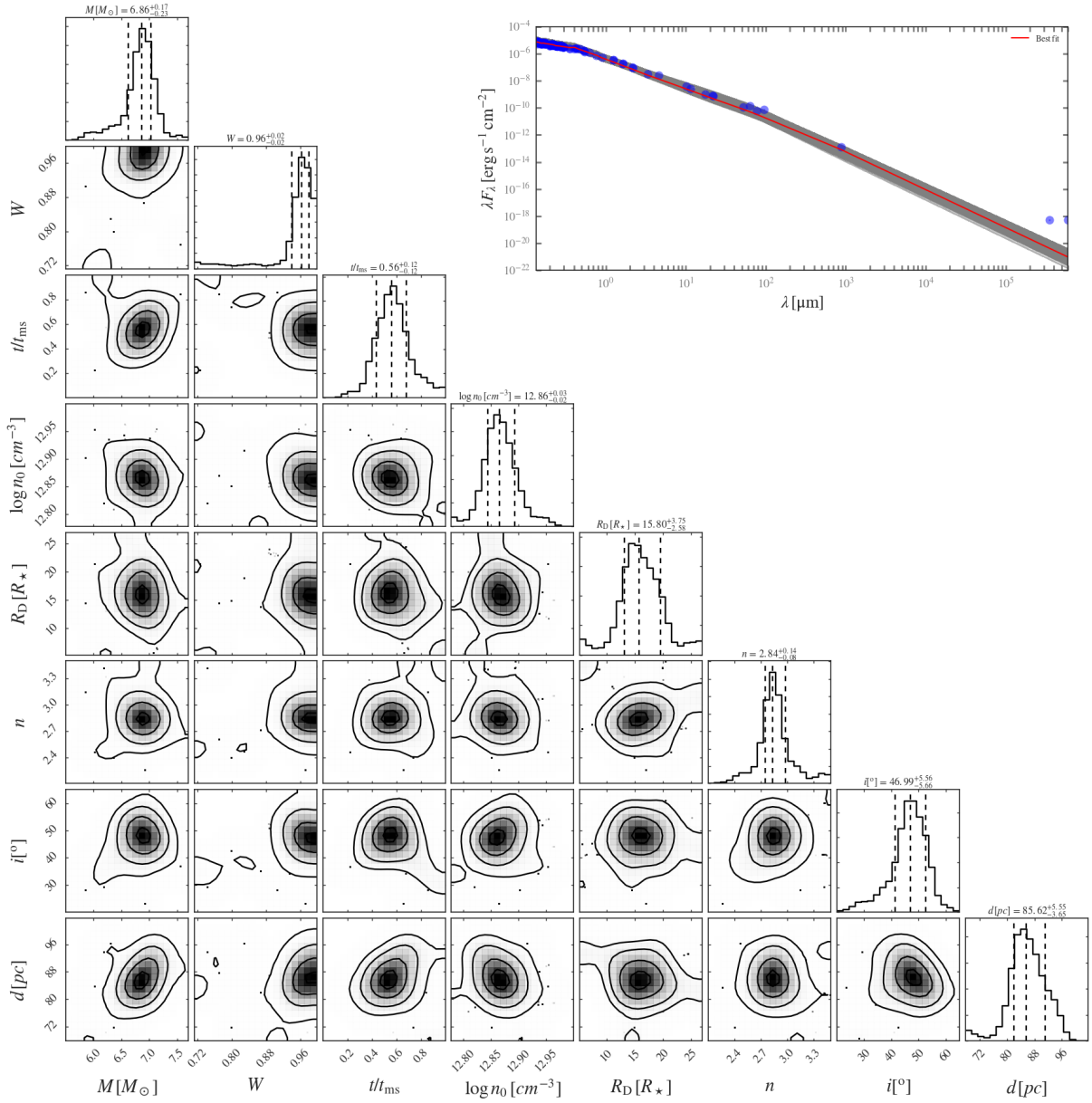

Figure 7.9: Corner plot for a BeAtlas simulation of α Arae. The inset shows the SED in the upper part and the residuals of the fit in the lower part. Blue points: observed data. Red line: best fit SED. Grey lines: random sample of 300 models of the MCMC chain, that can be used as an estimate of the model uncertainties.

7.5.2 Best-fit Parameters

Figure 7.12 shows the combination of the PDFs obtained from fitting the SED and the polarization. We adopted these results as the best-fit parameters of α Arae (Tab. 7.4).

To compare our results with previous studies, we discarded the results of Levenhagen and Leister (2006) (see Tab. 7.1), due to the large discrepancy seen with respect to all other studies. Comparison of Tables 7.1 and 7.2 with 7.4 shows a general agreement between our inferences

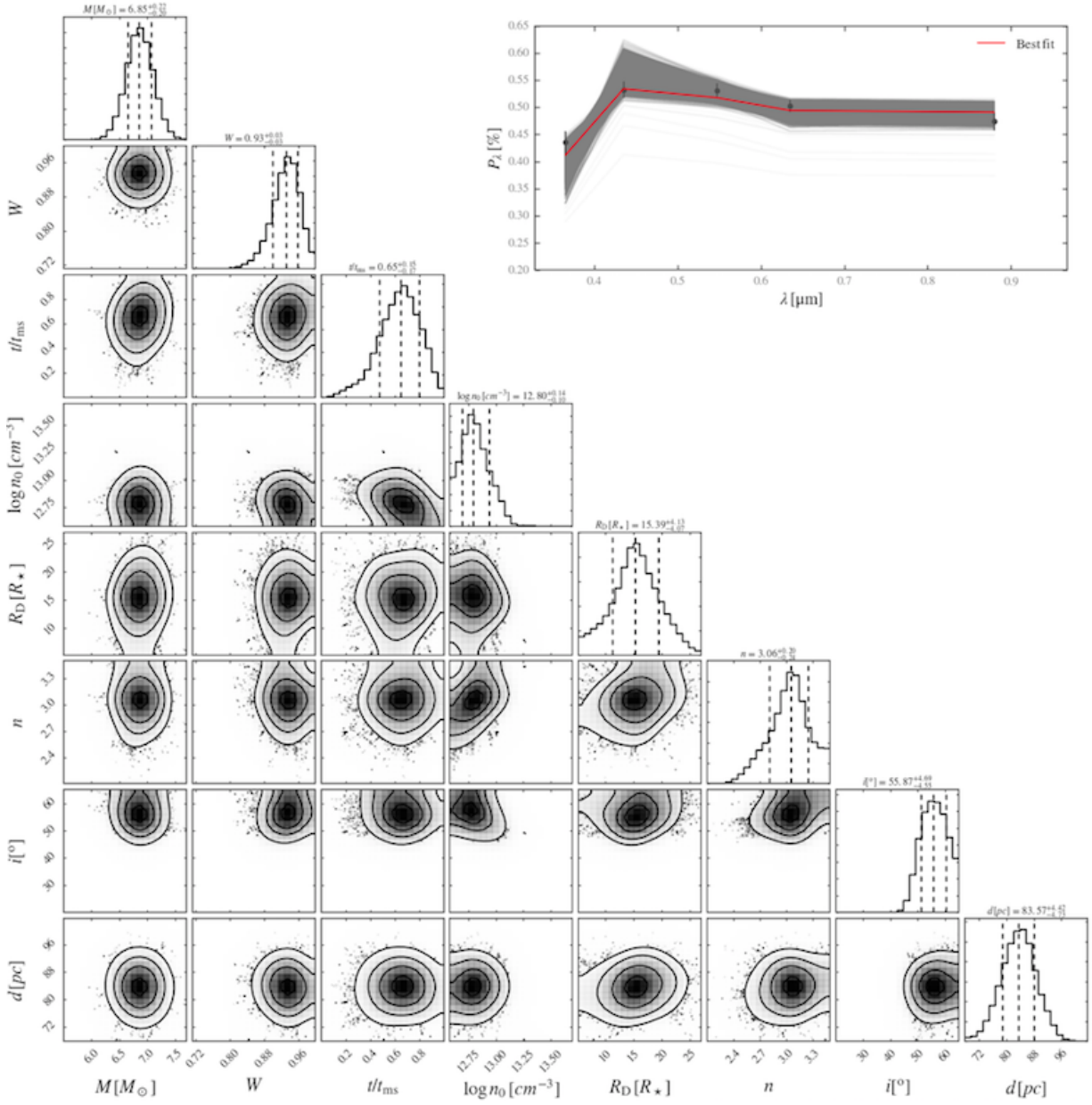

Figure 7.10: Same as the Fig. 7.9, but for the linear polarization using the KDE priors for the stellar parameters.

and the literature values. For the temperature, our result is compatible with the values published by Dachs et al. (1988, 1990), Chauville et al. (2001), Frémat et al. (2005), Meilland and Stee (2006), Meilland et al. (2007), Meilland et al. (2009), Hamed and Sigut (2013). For the inclination angle, our result agrees with Chesneau et al. (2005) and Frémat et al. (2005). Because the value obtained from Chesneau et al. (2005) was obtained from interferometry, this agreement is of great significance. In addition, it is worth noting that the parameter i greatly benefited from the combination of the SED and the polarization, as the combined PDF is much narrower than the individual ones.

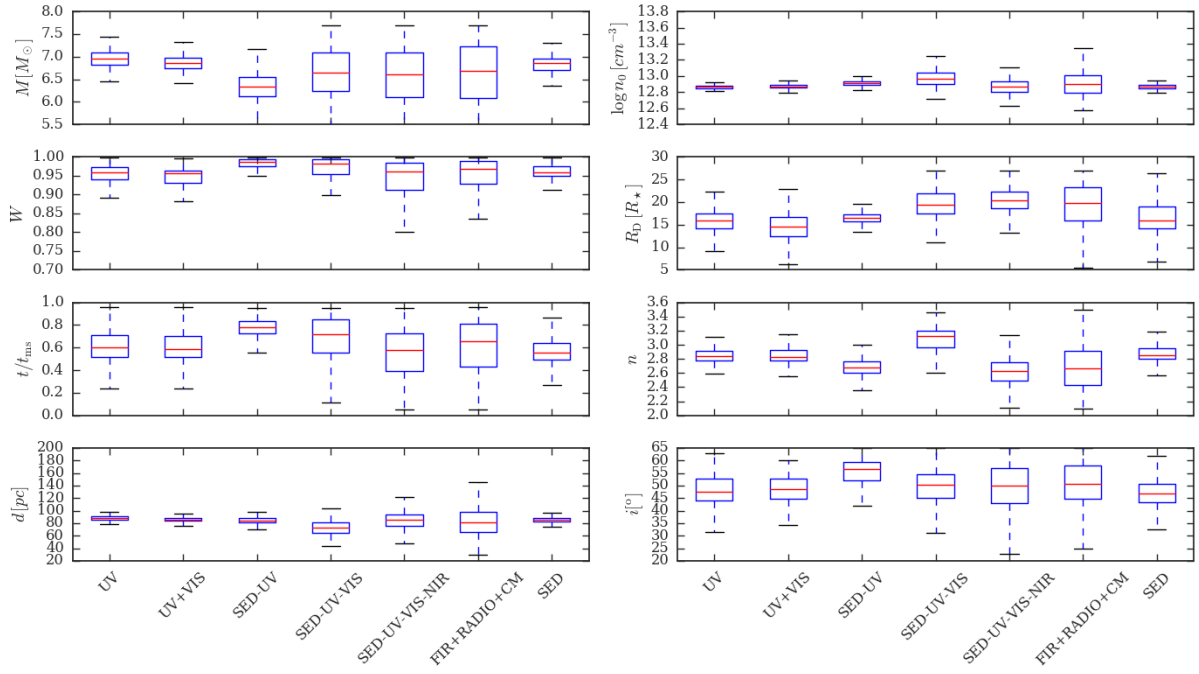

Figure 7.11: Box plot of the PDFs of different spectral domains for all parameters. The abscissa indicates the SED section (or combination of sections) used. Each plot corresponds to a given parameter, as indicated.

The inferred luminosity is in agreement with Chesneau et al. (2005). In the case of the stellar mass, our result just agrees with the values published by Zorec et al. (2005) and Meilland et al. (2009). Our result for the stellar radius also agrees with the value published by Zorec et al. (2005). The MS lifetime obtained for α Arae ($t/t_{\rm MS} = 0.55^{+0.15}_{-0.10}$) is compatible with Zorec et al., 2005 ($t/t_{\rm MS} = 0.43$). Moreover, our estimate for the $E(B-V)$ agrees with the well-known fact that the interstellar extinction is low at Arae region (see Sect.7.2).

Table 7.4 - Best fit parameters of α Arae.

Parameter	Value	Parameter	Value
M [M$_\odot$]	$6.85^{+0.17}_{-0.32}$	log n_0	$12.87^{+0.03}_{-0.02}$
log g	$4.1115^{+0.0003}_{-0.0008}$	$R_{\rm D}$ [R$_\star$]	$16.0^{+4.0}_{-3.0}$
$R_{\rm pole}$ [R$_\odot$]	$3.81^{+0.09}_{-0.09}$	n	$2.85^{+0.25}_{-0.10}$
L [L$_\odot$]	1940^{+323}_{-277}	i [$^{\rm o}$]	$46.7^{+6.3}_{-7.2}$
$T_{\rm eff}$ [K]	18216^{+496}_{-483}	d [pc]	$86.0^{+5.0}_{-4.0}$
W	$0.96^{+0.02}_{-0.04}$	$\beta_{\rm GD}$	$0.177^{+0.010}_{-0.012}$
$t/t_{\rm MS}$	$0.55^{+0.15}_{-0.10}$	$E(B-V)$ [mag]	$0.03^{+0.01}_{-0.01}$

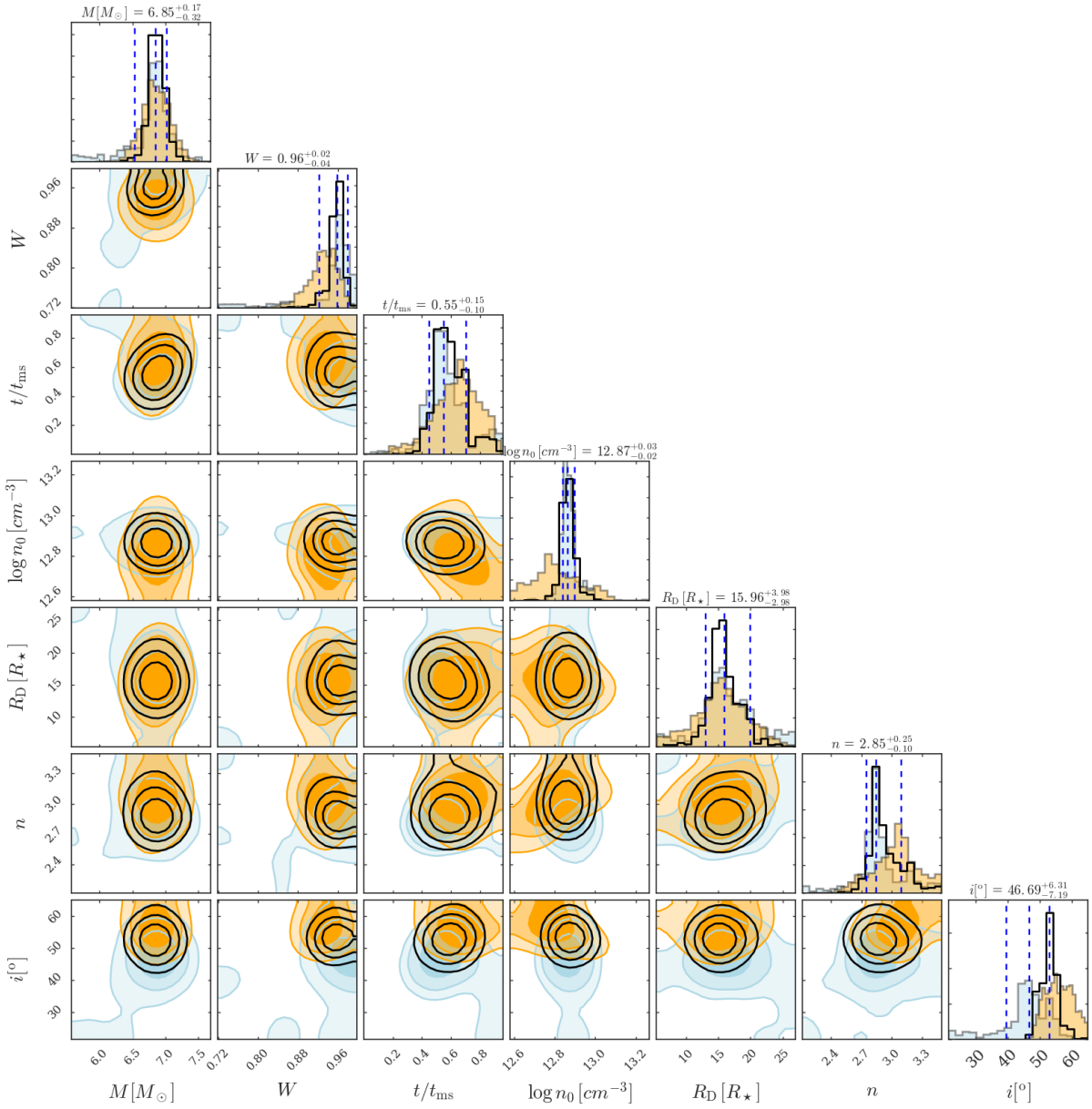

Figure 7.12: Contours in the diagram were obtained by combining the posterior probabilities of the fitted SEDs and polarization and normalizing its integral over the plane to unity.

7.6 Discussion

The disk parameters of α Arae, $n = 2.85^{+0.25}_{-0.10}$ and $\log n_0 = 12.87^{+0.03}_{-0.02}$, are in agreement with the average properties of Galactic Be stars of similar spectral type (Vieira et al., 2017). Our result also agrees with the affirmation that disks around early-type stars are denser (Chap. 1). Because the observational data established a very stable disk around α Arae, the situation is similar to the case of β CMi: the value of n lower than the canonical value of $n = 3.5$ for stable isothermal disks may be due to non-isothermal effects, an unseen companion, or both.

One quite significant result from the BeAtlas is that the model firmly indicates that the disk of α Arae is truncated, and the truncation radius is much smaller than that of β CMi, indicating a much closer companion. Both truncation radius and the mass enabled us to estimate roughly the period and the semi-major axis of the binary system. For this purpose, we assumed a companion with 2.0 $M_\odot$, resulting in a period of $P = 34.0 \pm 9.5$ days for a circular coplanar orbit. Here, we applied the correction proposed by Panoglou et al. (2016). Our values for the truncation radius and period do not agree with those of Chesneau et al. (2005) ($R_D = 32\,R_\star$ and $P \sim 74$ days) or Mennickent and Vogt (1991) (47.5 days). It must be emphasized that both results are rough estimates of periods obtained from radial velocity measurements and V/R variations. These estimates were made from data taken over a short observation period (less than two months), which clearly is not enough for a precise period determination. What can be concluded from their spectroscopic data with some confidence, however, is that the radial velocities do indicate the presence of a companion. We conclude that both our results and the spectroscopic data corroborate the hypothesis that α Arae has indeed a companion, but more spectroscopic data is necessary to obtain an independent estimate of the orbital period.

The full SED of α Arae is displayed in Fig. 7.13. Shown are the best-fit model for the star itself (blue line) and the star plus disk (green dashed line). The figure has many points of interest. Examining the UV part, we see that the star + disk model lies below the purely photospheric model. This is because the disk partially absorbs some of the stellar UV flux and reprocesses it towards longer wavelengths, thus causing the large IR excess (orange-shaded area). This stresses the importance of a self-consistent analysis of the SED, including both the star and the disk. The truncation caused by the unseen companion can also be observed around 10^6 Å. The position of the SED turndown is not well defined, due to the lack of observations at other wavelengths.

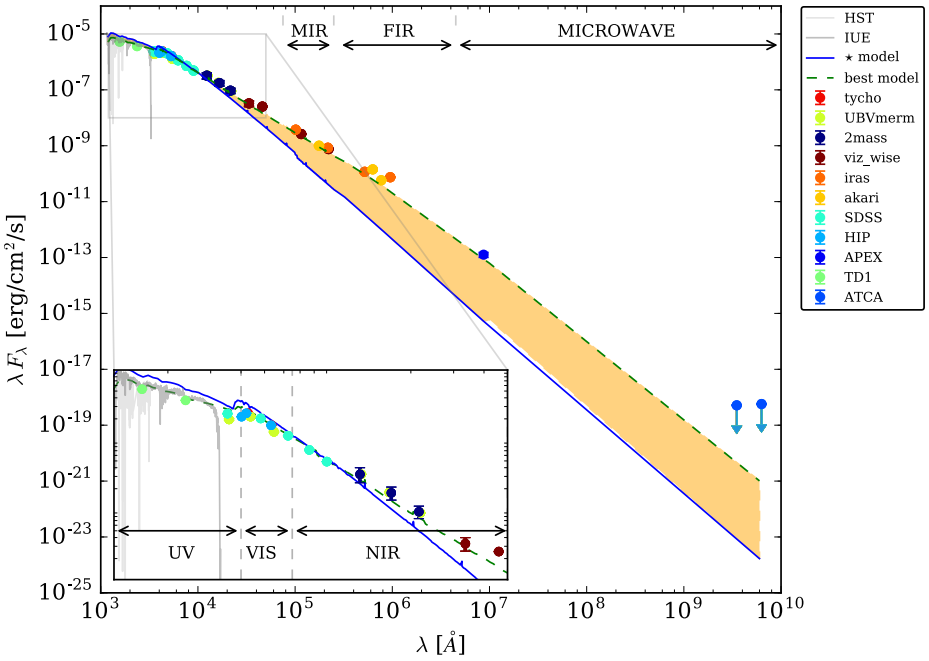

Figure 7.13: SED of α Arae showing the best-fit photospheric model (blue line) and the star + disk model (green dashed line). The orange-shaped area shows the IR excess. The spectral regions are highlighted in order to facilitate the identification of the different spectral regions.

The above discussion can be summarized as follows:

- The BeAtlas model of α Arae was able to constrain all fitted parameters. The model includes as priors the distance and the $v \sin i$, both of which greatly narrowed the confidence intervals of the fitted parameters;
- All parameters are fitted simultaneously, therefore their interdependence is properly taken into consideration;
- The model parameters were obtained under two theoretical assumptions:
  1. The stellar parameters are driven by the Geneva models. Therefore, the age of the star must be analyzed in this context;
  2. The disk parameters reflect a power law viscous decretion disk, and also must be analyzed in this context. Considering that α Arae has a stable disk, the inferred value for $n = 2.85^{+0.25}_{-0.10}$ suggests that other mechanisms may be controlling the slope of the density profile. Possibilities are binary or non-isothermal effects.

- A relevant result is that the independent analysis of the polarization and the SED yielded quite consistent results for the disk parameters. This is relevant because the SED and polarization are controlled by two very different processes;
- When combined the two analysis provided a better fit of some of the parameters, specially the inclination angle;
- Also noteworthy is the excellent agreement between our results and interferometric estimates for the inclination;
- Our analysis provided strong evidence of disk truncation for α Arae.

Chapter 8

Conclusions

Stars are mainly investigated via their photospheric parameters ($T_{\rm eff}$, log g, etc.). Even so, their determination is a difficult task since it involves the usage of models and various observational techniques. These parameters are usually determined by comparing theory (e.g. synthetic spectra from model atmosphere calculations) with observations. The analysis becomes more complex in the case of Be stars, because of the additional physical characteristics shown by these objects, i.e. their rapid rotation and the presence of circumstellar keplerian disks, in active phases, ruled by viscous processes (Chap. 1). These additional elements imply a profound modification of the emergent stellar spectrum whose impact on the derived physical parameters are not yet fully understood.

In this work we present BeAtlas, a homogeneous grid of theoretical spectra of Be Stars. It comprises two systematic grids of models: a purely-photospheric (i.e., diskless) grid, and a star plus disk grid ("disk grid"), computed according to the viscous decretion disk (VDD) formalism. We also introduce a new robust method, the Bemcee pipeline, for the determination of parameters of both rapid-rotating stars in the main sequence, as well as slow rotators, based on Bayesian Markov Chain Monte Carlo (MCMC) methods. These methods are designed to efficiently and seamlessly provide estimates of model parameters and their cross-correlations, even in multi-dimensional parameter spaces. A key advantage of our approach is the use of prior information about the object, which contributes to the inference process. The grid is composed of 366 100 synthetic spectra, calculated using a modern grid of stellar evolution models coupled with three-dimensional NLTE radiative transfer calculations.

As a first application of BeAtlas, we derived the stellar parameters, interstellar extinction and inclination angle of 111 OBA stars. We used UV data from the IUE satellite, which proved to be a powerful observable to constrain the stellar parameters, including the rotation rate and

the MS lifetime. Since we opted for a theoretically-oriented grid, the results must be interpreted in the context of the predictions of the Geneva code. By using the $v \sin i$ as a prior we were able to narrow down the confidence intervals obtained; this happens because $v \sin i$ is an implicit function of the inclination angle, rotation rate, mass, and stellar radius. We present an initial comparison between our results and those of the literature. Despite a good overall agreement, there are several deviant cases, which must still be investigated. As pointed out in the text, there are fundamental differences between our approach and some of the ones used in the literature (e.g., rotating vs. non-rotating models) which limits the applicability of a direct comparison. Additionally, from the global combination of our results, we could reproduce well-known statistical properties of B-type stars that served to consolidate our method.

We also demonstrated that BeAtlas can be used to perform multi-technique analysis of active Be stars, and we present a detailed study of two objects: β CMi and α Arae. In this context, the application of the disk grid provided important information about these systems: stellar, disk and geometrical parameters along with their uncertainties. This also helped us to understand better how the different spectral domains of the SED can be used to extract independent or correlated information about several parameters that describe these systems. For instance, the inclusion of the linear polarization in our analysis improved the inference of disk parameters and the inclination angle. In addition, the close match of our inferred inclination angles with literature values obtained from interferometric studies, shows that the combination of different observables and priors can put strong constraints in the inferred parameters, specially in the inclination angle. Next, we summarize the main results achieved for β CMi and α Arae.

The Be star β CMi was an important test for the BeAtlas. Being one of the rare cases of a Be star with a very stable disk, the star was previously studied in detail by Klement et al. (2015) who modeled a large and diverse dataset and showed that the VDD model could successfully reproduce all observations. The BeAtlas results, on the other hand, were based on only two observables (SED and optical polarization), plus the $v \sin i$ and distance priors. Surprisingly, we were able to recover all the parameters derived by Klement et al., and the final SED fit had a better χ^2 than the first model. Parameters such as inclination were recovered with similar precision as Klement et al., which is very interesting, since they had at their disposal several interferometric measurements of the star. Other important parameters, such as the disk truncation radius, density scale and slope, were also successfully reproduced.

One relevant point was that the BeAtlas results were produced in a matter of hours, versus the several months taken by Klement et al. Furthermore, despite being arguably the best model of a Be star to date, they were able only to run and test a limited number of models, and did not fully explore the necessary range of stellar parameters. Thus, the interdependence of the model parameters, which can be very strong, was missed in their analysis. The results for β CMi further consolidated BeAtlas as a quite useful and powerful tool for Be star research.

Next, BeAtlas was applied for a early-type star, α Arae, for which the previous models in the literature were either wrong (as they used incorrect physical assumptions) or insufficiently constrained. We presented a very comprehensive data search in the literature, that revealed that, like β CMi, α Arae has also a very stable disk. This is interesting, as early type Be stars tend to be much more intrinsically variable. We also present several of own observations (optical polarimetry, spectroscopy and sub-mm photometry) that greatly enriched the available dataset. Our main results are:

- The disk density slope ($n = 2.44^{+0.27}_{-0.16}$) is inconsistent with the standard theory that predicts that isothermal steady-state disks should have $n = 3.5$. Two effects may be responsible for this: non-isothermal effects in the disk, or the effects of a binary companion;
- α Arae is a typical Be star in the Galaxy, having a typical disk density scale for its spectral type;
- The derived inclination angle agrees with interferometric estimates, which is a result of great significance;
- We provide further evidence that α Arae is a binary system. In our case, evidence came from the change of the SED slope in the sub-mm domain, here interpreted as being caused by an unseen binary companion that truncates the disk of the primary.

The results for the three studies presented show that BeAtlas addresses successfully the issues raised in Section 1.6 that were the core motivation for this PhD thesis:

- Issue 1: BeAtlas self-consistently estimate the central star parameters provided the relevant data (e.g. UV spectrum) is available;
- Issue 2: Studies of many targets can be done easily with BeAtlas, with the advantage that multi-technique observations can be handled, and prior information can be included;

- Issue 3: BeAtlas allows for the exploration of the full parameter space, thus offering a much better alternative for slow, manual searches;

- Issue 4: In BeAtlas the star and the disk are modeled simultaneously. The final probability density functions of each parameter includes the (often strong) interrelation between stellar and disk parameters. This means that the error estimates obtained from BeAtlas are more realistic.

Chapter 9

Future Prospectives

BeAtlas represents an ongoing project. The computation time needed to finish this project is huge, and only subsets of the grid were finished in time for this thesis. Therefore, in the near future, we will continue to improve BeAtlas, expanding it to cover a planned parameter space. With the complete grid of models, we will be able to study large samples of Be stars.

Another important step forward is to complete the full range of planned observables (Chap. 3), including line profile and synthetic image calculations, to allow BeAtlas to fit also spectroscopic and interferometric data. In particular, the usage of photospheric line profiles in absorption as a proxy of the fundamental stellar properties will greatly improve the BeAtlas ability to constrain the stellar properties. This is already an ongoing effort being carried on by the IC student Matheus G. D. Xavier.

Three other students are already using BeAtlas in their research: Amanda Rubio (MSc student from IAG/USP), Keegan Marr (MSc student from the Univ. of Western Ontario) and Mark Suffak (PhD student from the Univ. of Western Ontario). One of the main prospects of BeAtlas is to extend its usage beyond our research group, so that it becomes a known tool for the community at large.

Finally, we will benefit, in the future, from optical broad-band polarimetry from the `South-Pol` survey (Magalhães, 2012). This project will image the entire southern Sky and, consequently, vastly increase the number of Be stars with polarimetric measurements. BeAtlas could prove an useful tool to extract physical information about the star and the disk from this huge database. In addition, the next data releases of Gaia to fix the issues with bright and nearby targets (de Bruijne et al., 2014). Improved distances will have large impact on the quality of the BeAtlas inference.

Bibliography

2015 EsoRex: ESO Recipe Execution Tool Astrophysics Source Code Library

Abt H. A., Levato H., Grosso M., Rotational Velocities of B Stars, ApJ, 2002, vol. 573, p. 359

Adelman S. J., The physical properties of normal A stars. In The A-Star Puzzle , vol. 224 of IAU Symposium, 2004, p. 1

Ammler-von Eiff M., Reiners A., New measurements of rotation and differential rotation in A-F stars: are there two populations of differentially rotating stars?, A&A, 2012, vol. 542, p. A116

Arcos C., Jones C. E., Sigut T. A. A., Kanaan S., Curé M., Evidence for Different Disk Mass Distributions between Early- and Late-type Be Stars in the BeSOS Survey, ApJ, 2017a, vol. 842, p. 48

Arcos C., Jones C. E., Sigut T. A. A., Kanaan S., Curé M., Evidence for Different Disk Mass Distributions Between Early and Late-Type Be Stars in the BeSOS Survey, ArXiv e-prints, 2017b

Arviset C., Barbarisi I., de La Calle I., Fajersztejn N., Freschi M., Gabriel C., Gomez P., Guainazzi M., Ibarra A., Laruelo A., Leon I., Micol A., Parrilla E., Ortiz I., Osuna P., Salgado J., Stebe A., Tapiador D., ESA Science Archives, VO tools and remote Scientific Data reduction in Grid Architectures. In Astronomical Data Analysis Software and Systems XVII , vol. 394 of Astronomical Society of the Pacific Conference Series, 2008, p. 227

Aufdenberg J. P., Mérand A., Coudé du Foresto V., Absil O., Di Folco E., Kervella P., Ridgway S. T., Berger D. H., ten Brummelaar T. A., McAlister H. A., Sturmann J., Sturmann L.,

Turner N. H., First Results from the CHARA Array. VII. Long-Baseline Interferometric Measurements of Vega Consistent with a Pole-On, Rapidly Rotating Star, ApJ, 2006, vol. 645, p. 664

Baade D., Binary Be-Stars and Be-Binaries. In Evolutionary Processes in Interacting Binary Stars , vol. 151 of IAU Symposium, 1992, p. 147

Baade D., Martayan C., Rivinius T., Be Stars as Seen Through Telescopes in Survey Mode Invited Review. In Bright Emissaries: Be Stars as Messengers of Star-Disk Physics , vol. 506 of Astronomical Society of the Pacific Conference Series, 2016, p. 175

Baade D., Rivinius T., Pigulski A., Carciofi A. C., Martayan C., Moffat A. F. J., Wade G. A., Weiss W. W., Grunhut J., Handler G., Kuschnig R., Mehner A., Pablo H., Popowicz A., Rucinski S., Whittaker G., Short-term variability and mass loss in Be stars. I. BRITE satellite photometry of η and μ Centauri, A&A, 2016, vol. 588, p. A56

Bagnulo S., Fossati L., Landstreet J. D., Izzo C., The FORS1 catalogue of stellar magnetic field measurements, A&A, 2015, vol. 583, p. A115

Bailey J. D., Landstreet J. D., Abundances determined using Si ii and Si iii in B-type stars: evidence for stratification, A&A, 2013, vol. 551, p. A30

Banerjee D. P. K., Rawat S. D., Janardhan P., Hα observations of Be stars, A&AS, 2000, vol. 147, p. 229

Bastian N., Cabrera-Ziri I., Niederhofer F., de Mink S., Georgy C., Baade D., Correnti M., Usher C., Romaniello M., A high fraction of Be stars in young massive clusters: evidence for a large population of near-critically rotating stars, MNRAS, 2017, vol. 465, p. 4795

Bayo A., Rodrigo C., Barrado y Navascues D., Solano E., Gutierrez R., Morales-Calderon M., Allard F., VizieR Online Data Catalog: VOSA: virtual observatory SED analyzer (Bayo+, 2008), VizieR Online Data Catalog, 2008, vol. 349

Becker J. C., Johnson J. A., Vanderburg A., Morton T. D., Extracting Radial Velocities of A- and B-type Stars from Echelle Spectrograph Calibration Spectra, The Astrophysical Journal Supplement Series, 2015, vol. 217, p. 29

Bernacca P. L., Perinotto M., A catalogue of stellar rotational velocities: I. Main sequence single stars. II. Main sequence spectroscopic binaries and eclipsing systems., Contributi dell'Osservatorio Astrofisica dell'Universita di Padova in Asiago, 1970, vol. 239, p. 1

Bhat S. S., Paul K. T., Subramaniam A., Mathew B., Spectroscopic study of Be-shell stars: 4 Her and 88 Her, Research in Astronomy and Astrophysics, 2016, vol. 16, p. 76

Bianchi L., Szalay A., Martin C., Friedman P., Madore B., Milliard B., Malina R., The Galaxy Evolution Explorer. In American Astronomical Society Meeting Abstracts #190 , vol. 190 of American Astronomical Society Meeting Abstracts, 1997, p. 09.09

Bjorkman J. E., Carciofi A. C., Modeling the Structure of Hot Star Disks. In The Nature and Evolution of Disks Around Hot Stars , vol. 337, 2005a, p. 75

Bjorkman J. E., Carciofi A. C., NLTE Monte Carlo Models of the Polarization of Circumstellar Disks. In Astronomical Polarimetry: Current Status and Future Directions , vol. 343 of Astronomical Society of the Pacific Conference Series, 2005b, p. 270

Bjorkman K. S., Miroshnichenko A. S., McDavid D., Pogrosheva T. M., A Study of π Aquarii during a Quasi-normal Star Phase: Refined Fundamental Parameters and Evidence for Binarity, ApJ, 2002, vol. 573, p. 812

Bless R. C., Percival J. W., The bolometric luminosities of stars.. In IAU Symposium , vol. 189 of IAU Symposium, 1997, p. 73

Bohlender D., Searching For and Monitoring Ae and A Shell Stars at the DAO. In Bright Emissaries: Be Stars as Messengers of Star-Disk Physics , vol. 506 of Astronomical Society of the Pacific Conference Series, 2016, p. 275

Bouffanais Y., Porter E. K., Bayesian inference for binary neutron star inspirals using a Hamiltonian Monte Carlo Algorithm, arXiv e-prints, 2018, p. arXiv:1810.07443

Bragança G. A., Daflon S., Cunha K., Bensby T., Oey M. S., Walth G., Projected Rotational Velocities and Stellar Characterization of 350 B Stars in the Nearby Galactic Disk, AJ, 2012, vol. 144, p. 130

Briot D., Ultraviolet fluxes of Be stars, A&A, 1978, vol. 66, p. 197

Carciofi A. C., The circumstellar discs of Be stars. In IAU Symposium , vol. 272 of IAU Symposium, 2011, p. 325

Carciofi A. C., Bjorkman J. E., Non-LTE Monte Carlo Radiative Transfer. I. The Thermal Properties of Keplerian Disks around Classical Be Stars, ApJ, 2006, vol. 639, p. 1081

Carciofi A. C., Bjorkman J. E., Non-LTE Monte Carlo Radiative Transfer. II. Nonisothermal Solutions for Viscous Keplerian Disks, apj, 2008, vol. 684, p. 1374

Carciofi A. C., Bjorkman J. E., Magalhães A. M., Effects of Grain Size on the Spectral Energy Distribution of Dusty Circumstellar Envelopes, ApJ, 2004, vol. 604, p. 238

Carciofi A. C., Bjorkman J. E., Otero S. A., Okazaki A. T., Štefl S., Rivinius T., Baade D., Haubois X., The First Determination of the Viscosity Parameter in the Circumstellar Disk of a Be Star, apjl, 2012, vol. 744, p. L15

Carciofi A. C., Bjorkman J. E., Zsargó J., HDUST3 - A chemically realistic, 3-D, NLTE radiative transfer code. In The Lives and Death-Throes of Massive Stars , vol. 329 of IAU Symposium, 2017, p. 390

Carciofi A. C., Magalhães A. M., Leister N. V., Bjorkman J. E., Levenhagen R. S., Achernar: Rapid Polarization Variability as Evidence of Photospheric and Circumstellar Activity, ApJ, 2007, vol. 671, p. L49

Carciofi A. C., Miroshnichenko A. S., Kusakin A. V., Bjorkman J. E., Bjorkman K. S., Marang F., Kuratov K. S., García-Lario P., Calderón J. V. P., Fabregat J., Magalhães A. M., Properties of the δ Scorpii Circumstellar Disk from Continuum Modeling, apj, 2006, vol. 652, p. 1617

Carciofi A. C., Okazaki A. T., Le Bouquin J.-B., Štefl S., Rivinius T., Baade D., Bjorkman J. E., Hummel C. A., Cyclic variability of the circumstellar disk of the Be star ζ Tauri. II. Testing the 2D global disk oscillation model, aap, 2009, vol. 504, p. 915

Cardelli J. A., Clayton G. C., Mathis J. S., The relationship between infrared, optical, and ultraviolet extinction, ApJ, 1989, vol. 345, p. 245

Cash W., The Far Ultraviolet Spectroscopic Explorer., Journal of the British Interplanetary Society, 1984, vol. 37, p. 81

Castelli F., Kurucz R. L., New Grids of ATLAS9 Model Atmospheres. In Modelling of Stellar Atmospheres , vol. 210 of IAU Symposium, 2003, p. A20

Catanzaro G., Spectroscopic atlas of Hα and Hβ in a sample of northern Be stars, A&A, 2013, vol. 550, p. A79

Chauville J., Zorec J., Ballereau D., Morrell N., Cidale L., Garcia A., High and intermediate-resolution spectroscopy of Be stars 4481 lines, A&A, 2001, vol. 378, p. 861

Chesneau O., Meilland A., Rivinius T., Stee P., Jankov S., Domiciano de Souza A., Graser U., Herbst T., Janot-Pacheco E., Koehler R., Leinert C., Morel S., Paresce F., Richichi A., Robbe-Dubois S., First VLTI/MIDI observations of a Be star: Alpha Arae, aap, 2005, vol. 435, p. 275

Chini R., Hoffmeister V. H., Nasseri A., Stahl O., Zinnecker H., A spectroscopic survey on the multiplicity of high-mass stars, MNRAS, 2012, vol. 424, p. 1925

Claret A., A new non-linear limb-darkening law for LTE stellar atmosphere models. Calculations for -5.0 = log[M/H] = +1, 2000 K = T_{eff} = 50000 K at several surface gravities, A&A, 2000, vol. 363, p. 1081

Clark J. S., Steele I. A., Fender R. P., Radio observations of IRAS-selected Southern hemisphere classical Be stars, MNRAS, 1998, vol. 299, p. 1119

Collins II G. W., Continuum Emission from a Rapidly Rotating Stellar Atmosphere., ApJ, 1963, vol. 138, p. 1134

Collins II G. W., The use of terms and definitions in the study of Be stars. In IAU Colloq. 92: Physics of Be Stars , 1987, p. 3

Collins II G. W., Harrington J. P., Theoretical H-Beta Line Profiles and Related Parameters for Rotating B Stars, ApJ, 1966, vol. 146, p. 152

Conti P. S., Leep E. M., Spectroscopic observations of O-type stars. V. The hydrogen lines and lambda 4686 He II., ApJ, 1974, vol. 193, p. 113

Cote J., Waters L. B. F. M., IRAS observations of Be stars. I - Statistical study of the IR excess of 101 Be stars, A&A, 1987, vol. 176, p. 93

Cotton D. V., Bailey J., Kedziora-Chudczer L., Bott K., Lucas P. W., Hough J. H., Marshall J. P., The linear polarization of Southern bright stars measured at the parts-per-million level, MNRAS, 2016, vol. 455, p. 1607

Cranmer S. R., Dynamical Models of Winds from Rotating Hot Stars, Bartol Research Institute, University of Delaware, 1996, Ph.D. Thesis

Cranmer S. R., A Statistical Study of Threshold Rotation Rates for the Formation of Disks around Be Stars, ApJ, 2005, vol. 634, p. 585

Cutri R. M., et al. VizieR Online Data Catalog: AllWISE Data Release (Cutri+ 2013), VizieR Online Data Catalog, 2014, vol. 2328

Cuypers J., Balona L. A., Marang F., Intensive photometry of southern Be variables. I - Winter objects, A&AS, 1989, vol. 81, p. 151

Cyr I. H., Jones C. E., Panoglou D., Carciofi A. C., Okazaki A. T., Be discs in binary systems - II. Misaligned orbits, MNRAS, 2017, vol. 471, p. 596

Cyr R. P., Jones C. E., Tycner C., Statistical Analysis of Interferometric Measurements of Axis Ratios for Classical Be Stars, ApJ, 2015, vol. 799, p. 33

Dachs J., Eichendorf W., Schleicher H., Schmidt-Kaler T., Stift M., Tug H., Photoelectric scanner measurements of Balmer emission line profiles for southern Be stars. II - A survey for variations, A&AS, 1981, vol. 43, p. 427

Dachs J., Hanuschik R., Kaiser D., Ballereau D., Bouchet P., Kiehling R., Kozok J., Rudolph R., Schlosser W., Measurements of Balmer emission line profiles for southern Be stars. II. New data and radial velocities., Astronomy and Astrophysics Supplement Series, 1986, vol. 63, p. 87

Dachs J., Kiehling R., Engels D., Optical and infrared continua of southern Be stars, A&A, 1988, vol. 194, p. 167

Dachs J., Rohe D., Loose A. S., A study of Balmer decrements in Be star emission-line spectra, A&A, 1990, vol. 238, p. 227

Dalla Vedova G., Millour F., Domiciano de Souza A., Petrov R. G., Moser Faes D., Carciofi A. C., Kervella P., Rivinius T., VLTI/PIONIER images the Achernar disk swell, A&A, 2017, vol. 601, p. A118

de Bruijne J. H. J., Rygl K. L. J., Antoja T., Gaia Astrometric Science Performance - Post-Launch Predictions. In EAS Publications Series , vol. 67-68 of EAS Publications Series, 2014, p. 23

Dekker H., D'Odorico S., Kaufer A., Delabre B., Kotzlowski H., Design, construction, and performance of UVES, the echelle spectrograph for the UT2 Kueyen Telescope at the ESO Paranal Observatory. In Optical and IR Telescope Instrumentation and Detectors , vol. 4008, 2000, p. 534

di Benedetto G. P., Towards a fundamental calibration of stellar parameters of A, F, G, K dwarfs and giants, A&A, 1998, vol. 339, p. 858

Divan L., Zorec J., Briot D., Correlations between BCD parameters of the continuous spectrum and the Balmer decrement of Be stars. In Be Stars , vol. 98, 1982, p. 53

Domiciano de Souza A., Kervella P., Moser Faes D., Dalla Vedova G., Mérand A., Le Bouquin J. B., Espinosa Lara F., Rieutord M., Bendjoya P., Carciofi A. C., Hadjara M., Millour F., Vakili F., The environment of the fast rotating star Achernar. III. Photospheric parameters revealed by the VLTI, A&A, 2014, vol. 569, p. A10

Dougherty S. M., Waters L. B. F. M., Burki G., Cote J., Cramer N., van Kerkwijk M. H., Taylor A. R., Near-IR excess of Be stars., A&A, 1994, vol. 290

Ducati J. R., VizieR Online Data Catalog: Catalogue of Stellar Photometry in Johnson's 11-color system., VizieR Online Data Catalog, 2002, vol. 2237

Dulaney N. A., Richardson N. D., Gerhartz C. J., Bjorkman J. E., Bjorkman K. S., Carciofi A. C., Klement R., Wang L., Morrison N. D., Bratcher A. D., Greco J. J., Hardegree-Ullman K. K., Lembryk L., Oswald W. L., Trucks J. L., A Spectroscopic Orbit for the Late-type Be Star β CMi, ApJ, 2017, vol. 836, p. 112

Dunstall P. R., Dufton P. L., Sana H., Evans C. J., Howarth I. D., Simón-Díaz S., de Mink S. E., Langer N., Maíz Apellániz J., Taylor W. D., The VLT-FLAMES Tarantula Survey. XXII. Multiplicity properties of the B-type stars, A&A, 2015, vol. 580, p. A93

Egan M. P., Price S. D., Kraemer K. E., Mizuno D. R., Carey S. J., Wright C. O., Engelke C. W., Cohen M., Gugliotti M. G., VizieR Online Data Catalog: MSX6C Infrared Point Source Catalog. The Midcourse Space Experiment Point Source Catalog Version 2.3 (October 2003), VizieR Online Data Catalog, 2003, vol. 5114

Ekström S., Georgy C., Eggenberger P., Meynet G., Mowlavi N., Wyttenbach A., Granada A., Decressin T., Hirschi R., Frischknecht U., Charbonnel C., Maeder A., Grids of stellar models with rotation. I. Models from 0.8 to 120 M at solar metallicity (Z = 0.014), A&A, 2012, vol. 537, p. A146

Ekström S., Georgy C., Meynet G., Maeder A., Granada A., Massive stellar models: rotational evolution, metallicity effects. In Active OB Stars: Structure, Evolution, Mass Loss, and Critical Limits , vol. 272 of IAU Symposium, 2011, p. 62

Ekström S., Meynet G., Maeder A., Barblan F., Evolution towards the critical limit and the origin of Be stars, A&A, 2008, vol. 478, p. 467

ESA VizieR Online Data Catalog: The Hipparcos and Tycho Catalogues (ESA 1997), VizieR Online Data Catalog, 1997, vol. 1239

Escolano C., Carciofi A. C., Okazaki A. T., Rivinius T., Baade D., Štefl S., 2.5D global-disk oscillation models of the Be shell star ζ Tauri. I. Spectroscopic and polarimetric analysis, A&A, 2015, vol. 576, p. A112

ESO, 2012 GASGANO: Data File Organizer Astrophysics Source Code Library

Espinosa Lara F., Rieutord M., Gravity darkening in rotating stars, A&A, 2011, vol. 533, p. A43

Faes D. M., An interferometric view of hot star disks, IAG-Universidade de Sao Paulo (Brazil), Lagrange-Universite de Nice (France) ¡EMAIL¿dmfaes@gmail.com¡/EMAIL¿, 2015, Ph.D. Thesis

Faes D. M., Domiciano de Souza A., Carciofi A. C., Bendjoya P., The photosphere and circumstellar environment of the Be star Achernar. In New Windows on Massive Stars , vol. 307 of IAU Symposium, 2015, p. 261

Feinstein A., A Survey of Southern Be Stars. II. Photometric data, ZAp, 1968, vol. 68, p. 29

Ferreira J., Pelletier G., Appl S., Reconnection X-winds: spin-down of low-mass protostars, MNRAS, 2000, vol. 312, p. 387

Fitzpatrick E. L., Correcting for the Effects of Interstellar Extinction, PASP, 1999, vol. 111, p. 63

Fitzpatrick E. L., Massa D., Determining the Physical Properties of the B Stars. I. Methodology and First Results, ApJ, 1999, vol. 525, p. 1011

Foreman-Mackey D., Hogg D. W., Lang D., Goodman J., emcee: The MCMC Hammer, PASP, 2013, vol. 125, p. 306

Freire Ferrero R., Morales Durán C., Halbwachs J.-L., Cabo Cubeiro A. M., High Ionization Species in the Nearby Interstellar Medium from an Exhaustive Analysis of the IUE INES Database, AJ, 2012, vol. 143, p. 28

Frémat Y., Zorec J., Hubert A.-M., Floquet M., Effects of gravitational darkening on the determination of fundamental parameters in fast-rotating B-type stars, A&A, 2005, vol. 440, p. 305

Freudling W., Romaniello M., Bramich D. M., Ballester P., Forchi V., García-Dabló C. E., Moehler S., Neeser M. J., Automated data reduction workflows for astronomy. The ESO Reflex environment, A&A, 2013, vol. 559, p. A96

Frost S. A., Conti P. S., The Relationship of the OE to the be Stars. In Be and Shell Stars , vol. 70 of IAU Symposium, 1976, p. 139

Gaia Collaboration VizieR Online Data Catalog: Gaia DR2 (Gaia Collaboration, 2018), VizieR Online Data Catalog, 2018, vol. 1345

Gaia Collaboration Brown A. G. A., Vallenari A., Prusti T., de Bruijne J. H. J., Babusiaux C., Bailer-Jones C. A. L., Biermann M., Evans D. W., Eyer L., Jansen Gaia Data Release 2. Summary of the contents and survey properties, A&A, 2018, vol. 616, p. A1

Georgy C., Ekström S., Granada A., Meynet G., Mowlavi N., Eggenberger P., Maeder A., Populations of rotating stars. I. Models from 1.7 to 15 $M_Ł$ at Z = 0.014, 0.006, and 0.002 with Ω/Ω_{crit} between 0 and 1, A&A, 2013, vol. 553, p. A24

Ghoreyshi M. R., Carciofi A. C., Rímulo L. R., Vieira R. G., Faes D. M., Baade D., Bjorkman J. E., Otero S., Rivinius T., The life cycles of Be viscous decretion discs: The case of ω CMa, MNRAS, 2018

Gies D. R., Glimpses of Be Binary Evolution. In IAU Colloq. 175: The Be Phenomenon in Early-Type Stars , vol. 214 of Astronomical Society of the Pacific Conference Series, 2000, p. 668

Gies D. R., Bagnuolo Jr. W. G., Baines CHARA Array K'-Band Measurements of the Angular Dimensions of Be Star Disks, ApJ, 2007, vol. 654, p. 527

Gies D. R., Bagnuolo Jr. W. G., Ferrara E. C., Kaye A. B., Thaller M. L., Penny L. R., Peters G. J., Hubble Space Telescope Goddard High Resolution Spectrograph Observations of the Be + sdO Binary Persei, ApJ, 1998, vol. 493, p. 440

Golden-Marx J. B., Oey M. S., Lamb J. B., Graus A. S., White A. S., Classical Oe Stars in the Field of the Small Magellanic Cloud, ApJ, 2016, vol. 819, p. 55

Goodman J., Weare J., Ensemble samplers with affine invariance, Communications in Applied Mathematics and Computational Science, Vol. 5, No. 1, p. 65-80, 2010, 2010, vol. 5, p. 65

Granada A., Ekström S., Georgy C., Krtička J., Owocki S., Meynet G., Maeder A., Populations of rotating stars. II. Rapid rotators and their link to Be-type stars, A&A, 2013, vol. 553, p. A25

Granada A., Haemmerlé L., Evolution of single B-type stars with a large angular momentum content, A&A, 2014, vol. 570, p. A18

Grevesse N., Sauval A. J., Standard Solar Composition, Space Sci. Rev., 1998, vol. 85, p. 161

Grudzinska M., Belczynski K., Casares J., de Mink S. E., Ziolkowski J., Negueruela I., Ribó M., Ribas I., Paredes J. M., Herrero A., Benacquista M., On the formation and evolution of the first Be star in a black hole binary MWC 656, MNRAS, 2015, vol. 452, p. 2773

Grunhut J. H., Wade G. A., MiMeS Collaboration The incidence of magnetic fields in massive stars: An overview of the MiMeS survey component. In American Institute of Physics Conference Series , vol. 1429 of American Institute of Physics Conference Series, 2012, p. 67

Halonen R. J., Jones C. E., On the Intrinsic Continuum Linear Polarization of Classical Be Stars during Disk Growth and Dissipation, ApJ, 2013, vol. 765, p. 17

Hamed G. E., Sigut T. A. A., Theoretical infrared continuum images for Be star disks, NRIAG Journal of Astronomy and Geophysics, 2013, vol. 2, p. 125

Hanuschik R. W., Hummel W., Dietle O., Sutorius E., V/R variability and global oscillations in Be star disks., A&A, 1995, vol. 300, p. 163

Hanuschik R. W., Hummel W., Sutorius E., Dietle O., Thimm G., Atlas of high-resolution emission and shell lines in Be stars. Line profiles and short-term variability., A&AS, 1996, vol. 116, p. 309

Hanuschik R. W., Kozok J. R., Kaiser D., High-resolution emission-line spectroscopy of Be stars. III - Balmer line profiles, A&A, 1988, vol. 189, p. 147

Hardorp J., Strittmatter P. A., Rotation and Evolution of be Stars. In IAU Colloq. 4: Stellar Rotation , 1970, p. 48

Harmanec P., Stellar masses and radii based on modern binary data, Bulletin of the Astronomical Institutes of Czechoslovakia, 1988, vol. 39, p. 329

Harmanec P., Hill G. M., Walker G. A. H., Dinshaw N., Yang S., Is Omicron Andromedae a quadruple or even quintuple system?, Publications of the Astronomical Institute of the Czechoslovak Academy of Sciences, 1987, vol. 70, p. 115

Hartkopf W. I., Tokovinin A., Mason B. D., Speckle Interferometry at SOAR in 2010 and 2011: Measures, Orbits, and Rectilinear Fits, AJ, 2012, vol. 143, p. 42

Haubois X., Carciofi A. C., Rivinius T., Okazaki A. T., Bjorkman J. E., Dynamical Evolution of Viscous Disks around Be Stars. I. Photometry, apj, 2012, vol. 756, p. 156

Haubois X., Mota B. C., Carciofi A. C., Draper Z. H., Wisniewski J. P., Bednarski D., Rivinius T., Dynamical Evolution of Viscous Disks around Be Stars. II. Polarimetry, ApJ, 2014, vol. 785, p. 12

Hekker S., Elsworth Y., Mosser B., Kallinger T., Basu S., Chaplin W. J., Stello D., Asteroseismic surface gravity for evolved stars, A&A, 2013, vol. 556, p. A59

Henry G. W., Smith M. A., Rotational and Cyclical Variability in γ Cassiopeiae. II. Fifteen Seasons, ApJ, 2012, vol. 760, p. 10

Hilbe J. M., de Souza R. S., Ishida E. E. O., Bayesian Models for Astrophysical Data Using R, JAGS, Python, and Stan, 2017

Hillier D. J., Miller D. L., The Treatment of Non-LTE Line Blanketing in Spherically Expanding Outflows, ApJ, 1998, vol. 496, p. 407

Hoffleit D., Jaschek C., The Bright Star Catalogue, 1982

Hog E., Fabricius C., Makarov V. V., Urban S., Corbin T., Wycoff G., Bastian U., Schwekendiek P., Wicenec A., VizieR Online Data Catalog: The Tycho-2 Catalogue (Hog+ 2000), VizieR Online Data Catalog, 2000, vol. 1259

Huang S.-S., Struve O., Stellar rotation, Annales d'Astrophysique, 1954, vol. 17, p. 85

Huang W., Gies D. R., Stellar Rotation in Young Clusters. I. Evolution of Projected Rotational Velocity Distributions, ApJ, 2006, vol. 648, p. 580

Huang W., Gies D. R., McSwain M. V., A Stellar Rotation Census of B Stars: From ZAMS to TAMS, ApJ, 2010, vol. 722, p. 605

Hunter I., Smoker J. V., Keenan F. P., Ledoux C., Jehin E., Cabanac R., Melo C., Bagnulo S., Early-type stars observed in the ESO UVES Paranal Observatory Project - I. Interstellar NaI UV, TiII and CaII K observations*, MNRAS, 2006, vol. 367, p. 1478

Hurwitz M., Sholl M., The CHIPS University-Class Explorer. In American Astronomical Society Meeting Abstracts , vol. 195, 1999, p. 88.06

Ishak B., Statistics, data mining, and machine learning in astronomy: a practical Python guide for the analysis of survey data, by Željko Ivezić, Andrew J. Connolly, Jacob T. VanderPlas and Alexander Gray, Contemporary Physics, 2017, vol. 58, p. 99

Ishihara D., Onaka T., Kataza H., Salama A., Alfageme C., Cassatella The AKARI/IRC mid-infrared all-sky survey, A&A, 2010, vol. 514, p. A1

Jarad M. M., Hilditch R. W., Skillen I., A radial-velocity study of 18 emission-line B stars, MNRAS, 1989, vol. 238, p. 1085

Jaschek M., Egret D., A Catalogue of Be-Stars. In Be Stars , vol. 98 of IAU Symposium, 1982, p. 261

Jaschek M., Slettebak A., Jaschek C., , 1981 Be star terminology. Be Star Newsletter

Johnston K. G., Robitaille T. P., Beuther H., Linz H., Boley P., Kuiper R., Keto E., Hoare M. G., van Boekel R., A Keplerian-like Disk around the Forming O-type Star AFGL 4176, ApJ, 2015, vol. 813, p. L19

Jones C. E., Tycner C., Sigut T. A. A., Benson J. A., Hutter D. J., A Parameter Study of Classical Be Star Disk Models Constrained by Optical Interferometry, ApJ, 2008, vol. 687, p. 598

Kaeufl H.-U., Ballester P., Biereichel P., Delabre B., Donaldson R., Dorn R., Fedrigo E., Finger G., Fischer CRIRES: a high-resolution infrared spectrograph for ESO's VLT. In Ground-based Instrumentation for Astronomy , vol. 5492, 2004, p. 1218

Katahira J.-I., Hirata R., Ito M., Katoh M., Ballereau D., Chauville J., Period Analysis of the Radial Velocity in PLEIONE, PASJ, 1996, vol. 48, p. 317

Kazmier L. J., Schaum's Outline Of Business Statistics / 4th edn. McGraw-Hill New York : Schaum ; London, c2004

Kee N. D., Owocki S., Sundqvist J. O., Line-driven ablation of circumstellar discs - I. Optically thin decretion discs of classical Oe/Be stars, MNRAS, 2016, vol. 458, p. 2323

Keller S. C., Wood P. R., Bessell M. S., Be stars in and around young clusters in the Magellanic Clouds, A&AS, 1999, vol. 134, p. 489

Kervella P., Domiciano de Souza A., The polar wind of the fast rotating Be star Achernar. VINCI/VLTI interferometric observations of an elongated polar envelope, A&A, 2006, vol. 453, p. 1059

Kervella P., Domiciano de Souza A., Bendjoya P., The close-in companion of the fast rotating Be star Achernar, A&A, 2008, vol. 484, p. L13

Kinman T., Castelli F., The determination of T_{eff} for metal-poor A-type stars using V and 2MASS J, H and K magnitudes, A&A, 2002, vol. 391, p. 1039

Kjurkchieva D., Marchev D., Sigut T. A. A., Dimitrov D., The B and Be States of the Star EM Cepheus, AJ, 2016, vol. 152, p. 56

Klement R., Carciofi A. C., Rivinius T., Matthews L. D., Vieira R. G., Ignace R., Bjorkman J. E., Mota B. C., Faes D. M., Bratcher A. D., Curé M., Štefl S., Revealing the structure of the outer disks of Be stars, A&A, 2017, vol. 601, p. A74

Klement R., Carciofi A. C., Rivinius T., Panoglou D., Vieira R. G., Bjorkman J. E., Štefl S., Tycner C., Faes D. M., Korčáková D., Müller A., Zavala R. T., Curé M., Multitechnique testing of the viscous decretion disk model. I. The stable and tenuous disk of the late-type Be star β CMi, A&A, 2015, vol. 584, p. A85

Kolb M., Baade D., High-precision continuum rectification. Towards an abundance analysis of Be and BN stars. In Pulsation; Rotation; and Mass Loss in Early-Type Stars , vol. 162 of IAU Symposium, 1994, p. 427

Koubský P., Kotková L., Votruba V., Šlechta M., Dvořáková Š., o Puppis: another Be+sdO binary?, A&A, 2012, vol. 545, p. A121

Kraemer G., Eberhard N., Grewing M., Gringel W., Haas C., Kaelble A., Kappelmann N., Petrik J., Riegger J., ORFEUS: A 1m-EUV/FUV-telescope on the space platform ASTROSPAS. In ESA Special Publication , vol. 2, 1988, p. 333

Kraus S., Monnier J. D., Che X., Schaefer G., Touhami Y., Gies D. R., Aufdenberg J. P., Baron F., Thureau N., ten Brummelaar T. A., McAlister H. A., Turner N. H., Sturmann J., Sturmann L., Gas Distribution, Kinematics, and Excitation Structure in the Disks around the Classical Be Stars β Canis Minoris and ζ Tauri, ApJ, 2012, vol. 744, p. 19

Krtička J., Owocki S. P., Meynet G., Mass and angular momentum loss via decretion disks, A&A, 2011, vol. 527, p. A84

Labadie-Bartz J., Chojnowski S. D., Whelan D. G., Outbursts and Disk Variability in Be Stars, AJ, 2018, vol. 155, p. 53

Labadie-Bartz J., Pepper J., McSwain M. V., Bjorkman J. E., Bjorkman K. S., Lund M. B., Rodriguez J. E., Stassun K. G., Stevens D. J., James D. J., Kuhn R. B., Siverd R. J., Beatty T. G., Photometric Variability of the Be Star Population, AJ, 2017, vol. 153, p. 252

Lamers H. J. G. L. M., Faraggiana R., Burger M., Observations of the mid-ultraviolet spectrum of peculiar A and B stars and of Be stars, BN stars and shell stars, A&A, 1980, vol. 82, p. 48

Langer N., Cantiello M., Yoon S.-C., Hunter I., Brott I., Lennon D., de Mink S., Verheijdt M., Rotation and Massive Close Binary Evolution. In Massive Stars as Cosmic Engines , vol. 250 of IAU Symposium, 2008, p. 167

Lee R. W., ed., 1991 A review of spectral line broadening relevant to hot dense plasmas

Levenhagen R. S., Leister N. V., Spectroscopic analysis of southern B and Be stars, MNRAS, 2006, vol. 371, p. 252

Macchetto F., The International Ultraviolet Explorer (IUE), Memorie della Societa Astronomica Italiana, 1976, vol. 47, p. 431

Maeder A., Physics, Formation and Evolution of Rotating Stars, 2009

Maeder A., Grebel E. K., Mermilliod J.-C., Differences in the fractions of Be stars in galaxies, A&A, 1999, vol. 346, p. 459

Magalhães A. M., SOUTH POL: Revealing the Polarized Southern Sky. In Science from the Next Generation Imaging and Spectroscopic Surveys , 2012, p. 7

Magalhaes A. M., Benedetti E., Roland E. H., A photoelectric polarimeter with tilt-scanning capability., Publications of the Astronomical Society of the Pacific, 1984, vol. 96, p. 383

Magalhaes A. M., Rodrigues C. V., Margoniner V. E., Pereyra A., Heathcote S., High Precision CCD Imaging Polarimetry. In Polarimetry of the Interstellar Medium , vol. 97 of Astronomical Society of the Pacific Conference Series, 1996, p. 118

Malina R. F., Bowyer S., Lampton M., Finley D., Paresce F., Penegor G., Heetderks H., The Extreme Ultraviolet Explorer., Optical Engineering, 1982, vol. 21, p. 764

Marco A., Negueruela I., NGC 7419 as a template for red supergiant clusters, A&A, 2013, vol. 552, p. A92

Martayan C., Frémat Y., Hubert A.-M., Floquet M., Zorec J., Neiner C., Effects of metallicity, star-formation conditions, and evolution in B and Be stars. II. Small Magellanic Cloud, field of NGC330, A&A, 2007, vol. 462, p. 683

Martins F., Schaerer D., Hillier D. J., A new calibration of stellar parameters of Galactic O stars, A&A, 2005, vol. 436, p. 1049

Mason B. D., ten Brummelaar T., Gies D. R., Hartkopf W. I., Thaller M. L., , 1997 A Speckle Survey of Southern Be Stars Be Star Newsletter

Mason B. D., Wycoff G. L., Hartkopf W. I., Douglass G. G., Worley C. E., The 2001 US Naval Observatory Double Star CD-ROM. I. The Washington Double Star Catalog, AJ, 2001, vol. 122, p. 3466

Massey P., MASSIVE STARS IN THE LOCAL GROUP: Implications for Stellar Evolution and Star Formation, ARA&A, 2003, vol. 41, p. 15

McEvoy C. M., Smoker J. V., Dufton P. L., Smith K. T., Kennedy M. B., Keenan F. P., Lambert D. L., Welty D. E., Lauroesch J. T., Early-type stars observed in the ESO UVES Paranal Observatory Project - V. Time-variable interstellar absorption, MNRAS, 2015, vol. 451, p. 1396

McGill M. A., Sigut T. A. A., Jones C. E., The Thermal Structure of Gravitationally Darkened Classical Be Star Disks, ApJ, 2011, vol. 743, p. 111

McLean I. S., Interpretation of the intrinsic polarizations of early-type emission-line stars, MNRAS, 1979, vol. 186, p. 265

McLean I. S., Brown J. C., Polarisation by Thomson scattering in optically thin stellar envelopes. III. A statistical study of the oblateness and rotation of Be star envelopes., A&A, 1978, vol. 69, p. 291

McLean I. S., Clarke D., Separation of the intrinsic and interstellar linear polarization components of southern hemisphere early-type emission-line stars., MNRAS, 1979, vol. 186, p. 245

McSwain M. V., Gies D. R., The Evolutionary Status of Be Stars: Results from a Photometric Study of Southern Open Clusters, ApJS, 2005, vol. 161, p. 118

Meilland A., Millour F., Kanaan S., Stee P., Petrov R., Hofmann K.-H., Natta A., Perraut K., First spectro-interferometric survey of Be stars. I. Observations and constraints on the disk geometry and kinematics, A&A, 2012, vol. 538, p. A110

Meilland A., Stee P., Recent results from the SIMECA code and VLTI observations. In EAS Publications Series , vol. 18 of EAS Publications Series, 2006, p. 273

Meilland A., Stee P., Chesneau O., Jones C., VLTI/MIDI observations of 7 classical Be stars, aap, 2009, vol. 505, p. 687

Meilland A., Stee P., Vannier M., Millour F., Domiciano de Souza A., Malbet F., Martayan C., Paresce F., Petrov R. G., Richichi A., Spang A., First direct detection of a Keplerian rotating disk around the Be star α Arae using AMBER/VLTI, aap, 2007, vol. 464, p. 59

Mennickent R. E., H-beta line profile variability of seven southern Be stars, A&AS, 1991, vol. 88, p. 1

Mennickent R. E., Vogt N., V/R variations in H-beta emission profiles of Be stars, A&A, 1991, vol. 241, p. 159

Mermilliod J.-C., VizieR Online Data Catalog: UBV Photoelectric Cat: Data 1986-1992 (Mermilliod 1994), VizieR Online Data Catalog, 1994, vol. 2193

Metropolis N., Rosenbluth A. W., Rosenbluth M. N., Teller A. H., Teller E., Equation of State Calculations by Fast Computing Machines, J. Chem. Phys., 1953, vol. 21, p. 1087

Meynet G., Maeder A., Stellar evolution with rotation. V. Changes in all the outputs of massive star models, A&A, 2000, vol. 361, p. 101

Miroshnichenko A. S., Pasechnik A. V., Manset N., The 2011 Periastron Passage of the Be Binary δ Scorpii, ApJ, 2013, vol. 766, p. 119

Negueruela I., Steele I. A., Bernabeu G., On the class of Oe stars, Astronomische Nachrichten, 2004, vol. 325, p. 749

Ochsenbein F., Bauer P., Marcout J., The VizieR database of astronomical catalogues, A&AS, 2000, vol. 143, p. 23

Okazaki A. T., On the confinement of one-armed oscillations in discs of Be stars., A&A, 1997, vol. 318, p. 548

Okazaki A. T., Viscous Transonic Decretion in Disks of Be Stars, pasj, 2001, vol. 53, p. 119

Okazaki A. T., Bate M. R., Ogilvie G. I., Pringle J. E., Evolution of truncated decretion disks in Be/X-Ray binaries. In The Physics of Cataclysmic Variables and Related Objects , vol. 261 of Astronomical Society of the Pacific Conference Series, 2002, p. 519

Oudmaijer R. D., Parr A. M., The binary fraction and mass ratio of Be and B stars: a comparative Very Large Telescope/NACO study, MNRAS, 2010, vol. 405, p. 2439

Owocki S., Formation and Evolution of Disks around Classical Be Stars. In Stars with the B[e] Phenomenon , vol. 355 of Astronomical Society of the Pacific Conference Series, 2006, p. 219

Panoglou D., Carciofi A. C., Vieira R. G., Cyr I. H., Jones C. E., Okazaki A. T., Rivinius T., Be discs in binary systems - I. Coplanar orbits, MNRAS, 2016, vol. 461, p. 2616

Panoglou D., Faes D. M., Carciofi A. C., Okazaki A. T., Baade D., Rivinius T., Borges Fernandes M., Be discs in coplanar circular binaries: Phase-locked variations of emission lines, MNRAS, 2018, vol. 473, p. 3039

Peters G. J., Gies D. R., Grundstrom E. D., McSwain M. V., Detection of a Hot Subdwarf Companion to the Be Star FY Canis Majoris, ApJ, 2008, vol. 686, p. 1280

Peters G. J., Pewett T. D., Gies D. R., Touhami Y. N., Grundstrom E. D., Far-ultraviolet Detection of the Suspected Subdwarf Companion to the Be Star 59 Cygni, ApJ, 2013, vol. 765, p. 2

Peters G. J., Wang L., Gies D. R., Grundstrom E. D., The Hot Companion and Circumbinary Disk of the Be Star HR 2142, ApJ, 2016, vol. 828, p. 47

Pollmann E., Period analysis of the Halpha line profile variation of the Be binary star pi Aqr, Information Bulletin on Variable Stars, 2012, vol. 6023, p. 1

Porter J. M., On the rotational velocities of Be and Be-shell stars, MNRAS, 1996, vol. 280, p. L31

Porter J. M., On outflowing viscous disc models for Be stars, aap, 1999, vol. 348, p. 512

Porter J. M., Rivinius T., Classical Be Stars, pasp, 2003, vol. 115, p. 1153

Pringle J. E., Accretion discs in astrophysics, araa, 1981, vol. 19, p. 137

Quirrenbach A., Bjorkman K. S., Bjorkman J. E., Hummel C. A., Buscher D. F., Armstrong J. T., Mozurkewich D., Elias II N. M., Babler B. L., Constraints on the Geometry of Circumstellar Envelopes: Optical Interferometric and Spectropolarimetric Observations of Seven Be Stars, apj, 1997, vol. 479, p. 477

Rauw G., Naze Y., Marique P. X., De Becker M., Sana H., Vreux J.-M., Long-term Spectroscopic Variability of Two Oe Stars, Information Bulletin on Variable Stars, 2007, vol. 5773

Reimann J. D., Frequency Estimation Using Unequally-Spaced Astronomical Data., UNIVERSITY OF CALIFORNIA, BERKELEY., 1994, Ph.D. Thesis

Rímulo L. R., Carciofi A. C., Vieira R. G., Rivinius T., Faes D. M., Figueiredo A. L., Bjorkman J. E., Georgy C., Ghoreyshi M. R., Soszyński I., The life cycles of Be viscous decretion discs: fundamental disc parameters of 54 SMC Be stars, MNRAS, 2018, vol. 476, p. 3555

Rivinius T., Baade D., Stefl S., Stahl O., Wolf B., Kaufer A., Stellar and circumstellar activity of the Be star MU Centauri. II. Multiperiodic low-order line-profile variability, A&A, 1998, vol. 336, p. 177

Rivinius T., Carciofi A. C., Martayan C., Classical Be stars. Rapidly rotating B stars with viscous Keplerian decretion disks, aapr, 2013, vol. 21, p. 69

Rivinius T., Štefl S., Baade D., Central quasi-emission peaks in shell spectra and the rotation of disks of Be stars, A&A, 1999, vol. 348, p. 831

Roche E., Recherches sur les atmospheres des cometes, Annales de l'Observatoire de Paris, 1859, vol. 5, p. 353

Royer F., Grenier S., Baylac M.-O., Gómez A. E., Zorec J., Rotational velocities of A-type stars in the northern hemisphere. II. Measurement of v sin i, A&A, 2002, vol. 393, p. 897

Royer F., Zorec J., Gómez A. E., Rotational velocities of A-type stars. III. Velocity distributions, A&A, 2007, vol. 463, p. 671

Ruždjak D., Božić H., Harmanec P., Fiřt R., Chadima P., Bjorkman K., Gies D. R., Kaye A. B., Koubský P., McDavid D., Richardson N., Sudar D., Šlechta M., Wolf M., Yang S., Properties and nature of Be stars. 26. Long-term and orbital changes of ζ Tauri, A&A, 2009, vol. 506, p. 1319

Sabogal B. E., Ubaque K. Y., García-Varela A., Álvarez M., Salas L., Evidence of Dissipation of Circumstellar Disks from L-band Spectra of Bright Galactic Be Stars, PASP, 2017, vol. 129, p. 014203

Sana H., de Mink S. E., de Koter A., Langer N., Evans C. J., Gieles M., Gosset E., Izzard R. G., Le Bouquin J.-B., Schneider F. R. N., Binary Interaction Dominates the Evolution of Massive Stars, Science, 2012, vol. 337, p. 444

Sana H., Le Bouquin J.-B., Lacour S., Berger J.-P., Duvert G., Gauchet L., Norris B., Olofsson J., Pickel D., Zins G., Absil O., de Koter A., Kratter K., Schnurr O., Zinnecker H., Southern Massive Stars at High Angular Resolution: Observational Campaign and Companion Detection, ApJS, 2014, vol. 215, p. 15

Schaller G., Schaerer D., Meynet G., Maeder A., New grids of stellar models from 0.8 to 120 M_solar at Z=0.020 and Z=0.001, Astronomy and Astrophysics Supplement Series, 1992, vol. 96, p. 269

Schmidt-Kaler T., , 1982 4.1.2 Intrinsic colors and visual absolute magnitudes (calibration of the MK system): Datasheet from Landolt-Börnstein - Group VI Astronomy and Astrophysics · Volume 2B: “Stars and Star Clusters” in SpringerMaterials, publisher=”Springer-Verlag Berlin Heidelberg

Schultz G. V., Wiemer W., Interstellar reddening and IR-excesses of O and B stars., A&A, 1975, vol. 43, p. 133

Secchi A., Schreiben des Herrn Prof. Secchi, Directors der Sternwarte des Collegio Romano, an den Herausgeber, Astronomische Nachrichten, 1866, vol. 68, p. 63

Serenelli A., Johnson J., Huber D., Pinsonneault M., Ball W. H., Tayar J., The First APOKASC Catalog of Kepler Dwarf and Subgiant Stars, The Astrophysical Journal Supplement Series, 2017, vol. 233, p. 23

Serkowski K., Intrinsic Polarization of Early-Type Stars with Extended Atmospheres, ApJ, 1970, vol. 160, p. 1083

Shajn G., Struve O., On the rotation of the stars, MNRAS, 1929, vol. 89, p. 222

Shokry A., Rivinius T., Mehner A., Martayan C., Hummel W., Townsend R. H. D., Mérand A., Mota B., Faes D. M., Hamdy M. A., Beheary M. M., Gadallah K. A. K., Abo-Elazm M. S., Stellar parameters of Be stars observed with X-shooter, A&A, 2018, vol. 609, p. A108

Sigut T. A. A., Tycner C., Jansen B., Zavala R. T., The Circumstellar Disk of the Be Star o Aquarii as Constrained by Simultaneous Spectroscopy and Optical Interferometry, ApJ, 2015, vol. 814, p. 159

Silaj J., Jones C. E., Carciofi A. C., Escolano C., Tycner C., Probing the Density Structure of 48 Librae's Circumstellar Disk. In Bright Emissaries: Be Stars as Messengers of Star-Disk Physics , vol. 506 of Astronomical Society of the Pacific Conference Series, 2016, p. 287

Silaj J., Jones C. E., Sigut T. A. A., Tycner C., The Hα Profiles of Be Shell Stars, ApJ, 2014, vol. 795, p. 82

Simón-Díaz S., Herrero A., The IACOB project. I. Rotational velocities in northern Galactic O- and early B-type stars revisited. The impact of other sources of line-broadening, A&A, 2014, vol. 562, p. A135

Slettebak A., The Be stars, pasp, 1988, vol. 100, p. 770

Smith K. C., Chemically Peculiar Hot Stars, Ap&SS, 1996, vol. 237, p. 77

Stecher T. P., UIT Science Team The Ultraviolet Imaging Telescope: Past and Future Results from the Astro-1 and Astro-2 Missions. In American Astronomical Society Meeting Abstracts #184 , vol. 184 of American Astronomical Society Meeting Abstracts, 1994, p. 26.03

Stellingwerf R. F., Period determination using phase dispersion minimization, ApJ, 1978, vol. 224, p. 953

Sterken C., Vogt N., Mennickent R. E., Long-term photometry of Be stars. II. Periodic variations on time scales of days to months., A&A, 1996, vol. 311, p. 579

Struve O., On the Origin of Bright Lines in Spectra of Stars of Class B, apj, 1931, vol. 73, p. 94

Touhami Y., Gies D. R., Schaefer G. H., Richardson N. D., McAlister H. A., Ridgway S. T., Brummelaar T. A. t., Goldfinger P. J., Sturmann L., Sturmann J., Turner N. H., Farrington C. D., A CHARA Array Long Baseline Interferometric Survey of Circumstellar Disks of Be

Stars. In Resolving The Future Of Astronomy With Long-Baseline Interferometry , vol. 487 of Astronomical Society of the Pacific Conference Series, 2014, p. 395

Townsend R. H. D., Owocki S. P., Howarth I. D., Be-star rotation: how close to critical?, mnras, 2004, vol. 350, p. 189

Tycner C., Gilbreath G. C., Zavala R. T., Armstrong J. T., Benson J. A., Hajian A. R., Hutter D. J., Jones C. E., Pauls T. A., White N. M., Constraining Disk Parameters of Be Stars using Narrowband Hα Interferometry with the Navy Prototype Optical Interferometer, AJ, 2006, vol. 131, p. 2710

Tycner C., Jones C. E., Sigut T. A. A., Schmitt H. R., Benson J. A., Hutter D. J., Zavala R. T., Constraining the Physical Parameters of the Circumstellar Disk of χ Ophiuchi, apj, 2008, vol. 689, p. 461

Tycner C., Lester J. B., Hajian A. R., Armstrong J. T., Benson J. A., Gilbreath G. C., Hutter D. J., Pauls T. A., White N. M., Properties of the Hα-emitting Circumstellar Regions of Be Stars, ApJ, 2005, vol. 624, p. 359

Uesugi A., Fukuda I., Catalogue of rotational velocities of the stars, 1970

Underhill A., Doazan V., B Stars with and without emission lines, parts 1 and 2, 1982

Vacca W. D., Garmany C. D., Shull J. M., The Lyman-Continuum Fluxes and Stellar Parameters of O and Early B-Type Stars, ApJ, 1996, vol. 460, p. 914

van Belle G. T., Interferometric observations of rapidly rotating stars, A&A Rev., 2012, vol. 20, p. 51

van Leeuwen F., Validation of the new Hipparcos reduction, A&A, 2007, vol. 474, p. 653

Vanbeveren D., Mennekens N., Evolution of Intermediate Mass and Massive Binary Stars: Physics, Mass Loss, and Rotation. In The B[e] Phenomenon: Forty Years of Studies , vol. 508 of Astronomical Society of the Pacific Conference Series, 2017, p. 121

VanderPlas J. T., Understanding the Lomb-Scargle Periodogram, ArXiv e-prints, 2017

VanderPlas J. T., Ivezić Ž., Periodograms for Multiband Astronomical Time Series, ApJ, 2015, vol. 812, p. 18

Vega E. I., Rabolli M., Feinstein A., Muzzio J. C., A search for H-alpha-emission objects in a region in ARA, AJ, 1980, vol. 85, p. 1207

Vieira R. G., Carciofi A. C., The viscous disk properties of 80 Be stars, ArXiv e-prints, 2017

Vieira R. G., Carciofi A. C., Bjorkman J. E., The pseudo-photosphere model for the continuum emission of gaseous discs, MNRAS, 2015, vol. 454, p. 2107

Vieira R. G., Carciofi A. C., Bjorkman J. E., Rivinius T., Baade D., Rímulo L. R., The life cycles of Be viscous decretion discs: time-dependent modelling of infrared continuum observations, MNRAS, 2017, vol. 464, p. 3071

Vinicius M.-M. F., Townsend R. H. D., Leister N. V., Determination of Be-star Inclinations from Gravity-Darkened Photospheric Spectra. In Active OB-Stars: Laboratories for Stellare and Circumstellar Physics , vol. 361 of Astronomical Society of the Pacific Conference Series, 2007, p. 518

von Zeipel H., The radiative equilibrium of a slightly oblate rotating star, MNRAS, 1924, vol. 84, p. 684

Štefl S., Rivinius T., Carciofi A. C., Le Bouquin J. B., Baade D., Bjorkman K. S., Hesselbach E., Hummel C. A., Okazaki A. T., Pollmann E., Rantakyrö F., Wisniewski J. P., Cyclic variability of the circumstellar disk of the Be star ζ Tauri. I. Long-term monitoring observations, A&A, 2009, vol. 504, p. 929

Wade G. A. N. C. A. E. G. J. H. P. V. B. B. d. B. D. A. C. D. H. H. H. F. K. O. s. J. D. M. N. M. F. M. S. O. M. E. O. S. P. R. T. S. M. E. S. J. O.,

Wall J. V., Jenkins C. R., Practical Statistics for Astronomers, 2012

Wang L., Gies D. R., Peters G. J., Detection of Additional Be+sdO Systems from IUE Spectroscopy, ApJ, 2018, vol. 853, p. 156

Waters L. B. F. M., Boland W., Taylor A. R., van de Stadt H., Lamers H. J. G. L. M., Millimeter observations of the Be stars Psi Persei and Gamma Cassiopeiae, A&A, 1989, vol. 213, p. L19

Wegner W., The total-to-selective extinction ratio determined from near IR photometry of OB stars, Astronomische Nachrichten, 2003, vol. 324, p. 219

Wheelwright H. E., Bjorkman J. E., Oudmaijer R. D., Carciofi A. C., Bjorkman K. S., Porter J. M., Probing the properties of Be star discs with spectroastrometry and NLTE radiative transfer modelling: β CMi, mnras, 2012, vol. 423, p. L11

Wisniewski J. P., Bjorkman K. S., The Role of Evolutionary Age and Metallicity in the Formation of Classical Be Circumstellar Disks. I. New Candidate Be Stars in the LMC, SMC, and Milky Way, ApJ, 2006, vol. 652, p. 458

Wood K., Bjorkman K. S., Bjorkman J. E., Deriving the Geometry of Be Star Circumstellar Envelopes from Continuum Spectropolarimetry. I. The Case of ζ Tauri, apj, 1997, vol. 477, p. 926

Yoon J., Peterson D. M., Kurucz R. L., Zagarello R. J., A New View of Vega's Composition, Mass, and Age, ApJ, 2010, vol. 708, p. 71

Yudin R. V., Statistical analysis of intrinsic polarization, IR excess and projected rotational velocity distributions of classical Be stars, A&A, 2001, vol. 368, p. 912

Yudin R. V., Statistical Analysis of Intrinsic Polarization Distributions of Classical Be Stars. In Astronomical Polarimetry: Current Status and Future Directions , vol. 343 of Astronomical Society of the Pacific Conference Series, 2005, p. 384

Zagury F., The 2200Å bump and the interstellar extinction curve, Astronomische Nachrichten, 2013, vol. 334, p. 1107

Zinnecker H., Yorke H. W., Toward Understanding Massive Star Formation, ARA&A, 2007, vol. 45, p. 481

Zorec J., Briot D., Absolute magnitudes of B emission line stars : correlation between the luminosity excess and the effective temperature., A&A, 1991, vol. 245, p. 150

Zorec J., Briot D., Critical study of the frequency of Be stars taking into account their outstanding characteristics., A&A, 1997, vol. 318, p. 443

Zorec J., Cidale L., Arias M. L., Frémat Y., Muratore M. F., Torres A. F., Martayan C., Fundamental parameters of B supergiants from the BCD system. I. Calibration of the (λ_1, D) parameters into T_{eff}, A&A, 2009, vol. 501, p. 297

Zorec J., Frémat Y., Cidale L., On the evolutionary status of Be stars. I. Field Be stars near the Sun, A&A, 2005, vol. 441, p. 235

Zorec J., Frémat Y., Domiciano de Souza A., Royer F., Cidale L., Hubert A.-M., Semaan T., Martayan C., Cochetti Y. R., Arias M. L., Aidelman Y., Stee P., Critical study of the distribution of rotational velocities of Be stars. I. Deconvolution methods, effects due to gravity darkening, macroturbulence, and binarity, A&A, 2016, vol. 595, p. A132

Zorec J., Frémat Y., Martayan C., Cidale L. S., Torres A. F., Rotation in the ZAMS: Be and Bn stars. In Active OB-Stars: Laboratories for Stellare and Circumstellar Physics , vol. 361 of Astronomical Society of the Pacific Conference Series, 2007, p. 539

Appendix

Appendix A

Additional Tables

A.1 Binary Be Stars

Table A.1 - : Some Be stars known as binaries.

Star	ST	Period	Ref.
FY CMa	B0.5IVe	-	Peters et al., 2008
γ Cas	B0.5IVpe	203.5 days	Henry and Smith, 2012
o Pup	B1IVe	29	Koubský et al., 2012
ζ Tau	B1IVe_shell	133 days	Ruždjak et al., 2009
η Tau	B7III	4.2 days	Jarad et al., 1989
59 Cyg	B1.5Vnne	29 days	Peters et al., 2013
κ CMa	B1.5Ve	~ years	Meilland et al., 2012
δ Cen	B2Vne	~ years	Meilland et al., 2012
μ Cen	B2Vnpe	-	Meilland et al., 2012
α Ara	B2Vne	74 days	Chesneau et al., 2005
HD 81654	B2/3V(e)	-	Labadie-Bartz et al., 2017
HR 2142	B3/5Vnne	~ 81 days	Peters et al., 2016
p Car	B4Vne	-	Meilland et al., 2012
ψ Per	B5Ve	-	Waters et al., 1989
κ Dra	B6IIIe	61.55 days	Gies et al., 2007
Achernar	B6Vpe	15 years	Kervella et al., 2008
o Aqr	B7IVe	-	Meilland et al., 2012
o And	B6III	33.1 days	Harmanec et al., 1987
ω Car	B8IIIe	-	Meilland et al., 2012

α Col	B9Ve	-	Meilland et al., 2012
δ Sco	B0.3IV	10.8 years	Miroshnichenko et al., 2013
17 Tau	B6III	4.3 days	Jarad et al., 1989
β Mon A	B3V	-	Hartkopf et al., 2012
π Aqr	B1III-IVe	$\sim$ 80 days	Pollmann, 2012
66 Oph	B2Ve	-	Mason et al., 2001
θ Circ	B2IV/V	-	Mason et al., 1997
ϕ Per	B1.5Ve-shell	127 days	Gies et al., 1998
28 Tau	B8Vne	218 days	Katahira et al., 1996
4 Her	B9pe	46 days	Bhat et al., 2016
88 Her	B6IIInp_sh	87 days	Bhat et al., 2016
ϵ Cap	B3V	95 days	Rivinius et al., 1999
β CMi	B3V	170.4 days	Dulaney et al., 2017

A.2 Field Stars used to infer the interstellar polarization

Table A.2 - Field stars used to infer the interstellar polarization in the region of α Arae.

Field Star	$P_{\max}$ [%]	$\lambda_{\max}$ [μm]	$< \theta >$ [º]	N
HIP 84956	$0.018^{+0.005}_{-0.005}$	$0.80^{+0.15}_{-0.46}$	64 ± 34	4
HIP 85241	$0.029^{+0.005}_{-0.004}$	$0.44^{+0.20}_{-0.16}$	97.5 ± 6.5	4
HIP 85610	$0.018^{+0.006}_{-0.005}$	$0.34^{+0.27}_{-0.18}$	105 ± 24	4
HIP 86248	$0.040^{+0.005}_{-0.005}$	$0.59^{+0.14}_{-0.14}$	94.5 ± 5.2	4
HIP 86247	$0.056^{+0.004}_{-0.004}$	$0.981^{+0.014}_{-0.030}$	93.0 ± 7.1	4
HIP 86247 (B)	$0.036^{+0.007}_{-0.006}$	$0.58^{+0.24}_{-0.24}$	109.6 ± 7.3	4
HIP 86516	$0.034^{+0.004}_{-0.004}$	$0.54^{+0.15}_{-0.16}$	104.2 ± 4.8	4

A.3 Photometric data of α Arae

Table A.3 - : Photometric dataset.

Filter	λ (Å)	F (erg/s/cm^2/Å)	σF (erg/s/cm^2/Å)	Source (Mission/Instrument)	Obs.Date (VO) (Gregorian)
Generic/Stromgren.u	3447.5	1.63×10^{-10}	-	Paunzen 2015	-
Generic/Johnson.U	3570.7	5.50×10^{-10}	1.54×10^{-11}	UBV, Mermilliod 1991	-
Generic/Stromgren.v	4110.4	4.82×10^{-10}	-	Paunzen 2015	-
TYCHO/TYCHO.B	4280.0	5.63×10^{-10}	7.26×10^{-12}	Tycho	-
Generic/Johnson.B	4378.1	4.91×10^{-10}	1.07×10^{-11}	UBV, Mermilliod 1991	-
Generic/Stromgren.b	4663.3	3.85×10^{-10}	-	Paunzen 2015	-
TYCHO/TYCHO.V	5340.0	3.04×10^{-10}	2.52×10^{-12}	Tycho	-
Generic/Johnson.V	5466.1	2.38×10^{-10}	4.61×10^{-12}	UBV, Mermilliod 1991	-
Generic/Stromgren.y	5472.4	2.28×10^{-10}	-	Paunzen 2015	-
2MASS/2MASS.J	12350.0	2.61×10^{-11}	6.33×10^{-12}	2MASS	2000-08-04
2MASS/2MASS.H	16620.0	1.05×10^{-11}	2.22×10^{-12}	2MASS	2000-08-04
2MASS/2MASS.Ks	21590.0	4.34×10^{-12}	8.78×10^{-13}	2MASS	2000-08-04
IRAS/IRAS.12mu	101464.6	3.70×10^{-14}	1.48×10^{-15}	IRAS	-
WISE/WISE.W3	115608.0	2.38×10^{-14}	8.33×10^{-16}	WISE	-
AKARI/IRC.L18W	176094.9	5.69×10^{-15}	2.85×10^{-16}	AKARI/IRC	-
IRAS/IRAS.25mu	217265.5	3.89×10^{-15}	2.34×10^{-16}	IRAS	-
WISE/WISE.W4	220883.0	3.46×10^{-15}	3.82×10^{-17}	WISE	-
IRAS/IRAS.60mu	519887.3	2.24×10^{-16}	2.02×10^{-17}	IRAS	-
AKARI/FIS.N60	629506.7	2.26×10^{-16}	2.13×10^{-17}	AKARI/FIS	-
AKARI/FIS.WIDE-S	769035.2	7.54×10^{-17}	2.44×10^{-18}	AKARI/FIS	-
SDSS	7634.9	9.41×10^{-11}	-	SDSS	-
SDSS	6247.0	1.84×10^{-10}	-	SDSS	-
SDSS	4820.0	4.21×10^{-10}	-	SDSS	-
SDSS	9017.9	5.42×10^{-11}	-	SDSS	-
SDSS	3519.0	6.75×10^{-10}	-	SDSS	-
HIP	4020.0	5.34×10^{-10}	-	HIP	-
HIP	5319.0	3.04×10^{-10}	-	HIP	-
HIP	4203.0	5.72×10^{-10}	-	HIP	-
APEX	8695652.2	1.45×10^{-20}	2.86×10^{-21}	APEX	-

TD	1565.00	3.40×10^{-09}	1.80×10^{-11}	TD	-
TD1	2365.0	1.56×10^{-09}	1.90×10^{-12}	TD1	-
Clark et al., 1998	3.5×10^{9}	$<1.47 \times 10^{-28}$	-	ATCA	-
Clark et al., 1998	6.3×10^{9}	$<9.07 \times 10^{-29}$	-	ATCA	-

A.4 α Arae polarimetric data

Table A.4 - : Polarimetric data from OPD (54260 < MJD < 57624) and historical data published by Serkowski, 1970 and McLean, 1979 (40085 < MJD < 42877).

MJD	Filter	$P_{obs}[\%]$	PA_{Pobs}	$\sigma_P[\%]$	σ_{PA}	MJD	Filter	$P_{obs}[\%]$	PA_{Pobs}	$\sigma_P[\%]$	σ_{PA}
54260.19	b	0.2614	145.96	0.0077	0.84	56816.22	r	0.4904	140.33	0.0171	1
54260.22	v	0.2635	142.97	0.0062	0.67	56816.22	i	0.4713	140.79	0.0038	0.23
54289.14	b	0.1488	142.38	0.0471	9.07	56817.28	b	0.5356	151.07	0.0185	0.99
54720.97	b	0.5985	145.72	0.0336	1.61	56840.24	b	0.5068	146.03	0.0205	1.16
55012.18	b	0.6397	141.52	0.0132	0.59	56840.25	v	0.5205	143.5	0.0259	1.43
55012.20	r	0.5082	142.01	0.0099	0.56	56840.26	r	0.4763	142.3	0.005	0.3
55334.30	b	0.5926	139.73	0.0244	1.18	56840.27	i	0.4789	142.36	0.0018	0.11
55334.30	v	0.6137	139.5	0.0169	0.79	56841.08	b	0.502	141.68	0.014	0.8
55334.31	r	0.5769	142.35	0.013	0.65	56841.09	v	0.5495	140.51	0.0128	0.67
55334.32	i	0.4705	143.34	0.0336	2.05	56841.09	r	0.4921	137.55	0.007	0.41
55355.21	b	0.6748	142.41	0.0089	0.38	56841.10	i	0.4706	138.22	0.0091	0.55
55355.22	v	0.5887	143.51	0.0115	0.56	56889.11	b	0.4968	143.72	0.0159	0.92
55355.23	r	0.4996	140.62	0.0151	0.87	56889.14	v	0.5416	142.39	0.0246	1.3
55355.24	i	0.4988	140.13	0.0224	1.29	56889.16	r	0.4969	142.78	0.0088	0.51
55426.03	b	0.6209	143.49	0.0145	0.67	56890.16	i	0.4177	146.24	0.0387	2.65
55426.04	v	0.605	139.49	0.0155	0.73	57142.24	b	0.4982	141.9	0.0096	0.55
55426.06	r	0.5304	144.62	0.0137	0.74	57142.25	v	0.473	141.27	0.0092	0.56
55426.07	i	0.4945	142.45	0.0158	0.92	57142.25	r	0.4472	141.44	0.0073	0.47
55441.00	i	0.4888	141.58	0.0125	0.73	57142.25	i	0.4568	141.31	0.0049	0.31
55441.01	r	0.5261	142.62	0.0097	0.53	57201.20	r	0.4648	140.14	0.0085	0.52
55441.02	v	0.5697	144.47	0.0086	0.43	57201.21	v	0.5096	136.28	0.0099	0.56
55441.02	b	0.6461	143.28	0.0134	0.59	57201.21	b	0.4979	141	0.0162	0.93
55496.90	v	0.5791	142.2	0.0076	0.38	57201.22	i	0.4421	138.45	0.0052	0.34
55496.91	r	0.5278	141.02	0.0065	0.35	57263.05	i	0.4512	140.66	0.0077	0.49
55496.91	i	0.4792	141.75	0.0089	0.53	57263.06	r	0.4983	138.96	0.0074	0.43
55496.92	b	0.5974	143.3	0.0126	0.6	57263.06	v	0.5202	141.18	0.0052	0.29
55497.94	v	0.6139	142.54	0.0065	0.3	57263.07	b	0.5218	143.01	0.0096	0.53
55497.94	r	0.5379	141.78	0.0085	0.45	57286.92	v	0.48	140.51	0.0205	1.22
55497.95	i	0.4956	141.92	0.0071	0.41	57286.93	b	0.5185	140.85	0.0141	0.78

55497.96	b	0.6107	143.62	0.0051	0.24	57286.94	r	0.4425	141.66	0.0151	0.98
55498.90	v	0.6	143.64	0.0069	0.33	57286.95	i	0.3993	140.84	0.0089	0.64
55498.91	r	0.5354	136.84	0.007	0.37	57553.15	r	0.4706	144.61	0.0128	0.78
55498.91	i	0.4843	138.15	0.005	0.3	57553.15	i	0.476	142.43	0.0118	0.71
55498.92	b	0.6035	144.63	0.0107	0.51	57553.15	v	0.5045	138.79	0.0121	0.69
55741.24	v	0.3671	142.82	0.0139	1.08	57553.16	b	0.5175	141.71	0.0069	0.38
55741.25	r	0.306	142.76	0.0135	1.26	57555.28	v	0.4745	143.13	0.0121	0.73
55741.26	i	0.3077	144.3	0.0082	0.76	57555.29	r	0.465	141.78	0.0098	0.6
55741.26	b	0.3833	144.48	0.0255	1.91	57555.30	b	0.4907	143.75	0.0094	0.55
55755.23	b	0.2728	145.52	0.0056	0.59	57577.16	i	0.4672	140.99	0.0169	1.04
55755.24	v	0.3686	140.05	0.0176	1.37	57577.16	r	0.4874	141.25	0.0095	0.56
55755.24	r	0.349	141.7	0.0068	0.56	57577.17	v	0.5182	139.7	0.012	0.66
55755.25	i	0.3719	141.11	0.0222	1.71	57577.18	b	0.5222	139.79	0.0088	0.48
55807.12	b	0.6035	139.33	0.0179	0.85	57604.05	i	0.421	143.39	0.0113	0.77
55807.13	v	0.5649	139.73	0.0076	0.39	57604.05	r	0.4714	144.11	0.0147	0.89
55807.13	r	0.4918	138.42	0.0035	0.2	57604.06	v	0.5159	145.22	0.0101	0.56
55807.14	i	0.4266	140.78	0.006	0.4	57604.06	b	0.5687	148.49	0.017	0.86
55832.00	b	0.6202	142.68	0.0052	0.24	57614.10	v	0.506	142.63	0.0162	0.92
55832.01	v	0.5487	140.67	0.0171	0.89	57614.10	r	0.506	142.09	0.0049	0.28
55832.02	r	0.4925	140.93	0.0043	0.25	57614.11	i	0.4695	142.14	0.0089	0.54
55832.03	i	0.4367	140.85	0.0039	0.26	57614.12	b	0.4938	143.66	0.0373	2.16
56052.30	b	0.6485	142.77	0.0081	0.36	57623.98	i	0.4854	141.99	0.0165	0.97
56052.30	v	0.6414	139.76	0.0098	0.44	57623.99	r	0.4682	143.07	0.0095	0.58
56052.31	r	0.5429	138.92	0.013	0.69	57623.99	v	0.5095	142.93	0.0195	1.1
56052.32	i	0.5243	138.6	0.012	0.66	57624.00	b	0.5098	144.36	0.0073	0.41
56052.32	u	0.4054	147.81	0.0227	1.6	40085	u	0.3076	-	-	-
56108.21	u	0.4842	150.99	0.0391	2.31	40100	u	0.2886	-	-	-
56108.22	b	0.626	144.84	0.03	1.37	40297	u	0.2984	-	-	-
56108.23	v	0.5897	138.99	0.024	1.17	40344	u	0.3370	-	-	-
56108.24	r	0.6127	141.57	0.0085	0.4	40349	u	0.3505	-	-	-
56108.25	i	0.5365	139.15	0.0044	0.23	40390	u	0.3520	-	-	-
56132.00	v	0.6198	142.38	0.0118	0.55	40437	u	0.3281	-	-	-
56132.01	r	0.5202	142.04	0.0364	2	40453	u	0.3581	-	-	-
56132.01	i	0.4882	145.57	0.0179	1.05	40623	u	0.2993	-	-	-

56132.02	b	0.625	142.82	0.0127	0.58	40637	u	0.3378	-	-	-
56132.03	u	0.4664	150.11	0.0171	1.05	40085.23	v	0.5578	-	-	-
56380.32	b	0.5652	139.54	0.018	0.91	40100	v	0.5814	-	-	-
56380.34	v	0.5617	139.56	0.0055	0.28	40296.92	v	0.5799	-	-	-
56380.35	r	0.5159	140.07	0.0061	0.34	40343.69	v	0.5969	-	-	-
56380.35	i	0.4945	139.36	0.0069	0.4	40348.61	v	0.6124	-	-	-
56406.24	b	0.5301	144.86	0.0118	0.64	40390.46	v	0.6296	-	-	-
56406.24	v	0.5272	141.15	0.0312	1.7	40437.23	v	0.5660	-	-	-
56406.25	r	0.4936	142.62	0.0218	1.27	40453.23	v	0.6407	-	-	-
56406.26	i	0.4857	140.35	0.0045	0.27	40623.07	v	0.5869	-	-	-
56503.13	b	0.5306	145.55	0.0138	0.75	40636.61	v	0.6799	-	-	-
56503.14	v	0.5209	141.49	0.0075	0.41	42877	v	0.5445	-	-	-
56503.15	r	0.4797	142.15	0.0122	0.73	40082.76	b	0.6644	-	-	-
56503.17	i	0.4515	139.16	0.0181	1.15	40098.76	b	0.6776	-	-	-
56517.07	b	0.5144	142	0.0141	0.79	40299.38	b	0.6907	-	-	-
56517.08	v	0.5235	141.99	0.0071	0.39	40344.92	b	0.6578	-	-	-
56517.08	r	0.4932	142.75	0.0098	0.57	40348.61	b	0.6842	-	-	-
56517.09	i	0.4587	142.41	0.0123	0.77	40389.23	b	0.6710	-	-	-
56714.33	v	0.5623	141.34	0.0197	1	40401.53	b	0.6644	-	-	-
56714.33	b	0.5562	140.27	0.0204	1.05	40452	b	0.6447	-	-	-
56714.33	i	0.4924	144.4	0.0112	0.65	40624.30	b	0.6381	-	-	-
56816.19	b	0.5916	144.31	0.0252	1.22	42877	b	0.6842	-	-	-
56816.21	v	0.506	140.52	0.009	0.51						

A.5 α Arae spectroscopic data

Table A.5 - : Spectroscopic data from several sources ($43332.72 \leq MJD \leq 58008$.

Instrument	MJD	Instrument	MJD	Instrument	MJD
HEROS	43332.72	FEROS	52003.35	OPD	53537.31
HEROS	43810.52	FEROS	52003.36	OPD	53537.31
HEROS	43814.52	FEROS	52004.27	OPD	53537.31
HEROS	45027.91	FEROS	52004.27	OPD	54562.10
HEROS	45211.00	FEROS	52004.28	OPD	54651.22
HEROS	45221.56	FEROS	52004.28	OPD	54658.14
HEROS	45398.88	FEROS	52004.28	OPD	54658.14
HEROS	46124.00	FEROS	52004.29	OPD	54658.14
HEROS	46835.00	FEROS	52004.29	OPD	54658.14
HEROS	47795.00	FEROS	52004.29	OPD	55694.00
HEROS	48705.00	FEROS	52004.30	OPD	55854.00
HEROS	49239.00	FEROS	52004.30	Hanuschik et al., 1996	56147.11
HEROS	51281.00	FEROS	52004.30	Hanuschik et al., 1996	56561.50
HEROS	51300.36	FEROS	52004.31	Hanuschik et al., 1996	56714.30
HEROS	51304.40	FEROS	52004.31	Hanuschik et al., 1996	56755.25
HEROS	51305.43	FEROS	52004.31	Hanuschik et al., 1996	56854.12
HEROS	51306.39	FEROS	52004.31	Hanuschik et al., 1996	56943.96
HEROS	51307.39	FEROS	52004.32	Dachs et al., 1981	57266.02
HEROS	51308.40	FEROS	52004.32	Dachs et al., 1981	57553.18
HEROS	51309.35	FEROS	52004.32	Dachs et al., 1981	57581.08
HEROS	51310.43	FEROS	52004.33	Dachs et al., 1981	57612.04
HEROS	51311.40	FEROS	52004.33	Dachs et al., 1981	57954.53
HEROS	51312.44	FEROS	52127.10	Dachs et al., 1981	57973.05
HEROS	51313.40	FEROS	52127.11	FEROS	51366.37
HEROS	51314.42	FEROS	52127.11	FEROS	51367.37
HEROS	51316.42	FEROS	52127.11	FEROS	51369.35
HEROS	51319.42	FEROS	52127.12	FEROS	51648.21
HEROS	51320.43	FEROS	52127.12	FEROS	51648.25

HEROS	51321.40	FEROS	52127.13	FEROS	51648.26
HEROS	51327.36	FEROS	52127.13	FEROS	51648.33
HEROS	51329.42	FEROS	52127.13	FEROS	52002.21
HEROS	51330.40	FEROS	52127.14	FEROS	52002.22
HEROS	51331.43	FEROS	52127.14	FEROS	52002.23
HEROS	51332.41	FEROS	52127.14	FEROS	52002.24
HEROS	51333.32	FEROS	52127.15	FEROS	52002.25
HEROS	51334.44	FEROS	52127.15	FEROS	52002.26
HEROS	51335.34	FEROS	52127.15	FEROS	52002.27
HEROS	51336.34	FEROS	52127.16	FEROS	52002.28
HEROS	51338.35	FEROS	52127.16	FEROS	52002.29
HEROS	51339.41	FEROS	52127.17	FEROS	52002.30
HEROS	51340.41	FEROS	52127.17	FEROS	52002.31
HEROS	51341.39	FEROS	52127.17	FEROS	52002.32
HEROS	51343.42	FEROS	52127.18	FEROS	52003.32
BESS	51347.36	FEROS	52127.18	FEROS	52003.32
BESS	51349.32	FEROS	52127.18	FEROS	52003.33
UVES	51350.38	FEROS	52127.19	FEROS	52003.34
FEROS	51352.38	FEROS	52127.19	FEROS	52003.34
FEROS	51353.33	HARPS	52127.20	FEROS	52003.34
FEROS	51354.39	HARPS	52127.20	FEROS	52003.35
FEROS	51355.39	HARPS	52127.21	Banerjee et al., 2000	58008.08
FEROS	51360.36	OPD	52127.21	Banerjee et al., 2000	58008.08
FEROS	51363.38	OPD	52127.21	BESS	55443.41
FEROS	51364.36	OPD	52127.22	BESS	54562.62
FEROS	52003.35	OPD	52776.25	BESS	56168.06

A.6 β CMi polarimetric data

Table A.6 - : Polarimetric data from OPD-LNA taken with the IAGPOL polarimeter.

MJD	Filter	$P_{\rm obs}[\%]$	$PA_{\rm Pobs}$	$\sigma_P[\%]$	σ_{PA}
55855.33	b	0.0365	65.33	0.0038	2.98
55855.34	r	0.0512	88.90	0.0040	2.24
55855.37	i	0.0714	78.06	0.0195	7.82
56022.03	i	0.0488	1.53	0.0151	8.87
56022.04	b	0.0194	72.54	0.0129	19.05
56022.05	v	0.0288	92.40	0.0152	15.12
56022.06	r	0.0425	17.03	0.0171	11.53
56610.19	v	0.0488	3.48	0.0111	6.52
56610.22	i	0.0567	0.00	0.0042	2.12
56610.23	r	0.0526	3.66	0.0242	13.18
56610.25	b	0.0637	1.90	0.0351	15.79
56714.09	v	0.1242	85.81	0.0127	2.93
56726.08	b	0.0601	75.52	0.0260	12.39
56726.09	v	0.0410	75.25	0.0233	16.28
56726.10	r	0.0656	80.67	0.0239	10.44
56726.11	i	0.0379	5.24	0.0209	15.8
56946.28	b	0.0826	86.66	0.0070	2.43
56946.30	v	0.0401	106.55	0.0152	10.86
56946.31	r	0.0601	79.15	0.0084	4.00
56946.32	i	0.0306	1.22	0.0136	12.73
56981.29	v	0.0823	3.00	0.0267	9.29
56981.30	r	0.0624	6.25	0.0089	4.09
56981.30	i	0.0505	12.85	0.0144	8.17

Table A.7 - : Spectro-polarimetric data from HPOL.

Data ID	Obs. Start Time	Exp. Time
bet-cmi_19910422	1991-04-22 02:07:32	3277
bet-cmi_19950208b	1995-02-08 00:00:00	768
bet-cmi_19950208r	1995-02-08 00:00:00	640
bet-cmi_19950325b	1995-03-25 00:00:00	1920
bet-cmi_19950325r	1995-03-25 00:00:00	640
bet-cmi_20000207r	2000-02-07 00:00:00	600
bet-cmi_20000212b	2000-02-12 00:00:00	1536
bet-cmi_20000212r	2000-02-12 00:00:00	640

A.7 Selected stars.

Table A.8 - : Stars used in the validation process.

main ID	Star	π (mas)	σ_π (mas)	v sin i (km s^{-1})	$\sigma_{v \sin i}$ (mas)	Sp. type (Simbad)	RA (J2000) (h:m:s)	DEC (J2000) (^{o}, ', ")	Ref. v sin i
* π And	HD3369	5.939	0.3628	25	-	B5V	00 36 52.8512	+33 43 09.651	Abt et al., 2002
* ν And	HD4727	6.9259	0.46	20	-	B5V	00 49 48.8460	+41 04 44.045	Abt et al., 2002
* π Ari	HD17543	4.18	0.69	51	20	B6V	02 49 17.5592	+17 27 51.516	Huang et al., 2010
HD 18537	HD18537	6.9745	0.1205	90	-	B7V	03 00 52.2119	+52 21 06.247	Abt et al., 2002
* 53 Ari	HD19374	3.1669	0.0881	0	24	B1.5V	03 07 25.6726	+17 52 47.971	Huang et al., 2010
* ksi Tau	HD21364	16.4494	0.9165	231	-	B9Vn	03 27 10.1384	+09 43 57.862	Royer et al., 2007
* ψ Per	HD22192	5.9627	0.873	200	-	B5Ve	03 36 29.3784	+48 11 33.508	Abt et al., 2002
* τ05 Eri	HD22203	12.4912	0.5487	73	-	B9V	03 33 47.2721	-21 37 58.375	Royer et al., 2007
* o Per	HD22951	3.031	0.2274	10	-	B0.5V	03 42 22.6477	+33 57 54.111	Abt et al., 2002
* 18 Tau	HD23324	7.3405	0.1237	185	-	B8V	03 45 09.7395	+24 50 21.349	Abt et al., 2002
* 24 Eri	HD23363	4.8394	0.1452	140	-	B7IV	03 44 30.5099	-01 09 47.120	Abt et al., 2002
* 21 Tau	HD23432	7.5658	0.1321	160	-	B8V	03 45 54.4767	+24 33 16.241	Abt et al., 2002
* 28 Tau	HD23862	7.7229	0.2039	220	-	B8Vne	03 49 11.2175	+24 08 12.172	Abt et al., 2002
* c Per	HD25940	5.9344	0.3278	155	-	B3Ve	04 08 39.6888	+47 42 45.042	Abt et al., 2002
HD 26326	HD26326	4.9039	0.1056	5	-	B5IV	04 09 17.8360	-16 23 09.075	Abt et al., 2002
* 62 Tau	HD27778	4.4566	0.0474	101	10	B3V	04 23 59.7629	+24 18 03.527	Huang et al., 2010
V* HU Tau	HD29365	7.7218	0.0851	70	-	B8V	04 38 15.8302	+20 41 05.011	Abt et al., 2002
* τ Tau	HD29763	10.7072	0.6001	100	-	B3V	04 42 14.6926	+22 57 24.894	Uesugi and Fukuda, 1970
HD 31726	HD31726	2.5701	0.1017	26	8	B2V	04 57 44.6843	-14 13 54.892	Bragança et al., 2012

* ψ Eri	HD32249	3.9274	0.2514	52	8	B3IV	05 01 26.3456	-07 10 26.271	Bragança et al., 2012
* 11 Cam	HD32343	4.6189	0.162	55	-	B3Ve	05 06 08.4523	+58 58 20.548	Abt et al., 2002
* 105 Tau	HD32991	3.0763	0.0908	175	-	B2Ve	05 07 55.4350	+21 42 17.350	Abt et al., 2002
HD 34748	HD34748	2.6618	0.0992	295	-	B3V	05 19 35.2871	-01 24 42.883	Abt et al., 2002
HD 34798	HD34798	4.1424	0.0643	30	-	B5Vs	05 19 17.4368	-18 31 11.696	Abt et al., 2002
* 113 Tau	HD35532	2.7358	0.0923	281	7	B2Vn	05 26 05.7215	+16 42 00.584	Huang et al., 2010
* κ Pic	HD35580	4.8587	0.0765	264	-	B8/9V	05 22 22.1470	-56 08 03.825	Royer et al., 2002
HD 35588	HD35588	2.8528	0.0774	170	-	B2V	05 25 47.0186	+00 31 12.875	Abt et al., 2002
* 115 Tau	HD35671	4.9316	0.2069	125	8	B5V	05 27 10.0943	+17 57 43.947	Huang et al., 2010
* 32 Ori	HD36267	10.77	0.64	155	-	B5V	05 30 47.0509	+05 56 53.292	Abt et al., 2002
* 35 Ori	HD36653	3.1116	0.1814	118	10	B3V	05 33 54.2872	+14 18 20.086	Bragança et al., 2012
V* VV Ori	HD36695	2.6531	0.2153	120	-	B9IV/V	05 33 31.4472	-01 09 21.859	Abt et al., 2002
V* V1046 Ori	HD37017	0.4468	0.1712	165	-	B2/3V	05 35 21.8676	-04 29 39.040	Abt et al., 2002
* c Ori	HD37018	3.69	1.2	20	-	B1V	05 35 23.1642	-04 50 18.088	Abt et al., 2002
HD 37303	HD37303	2.4339	0.1159	265	-	B2V(n)	05 37 27.3574	-05 56 18.197	Abt et al., 2002
HD 37744	HD37744	2.3209	0.0954	37	-	B2IV	05 40 37.2961	-02 49 30.847	Simón-Díaz and Herrero, 2014
* ζ Tau	HD37202	7.33	0.82	125	-	B1IVe_shell	05 37 38.6870	+21 08 32.834	Abt et al., 2002
* ω Ori	HD37490	3.1596	0.3589	180	-	B3Ve	05 39 11.1455	+04 07 17.290	Abt et al., 2002
* α Col	HD37795	7.2328	1.0229	195	-	B9Ve	05 39 38.9390	-34 04 26.750	Abt et al., 2002
* 57 Ori	HD39698	1.5872	0.1401	115	-	B2V	05 54 56.6871	+19 44 58.629	Abt et al., 2002
* ν Ori	HD41753	6.7656	0.3931	30	-	B3V	06 07 34.3252	+14 46 06.511	Abt et al., 2002
* f01 Ori	HD42545	4.4787	0.28	245	-	B5Vn	06 12 03.2806	+16 07 49.458	Abt et al., 2002

* ζ CMa	HD44402	9.9047	0.7158	25	-	B2.5V	06 20 18.7878	-30 03 48.121	Abt et al., 2002
HD 44506	HD44506	1.6226	0.1024	241	11	B3V	06 20 36.2399	-34 08 38.915	Bragança et al., 2012
HD 47054	HD47054	4.4762	0.128	220	-	B8IVe	06 36 35.3296	-05 12 40.100	Abt et al., 2002
* 16 Mon	HD48977	3.1699	0.1518	20	-	B3V	06 46 32.4144	+08 35 13.781	Abt et al., 2002
HD 49662	HD49662	6.17	0.75	90	-	B7IV	06 48 57.7366	-15 08 41.000	Abt et al., 2002
* κ CMa	HD50013	4.7425	0.3295	210	-	B1.5Ve	06 49 50.4601	-32 30 30.532	Abt et al., 2002
* ω CMa	HD56139	4.8816	0.4238	105	-	B2IV-Ve	07 14 48.6531	-26 46 21.556	Abt et al., 2002
* β CMi	HD58715	20.3535	1.222	210	-	B8Ve	07 27 09.0497	+08 17 21.488	Abt et al., 2002
HD 60098	HD60098	3.549	0.0422	41	5	B3V	07 31 25.7671	-36 09 11.729	Bragança et al., 2012
HD 60848	HD60848	0.3128	0.0839	362	-	O8:V:pe	07 37 05.7328	+16 54 15.303	Uesugi and Fukuda, 1970
HD 60855	HD60855	2.0486	0.1038	244	8	B2Ve	07 36 03.8931	-14 29 33.982	Huang and Gies, 2006
HD 67536	HD67536	2.3923	0.0519	292	-	B2Vn	08 04 42.9316	-62 50 10.842	Uesugi and Fukuda, 1970
* r Pup	HD68980	2.1661	0.1724	167	-	B2ne	08 13 29.5169	-35 53 58.260	Uesugi and Fukuda, 1970
HD 71459	HD71459	4.0543	0.1218	38	1	B3/5IV	08 25 51.9109	-42 09 11.067	Bragança et al., 2012
HD 74234	HD74234	1.3915	0.0511	192	11	B2IV	08 40 53.3999	-48 13 31.814	Bragança et al., 2012
* η Hya	HD74280	7.6128	0.3517	99.2	5	B3V	08 43 13.4759	+03 23 55.184	Ammler-von Eiff and Reiners, 2012
* κ Hya	HD83754	8.8837	0.3752	150	-	B3/5IV/V	09 40 18.3596	-14 19 56.215	Abt et al., 2002
* I Hya	HD83953	6.5733	0.2851	240	-	B5V	09 41 17.0078	-23 35 29.432	Abt et al., 2002
* α Leo	HD87901	41.13	0.35	300	-	B8IVn	10 08 22.3109	+11 58 01.951	Abt et al., 2002
* β Sex	HD90994	8.9613	0.2448	80	-	B5IV/V	10 30 17.4798	-00 38 13.303	Abt et al., 2002
* tet Car	HD93030	7.16	0.21	202	-	B0Vp	10 42 57.3575	-64 23 39.865	Uesugi and Fukuda, 1970
* π Cen	HD98718	9.12	0.34	350	-	B5Vn	11 21 00.4061	-54 29 27.665	Uesugi and Fukuda, 1970

* ρ Cen	HD105937	11.8348	0.3746	147	-	B3V	12 11 39.1280	-52 22 06.406	Uesugi and Fukuda, 1970
* ζ Cru	HD106983	10.4901	0.3308	188	-	B2/3V	12 18 26.2361	-64 00 11.114	Uesugi and Fukuda, 1970
HD 110432	HD110432	2.3834	0.1228	213	-	B0.5IVpe	12 42 50.2655	-63 03 31.048	Bernacca and Perinotto, 1970
HD 110956	HD110956	10.0283	0.3413	22	3	B2/3V	12 46 22.7143	-56 29 19.738	Bragança et al., 2012
* chi Cen	HD122980	7.7536	0.3819	16	7	B2V	14 06 02.7692	-41 10 46.676	Bragança et al., 2012
* ρ Lup	HD128345	10.1866	0.5381	240	-	B3/4V	14 37 53.2256	-49 25 33.025	Uesugi and Fukuda, 1970
* b Cen	HD129116	10.2435	0.6426	197	-	B3V	14 41 57.5930	-37 47 36.588	Uesugi and Fukuda, 1970
* λ Lup	HD133955	3.5406	0.5961	169	-	B3V	15 08 50.6128	-45 16 47.500	Uesugi and Fukuda, 1970
* mu. Lup	HD135734	9.72	0.71	308	-	B8Ve	15 18 32.0229	-47 52 30.995	Uesugi and Fukuda, 1970
* β Lib	HD135742	17.62	0.16	250	-	B8Vn	15 17 00.4138	-09 22 58.491	Abt et al., 2002
* phi02 Lup	HD136664	6.28	0.2	141	6	B4V	15 23 09.3275	-36 51 30.875	Bragança et al., 2012
* ζ04 Lib	HD138485	4.5302	0.1902	203	19	B3V	15 32 55.2197	-16 51 10.247	Bragança et al., 2012
* τ Lib	HD139365	4.1418	0.7621	100	-	B2.5V	15 38 39.3637	-29 46 39.988	Uesugi and Fukuda, 1970
* b Sco	HD141637	6.8954	0.2438	225	-	B1.5Vn	15 50 58.7451	-25 45 04.662	Abt et al., 2002
* 4 Her	HD142926	5.8913	0.0804	275	-	B9pe	15 55 30.5918	+42 33 58.287	Abt et al., 2002
* ω Sco	HD144470	7.0596	0.3975	95	7	B1V	16 06 48.4226	-20 40 09.118	Bragança et al., 2012
* ν Sco	HD145502	6.88	0.76	115	-	B2V	16 11 59.7356	-19 27 38.536	Abt et al., 2002
* 25 Her	HD148283	12.9109	0.1359	280	-	A5V	16 25 24.1681	+37 23 38.579	Royer et al., 2007
* i Sco	HD148605	8.5602	0.3723	169	4	B3V	16 30 12.4745	-25 06 54.811	Bragança et al., 2012
* τ Sco	HD149438	5.1232	1.11	3	2	B0.2V	16 35 52.9508	-28 12 57.730	Bragança et al., 2012
HD 155806	HD155806	1.0057	0.1306	211	-	O7.5V((f))z(e)	17 15 19.2484	-33 32 54.307	Uesugi and Fukuda, 1970
V* U Oph	HD156247	3.7432	0.1307	50	-	B3V	17 16 31.7132	+01 12 37.996	Abt et al., 2002

* α Ara	HD158427	4.1865	1.2735	288	-	B2Vne	17 31 50.5006	-49 52 34.093	Uesugi and Fukuda, 1970
* 66 Oph	HD164284	6.9762	0.5037	250	-	B2Ve	18 00 15.7981	+04 22 07.139	Abt et al., 2002
* λ Pav	HD173948	4.8003	0.4471	217	-	B2Ve	18 52 13.0368	-62 11 15.339	Uesugi and Fukuda, 1970
* β01 Sgr	HD181454	12.4748	0.6401	94	-	B9V	19 22 38.2988	-44 27 32.347	Uesugi and Fukuda, 1970
HD 183362	HD183362	1.7248	0.0538	220	-	B3Ve	19 27 36.3963	+37 56 28.304	Abt et al., 2002
* β Cyg B	HD183914	8.3779	0.1696	215	-	B8Ve	19 30 45.3960	+27 57 54.973	Abt et al., 2002
HD 183656	HD183656	3.6705	0.0607	186	-	B7III	19 30 33.1219	+03 26 39.858	Royer et al., 2002
* ι Cyg	HD184006	27.0603	0.3278	240	-	A5V	19 29 42.3595	+51 43 47.206	Royer et al., 2007
* 12 Vul	HD187811	5.7966	0.2206	195	-	B2.5Ve	19 51 04.1087	+22 36 36.165	Abt et al., 2002
* 57 Aql A	HD188293	7.2437	0.1495	190	-	B7Vn	19 54 37.6522	-08 13 38.244	Abt et al., 2002
* 23 Cyg	HD188665	5.9155	0.1728	105	-	B5V	19 53 17.3787	+57 31 24.480	Abt et al., 2002
* 17 Vul	HD190993	6.6847	0.2047	75	-	B3V	20 06 53.4080	+23 36 51.927	Abt et al., 2002
* b02 Cyg	HD191610	5.2947	0.2255	250	-	B2.5Ve	20 09 25.6190	+36 50 22.596	Abt et al., 2002
* 20 Vul	HD192044	2.7904	0.0726	205	-	B7Ve	20 12 00.7017	+26 28 43.698	Abt et al., 2002
HD 192685	HD192685	7.8952	0.5496	160	-	B3V	20 15 15.8976	+25 35 31.045	Abt et al., 2002
* λ Cyg	HD198183	4.24	0.43	100	-	B5V	20 47 24.5376	+36 29 26.573	Abt et al., 2002
HD 198625	HD198625	2.2256	0.0456	250	-	B4Ve	20 49 54.6433	+46 39 40.814	Abt et al., 2002
* 57 Cyg	HD199081	6.688	0.2395	30	-	B5V	20 53 14.7592	+44 23 14.138	Abt et al., 2002
* ϵ Cap	HD205637	6.5495	0.7048	210	-	B3V	21 37 04.8309	-19 27 57.627	Abt et al., 2002
* 16 Peg	HD208057	5.8309	0.264	110	-	B3Ve	21 53 03.7679	+25 55 30.506	Abt et al., 2002
* o Aqr	HD209409	6.9205	0.2583	205	-	B7IVe	22 03 18.8435	-02 09 19.320	Abt et al., 2002
HD 209522	HD209522	3.0964	0.119	260	-	B4IVe	22 04 36.7670	-26 49 20.492	Abt et al., 2002

HD 214240	HD214240	1.5419	0.067	55	-	B3V	22 35 53.3823	+50 04 14.835	Abt et al., 2002
* ϵ PsA	HD214748	8.0981	0.3582	185	-	B8Ve	22 40 39.3446	-27 02 36.967	Abt et al., 2002
* ι And	HD222173	7.8999	0.3357	67	5	B8V	23 38 08.1998	+43 16 05.073	Bailey and Landstreet, 2013
* ϵ Tuc	HD224686	9.2645	0.2741	174	-	B8V	23 59 54.9800	-65 34 37.666	Uesugi and Fukuda, 1970

A.8 Inferred parameters of the survey of stars

Table A.9 - : Stellar parameters and $E(B-V)$ inferred from the UV domain.

star	$\log(g)$ (dex)	W	$t/t_{\rm ms}$	$T_{\rm eff}$ (K)	L ($L_\odot$)	$R_{\rm pole}$ ($R_\odot$)	i ($^{\rm o}$)	$\beta_{\rm GD}$	d (pc)	$E(B-V)$ (mag)
HD3369	$3.987^{+0.000}_{-0.000}$	$0.76^{+0.09}_{-0.07}$	$0.70^{+0.04}_{-0.08}$	$17553.53^{+295.40}_{-280.61}$	$1450.40^{+142.19}_{-125.89}$	$4.13^{+0.06}_{-0.05}$	$3.99^{+0.49}_{-0.46}$	$0.21^{+-0.03}_{-0.03}$	$182.56^{+9.96}_{-8.41}$	$0.06^{+0.01}_{-0.01}$
HD4727	$3.980^{+0.001}_{-0.001}$	$0.04^{+0.01}_{-0.01}$	$0.72^{+0.03}_{-0.04}$	$17794.49^{+219.79}_{-236.09}$	$1607.06^{+115.22}_{-117.12}$	$4.23^{+0.04}_{-0.05}$	$62.85^{+18.55}_{-21.61}$	$0.25^{+-0.00}_{-0.00}$	$187.84^{+6.12}_{-5.56}$	$0.03^{+0.00}_{-0.00}$
HD17543	$4.074^{+0.004}_{-0.004}$	$0.44^{+0.22}_{-0.24}$	$0.56^{+0.14}_{-0.12}$	$18941.41^{+632.04}_{-625.03}$	$1733.12^{+360.91}_{-308.48}$	$3.88^{+0.11}_{-0.12}$	$14.86^{+19.48}_{-6.15}$	$0.24^{+-0.01}_{-0.01}$	$215.36^{+28.62}_{-25.68}$	$0.18^{+0.01}_{-0.01}$
HD18537	$4.089^{+0.001}_{-0.001}$	$0.21^{+0.27}_{-0.04}$	$0.58^{+0.11}_{-0.11}$	$15694.46^{+482.16}_{-499.83}$	$577.04^{+104.27}_{-94.11}$	$3.26^{+0.07}_{-0.08}$	$58.81^{+20.53}_{-36.74}$	$0.25^{+0.00}_{-0.00}$	$154.15^{+21.25}_{-18.71}$	$0.13^{+0.01}_{-0.01}$
HD19374	$4.317^{+0.002}_{-0.002}$	$0.05^{+0.06}_{-0.03}$	$0.01^{+0.02}_{-0.01}$	$27546.15^{+681.45}_{-648.02}$	$7718.59^{+1204.99}_{-1021.78}$	$3.87^{+0.09}_{-0.09}$	$41.15^{+38.93}_{-27.08}$	$0.25^{+0.00}_{-0.00}$	$377.29^{+20.72}_{-17.88}$	$0.19^{+0.01}_{-0.01}$
HD21364	$4.367^{+0.000}_{-0.000}$	$0.32^{+0.02}_{-0.03}$	$0.01^{+0.01}_{-0.01}$	$15573.43^{+136.86}_{-139.48}$	$257.44^{+13.51}_{-13.24}$	$2.21^{+0.02}_{-0.02}$	$78.37^{+8.47}_{-10.65}$	$0.24^{+-0.01}_{-0.01}$	$83.51^{+1.34}_{-1.92}$	$0.08^{+0.01}_{-0.01}$
HD22192	$3.829^{+0.002}_{-0.001}$	$0.71^{+0.21}_{-0.20}$	$0.86^{+0.07}_{-0.10}$	$17789.69^{+572.97}_{-526.07}$	$2394.24^{+454.46}_{-366.24}$	$5.16^{+0.12}_{-0.12}$	$41.76^{+26.66}_{-11.60}$	$0.22^{+-0.03}_{-0.03}$	$179.21^{+6.99}_{-6.94}$	$0.15^{+0.01}_{-0.01}$
HD22203	$4.119^{+0.000}_{-0.000}$	$0.17^{+0.15}_{-0.03}$	$0.55^{+0.04}_{-0.06}$	$12880.64^{+97.27}_{-90.94}$	$181.68^{+7.65}_{-6.87}$	$2.71^{+0.02}_{-0.01}$	$64.66^{+17.57}_{-35.46}$	$0.25^{+-0.00}_{-0.00}$	$90.14^{+1.69}_{-1.77}$	$0.03^{+0.00}_{-0.00}$
HD22951	$4.064^{+0.003}_{-0.001}$	$0.02^{+0.00}_{-0.00}$	$0.55^{+0.02}_{-0.03}$	$27798.42^{+562.08}_{-313.27}$	$16466.88^{+2301.40}_{-1166.00}$	$5.55^{+0.14}_{-0.08}$	$65.24^{+7.74}_{-3.10}$	$0.25^{+-0.00}_{-0.00}$	$309.70^{+14.94}_{-14.52}$	$0.23^{+0.00}_{-0.01}$
HD23324	$4.350^{+0.002}_{-0.002}$	$0.37^{+0.11}_{-0.05}$	$0.04^{+0.05}_{-0.03}$	$14855.50^{+205.89}_{-173.54}$	$209.19^{+17.00}_{-13.55}$	$2.19^{+0.03}_{-0.02}$	$58.19^{+16.78}_{-16.28}$	$0.24^{+-0.01}_{-0.01}$	$121.81^{+5.78}_{-4.75}$	$0.11^{+0.01}_{-0.01}$
HD23363	$3.981^{+0.001}_{-0.001}$	$0.48^{+0.28}_{-0.15}$	$0.70^{+0.06}_{-0.14}$	$14801.03^{+233.06}_{-214.97}$	$558.95^{+48.69}_{-42.19}$	$3.60^{+0.04}_{-0.04}$	$39.37^{+29.74}_{-15.65}$	$0.24^{+-0.01}_{-0.01}$	$196.45^{+8.95}_{-9.44}$	$0.06^{+0.01}_{-0.01}$
HD23432	$4.366^{+0.002}_{-0.001}$	$0.34^{+0.10}_{-0.06}$	$0.03^{+0.04}_{-0.02}$	$14396.81^{+218.60}_{-211.13}$	$169.10^{+15.14}_{-13.43}$	$2.10^{+0.03}_{-0.02}$	$55.20^{+26.10}_{-15.76}$	$0.24^{+-0.01}_{-0.01}$	$122.66^{+5.84}_{-4.75}$	$0.13^{+0.01}_{-0.01}$
HD23862	$3.979^{+0.001}_{-0.001}$	$0.68^{+0.24}_{-0.15}$	$0.71^{+0.07}_{-0.10}$	$13109.42^{+335.04}_{-383.11}$	$291.29^{+40.48}_{-41.34}$	$3.32^{+0.05}_{-0.06}$	$53.14^{+27.03}_{-15.96}$	$0.22^{+-0.02}_{-0.03}$	$117.10^{+4.21}_{-4.25}$	$0.09^{+0.02}_{-0.02}$
HD25940	$4.181^{+0.002}_{-0.004}$	$0.38^{+0.23}_{-0.12}$	$0.33^{+0.17}_{-0.18}$	$24179.70^{+768.97}_{-970.74}$	$5279.61^{+1141.62}_{-1192.23}$	$4.15^{+0.15}_{-0.19}$	$41.33^{+31.51}_{-17.09}$	$0.24^{+-0.00}_{-0.01}$	$146.15^{+3.53}_{-3.49}$	$0.27^{+0.02}_{-0.02}$
HD26326	$4.016^{+0.002}_{-0.000}$	$0.01^{+0.01}_{-0.00}$	$0.69^{+0.05}_{-0.06}$	$16463.26^{+704.43}_{-367.69}$	$932.95^{+261.58}_{-117.04}$	$3.76^{+0.15}_{-0.08}$	$58.85^{+18.74}_{-25.86}$	$0.25^{+-0.00}_{-0.00}$	$203.68^{+14.96}_{-11.09}$	$0.05^{+0.02}_{-0.01}$

HD27778	$3.831^{+0.003}_{-0.003}$	$0.58^{+0.28}_{-0.31}$	$0.85^{+0.09}_{-0.18}$	$15762.72^{+1220.70}_{-943.96}$	$1210.58^{+618.40}_{-351.50}$	$4.68^{+0.28}_{-0.22}$	$24.78^{+28.39}_{-8.48}$	$0.23^{+-0.01}_{-0.01}$	$254.72^{+40.28}_{-50.07}$	$0.40^{+0.03}_{-0.03}$
HD29365	$4.385^{+0.000}_{-0.000}$	$0.15^{+0.03}_{-0.02}$	$0.00^{+0.01}_{-0.00}$	$12152.84^{+80.01}_{-73.84}$	$62.55^{+2.25}_{-2.02}$	$1.79^{+0.01}_{-0.01}$	$47.82^{+19.15}_{-5.50}$	$0.25^{+-0.00}_{-0.00}$	$126.42^{+0.19}_{-0.72}$	$0.08^{+0.01}_{-0.01}$
HD29763	$4.356^{+0.000}_{-0.000}$	$0.18^{+0.03}_{-0.02}$	$0.00^{+0.00}_{-0.00}$	$19332.49^{+52.84}_{-72.66}$	$901.94^{+14.84}_{-20.11}$	$2.68^{+0.01}_{-0.01}$	$53.80^{+17.69}_{-7.40}$	$0.25^{+-0.00}_{-0.00}$	$187.10^{+0.48}_{-1.14}$	$0.05^{+0.00}_{-0.00}$
HD31726	$4.172^{+0.002}_{-0.002}$	$0.08^{+0.14}_{-0.03}$	$0.37^{+0.14}_{-0.24}$	$24139.37^{+580.32}_{-579.37}$	$5316.76^{+855.29}_{-758.25}$	$4.18^{+0.11}_{-0.12}$	$33.47^{+36.72}_{-22.63}$	$0.25^{+0.00}_{-0.00}$	$483.39^{+50.49}_{-65.04}$	$0.02^{+0.01}_{-0.01}$
HD32249	$4.159^{+0.001}_{-0.001}$	$0.31^{+0.39}_{-0.20}$	$0.41^{+0.13}_{-0.20}$	$21743.36^{+319.61}_{-343.33}$	$3017.43^{+273.38}_{-272.66}$	$3.88^{+0.06}_{-0.06}$	$16.60^{+37.58}_{-9.15}$	$0.25^{+0.00}_{-0.00}$	$225.72^{+13.40}_{-12.09}$	$0.04^{+0.00}_{-0.00}$
HD32343	$4.052^{+0.004}_{-0.001}$	$0.76^{+0.04}_{-0.62}$	$0.61^{+0.17}_{-0.07}$	$18909.01^{+730.74}_{-269.85}$	$1831.06^{+439.07}_{-144.64}$	$4.00^{+0.13}_{-0.05}$	$8.79^{+41.69}_{-1.19}$	$0.22^{+-0.03}_{-0.01}$	$228.65^{+11.13}_{-8.43}$	$0.12^{+0.01}_{-0.01}$
HD32991	$4.025^{+0.003}_{-0.003}$	$0.56^{+0.03}_{-0.03}$	$0.60^{+0.05}_{-0.08}$	$24347.15^{+424.76}_{-445.39}$	$8427.84^{+985.89}_{-949.15}$	$5.17^{+0.11}_{-0.12}$	$35.95^{+8.17}_{-8.03}$	$0.23^{+-0.02}_{-0.02}$	$283.75^{+15.03}_{-22.98}$	$0.49^{+0.00}_{-0.00}$
HD34748	$4.324^{+0.001}_{-0.001}$	$0.45^{+0.02}_{-0.03}$	$0.00^{+0.01}_{-0.00}$	$26389.03^{+192.38}_{-246.84}$	$6006.26^{+269.01}_{-332.40}$	$3.72^{+0.03}_{-0.04}$	$67.53^{+14.78}_{-10.84}$	$0.24^{+-0.01}_{-0.01}$	$392.26^{+2.10}_{-4.28}$	$0.19^{+0.00}_{-0.00}$
HD34798	$4.260^{+0.001}_{-0.000}$	$0.07^{+0.12}_{-0.02}$	$0.23^{+0.13}_{-0.12}$	$17570.92^{+522.41}_{-455.31}$	$686.12^{+130.56}_{-100.42}$	$2.83^{+0.08}_{-0.07}$	$44.29^{+34.67}_{-28.87}$	$0.25^{+0.00}_{-0.00}$	$266.62^{+28.37}_{-22.11}$	$0.04^{+0.01}_{-0.01}$
HD35532	$4.337^{+0.001}_{-0.001}$	$0.49^{+0.07}_{-0.05}$	$0.01^{+0.02}_{-0.01}$	$21808.81^{+234.06}_{-242.72}$	$1892.70^{+130.39}_{-128.55}$	$3.06^{+0.04}_{-0.04}$	$64.09^{+12.01}_{-11.40}$	$0.24^{+-0.01}_{-0.01}$	$268.52^{+5.38}_{-7.57}$	$0.18^{+0.00}_{-0.00}$
HD35580	$4.194^{+0.001}_{-0.001}$	$0.67^{+0.12}_{-0.09}$	$0.39^{+0.09}_{-0.11}$	$13974.12^{+248.78}_{-247.89}$	$231.53^{+23.06}_{-21.34}$	$2.60^{+0.03}_{-0.03}$	$62.43^{+17.53}_{-14.59}$	$0.22^{+-0.02}_{-0.02}$	$196.62^{+9.96}_{-9.47}$	$0.02^{+0.01}_{-0.01}$
HD35588	$4.109^{+0.002}_{-0.002}$	$0.41^{+0.20}_{-0.09}$	$0.49^{+0.14}_{-0.24}$	$21344.41^{+490.17}_{-500.58}$	$3105.46^{+451.26}_{-415.10}$	$4.09^{+0.09}_{-0.10}$	$44.96^{+22.77}_{-15.57}$	$0.24^{+-0.01}_{-0.01}$	$411.47^{+48.88}_{-41.33}$	$0.05^{+0.00}_{-0.00}$
HD35671	$4.304^{+0.002}_{-0.001}$	$0.27^{+0.11}_{-0.05}$	$0.10^{+0.08}_{-0.07}$	$18046.34^{+311.27}_{-321.73}$	$714.29^{+77.80}_{-74.27}$	$2.74^{+0.05}_{-0.05}$	$50.23^{+20.83}_{-18.06}$	$0.25^{+-0.00}_{-0.00}$	$160.08^{+7.99}_{-7.76}$	$0.10^{+0.01}_{-0.01}$
HD36267	$4.231^{+0.001}_{-0.001}$	$0.38^{+0.09}_{-0.06}$	$0.29^{+0.09}_{-0.07}$	$16255.06^{+193.45}_{-196.80}$	$480.23^{+33.11}_{-31.99}$	$2.77^{+0.03}_{-0.03}$	$48.05^{+14.28}_{-10.99}$	$0.24^{+-0.01}_{-0.01}$	$98.97^{+5.09}_{-4.89}$	$0.00^{+0.00}_{-0.00}$
HD36653	$4.359^{+0.001}_{-0.001}$	$0.28^{+0.05}_{-0.09}$	$0.01^{+0.01}_{-0.01}$	$18048.01^{+194.82}_{-242.63}$	$602.01^{+41.22}_{-48.56}$	$2.52^{+0.03}_{-0.04}$	$43.63^{+36.86}_{-7.34}$	$0.25^{+-0.00}_{-0.00}$	$161.48^{+5.22}_{-5.41}$	$0.06^{+0.00}_{-0.00}$
HD36695	$3.993^{+0.011}_{-0.006}$	$0.44^{+0.31}_{-0.20}$	$0.63^{+0.13}_{-0.21}$	$24841.45^{+1075.04}_{-976.48}$	$10266.28^{+3221.33}_{-2289.24}$	$5.48^{+0.29}_{-0.25}$	$28.25^{+31.77}_{-12.26}$	$0.24^{+-0.01}_{-0.01}$	$433.71^{+66.56}_{-56.96}$	$0.06^{+0.01}_{-0.01}$
HD37017	$4.175^{+0.004}_{-0.001}$	$0.36^{+0.16}_{-0.08}$	$0.37^{+0.19}_{-0.18}$	$21398.43^{+813.39}_{-738.10}$	$2641.87^{+673.51}_{-501.25}$	$3.75^{+0.15}_{-0.13}$	$50.96^{+25.55}_{-18.61}$	$0.24^{+-0.01}_{-0.01}$	$453.24^{+73.82}_{-55.68}$	$0.06^{+0.01}_{-0.01}$

HD37018	$4.198^{+0.002}_{-0.003}$	$0.77^{+0.03}_{-0.03}$	$0.26^{+0.04}_{-0.03}$	$27127.72^{+532.50}_{-593.78}$	$10036.13^{+1325.31}_{-1251.94}$	$4.55^{+0.11}_{-0.10}$	$2.47^{+0.26}_{-0.24}$	$0.21^{+-0.04}_{-0.04}$	$314.95^{+19.17}_{-23.21}$	$0.06^{+0.00}_{-0.00}$
HD37303	$4.275^{+0.002}_{-0.001}$	$0.66^{+0.01}_{-0.01}$	$0.10^{+0.10}_{-0.07}$	$25922.78^{+674.69}_{-470.83}$	$6325.08^{+1059.93}_{-669.20}$	$3.95^{+0.10}_{-0.08}$	$54.51^{+3.77}_{-8.53}$	$0.23^{+-0.02}_{-0.02}$	$488.32^{+42.38}_{-24.92}$	$0.01^{+0.01}_{-0.01}$
HD37744	$4.069^{+0.003}_{-0.003}$	$0.06^{+0.02}_{-0.01}$	$0.56^{+0.08}_{-0.07}$	$26194.78^{+508.56}_{-542.43}$	$11359.18^{+1397.78}_{-1361.30}$	$5.19^{+0.10}_{-0.11}$	$65.76^{+13.68}_{-22.00}$	$0.25^{+-0.00}_{-0.00}$	$644.43^{+53.00}_{-41.96}$	$0.04^{+0.01}_{-0.01}$
HD37202	$3.909^{+0.020}_{-0.016}$	$0.49^{+0.35}_{-0.23}$	$0.75^{+0.15}_{-0.30}$	$22746.58^{+2169.89}_{-1820.30}$	$7694.85^{+6202.02}_{-3133.52}$	$5.66^{+0.68}_{-0.51}$	$29.53^{+34.27}_{-12.35}$	$0.24^{+-0.01}_{-0.01}$	$134.98^{+15.33}_{-14.43}$	$0.13^{+0.05}_{-0.05}$
HD37490	$3.776^{+0.014}_{-0.001}$	$0.97^{+0.03}_{-0.09}$	$0.98^{+0.01}_{-0.03}$	$22667.90^{+895.94}_{-998.01}$	$10018.19^{+3179.30}_{-2208.66}$	$6.51^{+0.40}_{-0.22}$	$26.49^{+4.58}_{-2.89}$	$0.17^{+-0.08}_{-0.08}$	$347.36^{+33.54}_{-33.91}$	$0.15^{+0.02}_{-0.01}$
HD37795	$3.717^{+0.006}_{-0.006}$	$0.70^{+0.17}_{-0.11}$	$0.94^{+0.03}_{-0.04}$	$14267.17^{+326.89}_{-290.48}$	$930.96^{+102.09}_{-84.01}$	$5.01^{+0.03}_{-0.03}$	$50.77^{+20.00}_{-13.00}$	$0.22^{+-0.03}_{-0.03}$	$80.99^{+2.06}_{-1.89}$	$0.02^{+0.01}_{-0.01}$
HD39698	$3.758^{+0.001}_{-0.008}$	$0.89^{+0.09}_{-0.12}$	$0.98^{+0.02}_{-0.04}$	$19105.21^{+481.70}_{-608.86}$	$4060.27^{+652.30}_{-580.46}$	$5.83^{+0.15}_{-0.07}$	$19.45^{+3.78}_{-2.46}$	$0.20^{+-0.05}_{-0.05}$	$703.00^{+49.82}_{-55.87}$	$0.04^{+0.01}_{-0.01}$
HD41753	$4.185^{+0.001}_{-0.001}$	$0.29^{+0.20}_{-0.23}$	$0.39^{+0.11}_{-0.15}$	$17716.00^{+257.61}_{-245.25}$	$884.51^{+79.98}_{-71.42}$	$3.17^{+0.05}_{-0.04}$	$11.26^{+52.72}_{-4.92}$	$0.25^{+-0.00}_{-0.00}$	$164.43^{+7.68}_{-6.87}$	$0.01^{+0.01}_{-0.01}$
HD42545	$4.249^{+0.001}_{-0.002}$	$0.65^{+0.09}_{-0.24}$	$0.25^{+0.07}_{-0.14}$	$16701.05^{+391.37}_{-403.49}$	$533.82^{+78.39}_{-67.93}$	$2.77^{+0.06}_{-0.05}$	$75.39^{+9.34}_{-19.41}$	$0.23^{+-0.02}_{-0.02}$	$167.88^{+9.38}_{-11.15}$	$0.03^{+0.01}_{-0.01}$
HD44402	$4.122^{+0.000}_{-0.001}$	$0.11^{+0.26}_{-0.06}$	$0.50^{+0.06}_{-0.10}$	$20312.47^{+257.48}_{-256.94}$	$2235.17^{+178.53}_{-158.78}$	$3.83^{+0.05}_{-0.04}$	$22.81^{+42.72}_{-16.15}$	$0.25^{+0.00}_{-0.00}$	$111.37^{+1.67}_{-1.61}$	$0.04^{+0.01}_{-0.01}$
HD44506	$3.776^{+0.003}_{-0.003}$	$0.92^{+0.06}_{-0.15}$	$0.98^{+0.01}_{-0.03}$	$21724.35^{+439.32}_{-406.75}$	$7892.53^{+827.75}_{-710.81}$	$6.29^{+0.06}_{-0.06}$	$40.19^{+8.13}_{-3.55}$	$0.19^{+-0.06}_{-0.06}$	$551.15^{+35.71}_{-41.47}$	$0.03^{+0.01}_{-0.01}$
HD47054	$3.834^{+0.001}_{-0.001}$	$0.69^{+0.12}_{-0.04}$	$0.85^{+0.04}_{-0.04}$	$14456.70^{+291.89}_{-299.71}$	$743.72^{+81.36}_{-77.36}$	$4.36^{+0.05}_{-0.06}$	$58.92^{+14.77}_{-9.75}$	$0.22^{+-0.03}_{-0.03}$	$256.41^{+15.87}_{-15.63}$	$0.06^{+0.01}_{-0.00}$
HD48977	$4.142^{+0.001}_{-0.001}$	$0.04^{+0.04}_{-0.01}$	$0.50^{+0.01}_{-0.02}$	$16930.28^{+122.00}_{-117.24}$	$764.96^{+34.43}_{-32.03}$	$3.22^{+0.02}_{-0.02}$	$66.76^{+16.16}_{-37.81}$	$0.25^{+-0.00}_{-0.00}$	$304.00^{+6.16}_{-5.68}$	$0.00^{+0.00}_{-0.00}$
HD49662	$4.124^{+0.002}_{-0.001}$	$0.17^{+0.02}_{-0.02}$	$0.53^{+0.12}_{-0.08}$	$15893.43^{+540.42}_{-383.32}$	$562.70^{+114.85}_{-70.84}$	$3.14^{+0.08}_{-0.06}$	$81.00^{+5.85}_{-5.58}$	$0.25^{+-0.00}_{-0.00}$	$164.19^{+24.40}_{-11.82}$	$0.05^{+0.01}_{-0.01}$
HD50013	$3.738^{+0.009}_{-0.006}$	$0.62^{+0.11}_{-0.11}$	$0.95^{+0.03}_{-0.06}$	$22039.86^{+419.24}_{-271.05}$	$9939.94^{+1508.53}_{-895.35}$	$6.86^{+0.23}_{-0.15}$	$47.22^{+14.24}_{-9.50}$	$0.23^{+-0.02}_{-0.02}$	$203.37^{+3.79}_{-3.70}$	$0.05^{+0.01}_{-0.01}$
HD56139	$3.731^{+0.009}_{-0.006}$	$0.98^{+0.01}_{-0.14}$	$0.98^{+0.01}_{-0.02}$	$17670.45^{+429.15}_{-258.62}$	$2855.55^{+317.87}_{-179.37}$	$5.72^{+0.03}_{-0.02}$	$16.85^{+2.35}_{-1.73}$	$0.16^{+-0.09}_{-0.08}$	$290.35^{+7.16}_{-9.39}$	$0.01^{+0.01}_{-0.00}$
HD58715	$4.044^{+0.000}_{-0.000}$	$0.53^{+0.16}_{-0.04}$	$0.62^{+0.04}_{-0.07}$	$13402.12^{+112.77}_{-121.25}$	$273.60^{+12.52}_{-12.96}$	$3.08^{+0.02}_{-0.02}$	$81.28^{+6.07}_{-30.27}$	$0.24^{+-0.01}_{-0.01}$	$49.64^{+0.49}_{-0.48}$	$0.03^{+0.00}_{-0.00}$

HD60098	$4.221^{+0.001}_{-0.001}$	$0.11^{+0.21}_{-0.04}$	$0.33^{+0.09}_{-0.16}$	$17039.26^{+258.67}_{-295.25}$	$636.23^{+61.48}_{-62.65}$	$2.90^{+0.05}_{-0.05}$	$39.85^{+38.02}_{-27.20}$	$0.25^{+0.00}_{-0.00}$	$287.66^{+16.14}_{-17.69}$	$0.07^{+0.00}_{-0.00}$
HD60848	$3.864^{+0.011}_{-0.011}$	$0.97^{+0.02}_{-0.06}$	$0.81^{+0.10}_{-0.13}$	$22257.01^{+827.34}_{-1229.17}$	$7758.22^{+2219.70}_{-2333.70}$	$5.94^{+0.32}_{-0.38}$	$76.44^{+7.32}_{-11.30}$	$0.17^{+-0.08}_{-0.08}$	$722.91^{+106.22}_{-111.41}$	$0.01^{+0.01}_{-0.00}$
HD60855	$3.956^{+0.007}_{-0.005}$	$0.67^{+0.21}_{-0.16}$	$0.72^{+0.13}_{-0.18}$	$22644.73^{+654.37}_{-600.24}$	$6595.34^{+1420.49}_{-1032.05}$	$5.29^{+0.22}_{-0.16}$	$45.74^{+24.94}_{-13.25}$	$0.22^{+-0.02}_{-0.02}$	$389.89^{+47.39}_{-46.28}$	$0.19^{+0.01}_{-0.01}$
HD67536	$4.201^{+0.003}_{-0.004}$	$0.59^{+0.07}_{-0.10}$	$0.29^{+0.15}_{-0.17}$	$22940.77^{+593.35}_{-619.89}$	$3717.46^{+607.49}_{-561.37}$	$3.87^{+0.10}_{-0.10}$	$59.68^{+15.41}_{-13.72}$	$0.23^{+-0.02}_{-0.02}$	$374.03^{+24.55}_{-26.61}$	$0.15^{+0.01}_{-0.01}$
HD68980	$3.762^{+0.004}_{-0.002}$	$0.81^{+0.16}_{-0.22}$	$0.95^{+0.04}_{-0.08}$	$20038.59^{+553.95}_{-459.73}$	$5440.75^{+809.54}_{-704.39}$	$6.14^{+0.09}_{-0.14}$	$30.03^{+11.02}_{-5.36}$	$0.21^{+-0.04}_{-0.04}$	$293.01^{+7.74}_{-8.07}$	$0.05^{+0.01}_{-0.01}$
HD71459	$4.349^{+0.001}_{-0.001}$	$0.11^{+0.04}_{-0.03}$	$0.02^{+0.04}_{-0.02}$	$18593.40^{+247.96}_{-261.75}$	$736.51^{+61.29}_{-60.81}$	$2.62^{+0.04}_{-0.04}$	$31.47^{+11.20}_{-9.28}$	$0.25^{+-0.00}_{-0.00}$	$241.58^{+6.91}_{-6.38}$	$0.03^{+0.01}_{-0.01}$
HD74234	$4.111^{+0.004}_{-0.002}$	$0.46^{+0.15}_{-0.10}$	$0.47^{+0.13}_{-0.15}$	$23774.35^{+800.39}_{-698.79}$	$5754.84^{+1343.59}_{-980.99}$	$4.48^{+0.18}_{-0.15}$	$43.89^{+21.33}_{-12.42}$	$0.24^{+-0.01}_{-0.01}$	$926.14^{+129.95}_{-85.97}$	$0.07^{+0.01}_{-0.01}$
HD74280	$3.979^{+0.000}_{-0.003}$	$0.24^{+0.20}_{-0.05}$	$0.71^{+0.04}_{-0.08}$	$19420.50^{+354.63}_{-417.76}$	$2564.83^{+292.03}_{-300.07}$	$4.49^{+0.08}_{-0.08}$	$50.13^{+28.05}_{-24.78}$	$0.25^{+-0.00}_{-0.00}$	$178.77^{+8.73}_{-7.78}$	$0.02^{+0.01}_{-0.01}$
HD83754	$4.314^{+0.001}_{-0.001}$	$0.36^{+0.12}_{-0.09}$	$0.09^{+0.06}_{-0.06}$	$16893.92^{+208.79}_{-167.44}$	$473.92^{+34.03}_{-26.01}$	$2.55^{+0.03}_{-0.02}$	$45.67^{+28.17}_{-13.05}$	$0.24^{+-0.01}_{-0.01}$	$137.99^{+4.61}_{-4.65}$	$0.02^{+0.00}_{-0.00}$
HD83953	$4.075^{+0.000}_{-0.001}$	$0.69^{+0.19}_{-0.15}$	$0.59^{+0.09}_{-0.13}$	$16484.28^{+312.60}_{-258.23}$	$791.45^{+92.48}_{-69.49}$	$3.46^{+0.06}_{-0.05}$	$48.46^{+23.44}_{-12.39}$	$0.22^{+-0.03}_{-0.03}$	$155.75^{+4.69}_{-4.67}$	$0.05^{+0.01}_{-0.01}$
HD87901	$4.243^{+0.001}_{-0.001}$	$0.78^{+0.05}_{-0.04}$	$0.28^{+0.05}_{-0.05}$	$13813.83^{+225.27}_{-221.70}$	$191.24^{+17.86}_{-16.41}$	$2.42^{+0.03}_{-0.03}$	$67.82^{+11.10}_{-9.45}$	$0.21^{+-0.04}_{-0.04}$	$24.38^{+0.21}_{-0.21}$	$0.03^{+0.00}_{-0.00}$
HD90994	$4.253^{+0.001}_{-0.000}$	$0.23^{+0.29}_{-0.07}$	$0.25^{+0.10}_{-0.16}$	$15434.85^{+232.42}_{-240.19}$	$338.75^{+29.98}_{-29.00}$	$2.58^{+0.03}_{-0.03}$	$38.91^{+22.04}_{-22.78}$	$0.25^{+0.00}_{-0.00}$	$122.41^{+5.47}_{-5.53}$	$0.04^{+0.01}_{-0.01}$
HD93030	$4.125^{+0.004}_{-0.004}$	$0.44^{+0.15}_{-0.12}$	$0.39^{+0.11}_{-0.14}$	$28297.86^{+603.08}_{-524.97}$	$15678.31^{+2355.82}_{-1864.05}$	$5.22^{+0.15}_{-0.13}$	$44.55^{+26.77}_{-14.00}$	$0.24^{+-0.01}_{-0.01}$	$139.04^{+4.10}_{-4.05}$	$0.03^{+0.01}_{-0.01}$
HD98718	$4.304^{+0.002}_{-0.002}$	$0.67^{+0.05}_{-0.05}$	$0.09^{+0.07}_{-0.06}$	$19711.77^{+333.69}_{-328.18}$	$1190.38^{+120.52}_{-110.14}$	$2.97^{+0.04}_{-0.04}$	$65.43^{+7.50}_{-9.22}$	$0.23^{+-0.02}_{-0.02}$	$110.15^{+4.29}_{-3.49}$	$0.03^{+0.00}_{-0.01}$
HD105937	$4.169^{+0.001}_{-0.001}$	$0.48^{+0.13}_{-0.16}$	$0.40^{+0.17}_{-0.13}$	$18387.10^{+298.17}_{-296.73}$	$1146.19^{+112.68}_{-104.39}$	$3.34^{+0.05}_{-0.05}$	$34.90^{+25.74}_{-8.96}$	$0.24^{+-0.01}_{-0.01}$	$124.71^{+10.16}_{-9.02}$	$0.00^{+0.00}_{-0.00}$
HD106983	$4.269^{+0.001}_{-0.002}$	$0.38^{+0.10}_{-0.06}$	$0.17^{+0.07}_{-0.09}$	$19690.45^{+220.17}_{-233.21}$	$1288.48^{+86.10}_{-86.69}$	$3.09^{+0.03}_{-0.03}$	$57.22^{+21.40}_{-14.82}$	$0.24^{+-0.01}_{-0.01}$	$120.19^{+4.53}_{-4.84}$	$0.00^{+0.00}_{-0.00}$
HD110432	$3.919^{+0.012}_{-0.009}$	$0.58^{+0.18}_{-0.17}$	$0.70^{+0.09}_{-0.12}$	$26716.55^{+919.51}_{-724.47}$	$19500.74^{+5289.63}_{-3562.92}$	$6.54^{+0.35}_{-0.29}$	$41.10^{+22.67}_{-12.32}$	$0.23^{+-0.02}_{-0.02}$	$344.99^{+36.60}_{-33.12}$	$0.41^{+0.01}_{-0.01}$

HD110956	$4.363^{+0.001}_{-0.001}$	$0.05^{+0.05}_{-0.01}$	$0.01^{+0.02}_{-0.01}$	$16560.38^{+185.91}_{-167.75}$	$365.58^{+24.05}_{-20.72}$	$2.33^{+0.02}_{-0.02}$	$47.37^{+29.28}_{-26.76}$	$0.25^{+0.00}_{-0.00}$	$124.11^{+2.51}_{-2.46}$	$0.01^{+0.01}_{-0.01}$
HD122980	$4.329^{+0.001}_{-0.001}$	$0.04^{+0.09}_{-0.01}$	$0.01^{+0.02}_{-0.01}$	$23206.92^{+229.17}_{-223.27}$	$2735.07^{+166.98}_{-155.67}$	$3.24^{+0.03}_{-0.03}$	$59.56^{+23.74}_{-47.31}$	$0.25^{+0.00}_{-0.00}$	$156.40^{+4.01}_{-3.63}$	$0.04^{+0.00}_{-0.00}$
HD128345	$4.322^{+0.001}_{-0.001}$	$0.74^{+0.02}_{-0.03}$	$0.08^{+0.05}_{-0.06}$	$16857.32^{+113.06}_{-113.48}$	$462.92^{+17.93}_{-17.48}$	$2.53^{+0.01}_{-0.01}$	$34.80^{+5.81}_{-4.55}$	$0.22^{+-0.03}_{-0.03}$	$95.87^{+1.73}_{-1.56}$	$0.00^{+0.00}_{-0.00}$
HD129116	$4.287^{+0.001}_{-0.001}$	$0.44^{+0.11}_{-0.08}$	$0.13^{+0.07}_{-0.08}$	$19533.85^{+206.36}_{-204.71}$	$1178.22^{+74.45}_{-69.55}$	$3.00^{+0.03}_{-0.03}$	$53.46^{+22.43}_{-15.73}$	$0.24^{+-0.01}_{-0.01}$	$105.42^{+1.84}_{-1.92}$	$0.03^{+0.00}_{-0.00}$
HD133955	$3.999^{+0.003}_{-0.002}$	$0.75^{+0.05}_{-0.22}$	$0.67^{+0.07}_{-0.11}$	$21175.32^{+489.21}_{-477.35}$	$4023.69^{+586.85}_{-516.78}$	$4.73^{+0.11}_{-0.11}$	$27.80^{+12.55}_{-3.69}$	$0.22^{+-0.03}_{-0.03}$	$216.38^{+21.80}_{-21.77}$	$0.03^{+0.00}_{-0.00}$
HD135734	$3.673^{+0.004}_{-0.005}$	$0.96^{+0.02}_{-0.04}$	$0.96^{+0.03}_{-0.04}$	$13555.47^{+176.73}_{-288.21}$	$786.88^{+48.12}_{-77.72}$	$5.10^{+0.02}_{-0.05}$	$86.72^{+2.55}_{-6.96}$	$0.18^{+-0.07}_{-0.07}$	$126.56^{+5.45}_{-6.59}$	$0.00^{+0.00}_{-0.00}$
HD135742	$3.761^{+0.003}_{-0.002}$	$0.79^{+0.08}_{-0.08}$	$0.90^{+0.02}_{-0.02}$	$12684.88^{+236.27}_{-224.03}$	$442.69^{+44.51}_{-37.19}$	$4.37^{+0.05}_{-0.04}$	$71.24^{+11.80}_{-13.83}$	$0.21^{+-0.04}_{-0.04}$	$56.82^{+0.54}_{-0.54}$	$0.02^{+0.01}_{-0.01}$
HD136664	$4.257^{+0.000}_{-0.001}$	$0.35^{+0.19}_{-0.10}$	$0.18^{+0.11}_{-0.11}$	$20818.33^{+230.69}_{-246.56}$	$1801.00^{+123.69}_{-119.92}$	$3.27^{+0.04}_{-0.03}$	$40.75^{+22.55}_{-15.71}$	$0.24^{+-0.00}_{-0.01}$	$159.72^{+4.90}_{-5.02}$	$0.06^{+0.00}_{-0.00}$
HD138485	$4.330^{+0.002}_{-0.002}$	$0.43^{+0.08}_{-0.10}$	$0.02^{+0.03}_{-0.02}$	$21957.69^{+350.61}_{-426.96}$	$2007.10^{+206.36}_{-231.64}$	$3.10^{+0.05}_{-0.07}$	$46.91^{+30.35}_{-10.24}$	$0.24^{+-0.01}_{-0.01}$	$223.10^{+13.01}_{-11.59}$	$0.08^{+0.01}_{-0.01}$
HD139365	$4.120^{+0.001}_{-0.001}$	$0.18^{+0.03}_{-0.02}$	$0.50^{+0.04}_{-0.05}$	$19807.09^{+213.42}_{-200.96}$	$1955.94^{+122.32}_{-110.09}$	$3.77^{+0.03}_{-0.03}$	$77.09^{+9.64}_{-22.98}$	$0.25^{+-0.00}_{-0.00}$	$112.72^{+2.64}_{-2.43}$	$0.03^{+0.00}_{-0.00}$
HD141637	$4.327^{+0.000}_{-0.001}$	$0.13^{+0.01}_{-0.02}$	$0.00^{+0.00}_{-0.00}$	$24538.76^{+96.84}_{-137.69}$	$3756.10^{+90.22}_{-123.27}$	$3.40^{+0.01}_{-0.02}$	$84.48^{+4.13}_{-7.86}$	$0.25^{+-0.00}_{-0.00}$	$182.65^{+0.13}_{-0.46}$	$0.21^{+0.00}_{-0.00}$
HD142926	$4.241^{+0.001}_{-0.001}$	$0.67^{+0.09}_{-0.11}$	$0.29^{+0.10}_{-0.10}$	$13823.53^{+299.09}_{-286.00}$	$193.17^{+24.17}_{-21.13}$	$2.43^{+0.04}_{-0.04}$	$66.28^{+12.04}_{-10.99}$	$0.22^{+-0.03}_{-0.03}$	$168.70^{+6.26}_{-6.21}$	$0.02^{+0.02}_{-0.01}$
HD144470	$4.305^{+0.001}_{-0.003}$	$0.24^{+0.04}_{-0.03}$	$0.00^{+0.01}_{-0.00}$	$31339.74^{+385.43}_{-618.65}$	$17336.96^{+1129.65}_{-2077.82}$	$4.48^{+0.03}_{-0.11}$	$31.19^{+5.32}_{-6.18}$	$0.25^{+-0.00}_{-0.00}$	$162.81^{+3.58}_{-7.71}$	$0.28^{+0.00}_{-0.00}$
HD145502	$4.309^{+0.003}_{-0.001}$	$0.14^{+0.01}_{-0.01}$	$0.01^{+0.02}_{-0.01}$	$28963.21^{+948.74}_{-395.10}$	$10604.04^{+2455.27}_{-916.30}$	$4.10^{+0.17}_{-0.07}$	$76.84^{+7.08}_{-7.74}$	$0.25^{+-0.00}_{-0.00}$	$180.36^{+11.32}_{-5.73}$	$0.23^{+0.01}_{-0.01}$
HD148283	$3.912^{+0.004}_{-0.008}$	$0.87^{+0.10}_{-0.11}$	$0.76^{+0.06}_{-0.10}$	$9240.66^{+467.18}_{-351.00}$	$53.13^{+16.72}_{-10.66}$	$2.85^{+0.11}_{-0.10}$	$72.53^{+13.46}_{-16.12}$	$0.20^{+-0.05}_{-0.05}$	$74.63^{+2.19}_{-2.24}$	$0.15^{+0.05}_{-0.04}$
HD148605	$4.343^{+0.003}_{-0.004}$	$0.29^{+0.21}_{-0.03}$	$0.01^{+0.09}_{-0.01}$	$20874.05^{+419.60}_{-649.66}$	$1435.01^{+175.83}_{-239.42}$	$2.90^{+0.05}_{-0.08}$	$63.21^{+23.64}_{-28.10}$	$0.25^{+-0.00}_{-0.00}$	$140.81^{+2.82}_{-4.11}$	$0.08^{+0.01}_{-0.01}$
HD149438	$4.300^{+0.015}_{-0.003}$	$0.02^{+0.06}_{-0.01}$	$0.02^{+0.03}_{-0.01}$	$31113.86^{+611.30}_{-755.49}$	$16781.49^{+1685.11}_{-2401.61}$	$4.47^{+0.04}_{-0.12}$	$13.65^{+34.95}_{-10.44}$	$0.25^{+0.00}_{-0.00}$	$138.26^{+9.37}_{-8.19}$	$0.03^{+0.01}_{-0.01}$

HD155806	$4.208^{+0.017}_{-0.033}$	$0.38^{+0.12}_{-0.11}$	$0.35^{+0.15}_{-0.31}$	$30018.89^{+0.00}_{-0.00}$	$23463.42^{+0.00}_{-0.00}$	$5.68^{+0.00}_{-0.00}$	$45.86^{+19.77}_{-13.61}$	$0.24^{+-0.01}_{-0.01}$	$540.61^{+65.55}_{-62.53}$	$0.25^{+0.01}_{-0.01}$
HD156247	$4.314^{+0.001}_{-0.004}$	$0.08^{+0.04}_{-0.01}$	$0.00^{+0.00}_{-0.00}$	$29336.47^{+170.60}_{-1122.74}$	$11284.21^{+433.74}_{-2483.80}$	$4.12^{+0.03}_{-0.19}$	$57.64^{+24.13}_{-23.48}$	$0.25^{+-0.00}_{-0.00}$	$279.44^{+2.79}_{-23.04}$	$0.46^{+0.00}_{-0.01}$
HD158427	$4.078^{+0.000}_{-0.002}$	$0.79^{+0.04}_{-0.06}$	$0.56^{+0.08}_{-0.09}$	$20047.41^{+333.76}_{-347.66}$	$2354.15^{+247.01}_{-229.21}$	$4.03^{+0.07}_{-0.06}$	$53.74^{+9.94}_{-8.63}$	$0.21^{+-0.04}_{-0.04}$	$88.70^{+5.11}_{-5.13}$	$0.05^{+0.00}_{-0.00}$
HD164284	$4.295^{+0.003}_{-0.003}$	$0.42^{+0.12}_{-0.08}$	$0.05^{+0.07}_{-0.04}$	$26889.74^{+592.62}_{-604.77}$	$7278.74^{+1030.71}_{-950.42}$	$3.94^{+0.09}_{-0.10}$	$54.02^{+29.81}_{-13.09}$	$0.24^{+-0.01}_{-0.01}$	$198.51^{+9.32}_{-10.16}$	$0.21^{+0.01}_{-0.01}$
HD173948	$3.736^{+0.010}_{-0.010}$	$0.94^{+0.04}_{-0.08}$	$0.95^{+0.04}_{-0.08}$	$24275.80^{+824.57}_{-779.42}$	$17585.97^{+4170.28}_{-3392.61}$	$7.52^{+0.30}_{-0.31}$	$31.27^{+4.66}_{-3.45}$	$0.18^{+-0.07}_{-0.07}$	$364.66^{+28.32}_{-29.13}$	$0.11^{+0.01}_{-0.01}$
HD181454	$3.993^{+0.000}_{-0.000}$	$0.66^{+0.14}_{-0.23}$	$0.69^{+0.06}_{-0.11}$	$13077.44^{+228.01}_{-326.10}$	$276.89^{+26.08}_{-34.45}$	$3.25^{+0.03}_{-0.05}$	$19.84^{+10.49}_{-4.10}$	$0.23^{+-0.02}_{-0.02}$	$91.62^{+7.59}_{-12.30}$	$0.02^{+0.01}_{-0.01}$
HD183362	$3.727^{+0.006}_{-0.008}$	$0.75^{+0.03}_{-0.03}$	$0.98^{+0.02}_{-0.07}$	$17706.44^{+325.13}_{-410.45}$	$2931.37^{+252.27}_{-296.12}$	$5.77^{+0.03}_{-0.04}$	$61.01^{+7.15}_{-7.50}$	$0.22^{+-0.03}_{-0.03}$	$505.15^{+19.61}_{-43.39}$	$0.05^{+0.01}_{-0.01}$
HD183914	$4.186^{+0.000}_{-0.000}$	$0.69^{+0.04}_{-0.03}$	$0.40^{+0.08}_{-0.07}$	$14251.12^{+183.03}_{-180.34}$	$261.77^{+19.13}_{-17.27}$	$2.66^{+0.03}_{-0.02}$	$42.52^{+7.15}_{-5.81}$	$0.22^{+-0.03}_{-0.03}$	$123.64^{+4.08}_{-3.68}$	$0.07^{+0.00}_{-0.00}$
HD183656	$4.267^{+0.004}_{-0.003}$	$0.47^{+0.30}_{-0.15}$	$0.19^{+0.25}_{-0.13}$	$17908.96^{+837.64}_{-726.30}$	$761.62^{+239.09}_{-170.20}$	$2.87^{+0.13}_{-0.12}$	$43.83^{+38.89}_{-17.21}$	$0.24^{+-0.01}_{-0.01}$	$250.25^{+18.71}_{-19.11}$	$0.22^{+0.03}_{-0.03}$
HD184006	$3.996^{+0.004}_{-0.004}$	$0.75^{+0.18}_{-0.12}$	$0.69^{+0.07}_{-0.09}$	$9040.58^{+317.53}_{-296.01}$	$37.59^{+8.00}_{-6.45}$	$2.51^{+0.07}_{-0.07}$	$63.43^{+19.53}_{-15.56}$	$0.22^{+-0.03}_{-0.03}$	$37.32^{+0.14}_{-0.13}$	$0.08^{+0.04}_{-0.03}$
HD187811	$4.228^{+0.002}_{-0.001}$	$0.70^{+0.01}_{-0.01}$	$0.28^{+0.07}_{-0.03}$	$18640.39^{+294.54}_{-265.79}$	$1069.41^{+102.96}_{-86.91}$	$3.14^{+0.05}_{-0.04}$	$30.27^{+5.07}_{-2.79}$	$0.22^{+-0.03}_{-0.03}$	$184.48^{+6.06}_{-5.61}$	$0.04^{+0.01}_{-0.00}$
HD188293	$4.353^{+0.002}_{-0.002}$	$0.41^{+0.09}_{-0.10}$	$0.02^{+0.03}_{-0.02}$	$17196.05^{+222.80}_{-260.13}$	$466.54^{+35.83}_{-39.34}$	$2.44^{+0.03}_{-0.03}$	$50.04^{+32.30}_{-9.70}$	$0.24^{+-0.01}_{-0.01}$	$161.14^{+6.43}_{-7.23}$	$0.11^{+0.01}_{-0.01}$
HD188665	$3.990^{+0.001}_{-0.000}$	$0.23^{+0.03}_{-0.03}$	$0.71^{+0.03}_{-0.05}$	$16210.20^{+517.19}_{-240.09}$	$914.52^{+184.65}_{-77.27}$	$3.84^{+0.11}_{-0.05}$	$73.26^{+8.90}_{-7.15}$	$0.25^{+-0.00}_{-0.00}$	$190.92^{+6.90}_{-6.36}$	$0.03^{+0.01}_{-0.01}$
HD190993	$4.345^{+0.001}_{-0.001}$	$0.16^{+0.08}_{-0.04}$	$0.01^{+0.02}_{-0.01}$	$20157.46^{+223.28}_{-232.16}$	$1174.31^{+77.94}_{-77.09}$	$2.82^{+0.03}_{-0.03}$	$47.85^{+34.60}_{-18.82}$	$0.25^{+-0.00}_{-0.00}$	$161.91^{+4.22}_{-4.17}$	$0.05^{+0.00}_{-0.00}$
HD191610	$3.926^{+0.002}_{-0.002}$	$0.72^{+0.08}_{-0.06}$	$0.76^{+0.08}_{-0.08}$	$21456.75^{+443.14}_{-440.29}$	$5268.49^{+671.18}_{-608.56}$	$5.27^{+0.10}_{-0.10}$	$46.55^{+9.39}_{-8.52}$	$0.22^{+-0.03}_{-0.03}$	$317.86^{+18.00}_{-19.72}$	$0.09^{+0.01}_{-0.01}$
HD192044	$3.608^{+0.040}_{-0.001}$	$0.94^{+0.04}_{-0.02}$	$0.99^{+0.01}_{-0.01}$	$12576.55^{+1764.51}_{-98.90}$	$608.45^{+505.65}_{-22.61}$	$5.21^{+0.21}_{-0.02}$	$34.84^{+22.74}_{-18.28}$	$0.18^{+-0.07}_{-0.07}$	$223.24^{+17.87}_{-34.13}$	$0.15^{+0.07}_{-0.03}$
HD192685	$3.939^{+0.003}_{-0.002}$	$0.43^{+0.26}_{-0.11}$	$0.73^{+0.09}_{-0.16}$	$20440.65^{+800.31}_{-783.13}$	$3834.75^{+972.13}_{-800.19}$	$4.95^{+0.18}_{-0.19}$	$48.78^{+29.58}_{-21.36}$	$0.24^{+-0.01}_{-0.01}$	$275.86^{+41.85}_{-40.73}$	$0.03^{+0.01}_{-0.01}$

HD198183	$3.888^{+0.000}_{-0.000}$	$0.70^{+0.16}_{-0.27}$	$0.81^{+0.08}_{-0.10}$	$17234.79^{+573.92}_{-503.57}$	$1715.77^{+340.21}_{-261.10}$	$4.66^{+0.12}_{-0.11}$	$19.22^{+11.72}_{-4.16}$	$0.22^{+-0.03}_{-0.02}$	$221.48^{+26.81}_{-28.34}$	$0.08^{+0.01}_{-0.01}$
HD198625	$3.872^{+0.002}_{-0.002}$	$0.73^{+0.13}_{-0.15}$	$0.82^{+0.10}_{-0.14}$	$18562.38^{+591.89}_{-607.91}$	$2678.80^{+535.20}_{-453.54}$	$5.02^{+0.14}_{-0.13}$	$50.69^{+19.64}_{-12.03}$	$0.22^{+-0.03}_{-0.03}$	$485.78^{+57.07}_{-67.06}$	$0.15^{+0.01}_{-0.01}$
HD199081	$4.042^{+0.000}_{-0.001}$	$0.09^{+0.71}_{-0.02}$	$0.66^{+0.06}_{-0.25}$	$14641.70^{+291.66}_{-309.23}$	$452.06^{+52.20}_{-49.72}$	$3.31^{+0.05}_{-0.05}$	$44.47^{+26.82}_{-39.88}$	$0.25^{+0.03}_{-0.00}$	$160.21^{+5.99}_{-5.66}$	$0.02^{+0.01}_{-0.01}$
HD205637	$3.776^{+0.002}_{-0.007}$	$0.91^{+0.06}_{-0.29}$	$0.98^{+0.01}_{-0.03}$	$21682.22^{+1129.81}_{-893.35}$	$7829.22^{+2668.92}_{-1485.55}$	$6.29^{+0.29}_{-0.13}$	$35.21^{+14.33}_{-4.81}$	$0.19^{+-0.06}_{-0.05}$	$303.20^{+21.36}_{-21.43}$	$0.08^{+0.02}_{-0.02}$
HD208057	$4.148^{+0.001}_{-0.001}$	$0.38^{+0.25}_{-0.14}$	$0.45^{+0.09}_{-0.16}$	$18099.35^{+269.72}_{-271.65}$	$1105.65^{+99.86}_{-93.32}$	$3.39^{+0.05}_{-0.05}$	$31.86^{+26.35}_{-12.97}$	$0.24^{+-0.00}_{-0.01}$	$194.46^{+8.67}_{-8.57}$	$0.02^{+0.00}_{-0.00}$
HD209409	$3.988^{+0.000}_{-0.001}$	$0.73^{+0.18}_{-0.16}$	$0.70^{+0.06}_{-0.10}$	$14443.70^{+294.17}_{-288.53}$	$482.42^{+57.47}_{-50.54}$	$3.52^{+0.06}_{-0.05}$	$42.15^{+17.75}_{-9.67}$	$0.22^{+-0.03}_{-0.03}$	$134.94^{+3.63}_{-3.39}$	$0.07^{+0.01}_{-0.01}$
HD209522	$4.072^{+0.004}_{-0.004}$	$0.69^{+0.06}_{-0.11}$	$0.58^{+0.11}_{-0.11}$	$19305.26^{+573.92}_{-540.79}$	$1942.60^{+353.62}_{-293.77}$	$3.95^{+0.10}_{-0.10}$	$51.93^{+15.13}_{-9.36}$	$0.22^{+-0.03}_{-0.03}$	$344.97^{+45.09}_{-33.94}$	$0.05^{+0.01}_{-0.01}$
HD214240	$3.898^{+0.001}_{-0.001}$	$0.94^{+0.03}_{-0.04}$	$0.80^{+0.13}_{-0.10}$	$15647.52^{+235.05}_{-301.90}$	$962.97^{+86.19}_{-100.87}$	$4.23^{+0.06}_{-0.07}$	$8.80^{+1.02}_{-0.74}$	$0.18^{+-0.07}_{-0.07}$	$372.23^{+75.88}_{-39.90}$	$0.12^{+0.01}_{-0.01}$
HD214748	$3.649^{+0.005}_{-0.005}$	$0.68^{+0.09}_{-0.03}$	$0.97^{+0.02}_{-0.04}$	$14149.56^{+249.96}_{-249.73}$	$1052.17^{+87.13}_{-82.67}$	$5.41^{+0.03}_{-0.03}$	$53.43^{+7.93}_{-8.40}$	$0.22^{+-0.03}_{-0.03}$	$174.96^{+7.86}_{-9.56}$	$0.04^{+0.01}_{-0.00}$
HD222173	$3.921^{+0.000}_{-0.001}$	$0.15^{+0.02}_{-0.01}$	$0.79^{+0.01}_{-0.02}$	$13484.49^{+173.08}_{-236.23}$	$405.00^{+29.64}_{-37.20}$	$3.70^{+0.04}_{-0.05}$	$83.47^{+4.34}_{-15.47}$	$0.25^{+-0.00}_{-0.00}$	$152.84^{+4.48}_{-3.89}$	$0.05^{+0.01}_{-0.01}$
HD224686	$3.942^{+0.000}_{-0.000}$	$0.88^{+0.07}_{-0.08}$	$0.75^{+0.03}_{-0.03}$	$12380.41^{+219.25}_{-152.92}$	$238.15^{+23.15}_{-15.18}$	$3.36^{+0.04}_{-0.03}$	$33.37^{+6.39}_{-4.47}$	$0.20^{+-0.05}_{-0.05}$	$114.74^{+2.32}_{-2.25}$	$0.05^{+0.01}_{-0.01}$

Appendix B

Convergence Plots

B.1 β CMi

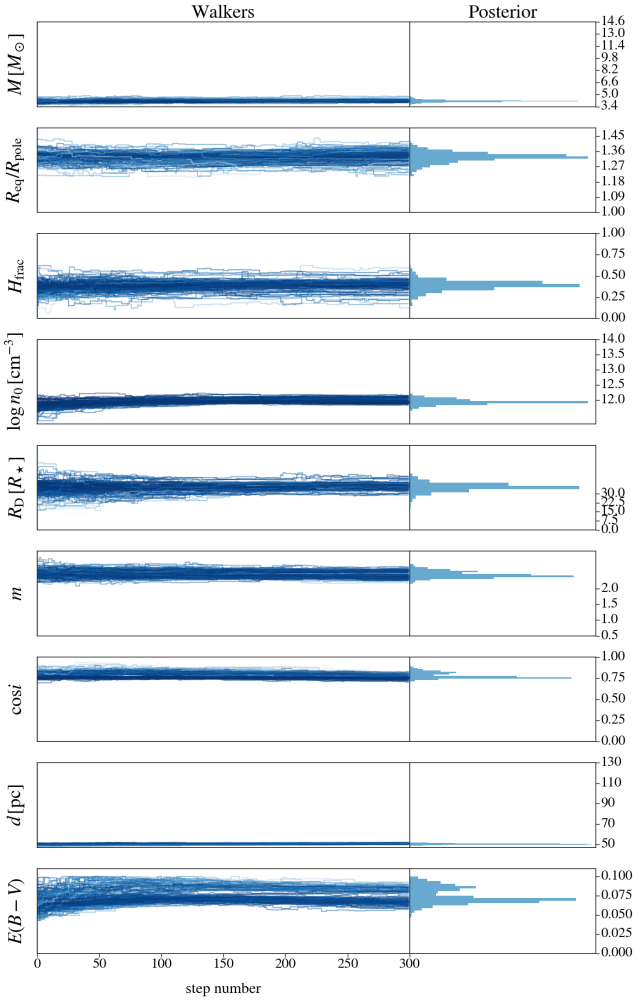

Figure B.1: Convergence plot of the Figure 6.2.

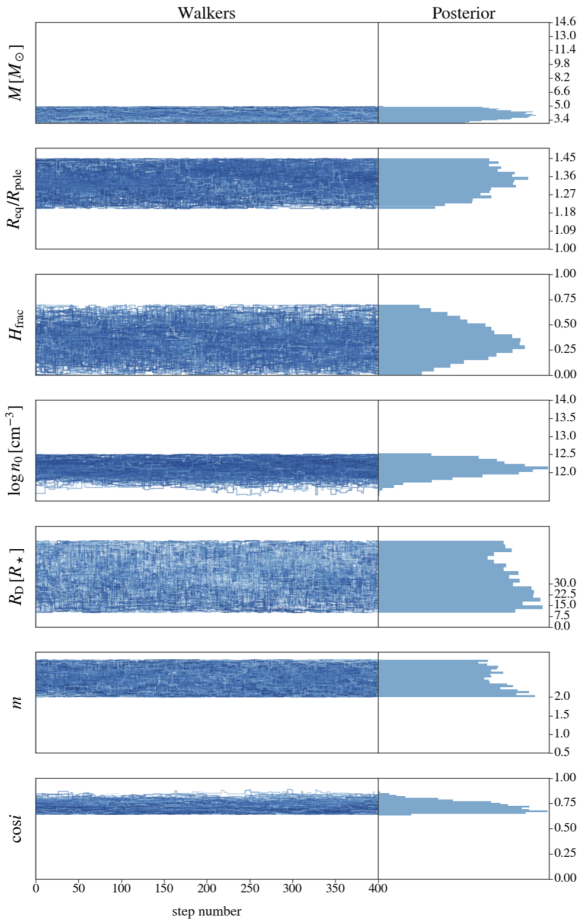

Figure B.2: Convergence plot of the Figure 6.5.

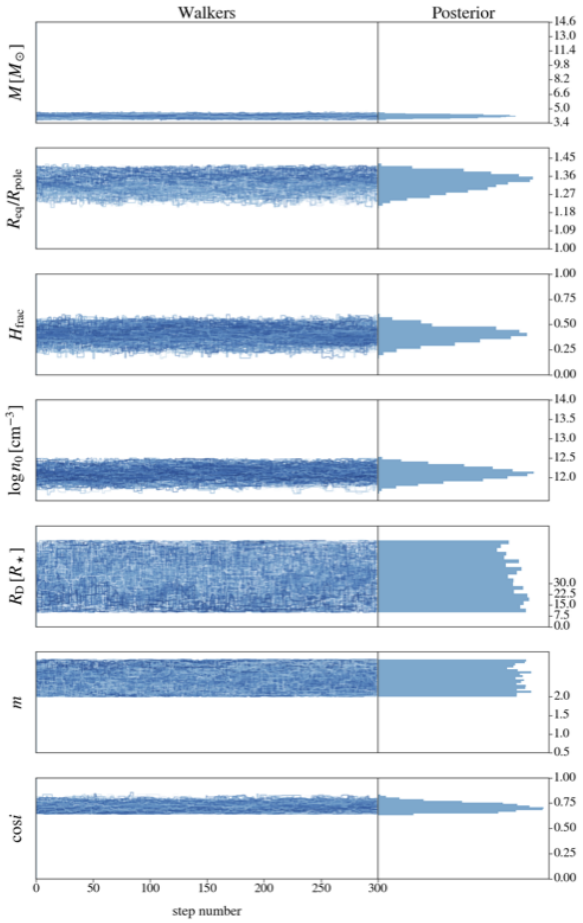

Figure B.3: Convergence plot of the Figure 6.6.

Appendix C

Bemcee Tutorial

Bemcee Documentation

Beacon

Oct 20, 2018

CONTENTS

ii

CHAPTER

ONE

THE BEMCEE CODE

In this document we present a brief documentation of the developed code Bemcee. All the routines can be acessed thought the GitHub link: **https://github.com/tangodaum/bemcee**.

1.1 Main Routine: bemcee.py

Having defined properly all folders and options, the code can be runned in terminal by typing

```
python3 bemcee.py list_of_stars.txt
```

The file list_of_stars.txt has the format #star plx splx vsini svsi ebmv inc bump HD23466 5.31 0.24 90.0 8.0 0.0 nan True HD23793 7.74 0.17 20.0 0.0 0.0 nan True HD23862 7.72 0.20 220.0 0.0 0.0 nan True

star	plx	sig_plx	vsini	sig_vsini
HDXXXXXX	parallax	plx error	vsini value	vsini error

The main code is

```
# ================================================================================
# -*- coding:utf-8 -*-
# ================================================================================
# importing packages
from reading_routines import read_stars, read_models
from emcee.utils import MPIPool
from emcee_routines import run
import sys
# import matplotlib
from sys import argv
# matplotlib.use('Agg')

# ================================================================================
# General Options
a_parameter = 2  # Set internal steps of each walker
extension = '.png'  # Figure extension to be saved
include_rv = False  # If False: fix Rv = 3.1, else Rv will be inferead
af_filter = True  # Remove walkers outside the range 0.2 < af < 0.5
long_process = True  # Run with few walkers or many?
list_of_stars = argv[1]  # 'bcmi.txt', 'aara.txt', argv[1]
plot_fits = True  # Include fits in the corner plot
Nsigma_dis = 5.  # Set the range of values for the distance
```

(continues on next page)

Bemcee Documentation

(continued from previous page)

```
# 'beatlas', 'befavor', 'befavor_new' 'aara', 'bcmi' or 'acol' (equals)
# 'bcmi_pol'
# model = 'bcmi'
model = 'bcmi_pol'
tag = '+' + model + '_xdr' + '+hip+hpol'  # Suffix for the figures

# General Options
doconvpol = False
table_csv = 'hpol.npy'  # 'bcmi_iscor.csv', 'bcmi_iscor_2.csv'

# ------------------------------------------------------------------------
# Alphacrucis' options
acrux = False  # If True, it will run in Nproc processors in the cluster
Nproc = 24  # Number of processors to be used in the cluster

# ------------------------------------------------------------------------
# if True: M, Age, Oblat are set as priors for the choosen input, npy_star
stellar_prior = False
npy_star = 'Walkers_500_Nmcmc_1000_af_0.28_a_1.4_rv_false+hip.npy'

# lbd_range = 'UV'
# lbd_range = 'UV+VIS+NIR+MIR+FIR+MICROW+RADIO'
lbd_range = 'MIR+FIR+MICROW+RADIO'

if lbd_range == 'UV':
    votable = False
else:
    votable = True

if lbd_range == 'bcmi_pol':
    lbd_range = ''

if lbd_range == 'UV' or lbd_range == 'UV+VIS' or\
   lbd_range == 'UV+VIS+NIR' or lbd_range == 'UV+VIS+NIR+MIR' or\
   lbd_range == 'FIR+MICROW+RADIO' or lbd_range == 'MICROW+RADIO' or\
   lbd_range == 'RADIO':
    plot_in_log_scale = False  # yscale in log for fits
else:
    plot_in_log_scale = True

# ========================================================================
# Acrux
if acrux is True:
    pool = MPIPool()
    if not pool.is_master():
        pool.wait()
        sys.exit(0)
else:
    pool = False

# ========================================================================
# Reading the list of stars
stars, list_plx, list_sig_plx, list_vsini_obs, list_sig_vsin_obs,\
    list_pre_ebmv, incl0, bump0 = read_stars(list_of_stars)

# Reading Models
ctrlarr, minfo, models, lbdarr, listpar, dims, isig = read_models(model)
```

(continues on next page)

(continued from previous page)

```
# ============================================================================
# Run code
input_params = stars, list_plx, list_sig_plx, list_vsini_obs,\
    list_sig_vsin_obs, list_pre_ebmv, lbd_range,\
    Nsigma_dis, include_rv, model, ctrlarr, minfo, models,\
    lbdarr, listpar, dims, isig, a_parameter, af_filter,\
    tag, plot_fits, plot_in_log_scale, long_process,\
    extension, acrux, pool, Nproc, stellar_prior, npy_star, votable,\
    table_csv

run(input_params)

# ============================================================================
# The End
print(75 * '=')
print('\nSimulation Finished\n')
print(75 * '=')

if acrux is True:
    pool.close()

# ============================================================================
```

1.2 Routine: emcee_routines

It is the main module of our code.

emcee_routines.**emcee_inference**(*star*, *Ndim*, *ranges*, *lbdarr*, *wave*, *logF*, *dlogF*, *minfo*, *listpar*, *logF_grid*, *vsin_obs*, *sig_vsin_obs*, *dist_pc*, *sig_dist_pc*, *isig*, *dims*, *include_rv*, *a_parameter*, *af_filter*, *tag*, *plot_fits*, *long_process*, *log_scale*, *model*, *acrux*, *pool*, *Nproc*, *stellar_prior*, *npy_star*, *pdf_mas*, *pdf_obl*, *pdf_age*, *pdf_dis*, *pdf_ebv*, *grid_mas*, *grid_obl*, *grid_age*, *band*)

Returns the posterior probability function. :param star: star name (string) :param Ndim: number of dimensions (integer) :param lbdarr: model wavelength (array) :param wave: observed wavelength (array) :param logF: observed flux (array) :param dlogF: observed flux error (array) :param minfo: models info (array) :param listpar: list of parameters (array) :param logF_grid: flux model (array) :param vsin_obs: observed vsini (float) :param sig_vsin_obs: observed vsini error (float) :param dist_pc: distance in parsec (float) :param sig_dist_pc: distance error (float) :param isig: float :param dims: float :param include_rv: to set rv as a free parameter (boolean) :param a_parameter: internal paramenter (float) :param af_filter: remove bad walkers (boolean) :param tag: string to be added to the final results :param plot_fits: plot fits? (boolean) :param long_process: long mcmc process? (boolean) :param log_scale: log scale? (boolean) :param model: grid model adopted (string) :param acrux: use acrux? (boolean) :param pool: internal paramenter (function) :param Nproc: number of processors (integer) :param stellar_prior: use stellar prior? (boolean) :param npy_star: npy file (string) :param pdf_mas: (float) :param pdf_obl: (float) :param pdf_age: (float) :param pdf_dis: (float) :param pdf_ebv: (float) :param grid_mas: (float) :param grid_obl: (float) :param grid_age: (float) :param band: wavelength range (string)

:return : results

emcee_routines.**lnlike**(*params*, *lbd*, *logF*, *dlogF*, *logF_mod*, *include_rv*, *model*)

Returns the likelihood probability function.

Parameters

- **params** – mass, oblat, age, inclination, ebmv, distance
- **lbd** – wavelength (float)
- **logF** – flux (float)
- **dlogF** – flux error (float)
- **logF_mod** – model flux (float)
- **include_rv** – distance (float)
- **model** – grid model (string)

:return : likelihood

emcee_routines.**lnprior**(*params*, *vsin_obs*, *sig_vsin_obs*, *dist_pc*, *sig_dist_pc*, *model*, *stellar_prior*, *npy_star*, *pdf_mas*, *pdf_obl*, *pdf_age*, *pdf_dis*, *pdf_ebv*, *grid_mas*, *grid_obl*, *grid_age*, *grid_dis*, *grid_ebv*)

Returns the prior probability function. :param params: mass, oblat, age, inclination, ebmv, distance :param vsin_obs: observed vsini (float) :param sig_vsin_obs: observed vsini error (float) :param dist_pc: distance in parsec (float) :param sig_dist_pc: distance error (float) :param model: grid model adopted (string) :param stellar_prior: use stellar prior? (boolean) :param npy_star: npy file (string) :param pdf_mas: (float) :param pdf_obl: (float) :param pdf_age: (float) :param pdf_dis: (float) :param pdf_ebv: (float) :param grid_mas: (float) :param grid_obl: (float) :param grid_age: (float) :param grid_dis: (float) :param grid_ebv: (float)

:return : prior

emcee_routines.**lnprob**(*params*, *lbd*, *logF*, *dlogF*, *minfo*, *listpar*, *logF_grid*, *vsin_obs*, *sig_vsin_obs*, *dist_pc*, *sig_dist_pc*, *isig*, *ranges*, *dims*, *include_rv*, *model*, *stellar_prior*, *npy_star*, *pdf_mas*, *pdf_obl*, *pdf_age*, *pdf_dis*, *pdf_ebv*, *grid_mas*, *grid_obl*, *grid_age*)

Returns the posterior probability function. :param params: mass, oblat, age, inclination, ebmv, distance :param lbd: wavelength (array) :param logF: observed flux (array) :param dlogF: observed flux error (array) :param minfo: models info (array) :param listpar: list of parameters (array) :param logF_grid: flux model (array) :param vsin_obs: observed vsini (float) :param sig_vsin_obs: observed vsini error (float) :param dist_pc: distance in parsec (float) :param sig_dist_pc: distance error (float) :param isig: float :param ranges: paramter's ranges :param dims: float :param model: grid model adopted (string) :param stellar_prior: use stellar prior? (boolean) :param npy_star: npy file (string) :param pdf_mas: (float) :param pdf_obl: (float) :param pdf_age: (float) :param pdf_dis: (float) :param pdf_ebv: (float) :param grid_mas: (float) :param grid_obl: (float) :param grid_age: (float)

:return : posterior

emcee_routines.**run**(*input_params*)

Main function :param input_params: array :return : Final results

emcee_routines.**run_emcee**(*p0*, *sampler*, *nib*, *nimc*, *Ndim*, *file_name*)

Core emcee code :params p0: initial position of the walkers (matrix) :params sampler: sampler (matrix) :params nib: number of steps in the burning phase (integer) :params nimc: number of steps in the mcmc (integer) :params Ndim: number of dimensions (integer) :params file_name: file name (string) :return : arrays

1.3 Routine: utils

Module with math functions envolved in different processes as: interpolation, binning, etc.

utils.**bin_data**(*x*, *y*, *nbins*, *xran=None*, *exclude_empty=True*)

Bins data

Usage: xbin, ybin, dybin = bin_data(x, y, nbins, xran=None, exclude_empty=True)

where dybin is the standard deviation inside the bins. Find the nearest value inside an array

Parameters

- **x** – array
- **y** – array
- **nbins** – number of bins
- **xran** – x range
- **exclude_empty** – remove empty values

:return : array

utils.**find_nearest**(*array*, *value*)
Find the nearest value inside an array :param array: array :param value: value (float) :return : array

utils.**find_neighbours**(*par*, *par_grid*, *ranges*)
Finds neighbours' positions of par in par_grid.

Usage: keep, out, inside_ranges, par_new, par_grid_new = find_neighbours(par, par_grid, ranges):

where redundant columns in 'new' values are excluded, but length is preserved (i.e., par_grid[keep] in griddata call).

Parameters

- **par** – list of parameters (array)
- **par_grid** – grid of parameters (float)
- **ranges** – parameter ranges

:return : array

utils.**geneva_interp_fast**(*Par*, *oblat*, *t*, *neighbours_only=True*, *isRpole=False*)
Interpolates Geneva stellar models, from grid of pre-computed interpolations.

Usage: Rpole, logL = geneva_interp_fast(Mstar, oblat, t,

neighbours_only=True, isRpole=False)

or Mstar, logL = geneva_interp_fast(Rpole, oblat, t,

neighbours_only=True, isRpole=True)

(in this case, the option 'neighbours_only' will be set to 'False')

where t is given in tMS, and tar is the open tar file. For now, only Z=0.014 is available.

Parameters

- **Par** – list of parameters (array)
- **oblat** – oblateness (float)
- **t** – stellar age
- **neighbours_only** – boolean
- **isRpole** – boolean

:return : array

utils.**griddataBA**(*minfo*, *models*, *params*, *listpar*, *dims*)
Moser's routine to interpolate BeAtlas models obs: last argument ('listpar') had to be included here :param

minfo: model's info (matrix) :param models: matrix of models :param params: free parameters (array) :param listpar: list of parameters (array) :param dims: array :return : array

utils.**griddataBA_new**(*minfo*, *models*, *params*, *isig*, *silent=True*)
Interpolates model grid

Usage: model_interp = griddata(minfo, models, params, isig, silent=True)

where minfo = grid of parameters models = grid of models params = parameters, isig = (normalized) sigma0 index

Ex: # read grid xdrpath = 'beatlas/disk_flx.xdr' listpar, lbdarr, minfo, models = bat.readBAsed(xdrpath, quiet=True) # find isig dims = ['M', 'ob', 'sig0', 'nr', 'cosi'] dims = dict(zip(dims, range(len(dims)))) isig = dims["sig0"] # interpolation params = [12.4, 1.44, 0.9, 4.4, 0.1] model_interp = np.exp(griddataBA(minfo, np.log(models), params, isig))

If photospheric models are interpolated, let isig=None. For spectra, it is recommended to enter the log of the grid of spectra as input, as shown in the example above.

Parameters

- **minfo** – model info (matrix)
- **models** – list of models (matrix)
- **params** – free parameters (array)
- **isig** – internal value (float)
- **silet** – boolean

:return : array

utils.**griddataBAtlas**(*minfo*, *models*, *params*, *listpar*, *dims*, *isig*)
Interpolation routine

Parameters

- **minfo** – model info (matrix)
- **models** – list of models (matrix)
- **params** – free parameters (array)
- **listpar** – list of parameters (array)
- **dims** – internal value (float)
- **isigt** – boolean

:return : array

utils.**hfrac2tms**(*Hfrac*, *inverse=False*)
Converts nuclear hydrogen fraction into fractional time in the main-sequence, (and vice-versa) based on the polynomial fit of the average of this relation for all B spectral types and rotational velocities.

Usage: t = hfrac2tms(Hfrac, inverse=False) or Hfrac = hfrac2tms(t, inverse=True) :param Hfrac: core hydrogen fraction (float) :param isigt: calculate inverse (boolean) :return : array

utils.**kde_scipy**(*x*, *x_grid*, *bandwidth=0.2*)
Kernel Density Estimation with Scipy :param x: array :param x: x grind :param bandwidth: band width :return : kde distribution

1.4 Routine: be_theory

The module be_theory is a Python routine that comprises the basic physical functions regarding Be stars. Their functions are read

be_theory.**W2oblat**(*W*)
Calculates oblateness from W = v/v_orb :param W: rotation rate (W = v/v_orb) :return: oblateness

be_theory.**hfrac2tms**(*Hfrac*, *inverse=False*)
Converts nuclear hydrogen fraction into fractional time in the main-sequence, (and vice-versa) based on the polynomial fit of the average of this relation for all B spectral types and rotational velocities.

Usage: t = hfrac2tms(Hfrac, inverse=False) or Hfrac = hfrac2tms(t, inverse=True)

Parameters

- **Hfrac** – hydrogen fraction in the core (float)
- **Inverse** – If you wish to convert from ttms to hfrac (boolean)

Returns main sequence lifetime

be_theory.**obl2W**(*oblat*)
Calculates rotation range (W = v/v_orb) from oblateness :param oblat: oblateness (Req/Rpole) :return: rotation rate (W)

be_theory.**oblat2w**(*oblat*)
Converts oblateness (Req/Rpole) into w=Omega/Omega_crit Ekstrom et al. 2008, Eq. 9

Usage: w = oblat2w(oblat)

Parameters **oblat** – oblateness (Req/Rpole) (float)

Returns angular rotation rate (omega)

be_theory.**t_tms_from_Xc**(*M*, *savefig=None*, *plot_fig=None*, *ttms_true=None*, *Xc=None*)
Calculates the t(tms) for a given Xc and mass :param Xc: hydrogen fraction in the core (float) :param M: stellar mass (Msun) :param plot_fig: plot figure? (boolean) :param ttms_true: a fixed value :return: main sequence lifetime

1.5 Routine: Reading Routines

Set of functions for: reading lists of stars, informations about the targets, models, observational data, VO catalogues, etc.

reading_routines.**npy2csv**(*npy_file*)
Function to convert npy file to csv table :param npy_file: npy file (string) :return : csv_file

reading_routines.**read_acol_xdr**(*xdr_name*)
Function to read the grid model (alpha col grid model) :param xdr_name: xdr name (string) :return : array

reading_routines.**read_bcmi_pol**()
Function to read the grid model (alpha col polarimetric grid model) :param xdr_name: xdr name (string) :return : array

reading_routines.**read_beatlas_xdr**()
Function to read the grid model (V1-Beatlas) :return : array

reading_routines.**read_befavor_xdr**()
Function to read the grid model (stellar models) :return : array

reading_routines.**read_befavor_xdr_complete**()
Function to read the grid model (stellar models) :return : array

reading_routines.**read_befavor_xdr_new**()
Function to read the grid model (stellar models) :return : array

reading_routines.**read_iue**(*models*, *lbdarr*, *wave0*, *flux0*, *sigma0*, *folder_data*, *folder_fig*, *star*, *cut_iue_regions*, *model*, *lbd_range*)
Function to read IUE data :param models: adopted grid model :param lbdarr: model wavelenght (array) :param wave0: wavelength (array) :param flux0: observed flux (array) :param sigma0: observed flux error (array) :param folder_data: folder data (string) :param folder_fig: folder figure (string) :param star: star name (string) :param cut_iue_regions: cut regions with large errors (boolean) :param model: string :param lbd_range: wavelength range :return : array

reading_routines.**read_models**(*model*)
Function to read models :param models: model name (string) :return : array

reading_routines.**read_opd_pol**(*folder_data*, *star*, *table_csv*)
Function to read OPD polarimetric data :param folder_data: folder data (string) :param star: star name (string) :param table_csv: boolean :return : wave, flux, sigma

reading_routines.**read_star_info**(*stars*, *list_plx*, *list_sig_plx*, *list_vsini_obs*, *list_sig_vsin_obs*, *list_pre_ebmv*, *lbd_range*, *listpar*, *Nsigma_dis*, *include_rv*, *model*)
Function to read the info about the stars :param stars: list of stars (array) :param list_plx: list of parallaxes (array) :param list_sig_plx: list of parallaxes errors (array) :param list_vsini_obs: list of observed vsini (array) :param list_sig_vsin_obs: list of observed vsini errors (array) :param list_pre_ebmv: list of previous ebmv values (array) :param lbd_range: wavelengths ranges :param listpar: list of parameters (array) :param Nsigma_dis: define the distance range :param include_rv: set rv as a free parameter :param model: adopted grid model :return : array

reading_routines.**read_stars**(*stars_table*)
Function to read the list of stars :param stars_table: list name (string) :return : array

reading_routines.**read_votable**(*folder_data*, *star*)
Function to read VO tables :param folder_data: folder data (string) :param star: star name (string) :return : wave, flux, sigma

1.6 Routine: Plotting Routines

Group of routines developed to plot the outputs of the inference process.

plot_routines.**par_errors**(*flatchain*)
Most likely parameters and respective asymmetric errors

Usage: par, errors = par_errors(flatchain)

Parameters **flatchain** – array

:return : par, errors

plot_routines.**plot_fit_last**(*par*, *lbd*, *logF*, *dlogF*, *minfo*, *listpar*, *lbdarr*, *logF_grid*, *isig*, *dims*, *Nwalk*, *Nmcmc*, *ranges*, *include_rv*, *npy*, *log_scale*, *model*)
Plots best model fit over data

Usage: plot_fit(par, lbd, logF, dlogF, minfo, logF_grid, isig, Nwalk, Nmcmc) where par = np.array([Mstar, oblat, Sig0, Rd, n, cosi, dist])

Parameters

- **par** – free parameters (array)

- **lbd** – observed wavelength (array)
- **logF** – observed flux (array)
- **dlogF** – observed flux error (array)
- **minfo** – models informations (matrix)
- **listpar** – list of parameters (array)
- **lbdarr** – model wavelenght (array)
- **logF_grid** – grid of models (array)
- **isig** – internal parameter
- **dims** – internal parameter
- **Nwalk** – number of walkers (integer)
- **Nmcmc** – number of steps (integer)
- **ranges** – ranges of the grid parameters (array)
- **include_rv** – set rv as free parameter (boolean)
- **npy** – npy file (string)
- **log_scale** – boolean
- **model** – grid model (string)

:return : figures

plot_routines.**plot_residuals**(*par*, *lbd*, *logF*, *dlogF*, *minfo*, *listpar*, *lbdarr*, *logF_grid*, *isig*, *dims*, *Nwalk*, *Nmcmc*, *ranges*, *include_rv*, *npy*, *log_scale*, *model*)

Plots best model fit over data

Usage: plot_fit(par, lbd, logF, dlogF, minfo, logF_grid, isig, Nwalk, Nmcmc) where par = np.array([Mstar, oblat, Sig0, Rd, n, cosi, dist])

Parameters

- **par** – free parameters (array)
- **lbd** – observed wavelength (array)
- **logF** – observed flux (array)
- **dlogF** – observed flux error (array)
- **minfo** – models informations (matrix)
- **listpar** – list of parameters (array)
- **lbdarr** – model wavelenght (array)
- **logF_grid** – grid of models (array)
- **isig** – internal parameter
- **dims** – internal parameter
- **Nwalk** – number of walkers (integer)
- **Nmcmc** – number of steps (integer)
- **ranges** – ranges of the grid parameters (array)
- **include_rv** – set rv as free parameter (boolean)

- **npy** – npy file (string)
- **log_scale** – boolean
- **model** – grid model (string)

:return : figures

plot_routines.**print_output**(*params_fit*, *errors_fit*)
Function to print output results :param params_fit: array :param errors_fit: array :return : results

1.6.1 Routine: Chord Diagram

Module with the functions used to create the chord diagram.

chord_diagram.**chord_plot**(*folder*, *file*)
Function that plots the chord plot for the stellar grid :param Xc: folder data (string) :param file: file name (string) :return: figure

chord_diagram.**chord_plot_complete**(*folder*, *file*)
Function that plots the chord plot for the disk+star grid :param Xc: folder data (string) :param file: file name (string) :return: figure

chord_diagram.**chord_plot_pol**(*folder*, *file*)
Function that plots the chord plot for polarization measurements :param Xc: folder data (string) :param file: file name (string) :return: figure

1.6.2 Routine: Convergence Routines

Module with the functions developed to make the convergence routines.

convergence_routines.**plot_convergence**(*npy*, *file_name*, *model*)
Function to plot the convergence :param npy: npy file (string) :param file_name: file name (string) :param model : model name (string) :return: figure

CHAPTER

TWO

INDICES AND TABLES

- genindex
- modindex
- search

PYTHON MODULE INDEX

INDEX

Appendix D

Thesis article

Astronomy & Astrophysics manuscript no. output
October 21, 2018

BeAtlas: A grid of synthetic spectra for Be stars

I. Application: the Bayesian inference of physical properties of main-sequence hot stars

B. C. Mota[1], A. C. Carciofi[1], R. G. Vieira[1], D. M. Faes[1], M. R. Ghoreyshi[1], L. R. Rímulo[1], D. Bednarski[1], A. L. Figueiredo[1], D. B. Seriacopi[1] and A. Rubio[1].

Instituto de Astronomia, Geofísica e Ciências Atmosféricas, Universidade de São Paulo, Rua do Matão 1226, Cidade Universitária, 05508-900, São Paulo, SP, Brazil, bruno.mota@usp.br, carciofi@usp.br, moser@usp.br

Received July 20, 2018; accepted November 05, 2018

ABSTRACT

Context. Be, Bn, Ae and Oe stars are fast rotators in the main sequence phase or at the beginning of the subgiant phase. The rapid rotation and the presence of circumstellar disks in active phases imply in a profound modification of the photospheric parameters whose impact on the observables are not fully characterized.
Aims. Our goal is to infer stellar, disk, geometrical parameters, and the interstellar extinction, without neglecting their uncertainties and correlations, for one specific case (β CMi) and for a set of rapid rotating main sequence stars. For such a purpose, we make use of different observables.
Methods. The modern statistical procedure employed by the code EMCEE and stellar parameters based on evolutionary models of the astrophysics group of University of Geneva are used. To constrain the solutions, domain knowledge of $v \sin i$ and parallax are applied.
Results. We provide a useful new inference tool for the Monte Carlo Markov Chain modeling of Be stars and hot main-sequence O, B and A stars. Our tool includes important effects due to the rapid rotation. The potential of the observables in constraining the stellar parameters is discussed. A catalog of the inferred parameters and a discussion about their correlations are shown. We also present the first multi-technique treatment of an late-type Be star, β CMi.
Conclusions. The correlations found show that the parameters are coupled. This corroborates the hypothesis that an independent inference of any parameter could propagate errors. For β CMi, the analysis reveals a circumstellar disk truncated by a companion or a dissipating disk. Moreover, our results suggest a later sub-spectral type (B3/4) than the inferred from previous studies.

Key words. Stars: emission-line, Be, Oe, Ae, Bn, B, circumstellar matter, rotation, fundamental parameters, β CMi, HD58715, HR2845. ISM: dust, extinction. Astronomical databases: miscellaneous. Techniques: photometric, polarimetric. Methods: statistical.

1. Introduction

The B spectral domain comprises several complex subclasses of stars, including the non-supergiant, main-sequence B whose spectrum has, or had at some time, one or more Balmer lines in emission (Jaschek et al. 1981; Collins 1987), the Classical Be stars (hereafter, CBe). They are notoriously recognized by their outwardly diffusing gaseous, dust-free Keplerian circumstellar disk (hereafter, CSD) that arises in active phases (Rivinius et al. 2013) and by showing the highest rotation rates among the main-sequence (MS) stars (Granada & Haemmerlé 2014) (e.g. Townsend et al. 2004; Frémat et al. 2005).

Since the discovery of the CBe, many efforts have been made to understand their characteristics. For instance, the observational techniques progress in the last decades has provided the basis data to study these objects. Adding this to the advances in our understanding of Be star theory and in the computational simulations, our knowledge of the physics of Be stars and their detailed theoretical models reached an unprecedented level (Sect. 2). These efforts allowed us to draw a wide overview regarding the *Be phenomenon*. The current status progress is partially summarized in the review paper Rivinius et al. (2013), but since then many other theoretical and observational works have added to our knowledge (Sect. 1.1).

The life cycle of a Be CSD is quite complex, since the vast majority of Be stars shows variability in different temporal scales (e.g. Rivinius et al. 2001; Draper et al. 2011), the dynamical evolution of the disk depends strongly on the mass injection rates. Different scenarios of mass injection rates have already been studied by Haubois et al. (2012) and are beyond the scope of this paper. Conceptually, the disk formation starts from material ejected from the star through some still unknown process (Sect. 1.1). After being ejected, the material starts to be diffused outwards by viscous torques resulting in the formation of a decretion CSD. The dissipation of the CSD, after cease the injection of matter, part of the material in the inner disk is re-accreted onto the star, providing the necessary angular momentum to diffuse the disk outwardly (e.g. Ghoreyshi et al. 2018). The current paradigm that comprises the theory behind the CSD of CBe is the viscous decretion disk model (VDD, Sect. 1.1).

The study of Be stars is essential for several reasons. For instance, despite the paucity of massive stars[1], they play a crucial role in the evolution of the Universe, being regarded as one of

[1] The terms massive star and high-mass star denote OB stars sufficiently massive to produce type II supernovae ($M_\star / M_\odot > 8$) to the solar abundances. Then, the term high-mass protostar denotes objects with $M_\star / M_\odot > 8$ which have not started the hydrogen burning.

Appendix E

Stellar parameters of Be stars observed with X-shooter

A&A 609, A108 (2018)
DOI: 10.1051/0004-6361/201731536

Astronomy & Astrophysics

Stellar parameters of Be stars observed with X-shooter[⋆,⋆⋆]

A. Shokry[1,2,3], Th. Rivinius[1], A. Mehner[1], C. Martayan[1], W. Hummel[4], R. H. D. Townsend[5], A. Mérand[1], B. Mota[6], D. M. Faes[6], M. A. Hamdy[2,⋆⋆⋆], M. M. Beheary[7], K. A. K Gadallah[7], and M. S. Abo-Elazm[2]

[1] ESO – European Organisation for Astronomical Research in the Southern Hemisphere, Casilla 19001, Santiago, Chile
e-mail: ahmedsh2911@gmail.com
[2] Astronomy Department, National Research Institute of Astronomy and Geophysics (NRIAG), 11421 Helwan, Cairo, Egypt
[3] Kottamia Center of Scientific Excellence in Astronomy and Space Science (KCScE, STDF, ASRT), Cairo, Egypt
[4] ESO – European Organisation for Astronomical Research in the Southern Hemisphere, Karl-Schwarzschild-Str. 2, Garchingnwt, Germany
[5] Department of Astronomy, University of Wisconsin-Madison, Madison, WI 53706, USA
[6] Instituto de Astronomia, Geofísica e Ciências Atmosféricas, Universidade de São Paulo (USP), Rua do Matão 1226, Cidade Universitária, 05508-900 São Paulo, Brazil
[7] Astronomy and Meteorology Department, Faculty of Science, Al-Azhar University, Cairo, Egypt

Received 9 July 2017 / Accepted 26 October 2017

ABSTRACT

Aims. The X-shooter archive of several thousand telluric standard star spectra was skimmed for Be and Be shell stars to derive the stellar fundamental parameters and statistical properties, in particular for the less investigated late-type Be stars and the extension of the Be phenomenon into early A stars.
Methods. An adapted version of the BCD method is used, using the Balmer discontinuity parameters to determine effective temperature and surface gravity. This method is optimally suited for late B stars. The projected rotational velocity was obtained by profile fitting to the Mg II lines of the targets, and the spectra were inspected visually for the presence of peculiar features such as the infrared Ca II triplet or the presence of a double Balmer discontinuity. The Balmer line equivalent widths were measured, but they are only useful for determining the pure emission contribution in a subsample of Be stars owing to uncertainties in determining the photospheric contribution.
Results. A total of 78, mostly late-type, Be stars, were identified in the X-shooter telluric standard star archive, out of which 48 had not been reported before. We confirm the general trend that late-type Be stars have more tenuous disks and are less variable than early-type Be stars. The relatively large number (48) of relatively bright ($V > 8.5$) additional Be stars casts some doubt on the statistics of late-type Be stars; they are more common than currently thought. The Be/B star fraction may not strongly depend on spectral subtype.

Key words. circumstellar matter – stars: emission-line, Be – stars: activity

1. Introduction

Be stars are non-supergiant B stars that show or have shown Hα emission, as defined by Jaschek et al. (1981). Emission does not only occur in the first members of the Balmer line series, but can affect the continuum and line profiles of other species as well, most often singly ionized metals, such as Fe II. It is generally agreed that, in classical Be stars, this emission is due to the presence of a gaseous Keplerian disk that is concentrated in the equatorial plane. This disk is a decretion disk, i.e., the source of the disk material is the central star, generated by the equatorial flow of stellar material. One of the key factors in creating the disk is supposed to be the very high rotational velocity. In fact, Be stars are known to have higher rotational velocities than normal B-type stars (Catanzaro 2013). For a complete review on the topic, see Porter & Rivinius (2003) and Rivinius et al. (2013a).

Classical Be stars are known to vary both in brightness and spectral line appearance with a large range of timescales from years to minutes (Okazaki 1997; Floquet et al. 2002; Kogure & Leung 2007). While long-term variations are associated with formation and dissipation of the disk (Okazaki 1997), the origin of short-term variability is usually attributed to pulsations within the B star photosphere (Baade 2000; Huat et al. 2009). Photometric studies show that earlier type Be stars are more likely to be variable (e.g., Hubert & Floquet 1998).

Chojnowski et al. (2015) have demonstrated that Be stars can often be found among stars observed for the purpose of removing telluric absorption in the near-infrared domain because main sequence B stars are among the preferred objects for this task. Inspired by this example, we decided to search for Be stars in a similarly extensive database of telluric standard star observations, namely that taken at the Very Large Telescope (VLT) with the X-shooter instrument.

2. Observations and data reduction

All spectra were acquired with the VLT/X-shooter instruments. Most data were taken as telluric standard stars for other observations from the commissioning of X-shooter in 2007 until

⋆ Based on observations made with ESO Telescopes at the La Silla Paranal Observatory under program IDs 60.A-9022, 60.A-9024, 077.D-0085, 085.A-0962, 185.D-0056, 091.B-0900, and 093.D-0415.
⋆⋆ Table 6 is only available at the CDS via anonymous ftp to cdsarc.u-strasbg.fr (130.79.128.5) or via http://cdsarc.u-strasbg.fr/viz-bin/qcat?J/A+A/609/A108
⋆⋆⋆ Deceased.

Appendix F

Revealing the structure of the outer disks of Be stars

Astronomy & Astrophysics manuscript no. 29932JN
March 22, 2017

Revealing the structure of the outer disks of Be stars⋆

R. Klement[1,2], A. C. Carciofi[3], T. Rivinius[1], L. D. Matthews[4], R. G. Vieira[3], R. Ignace[5], J. E. Bjorkman[6], B. C. Mota[3], D. M. Faes[3], A. D. Bratcher[6], M. Curé[7], and S. Štefl⋆⋆

[1] European Southern Observatory, Alonso de Córdova 3107, Vitacura, Casilla 19001, Santiago, Chile
e-mail: robertklement@gmail.com
[2] Astronomical Institute of Charles University, Charles University, V Holešovičkách 2, 180 00 Prague 8
[3] Instituto de Astronomia, Geofísica e Ciências Atmosféricas, Universidade de São Paulo, Rua do Matão 1226, Cidade Universitária, 05508-090, São Paulo, SP, Brazil
[4] MIT Haystack Observatory, off Route 40, Westford MA 01886, USA
[5] Department of Physics & Astronomy, East Tennessee State University, Johnson City, TN 37614, USA
[6] Ritter Observatory, Department of Physics & Astronomy, University of Toledo, Toledo, OH 43606, USA
[7] Instituto de Física y Astronomía, Facultad de Ciencias, Universidad de Valparaíso, Casilla 5030, Valparaíso, Chile

ABSTRACT

Context. The structure of the inner parts of Be star disks ($\lesssim$ 20 stellar radii) is well explained by the viscous decretion disk (VDD) model, which is able to reproduce the observable properties of most of the objects studied so far. The outer parts, on the other hand, are not observationally well-explored, as they are observable only at radio wavelengths. A steepening of the spectral slope somewhere between infrared and radio wavelengths was reported for several Be stars that were previously detected in the radio, but a convincing physical explanation for this trend has not yet been provided.
Aims. We test the VDD model predictions for the extended parts of a sample of six Be disks that have been observed in the radio to address the question of whether the observed turndown in the spectral energy distribution (SED) can be explained in the framework of the VDD model, including recent theoretical development for truncated Be disks in binary systems.
Methods. We combine new multi-wavelength radio observations from the Karl. G. Jansky Very Large Array (JVLA) and Atacama Pathfinder Experiment (APEX) with previously published radio data and archival SED measurements at ultraviolet, visual, and infrared wavelengths. The density structure of the disks, including their outer parts, is constrained by radiative transfer modeling of the observed spectrum using VDD model predictions. In the VDD model we include the presumed effects of possible tidal influence from faint binary companions.
Results. For 5 out of 6 studied stars, the observed SED shows strong signs of SED turndown between far-IR and radio wavelengths. A VDD model that extends to large distances closely reproduces the observed SEDs up to far IR wavelengths, but fails to reproduce the radio SED. Using a truncated VDD model improves the fit, leading to a successful explanation of the SED turndown observed for the stars in our sample. The slope of the observed SEDs in the radio is however not well reproduced by disks that are simply cut off at a certain distance. Rather, some matter seems to extend beyond the truncation radius, where it still contributes to the observed SEDs, making the spectral slope in the radio shallower. This finding is in agreement with our current understanding of binary truncation from hydrodynamical simulations, in which the disk does extend past the truncation radius. Therefore, the most probable cause for the SED turndown is the presence of binary companions that remain undetected for most of our sources.

Key words. Stars: emission-line, Be – Stars: circumstellar matter – Stars: binaries: general – Radio continuum: stars – Submillimeter: stars

1. Introduction

Be stars offer unique possibilities for studying circumstellar disks. Because they are common among the bright, nearby stars – 17% of B-type stars are Be stars (Zorec & Briot 1997) – their disks are among typical targets for modern optical/near-infrared interferometers that have resolved them at the milliarcsec level. As a result, the structure of the inner parts of the disks is now well understood in the framework of the viscous decretion disk (VDD) model, first proposed by Lee et al. (1991) and further developed by, for example, Bjorkman (1997), Porter (1999), Okazaki (2001), and Bjorkman & Carciofi (2005). The central stars rotate close to break-up velocities, and an uncertain mechanism – the so-called Be phenomenon – acts in addition to rotation, leading to episodic or continuous mass ejection from the stellar equator. Subsequently, outflowing, ionised, purely gaseous disks, rotating in a nearly Keplerian way are formed (see Rivinius et al. 2013, for a recent review). In the VDD model, it is the turbulent viscosity that is responsible for the transport of the angular momentum outwards, and therefore for the growth of the disk.

In the last decades, observational techniques such as spectroscopy, linear polarimetry, and optical/near-IR interferometry have been used to constrain the physical structure of VDDs. Combining polarimetric and interferometric measurements, the disk-like structure of the circumstellar matter was unambiguously confirmed (Quirrenbach et al. 1997) and the rotation law was subsequently confirmed to be nearly Keplerian (Meilland et al.

⋆ Based on observations from the Karl J. Jansky Very Large Array collected via programme 10B-143, on observations from APEX collected via CONICYT programmes C-092.F-9708A-2013 and C-095.F-9709A-2015 and on observations from CARMA collected via programme c1100-2013a.
⋆⋆ Deceased

Appendix G

Disk-loss and disk-renewal phases in classical Be stars. II. Constrating with stable and variable disks

The Astrophysical Journal, 786:120 (15pp), 2014 May 10 doi:10.1088/0004-637X/786/2/120

DISK-LOSS AND DISK-RENEWAL PHASES IN CLASSICAL Be STARS. II. CONTRASTING WITH STABLE AND VARIABLE DISKS

Zachary H. Draper[1,2], John P. Wisniewski[3], Karen S. Bjorkman[4], Marilyn R. Meade[5], Xavier Haubois[6,7], Bruno C. Mota[6], Alex C. Carciofi[6], and Jon E. Bjorkman[4]
[1] Department of Physics and Astronomy, University of Victoria, 3800 Finnerty Rd, Victoria, BC V8P 5C2, Canada
[2] Herzberg Institute of Astrophysics, National Research Council of Canada, Victoria, BC V9E 2E7, Canada
[3] HL Dodge Department of Physics & Astronomy, University of Oklahoma, 440 W Brooks St, Norman, OK 73019, USA; wisniewski@ou.edu
[4] Ritter Observatory, Department of Physics & Astronomy, Mail Stop 113, University of Toledo, Toledo, OH 43606, USA; karen.bjorkman@utoledo.edu, jon@physics.utoledo.edu
[5] Space Astronomy Lab, University of Wisconsin-Madison, 1150 University Avenue, Madison, WI 53706, USA; meade@astro.wisc.edu
[6] Instituto de Astronomia, Geofísica e Ciências Atmosféricas, Universitária de São Paulo, Rua do Matão 1226, Cidade Universitária, 05508-900 São Paulo, SP, Brazil; xhaubois@astro.iag.usp.br, carciofi@usp.br
[7] Sydney Institute for Astronomy, School of Physics, University of Sydney, NSW 2006, Australia
Received 2013 December 6; accepted 2014 March 18; published 2014 April 24

ABSTRACT

Recent observational and theoretical studies of classical Be stars have established the utility of polarization color diagrams (PCDs) in helping to constrain the time-dependent mass decretion rates of these systems. We expand on our pilot observational study of this phenomenon, and report the detailed analysis of a long-term (1989–2004) spectropolarimetric survey of nine additional classical Be stars, including systems exhibiting evidence of partial disk-loss/disk-growth episodes as well as systems exhibiting long-term stable disks. After carefully characterizing and removing the interstellar polarization along the line of sight to each of these targets, we analyze their intrinsic polarization behavior. We find that many steady-state Be disks pause at the top of the PCD, as predicted by theory. We also observe sharp declines in the Balmer jump polarization for later spectral type, near edge-on steady-state disks, again as recently predicted by theory, likely caused when the base density of the disk is very high, and the outer region of the edge-on disk starts to self absorb a significant number of Balmer jump photons. The intrinsic V-band polarization and polarization position angle of γ Cas exhibits variations that seem to phase with the orbital period of a known one-armed density structure in this disk, similar to the theoretical predictions of Halonen & Jones. We also observe stochastic jumps in the intrinsic polarization across the Balmer jump of several known Be+sdO systems, and speculate that the thermal inflation of part of the outer region of these disks could be responsible for producing this observational phenomenon. Finally, we estimate the base densities of this sample of stars to be between $\approx 8 \times 10^{-11}$ and $\approx 4 \times 10^{-12}$ g cm^{-3} during quasi steady state periods given there maximum observed polarization.

Key words: circumstellar matter – stars: individual (pi Aquarii, 60 Cygni, 48 Librae, psi Persei, phi Persei, 28 Cygni, 66 Ophiuchi, gamma Casseopia, omega Orionis, FY CMa, 59 Cyg)

Online-only material: color figures, machine-readable tables

1. INTRODUCTION

Classical Be stars are a subset of B-type main sequence stars which are characterized by their rapid rotational velocities ranging from 60% to 100% of their critical rate (Rivinius et al. 2013). They have a geometrically flattened decretion disk that is fed by material from the stellar photosphere as diagnosed from studies of their optical/IR emission lines, polarization, and interferometric signatures (see, e.g., Porter & Rivinius 2003; Stee 2011). A large volume of observations suggest the kinematic properties of these gas disks is best represented by near Keplerian rotation (Hummel & Vrancken 2000; Meilland et al. 2007; Pott et al. 2010; Wheelwright et al. 2012; Kraus et al. 2012). For the most up to date review of Classical Be stars, see Rivinius et al. (2013).

As summarized in Carciofi (2011), the viscous decretion disk model developed by Lee et al. (1991) can explain many of the observational signatures of Be disks, although other models have been explored to explain the structure of these disks (Bjorkman & Cassinelli 1993; Cassinelli et al. 2002; Brown et al. 2008). One key unanswered question in the study of Be disks is what mechanism(s) are responsible for injecting material into these disks. Non-radial pulsations have been suggested to be one contributing factor to supplying material to some of these disks (Cranmer 2009; Rivinius et al. 1998; Neiner et al. 2002), while periastron passage of binary companions may contribute in other systems such as δ Scorpii (Miroshnichenko et al. 2001, 2003). This scenario for δ Scorpii is now questionable given the disk's growth prior to the periastron passage of 2011 (Miroshnichenko et al. 2013). Nonetheless, binarity may play a role in the phenomenon and disk variability. For example, the source of material and angular momentum in non-classical Be stars can be the result of a red giant phase binary transferring material to create a Be+sdO system Gies et al. (1998). Characterizing the evolution of Be stars' mass-loss rates is another promising approach to constrain the disk-feeding mechanism. On short time-scales, Carciofi et al. (2007) noted polarimetric variability in Archernar likely arising from injections of discrete blobs of mass into the inner disk, that subsequently circularize into rings. Studying longer duration disk-loss and disk-regeneration events (Underhill & Doazan 1982; Doazan et al. 1983; Clark et al. 2003; Vinicius et al. 2006; Haubois et al. 2012), including the time-scales (Wisniewski et al. 2010) and statistical frequency (McSwain et al. 2008, 2009) of these episodes, is another way to diagnose the mechanism feeding Be disks.

Polarimetry has been used to study the Be phenomenon for both individual Be stars (Quirrenbach et al. 1997; Wood et al. 1997; Clarke & Bjorkman 1998) and larger statistical

Appendix H

Dynamical evolution of viscous disks around Be stars. II. Polarimetry

The Astrophysical Journal, 785:12 (13pp), 2014 April 10 doi:10.1088/0004-637X/785/1/12

DYNAMICAL EVOLUTION OF VISCOUS DISKS AROUND BE STARS. II. POLARIMETRY

X. Haubois[1,2,3], B. C. Mota[2], A. C. Carciofi[2], Z. H. Draper[4,5], J. P. Wisniewski[6], D. Bednarski[2], and Th. Rivinius[7]
[1] LESIA, Observatoire de Paris, CNRS UMR 8109, UPMC, Université Paris Diderot, 5 place Jules Janssen, F-92195 Meudon, France; xavier.haubois@obspm.fr
[2] Instituto de Astronomia, Geofísica e Ciências Atmosféricas, Universidade de São Paulo, Rua do Matão 1226, Cidade Universitária, São Paulo, SP 05508-090, Brazil
[3] Sydney Institute for Astronomy, School of Physics, University of Sydney, NSW 2006, Australia
[4] Department of Physics and Astronomy, University of Victoria, 3800 Finnerty Road, Victoria, BC V8P 5C2, Canada
[5] Herzberg Institute of Astrophysics, National Research Council of Canada, Victoria, BC V9E 2E7, Canada
[6] H. L. Dodge Department of Physics and Astronomy, University of Oklahoma, 440 West Brooks St Norman, OK 73019, USA
[7] European Organisation for Astronomical Research in the Southern Hemisphere, Casilla 19001, Santiago 19, Chile
Received 2013 November 28; accepted 2014 February 8; published 2014 March 21

ABSTRACT

Be stars exhibit variability for a great number of observables. Putting the pieces of the disk dynamics together is not an easy task and requires arduous modeling before achieving a good fit to the observational data. In order to guide the modeling process and make it more efficient, it is very instructive to investigate reference dynamical cases. This paper focuses on continuum polarimetric quantities and is the second of a series that aims to demonstrate the capacity of deriving the dynamical history and fundamental parameters of a classical Be star through follow-up of various observables. After a detailed study of the different opacities at play in the formation of polarized spectra, we investigate predictions of polarimetric observables in the continuum for different dynamical scenarios. Our models are based on a coupling of a hydrodynamic viscous decretion simulations in a disk and a three-dimensional non-LTE radiative transfer code. Through introduction of the polarization color diagram (PCD), we show that certain combinations of polarimetric observables exhibit features that are characteristic of a mass-loss history. This diagram also enables estimates of fundamental parameters such as the inclination angle, disk density scale, and the α viscous diffusion parameter. We present the PCD as a powerful diagnosis tool to track the dynamical phases of a Be star, such as disk build-up, dissipation, periodic, and episodic outbursts. Finally, we confront our models with observations of four Be stars that exhibited long-term polarimetric activity.

Key words: circumstellar matter – radiative transfer – stars: emission-line, Be – stars: individual (π Aquarii, 60 Cygni, δ Scorpii and ψ Persei) – techniques: polarimetric

Online-only material: color figures

1. INTRODUCTION

Be stars are non-supergiant, early-type stars with a circumstellar (CS) disk that is created from matter ejected from the star. Recent observational facts brought by spectro-interferometry and spectro-astrometry (e.g., Meilland et al. 2012; Wheelwright et al. 2012) support the fact that so far, all studied Be star disks rotate in a Keplerian fashion. This characteristic, together with other observational signatures of the disk outlined in Carciofi (2011), are properties that only the viscous decretion disk (VDD) model can reproduce. This model, first suggested by Lee et al. (1991) and further developed by Bjorkman (1997), Porter (1999), Okazaki (2001), Bjorkman & Carciofi (2005), and Jones et al. (2008), among others, uses the angular momentum transport by turbulent viscosity to lift material into higher orbits, thereby causing the disk to grow in size. This model has already been successfully applied to systems showing stable continuum emission, e.g., ζ Tauri (Carciofi et al. 2009), χ Oph (Tycner et al. 2008), β CMi (Wheelwright et al. 2012), and systems exhibiting a more variable photometric activity (28 CMa; Carciofi et al. 2012). In a recent review paper, Rivinius et al. (2013) discuss in detail the observational and theoretical evidences in support of the VDD scenario for Be stars.

Polarization is a powerful tool to study the geometry of the disk (opening angle, flaring) of Be stars without angularly resolving it. Polarized flux originates from electron scattering off the disk, and is affected by both pre- and post-scattering absorption by H I atoms (Wood et al. 1996; Halonen & Jones 2013a). Since H I opacity depends on the physical state of the gas, studying polarimetric observables at different wavelengths allows one to probe different regions of the disk. In the literature, the polarimetric technique has an established history of providing a unique diagnosis in identifying and studying the detailed CS environments of Be stars (Wood et al. 1997; Carciofi et al. 2007, 2009; Wisniewski et al. 2010; Draper et al. 2011).

Haubois et al. (2012, hereafter Paper I), studied the temporal variability of Be disks, based on SINGLEBE VDD hydrodynamic simulations (Okazaki 2007). SINGLEBE solves the one-dimensional surface density evolution equation for a viscous isothermal Keplerian decretion disk. The effects of variable mass injection rates on the disk structure, and their corresponding effect on the photometry, were studied at different wavelengths and compared to observations. More specifically, we first studied the different timescales that characterize the evolution of the disk surface density and how this surface density responds to changes in mass injection rates. These surface density profiles were used as inputs to the three-dimensional non-LTE Monte Carlo radiative transfer code HDUST (Carciofi & Bjorkman 2006, 2008) that allowed the calculation of photometric observables at various wavelengths. The characteristic shapes of these lightcurves agree qualitatively well with observations, which provide strong circumstantial evidence that viscosity is indeed the mechanism that redistributes matter along the CS disk. The first successful confrontation of theoretical VDD lightcurves with observations was done by Carciofi et al. (2012) for the Be star 28 CMa. To summarize, Paper I provides the reader with a description of the photometric variability from a Be star in the framework of the VDD model. With the present

Appendix I

ESO Short-term internship

Project Report: "Binarity and the distribution of rotational velocities in Galactic main-sequence B stars"

Release 2.5

B. C. Mota, C. Martayan, T. Rivinius, D. Moser and A. Shoky

April 15, 2016

CONTENTS

ii

Project Report: "Binarity and the distribution of rotational velocities in Galactic main-sequence B stars", Release 2.5

For several types of stars the distribution of rotational velocities (v sini) is bi- or even multi-modal and is a key tracer of star formation and evolution. Binarity and magnetism are among the main contenders for the explanation. Nominally, the frequency of binaries is a strong function of stellar mass, and the distribution of vsini values appears bimodal in O and A stars and the situation is unclear in B stars (flat or bimodal distribution). But this may be entirely spurious. The sample of telluric standard stars used with X-shooter offers a both large and inexpensive initial database comprising more than a thousand B-type stars. The proposed project aims at consolidating and homogenizing the database, extracting the fraction of binaries and the distribution of v sini for analysis in a star formation and evolution context, and improving the quality of telluric standard stars available for X-shooter and other Paranal instruments.

Full goals:

1. Inspect the data and reduce all spectra with an homogeneous manner and with adapted parameters depending on the sky condition and objects. It is not possible to use the automatically reduced data from the archive because of:

1. the very different sky conditions (extraction problem);
2. the presence of visual binaries/companions (extraction problem);
3. the response curve used is an old one;

2. find the binaries in the sample, looking at the acquisition frames, at the spectra (SB2 or multiple stars from the U to the K band), and with the radial velocity follow-up (SB1);
3. determine if the binaries may have an impact on the evolution and day to day life of the main star of the system;
4. determine the fundamental parameters (T_{eff}, logg, vsini, M, etc) and create observational tracks of the rotational velocity evolution in the Main Sequence for B stars. Determine the chemical abundances. And for the binaries to determine the orbital parameters if possible;
5. provide clean catalogues of telluric standard stars (good spectral classification, no binary) to Paranal and other observatories. This legacy aspect was highlighted by the OPC in its comments;
6. give constraints to the theoretical models and cooperate with the Geneva team lead by G. Meynet.

The purpose of this DGDF is to get some help on items a and b. The project at longer time scale is to obtain a student with Geneva to work on other items and enlarge the cooperation observations/theory.

Project Report: "Binarity and the distribution of rotational velocities in Galactic main-sequence B stars", Release 2.5

CHAPTER

ONE

INTRODUCTION

The B stars represent a significant fraction of massive stars. If only stochastic processes at the time of formation govern the distribution of rotational velocities, the distribution of the latter in any sample of stars of similar age and mass should be smooth and in particular not have multiple maxima. However, exactly the latter is observed in some groups of stars. For both O and A stars the rotational velocity distribution appears to be bimodal. For A main sequence stars (cleaned of binaries and peculiar stars), Royer et al. (2007, A&A,463,671) found this bimodal distribution and explained it by an angular momentum loss and its redistribution in the star before it reaches the main sequence (MS). Zorec & Royer (2012,A&A,537,A120) studied the evolution of A type stars rotational velocities and found 2 different behaviours. The less massive A stars have a monomodal equatorial velocity distribution and have a monotonical acceleration with age during the MS. The most massive A stars show a strong acceleration in the first third part of MS but do not show any angular momentum redistribution in the last third of the MS, which could be related to some differential rotation. Guthrie (1982,MNRAS,198,795) also found a bimodal rotational velocity distribution for late B stars in open clusters while B stars in the field show a flat distribution. The author argues that this difference should come from the way the stars formed.

While Abt et al. (2002, ApJ,573,359) explain that the distributions are massdependent and would be explained by magnetic braking or the presence of lowmass companion or planets. Dufton et al. (2013, A&A, 550, A109) also found for late O to early B in the LMC clusters of the Tarantula region a bimodal or even more complex rotational velocity distribution. They argue that this could be explained by similar mechanism that occurs in A type stars. However, if potential binaries are removed, because the spectral classification has not been performed, one cannot disentangle the effects of stellar evolution from original multi-modal distribution of the rotational velocities.

1.1 Impact on the stellar models

Standard evolutionary tracks do not explain this. The two most relevant additional ingredients are magnetic braking and spin-up in binaries through mass transfer or even mergers. Not only have these properties opposite effects but each of them alone can lead to a bi-modal distribution. Moreover, in binaries, the distribution of angular momentum between spin and orbit introduces an additional complex parameter during the period of their formation. The challenge is to disentangle them, especially if binarity and magnetic-field strength depend on mass. An obvious prerequisite for an improved understanding is to know the initial frequencies of relevant binarity and magnetism. Here, we focus on the binarity of at most moderately evolved B-type stars. In addition this knowledge would possibly also allow understanding some discrepancies between theoretical models of stellar and chemical evolution and some observational results (Hunter et al. 2007,A&A,466,277). Possibly unknown angular momentum transfer phenomenon may have to be discovered and taken into account in the models.

1.2 Binarity

To avoid a bias one must find first the binaries in the sample. The fraction of binaries can reach up to 75 % of O stars (Sana et al. 2012, Sci,337, 444), while the fraction for A-type stars would be around 50 % (Duchene

Project Report: "Binarity and the distribution of rotational velocities in Galactic main-sequence B stars", Release 2.5

& Kraus 2013,ARA&A,51,269) and for F to G type stars this fraction would also be around 55 % (Raghavan et al.,2010,ApJS,190,1). However, the situation for B stars is not so clear and the estimates differ a lot from a study to another. For instance Abt et al. (1990,ApJS,74,551) found about 30 % of spectroscopic binaries in their sample with potentially 40 % more of visual binaries (without certainty whether they are bound or not). Raboud (1996,A&A,315,384) evaluated it in the NGC6231 cluster to be about 52 %, Martayan et al. (2008,A&A,489,459) found a binary fraction of 27 % in NGC6611, while Oudmajer et al. (2010,MNRAS,405,2439) estimated the B binary fraction to range from 22 to 38 % with NACO adaptive optics images. Chini et al. (2012,MNRAS,424,1925) found that the binary fraction varies with the stellar mass and ranges from 80 % for O stars to 60-70 % for early-B stars and 20-40 % for late B stars. Indeed Duchene & Kraus (2013,ARA&A,51,269) indicate a B binary fraction ranging from 40 to 60 %. Recently Nasseri et al. (2013,CEAB,37,51) with a spectroscopic monitoring found a similar B binary fraction ranging from 50% in early types to 15% in late types with orbital periods from 1 to 1000 days. Such a discrepancy between the fraction of O binaries (70-80 %) and B binaries (70-20 %), while for A binaries it is 50 %, is difficult to believe. It would indicate a different star formation mechanism for creating B stars while it is still critical to reduce the angular momentum during the star formation. The obvious possibility to decrease it is to form binaries with stellar or planetary companions.

CHAPTER

TWO

OBSERVATIONAL DATA

2.1 The sample

The sample is based on the observatory project 093.D-0415(A,B,C) PI: Martayan.

1. About 200 B stars were observed in this project.
2. About 2500 science spectra were obtained.
3. 65% complete in term of OBs and time (strongly vary with the run)
   (a) run A: 162 of 190 OBs, 85.3%, 29.1 of 34h, 85.5%
   (b) run B: 116 of 204 OBs, 56.9%, 19.4 of 34h, 57.0%
   (c) run C: 58 of 126 OBs, 46.0%, 9.7 of 21h, 46.2%

In addition to the observations, most of the stars have 1 to 3 spectra in the X-Shooter archive:

- Run A, at least 1 spectrum in the archive, and for run B and run C, generally at least 2 spectra;
- In total each object has about 4 to 6 different epochs of observation;
- The objects were observed under photometric transparency to thick clouds, seeing of 0.6” to 4”, Full Moon or no Moon;
- Some of the objects are known to host a binary companion or an exoplanet candidate. They will be used as test bench to probe the radial velocity accuracy and stability of X-Shooter on real data.

2.2 The instrument

X-Shooter is a single target spectrograph for the Cassegrain focus of one of the VLT UTs (Vernet et al. 2011, A&A, 536A, 105), convering, in a single exposure, the spectral range from the UV to the K’ band (300-2500 nm) at intermediate spectral resolution (R ~ 4000-17000, depending on wavelength and slit width) with fixed echelle spectral format. The instrument consists of four arms with two cameras, namely: Aquisition and Guinding. The 3 spectroscopic arms cover the ranges:

1. UVB - 300-559.5 nm
2. VIS - 559.5-1024 nm
3. NIR - 1024-2480 nm

Project Report: "Binarity and the distribution of rotational velocities in Galactic main-sequence B stars", Release 2.5

CHAPTER

THREE

TOOLS

In this chapter, we describe the tool used to do the data reduction, and the three python routines developed to study the reduced data: Py-XShooter, PharaohUS, and calc_vsini.

3.1 Reflex

Reflex is the ESO Recipe Flexible Execution Workbench recommended in the reduction of ESO data. This recipe offers some facilities to the user, such as a global graphical vision of the data reduction cascade (workflow), for more details we suggest the reading of Freudling et al. 2013. Briefly, this recipe automatically organizes input files according to their category before run the reduction chain. The user has the option to inspect and interact in each reduction step, having the possibility of rerun any step.

3.1.1 Installation

In order to install the *eso-reflex*, we suggest the procedure described in http://www.eso.org/sci/software/pipelines/reflex_workflows/index.html. After that, it is important to define the amount of memory that will be reserved to the Reflex, it may be done by the command line */bin/esoreflex_set_memory* (p.e. 1024; 2018m).

3.1.2 Reduction

Reflex X-shooter Tutorial can be acessed in ftp://ftp.eso.org/pub/dfs/pipelines/xshooter/. The raw data was reduced following the procedure described in the manual **xshoo-pipeline-manual-12.7.pdf**. The results from this recipe are generally very robust with the default parameters, then, after some attempts to improve the residuals, we have decided to adopt the default parameters in the workflow. Basically, as simple procedure we must access the esoreflex and define the folders where are the raw data and where the results will be saved. After, the data organisation process is done automatically by the recipe. A simple reduction procedure is,

1. Uncompress the data before executing Reflex;
2. $esoreflex &
3. open the X-shooter workflow by clicking on File -> Open File, selecting the file xshoo-2.6.8/xshooter.xml;
4. Tools -> Animate at Runtime, enter the number of milliseconds representing the animation interval (1 ms is recommended);
5. Under “Setup Directories” in the workflow canvas there are seven parameters that specify important directories (green dots). When you have finished, click OK to save your changes;
6. Play start button;
7. Follow the workflow.

Project Report: "Binarity and the distribution of rotational velocities in Galactic main-sequence B stars", Release 2.5

The final products that are copied and renamed are:

1. *<HIERARCH.ESO.OBS.NAME>_SCI_SLIT_FLUX_MERGE1D_<ARM>.fits* - The flux-calibrated, extracted and merged science spectrum. This product is only generated if an appropriate instrument response curve (master or otherwise) was used as an input to the Science Reduction actor.
2. *<HIERARCH.ESO.OBS.NAME>_SCI_SLIT_MERGE1D_<ARM>.fits* - The extracted and merged science spectrum.
3. *<HIERARCH.ESO.OBS.NAME>_SCI_SLIT_MERGE2D_<ARM>.fits* - The merged 2-dimensional science spectrum.
4. *<HIERARCH.ESO.OBS.NAME>_SKY_SLIT_MERGE1D_<ARM>.fits* - The merged 2-dimensional sky spectrum (not for nodding mode data).
5. *<HIERARCH.ESO.OBS.NAME>_SCI_SLIT_IDP_<ARM>.fits* - The corresponding final 1D extracted spectra in a format compatible with the Science Data Product Standard needed to submit files to ESO's Science Archive Facility. The standard itself is described in http://www.eso.org/sci/observing/phase3/p3sdpstd.pdf and tips on how to handle the data with common tools are here http://archive.eso.org/cms/eso-data/help/1dspectra.html.

3.2 PY-XShooter

PY-XShooter is an python routine developed to generate, in an easy way, the desired outputs by the user. This routine depends on several python packages: numpy, matplotlib, astropy, pyfits, gzip, re, scipy, math, astropy, csv, astroquery, aplpy, lineid_plot, pyhdust, pyraf, ureka.

3.2.1 Running

To run the routine is required to define the folders where are the input files (raw data to create the images, tag **input_data_raw**, and the end products data to create the science figures, tag **input_data**). Having defined these folders, the user must define the path where the routine is installed in the tag **commum_folder**.

Having defined properly all folders and options, the code can be runned in terminal by typing

```
ur_setup
python xshooter.py or ipython xshooter.py
```

The routine creates a folder with the following structure for each star observed:

1. Star name
   (a) lines
   (b) sed
   (c) images
   (d) bcd
   (e) vsini

Important: This structure is preserved when is started the second step, i.e. when the routine PharaohUS begins to calculate the stellar parameters (see details in the next section).

Inside the folder **lines**, all given lines (defined in lists for each xshooter arm) are saved separatelly, i.e. one by folder. Each of these folders contains three files: two for the line profile (flux vs wavelength and flux vs velocity) and one showing the temporal evolution of the line equivalent width.

The second folder, **sed**, two files, one with all sed's plotted in only one plot area, and another with the fluxes separeted by arm.

The folder **images** has the aquisition images taken from the raw data. These figures can be used in order to check for potential visual companion.

The folder **bcd** has the results of the BCD analysis (which is not impacted by the circumstellar environment). In this folder, we have a text table with the inferred fundamental stellar parameters (Teff, logg, etc), a figure illustrating BCD procedure, and four figures that show the resulting interpolation for each stellar parameter.

The last folder, **vsini**, contains the results for the independently calculated vsini for each X-Shooter arm.

3.2.2 Some Options

There are five variables that can be modified:

1. interact = 'yes' or 'no'
2. plot_images = True or False
3. plot_sed_lines = True or False
4. delta = 50. #Angstrom

Trought the option *interact*, the user could visualize the normalization by interacting with an iraf window. Then, it is possible to check the quality of the normalization, as well as change some standard adopted parameters.

The option *plot_images* is used for the cases in which the user is not interested in save the aquisition images. If this option is True, the images will be saved automatically in the same folder from that of the science figures.

The option *plot_sed_lines* should be equal True, if you want to generate the science figures (line profiles, SEDs, the BCD analysis results, and inferred stellar parameters).

Delta is the range around the line that must be considered during the simulation. This value must be choosen correctly, otherwise it is possible to take another line during the simulation, instead of the correct one.

Following are the description of the functions in this routine:

`py_xshooter.`**`bcd_analysis`**(*obj*, *wave*, *flux*, *flux_norm*, *folder_fig*)
This function performs the BCD analysis.

Parameters

- **`obj`** – star name (string)
- **`wave`** – Array with the wavelenghts in Angstrom (numpy array)
- **`flux`** – Array with the fluxes (numpy array)
- **`flux_norm`** – Array with the normalized fluxes (numpy array)
- **`folder_fig`** – folder where the figures will be saved (string)

Star_name star name (string)

Returns D and lambda_0 (BCD parameters)

`py_xshooter.`**`calc_dlamb`**(*wave*, *flux*, *center_wave*, *delta*)
This function calculates the shift of the line.

Parameters

- **`wave`** – Observed wavelenght of the line (float, ex: 6562.81 #AA)
- **`flux`** – Array with the fluxes (numpy array)
- **`center_wave`** – Lab central wave (float)
- **`delta`** – range to be considered around the lamb_obs (float)

Project Report: "Binarity and the distribution of rotational velocities in Galactic main-sequence B stars", Release 2.5

Returns delta lambda (float)

py_xshooter.**create_class_object**(*list_files*, *obj*)
Create object class for all targets in a list.

Parameters **list_files** – list of XShooter fits files (array)

Returns data (class object)

py_xshooter.**create_images**(*list_files*, *folder_fig*)
Plot the images for each observed star from the aquisition images.

Parameters

- **list_files** – list of XShooter fits files (array)
- **folder_fig** – folder where the figures will be saved (string)

Returns images

py_xshooter.**create_list_files**(*list_name*, *folder*, *folder_table*)
Creates a list of the files inside a given folder.

Parameters

- **list_name** – list's name (string)
- **folder** – files' folder (string)

Returns creates a txt file, with the files' paths

py_xshooter.**create_list_stars**(*list_files*)
Create list of the observed stars.

Parameters **list_files** – text list with the files' paths

Returns list of stars (array)

py_xshooter.**create_list_stars_img**(*list_files*)
Create list of the observed stars.

Parameters **list_files** – text list with the files' paths

Returns list of stars (array)

py_xshooter.**create_txt_file**(*x*, *y*, *file_name*)
Create a txt file.

Parameters

- **x** – array with n elements (array)
- **y** – array with n elements (array)
- **file_name** – file's name (string)

Returns txt file

class py_xshooter.**data_object**(*name*, *arm*, *mjd*, *list_files*, *name_ffit*, *wave=None*, *flux=None*, *sigm=None*, *wave_vis=None*, *flux_vis=None*, *sigm_vis=None*, *wave_nir=None*, *flux_nir=None*, *sigm_nir=None*)
Class of the stellar objects. Using this class, we can store for each star a sort of variables, which can be easily accessed.

py_xshooter.**find_nearest**(*array*, *value*)
Find the nearest value inside an array.

Parameters

- **array** – array
- **value** – desired value (float)

Returns nearest value and its index (float)

py_xshooter.**fluxXvel**(*wave*, *flux*, *flux_plus_i*, *central_wave*, *delta*, *label*, *ax*, *fit=None*)
Function to plot a line profile.

Parameters

- **wave** – Observed wavelenght of the line (numpy array)
- **flux** – Array with the fluxes (numpy array)
- **flux_plus_i** – Array with the fluxes add by a constant value (numpy array)
- **delta** – range to be considered around the lamb_obs (float)
- **central_wave** – Lab central wave (float)
- **label** – label to be plotted in the legend
- **ax** – subfigure name (ax, ay or az)
- **fit** – Do nothing (boolean)

Returns velocity and associated flux (arrays)

py_xshooter.**ger_tbdata**(*file_name*)
Creates tbdata from hdulist and check if there is fields.

Parameters **file_name** – fits file (string)

Returns tbdata

py_xshooter.**identify_object**(*file_name*)
Function to identify the object.

Parameters **file_name** – fits file (string)

Returns object name (string)

py_xshooter.**normalize_spectrum**(*wave*, *flux*, *input_file*, *output_folder*, *arm*)
Function of normalization.

Source: http://stsdas.stsci.edu/cgi-bin/gethelp.cgi?continuum :param wave: Array with the wavelenght (numpy array) :param flux: Array with the fluxes (numpy array) :param input_file: fits file (string) :param output_folder: folder where it will be saved the output (string) :return: normalized fits file and normalized flux (output_file.fits)

py_xshooter.**plot_arm_lines**(*data*, *folder_fig*, *folder_temp*, *delta*, *star_name*)
Plot the lines for each star inside the data structure.

Parameters

- **data** – list of XShooter fits files (array)
- **folder_fig** – folder where the figures will be saved (string)
- **delta** – plot parameter (float)
- **folder_temp** – folder of the temporary files (string)

Star_name star name (string)

Returns figures and tables

py_xshooter.**plot_fits_image**(*folder_fig*, *fits_file*, *obj*, *mjd*, *scale=None*, *zoom=None*)
Read a simple txt file.

Parameters

- **folder_fig** – folder where it will be saved the figures (string)
- **fits_file** – name of fits file (string)
- **obj** – object name (string)
- **mjd** – MJD (float)
- **scale** – linear, log, and other options (string)
- **zoom** – Plot a zoom of the image? (boolean)

Returns Image

py_xshooter.**plot_line**(*wave*, *flux*, *center_wave*, *delta*, *vel*, *label*, *ax*, *calc_central_wave*, *save_fig=None*, *fig_name=None*, *gauss_fit=None*)

Function to plot a line profile.

Parameters

- **wave** – Observed wavelenght of the line (float, ex: 6562.81 #AA)
- **flux** – Array with the fluxes (numpy array)
- **center_wave** – Lab central wave (float)
- **delta** – range to be considered around the lamb_obs (float)
- **vel** – parameter for the function fit_line (float)
- **label** – label to be plotted in the legend
- **ax** – subfigure name (ax, ay or az)
- **calc_central_wave** – Do calculate the central wave? (boolean)
- **save_fig** – Save the figure? (boolean)
- **gauss_fit** – Would you like to perform a gaussian fit? (boolean)

Returns figures

py_xshooter.**plot_sed**(*data*, *folder_fig*, *folder_temp*, *star_name*)

Plot the SED for each star inside the data structure.

Parameters

- **data** – list of XShooter fits files (array)
- **folder_fig** – folder where the figures will be saved (string)
- **folder_temp** – folder of the temporary files (string)

Star_name star name (string)

Returns data (class object)

py_xshooter.**print_keys**(*file_name*)

Simple function to print the keys header of a fits file.

Parameters **file_name** – fits file (string)

Returns keys

py_xshooter.**read_fits_star_name**(*file_name*, *typ*)

Read XShooter's fits files.

Parameters

- **file_name** – name of the file in fit extension (string)
- **typ** – define if it will be used to read a image (typ='img')or a

bintable (typ='data'). :return: parameters (object if typ='data', file_name if typ='img')

py_xshooter.**read_fits_xshooter**(*file_name*, *print_obj*)
Read XShooter's fits files.

Parameters **file_name** – name of the file in fit extension (string)

Returns parameters (obj, obs_date, mjd, arm, wave, flux,

sigma, qual, snr, flux_red, sigm_red)

py_xshooter.**read_header**(*file_name*)
Simple function to read the header of a fits file.

Parameters **file_name** – fits file (string)

Returns header

py_xshooter.**read_header_aquisition**(*file_name*)
Read header of the aquisition images.

Parameters **file_name** – name of the fits file (string)

Returns object name (string), MJD (float), xshooter arm (string)

py_xshooter.**read_header_simple**(*file_name*)
Read header of a simple fits file.

Parameters **file_name** – name of the fits file (string)

Returns header_1 (string), header_2 (string)

Note: Somethimes, some fits file exhibit two headers.

py_xshooter.**read_list_files_all**(*table_name*, *folder_table*)
Read list of files in a table, and returns all fits file in an array.

Parameters

- **folder_table** – table's folder (string)
- **table_name** – Table's name (string)

Returns list of files (txt file)

py_xshooter.**read_list_files_star**(*table_name*)
Read list of files listed in a table, and returns the star's fits names in an array.

Parameters **table_name** – Table's name (string)

Returns list of files (txt file)

py_xshooter.**read_norm_fits**(*file_name*)
Read XShooter's normalized fits files.

Parameters **file_name** – name of the fits file (string)

Returns normalized flux (array)

py_xshooter.**read_txt**(*table_name*, *ncols*)
Read a simple txt file.

Parameters

- **table_name** – name of the table
- **ncols** – number of columns

Returns x, y (arrays) or x, y, z (arrays)

py_xshooter.**read_zipfile**(*folder*, *zip_file*)
Read the content of a zip file.

Parameters

- **folder** – folder with the files (string)
- **zip_file** – name of the file

Returns file content

py_xshooter.**remove_negs**(*num_list*)
Removes the negative values from a list.

Parameters **num_list** – array of values (array)

Returns keys

py_xshooter.**smooth_spectrum**(*wave*, *flux*, *doplot=None*)
Smooth the spectrum by convolving with a (normalized) Hann window of 400 points.

Parameters

- **wave** – Array with the wavelenght (numpy array)
- **flux** – Array with the fluxes (numpy array)
- **doplot** – Would you like to see the plot? (boolean)

Returns smoothed flux (array)

py_xshooter.**unzip_file**(*folder*, *folder_table*, *zip_file=None*, *list=None*)
This routine unzip a file or a list of files in a given folder.

Parameters

- **folder** – file's folder (string)
- **zip_file** – file's names (string)
- **list** – to unzipped more than one file put list=True, otherwise False

Returns unzipped file

Example:

folder = '/run/media/sysadmin/SAMSUNG/reduzindo/runC/' folder_table = '/run/media/sysadmin/SAMSUNG/reduzindo/' unzip_file(folder, folder_table, list=True)

3.3 PharaohUS

PharaohUS is an python routine that, given the BCD parameters, uses a Scipy interpolation method (*griddata*) to interpolate the stellar parameters from a stellar grid models. The importance of this interpolator is that it is capable of Interpolate unstructured D-dimensional data.

3.3.1 Some Options

The user can define these parameters:

1. resolution = 1000. # resolution of the color maps
2. read_files = True # If you want to read the files
3. interpol = True # Do you want to execute the interpolation?
4. plot3d = False # Plot 3D maps
5. plot_labels = False # Plot values alongside the points
6. cmap = 'plasma' # color map (many options)
7. interpol_method # 'linear', 'nearest', 'cubic'
8. list_models # Define file with the models data: '1.0_all' #'0.5_all'

3.3.2 Running

To run the routine is necessary to define the folders where are the input files (data tables, tag **folder_table**, and the folder where the data will be saved, tag **folder_results**). Having defined these folders, the user must define the path where the routine is installed in the tag **commum_folder**.

Having defined properly all folders and options, the code can be run in terminal by:

```
ur_forget
python pharaohus.py or ipython pharaohus.py
```

Following are the description of the functions in this routine:

pharaohus.**create_class_object**(*list_files*)
Create object class for all targets in a list.

Parameters **list_files** – list of XShooter fits files (array)

Returns data (class object)

pharaohus.**create_list_files**(*list_name*, *folder*, *folder_table*)
Creates a list of the names inside a given folder.

Parameters

- **list_name** – list's name (string)
- **folder** – files' folder

Returns creates a txt file, with the files' paths

pharaohus.**create_txt_file**(*x*, *y*, *w*, *z*, *h*, *q*, *file_name*)
Create a txt file.

Parameters

- **x** – array with n elements (array)
- **y** – array with n elements (array)
- **file_name** – file's name (string)

Returns txt file

Project Report: "Binarity and the distribution of rotational velocities in Galactic main-sequence B stars", Release 2.5

class pharaohus.**data_object**(*name*, *lamb0*, *D*)
Class of the stellar objects. Using this class, we can store for each star a sort of variables, which can be easily accessed.

pharaohus.**find_nearest**(*array*, *value*)
Find the nearest value inside an array.

Parameters

- **array** – array
- **value** – desired value (float)

Returns nearest value and its index (float)

pharaohus.**read_list_files_all**(*table_name*, *folder_table*)
Read list of files in a table, and returns all fits file in an array.

Parameters

- **table_name** – Table's name (string)
- **reflex** – If you want to unzip the files to run reflex

Returns list of files (txt file)

pharaohus.**read_txt**(*table_name*)
Read a simple txt file.

Parameters

- **table_name** – name of the table
- **ncols** – number of columns

Returns x, y (arrays) or x, y, z (arrays)

pharaohus.**read_txt_2**(*table_name*, *ncols*)
Read a simple txt file.

Parameters

- **table_name** – name of the table
- **ncols** – number of columns

Returns x, y (arrays)

pharaohus.**rotate**(*matrix*, *degree*)
Function to rotate a matrix.

Parameters

- **matrix** – matrix (array)
- **degree** – rotation (float)

Returns matrix (array)

3.4 calc_vsini

calc_vsini is an python routine that calculates vsini values for a list of stars. The method uses the rotational broadening pyasl.rotBroad function and the Grids of model atmospheres - Kurucz. The routine reads the effective temperature and logg inferred by the BCD method applied by the Pharaohus routine. Its results are save in the folder *star_name/vsini*.

3.4.1 Some Options

The user can define these parameters:

1. delta = 200 # Range of points to be considered around the central wave;
2. plotchi2_map = True # Plotting the χ^2_{red} map;
3. center_wave_vis = 6562.8 # A choosen line in visible arm ;
4. center_wave_uvb = 4861. # A choosen line in uvb arm;
5. center_wave_nir = 21654. # A choosen line in nir arm;
6. vsini_arr = np.arange(1., 600., 10.) # Range of vsini's to be analysed (unit: km/s);
7. limbdark = np.arange(0,1.1,0.2) # Range of limbdarks to be analysed (dimensionless).

Note: The center waves must be given in Angstrom.

3.4.2 Running

To run the routine it is necessary to define the folders where are the input files (data tables, tag **folder_table**, and the folder where the data will be saved, tag **folder_results**). Having defined these folders, the user must define the path where the routine is installed in the tag **commum_folder**.

Having defined properly all folders and options, the code can be run in terminal by:

```
ur_forget
python calc_vsini.py or ipython calc_vsini.py
```

Following are the description of the functions in this routine:

calc_vsini.**create_class_object**(*list_files*, *obj*)
Create object class for all targets in a list.

Parameters **list_files** – list of XShooter fits files (array)

Returns data (class object)

calc_vsini.**create_list_files**(*list_name*, *folder*, *folder_table*)
Creates a list of the files inside a given folder.

Parameters

- **list_name** – list's name (string)
- **folder** – files' folder (string)

Returns creates a txt file, with the files' paths

calc_vsini.**create_list_stars**(*list_files*)
Create list of the observed stars.

Parameters **list_files** – text list with the files' paths

Returns list of stars (array)

calc_vsini.**cut_spec**(*wave*, *flux*, *err*, *center_wave*, *delta*)
Cut a spectra to a given range.

Parameters

- **wave** – array with the wavelengths (array)
- **flux** – array with the wavelengths (array)

- **center_wave** – central wavelength (float)
- **delta** – interval to be considered around the central wavelength (float)

Returns cut arrays (x, y, z)

class calc_vsini.**data_object**(*name*, *arm*, *mjd*, *list_files*, *name_ffit*, *wave=None*, *flux=None*, *sigm=None*, *wave_vis=None*, *flux_vis=None*, *sigm_vis=None*, *wave_nir=None*, *flux_nir=None*, *sigm_nir=None*)

Class of the stellar objects. Using this class, we can store for each star a sort of variables, which can be easily accessed.

calc_vsini.**find_nearest**(*array*, *value*)

Find the nearest value inside an array.

Parameters

- **array** – array
- **value** – desired value (float)

Returns nearest value and its index

calc_vsini.**plot_vsini**(*data*, *vsini_arr*, *limbdark*, *folder_fig*, *folder_temp*, *folder_table*, *star_name*, *center_wave_uvb*, *center_wave_vis*, *center_wave_nir*, *delta*, *plotchi2_map*, *lbdc*, *ltem*, *llog*, *lambd*, *prof*)

Plot the SED for each star inside the data structure.

Parameters

- **data** – list of XShooter fits files (array)
- **folder_fig** – folder where the figures will be saved (string)
- **folder_temp** – folder of the temporary files (string)
- **limbdark** – between 0 (no) to 1 (maximum)
- **center_wave** – centre wavelength of the line (float)
- **vsini** – array of possible values of vsini (array)
- **mjd** – modified Julian date (float)
- **star_name** – star name (string)
- **lbdc** – list of wavelengths from the model (array)
- **ltem** – list of temperatures from the model (array)
- **llog** – list of logg from the model (array)
- **lambd** – wavelenghts from the model (array)
- **prof** – fluxes from the model (array)

Returns plots, best vsini, best limbdark, and reduced chi2 values

calc_vsini.**read_fits**(*file_name*)

Read XShooter's fits files.

Parameters **file_name** – name of the file in fit extension (string)

Returns parameters

calc_vsini.**read_fits_star_name**(*file_name*, *typ*)

Read XShooter's fits files.

Parameters

- **file_name** – name of the file in fit extension (string)
- **typ** – define if it will be used to read a image

(typ='img')or a bintable (typ='data'). :return: parameters (object if typ='data', file_name if typ='img')

calc_vsini.**read_fits_xshooter**(*file_name*, *print_obj*)
Read XShooter's fits files.

Parameters **file_name** – name of the file in fit extension (string)

Returns parameters

calc_vsini.**read_list_files_all**(*table_name*, *folder_table*)
Read list of files in a table, and returns all fits file in an array.

Parameters

- **folder_table** – table's folder (string)
- **table_name** – Table's name (string)

Returns list of files (txt file)

calc_vsini.**read_params_star**(*table_name*)
Read the output of the bcd method (txt file).

Parameters **table_name** – name of the table (string)

Returns stellar parameters

calc_vsini.**read_txt**(*table_name*, *ncols*)
Read a simple txt file.

Parameters

- **table_name** – name of the table
- **ncols** – number of columns

Returns x, y (arrays) or x, y, z (arrays)

calc_vsini.**smooth_spectrum**(*wave*, *flux*, *doplot=None*)
Smooth the spectrum by convolving with a (normalized) Hann window of 400 points.

Parameters

- **wave** – Array with the wavelenght (numpy array)
- **flux** – Array with the fluxes (numpy array)
- **doplot** – Would you like to see the plot? (boolean)

Returns smoothed flux (array)

calc_vsini.**vsini_calc_kurucz**(*wvl*, *flux*, *teff*, *logg*, *center_wave*, *flux_err*, *limbdark*, *vsini*, *color*, *folder_fig*, *mjd*, *star_name*, *lbdc*, *ltem*, *llog*, *lambd*, *prof*, *arm*)
Function that calculate vsini using rotational broadening pyasl.rotBroad and the Kurucz Grids of model atmospheres.

Parameters

- **limbdark** – between 0 (no) to 1 (maximum)
- **wvl** – observational wavelength (array)
- **flux** – observational flux (array)
- **flux_err** – observational flux error (array)

Project Report: "Binarity and the distribution of rotational velocities in Galactic main-sequence B stars", Release 2.5

- **teff** – effective temperature (float)
- **logg** – gravitational acceleration (float)
- **center_wave** – centre wavelength of the line (float)
- **vsini** – array of possible values of vsini (array)
- **color** – array of colors (array)
- **folder_fig** – folder where the figures will be save (string)
- **mjd** – modified Julian date (float)
- **star_name** – star name (string)
- **lbdc** – list of wavelengths from the model (array)
- **ltem** – list of temperatures from the model (array)
- **llog** – list of logg from the model (array)
- **lambd** – wavelenghts from the model (array)
- **prof** – fluxes from the model (array)
- **arm** – xshooter arm (string)

Returns plots, best vsini, best limbdark, and reduced chi2 values

3.5 Shell Script

There is a option to submit all routines simultaneously. In order to do that, we must turn the file *run_all_eso.sh* executable, and after run it:

```
chmod 777 run_all_eso.sh
./run_all_eso.sh
```

This procedure will start to running the routine PY-XShooter. When it is finished, the routine PharaohUS starts. At this point, all the structure created by PY-XShooter will be preserved and used by PharaohUS as well. Finally, the routine calc_vsini evaluates, for the same data, the vsini values by broadening a model atmospheric profile line (without rotation) until achieve the observational line profile.

CHAPTER

FOUR

PRELIMINARY RESULTS

The results, for each star, are saved in the folder */XShooter/results/star_name/*. Inside each folder *star_name*, it will have five other folders: *lines* (line profiles separed by folder), *SED* (all sed's), *bcd* (the BCD fit done in the balmer jump region), *images* (aquisition images), and *vsini* (vsini fits). Following, we present three examples of output, one for a single B star, one for a binary, and another output showing an example of vsini determination.

4.1 A Simple B star

As mentioned previously, it is created a figure with the smoothed spectra separeted by arm. The lines selected by the user appear in this plot, which helps in the visualization of interesting features. In the case of interest in a single line and about any other information about it, the user can visualize them in the folder *star_name/lines/line_name/*.

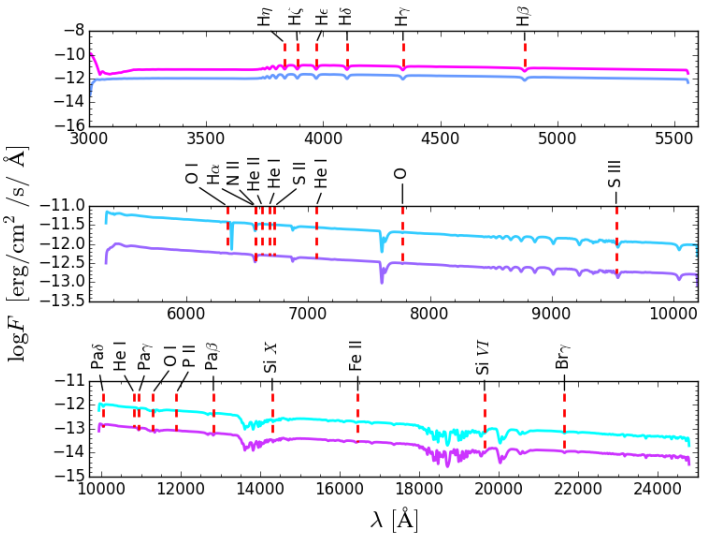

Fig. 4.1: Smoothed SED for all observations by arm for the program star Hip109155.

Beyond the line profiles, the procedure uses the region of the Balmer Jump to determine the input values of the BCD method (see J. Zorec et al. 2009).

Project Report: "Binarity and the distribution of rotational velocities in Galactic main-sequence B stars", Release 2.5

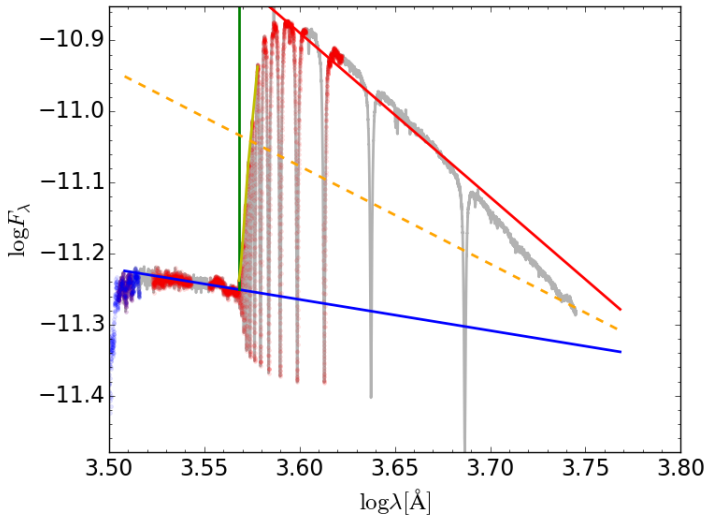

Fig. 4.2: BCD adjust for the program star Hip109155.

After the determination of the parameters (D, λ_0) needed to the BCD method, we execute an interpolation of the stellar parameters. At the end of this step, it generates a table with the inferred stellar parameters.

4.2 v sini

Figure 4.5 shows a example of the procedure adopted to found the vsini. The original line profile (blue curve) is compared with the broadened one, which depends on the values of vsini and limbdark. For each step of the interaction, these values are stored and the it performs a χ^2_{red} minimization (Fig. 4.6).

4.3 Binaries

For the study of binaries, one first step was looking at the raw frames, especially the acquisition images (Fig. 4.7) and some characteristic double-lined spectra (Fig. 4.8), reporting which objects are visible binary with a true or apparent companion from the acquisition images.

The determination of parameters of binary stars will need an implementation of another methods, because, in principle, it is needed a more precise study of the time series of measures. For this task, a more specific tool may be util as the Phoebe Project avaiable at http://www.phoebe-project.org/.

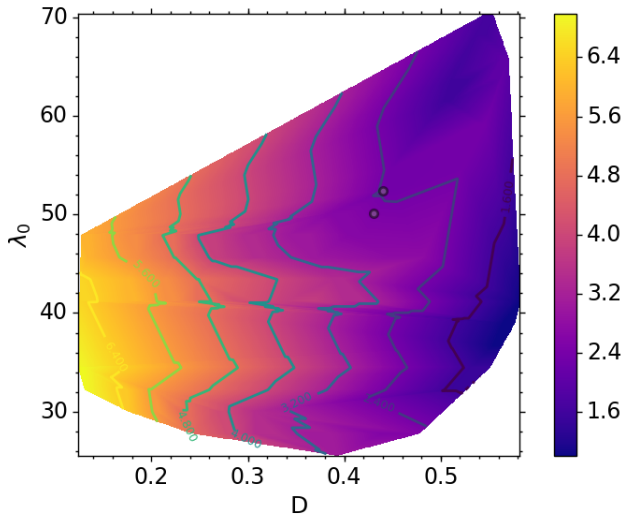

Fig. 4.3: Griddata interpolation of the stellar mass for the program star Hip076442.

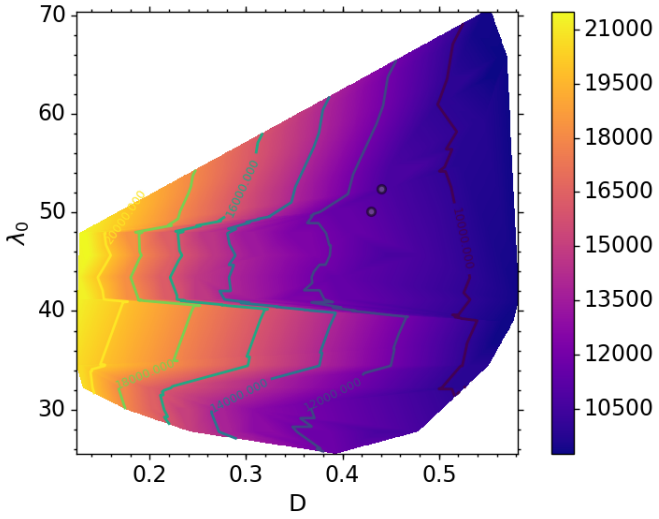

Fig. 4.4: Griddata interpolation of the T_{eff} for the program star Hip076442. The same procedure is done to interpolate the other stellar parameters.

Project Report: "Binarity and the distribution of rotational velocities in Galactic main-sequence B stars", Release 2.5

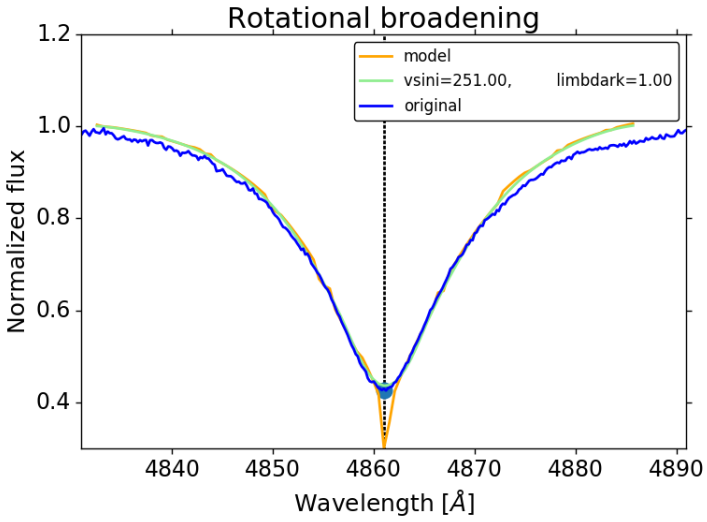

Fig. 4.5: Observational H:math:*alpha* line profile of the star Hip109155 (blue curve), original line profile from the models (orange curve), and best adjust (green curve).

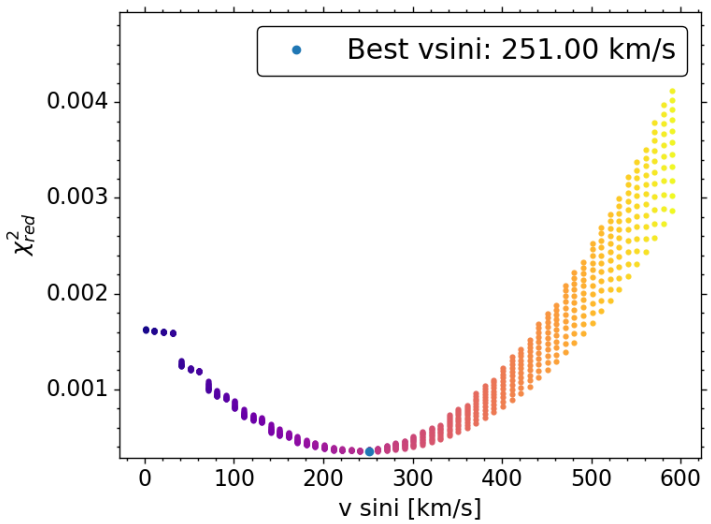

Fig. 4.6: Map of math:*chi*^2_*{red}* showing the best adjust.

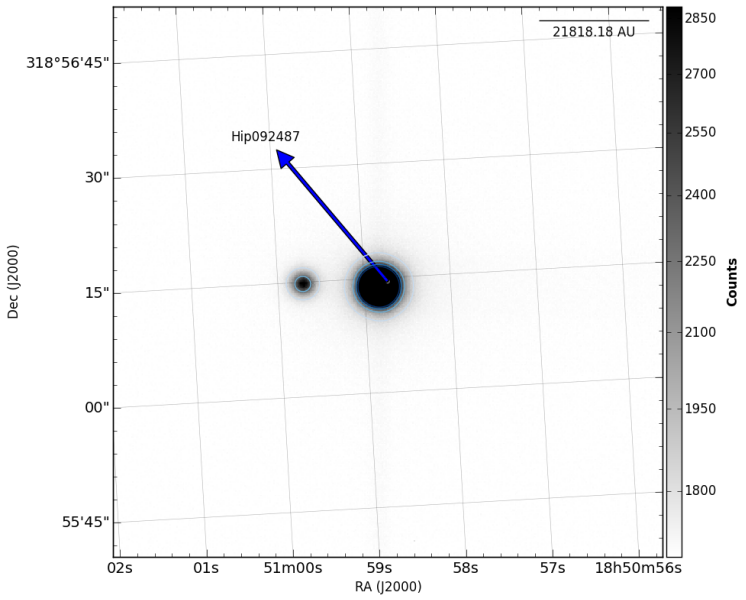

Fig. 4.7: Aquisition image of the program star Hip092487.

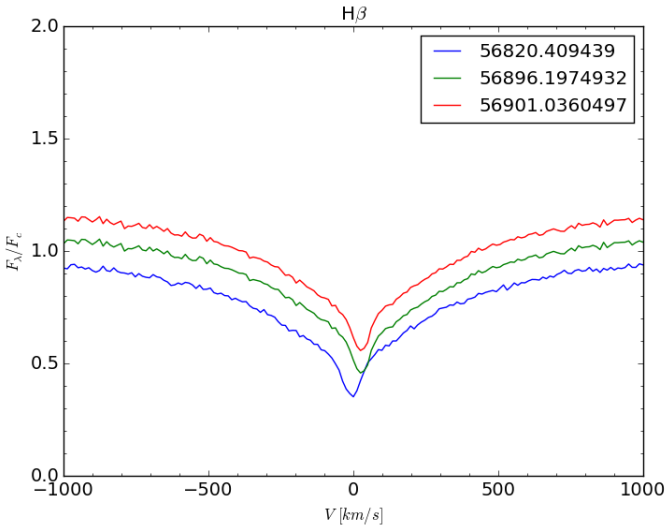

Fig. 4.8: H:math:*alpha* line profile of the program star Hip092487.

Project Report: "Binarity and the distribution of rotational velocities in Galactic main-sequence B stars", Release 2.5

Appendix J

Scientific Initiation Project - Artur Alegre

PROJETO DE INICIAÇÃO CIENTÍFICA

BE-FAVOR: Be Stars - Facilities in VO Research
Uma Ferramenta para a determinação de parâmetros de estrelas Be

Artur C. Alegre & Alex C. Carciofi

9 de outubro de 2016

1 RESUMO

O Observatório Astronômico Virtual (VO) é uma iniciativa internacional liderada pelo IVOA que visa integrar, através de ferramentas interoperacionais, diferentes bancos de dados e diferentes serviços no sentido de modelos, ferramentas de análise e outros.

Neste contexto, nosso trabalho visa disponibilizar uma ferramenta de análise *online* que proporcionará uma interface de integração entre o usuário e ferramentas desenvolvidas pelo grupo de pesquisa BEACON, coordenado pelo professor Dr. Alex C. Carciofi.

Esta ferramenta *online* irá permitir ao usuário estimar as propriedades fundamentais básicas de estrelas Be clássicas a partir de dados fotométricos. A base para esta ferramenta são os dados disponíveis em inúmeras bases de dados do VO, bem como os códigos HDUST de transferência radiativa e o código EMCEE de minimização de múltiplos parâmetros.

2 INTRODUÇÃO: O FENÔMENO BE

Apesar de terem sido descobertas há quase 150 anos por Secchi [1866], estrelas Be continuam sendo verdadeiros enigmas. Estrelas Be clássicas são estrelas que apresentam a maior taxa de rotação entre as estrelas da Sequência Principal [Rivinius, Carciofi, and Martayan, 2013]. Hoje, há consenso na comunidade de que a alta rotação está na base do surgimento dos efeitos peculiares apresentados por estas estrelas.

As características peculiares destas estrelas fazem delas verdadeiros laboratórios de astrofísica estelar, pois podem ser utilizadas para testar teorias sobre discos astrofísicos e sobre os efeitos da rotação sobre a estrela. Além disso, existem várias estrelas Be muito próximas e brilhantes, o que torna o estudo dessas estrelas mais fácil e ainda mais interessante para a Astronomia em geral.

Um dos problemas centrais no estudo de estrelas do tipo Be é a obtenção de parâmetros fundamentais da estrela, tais como massa, idade, taxa de rotação, e inclinação. Suas características particulares tornam essa tarefa difícil: estrelas Be são achatadas em seus polos, apresentam efeito de escurecimento gravitacional e quando vistas de ângulos diferentes apresentam distribuições espectrais de energia (SED) com diferentes características. A característica mais marcante, entretanto, é a presença de um disco circunstelar que altera de forma significativa o espectro estelar.

2.1 O Modelo de Disco de Decréscimo Viscoso

As observações fornecem-nos importantes informações estruturais sobre os discos de Be, que devem ser necessariamente reproduzidas por qualquer teoria que se proponha a descrever como estes discos se formam. Por exemplo, a polarimetria e a interferometria (Quirrenbach et al. [1997]; Wood et al. [1997]) determinaram que os discos são geometricamente finos, enquanto que a espectro-interferometria determinou que o material do disco gira em torno da estrela de forma kepleriana. Até o momento, a única teoria capaz de satisfazer os vínculos observacionais é o modelo de disco de decréscimo viscoso (*viscous decretion disk*, VDD) proposto por Lee [1991] e desenvolvido por outros autores (Porter [1999]; Okazaki [2001]; Bjorkman & Carciofi [2005]).

Este modelo é semelhante ao empregado para discos protoestelares [Pringle, 1981], a diferença primária sendo que discos de Be são *outflowing*, enquanto discos da pré-sequência principal são *inflowing*. No modelo VDD, é suposto que algum mecanismo, ainda desconhecido, injeta material numa velocidade orbital kepleriana na base do disco. Neste ponto, a viscosidade turbulenta começa a atuar, transportando o momento angular do material das regiões internas para as externas do disco.

Este modelo foi aplicado com sucesso a sistemas que apresentam emissão estável contínua tais como as estrelas β CMi [Wheelwright et al., 2012], χ Oph [Tycner et al., 2008] e ζ Tauri [Carciofi et al., 2009]. Destas estrelas, ζ Tauri e β CMi [Klement et al., 2015] foram as únicas estudadas de forma aprofundada, pois tanto Wheelwright et al. [2012] quanto Tycner et al. [2008] usaram um conjunto limitado de dados.

3 Observatórios Virtuais

Nos últimos anos a Astronomia tem apresentado um crescimento de volume e de complexidade de dados sem precedentes. O valor acumulado de dados é da ordem de 100 Pb e vem crescendo a uma espantosa taxa de 2 - 4 Pb/ano. Comparando essa taxa de geração de dados em diferentes áreas da ciência, vemos que a Astronomia está gerando dados no mesmo passo que experimentos na área de Física de partículas, área que recebe muito mais investimentos do que a de Astronomia. Pensando em lidar com essa quantidade enorme de dados foi formada, em junho de 2002, a IVOA - *International Virtual Observatory Alliance* [1], com a missão de facilitar a coordenação e colaboração internacional necessária para o desenvolvimento e

[1] http://www.ivoa.net/

implantação de ferramentas, sistemas e estruturas organizacionais necessárias para permitir a utilização internacional de arquivos astronômicos.

Atualmente o IVOA compreende 19 programas de Observatórios Virtuais espalhados pelo mundo, dentre eles um brasileiro, o BRAVO - *Brazilian Virtual Observatory*, que começou formalmente em 2006. O BRAVO está presente em diversas instituições astronômicas do Brasil.

Nosso grupo já conduz um projeto que visamos integrar ao BRAVO, o BEATLAS (Faes [2015]). Esta ferramenta colocará à disposição da comunidade cerca de 70.000 espectros sintéticos de estrelas Be.

4 MOTIVAÇÃO

Um dos grandes desafios na modelagem de estrelas Be vem sendo abordado pelo doutorando Bruno C. Mota, cujo trabalho, em uma de suas etapas, consiste em determinar os parâmetros estelares de uma grade de estrelas Be austrais. O método desenvolvido para este propósito utiliza espectros da missão IUE[2] que são confrontados com uma grade de modelos fotosféricos que levam em consideração a rotação. Utilizando-se esta grade e a implementação do MCMC[3] no PYTHON - EMCEE[4] - o método retorna dados confiáveis com estimativa de erro robusta dos parâmetros estelares de uma dada lista de estrelas (Fig. 4.1).

Pensando neste problema, nosso projeto, da mesma forma que o BEATLAS, visará disponibilizar esta ferramenta à comunidade, na forma de um VO *service* ligado à infraestrutura do BRAVO, mas hospedado na *homepage* do grupo BeACoN.

5 METODOLOGIA

O projeto possui 2 etapas. Na primeira (Seç. 5.1), efetuaremos a leitura dos dados observacionais diretamente através do servidor. Na segunda (Seç. 5.2), será realizada a implementação da rotina PYTHON de determinação dos parâmetros estelares apresentada na seção 4.

5.1 LEITURA DOS DADOS OBSERVACIONAIS

Uma das preocupações deste projeto é fazer com que o usuário não necessite baixar os dados das estrelas que deseja estudar. Desta maneira, um usuário que busque analisar um conjunto de dados não precisará baixá-los de um serviço de VO e selecioná-los no próprio computador para, em seguida, enviá-los para o servidor analisar: o *web service* fará isto automaticamente.

Esta interface inicial utilizará as coordenadas ou nome de uma estrela para baixar os dados do repositório, graficando-os de forma pré-determinada. Logo, bastará ao usuário apenas selecionar os espectros com os quais deseja trabalhar.

Para tornar possível esta primeira etapa de funcionamento da interface de integração, o aluno de IC deverá, ao longo do início deste projeto, concentrar seus esforços no aprendizado de *web scripting*.

[2] *International Ultraviolet Explorer*
[3] Markov Chain Monte Carlo
[4] Foreman-Mackey et al. [2013]

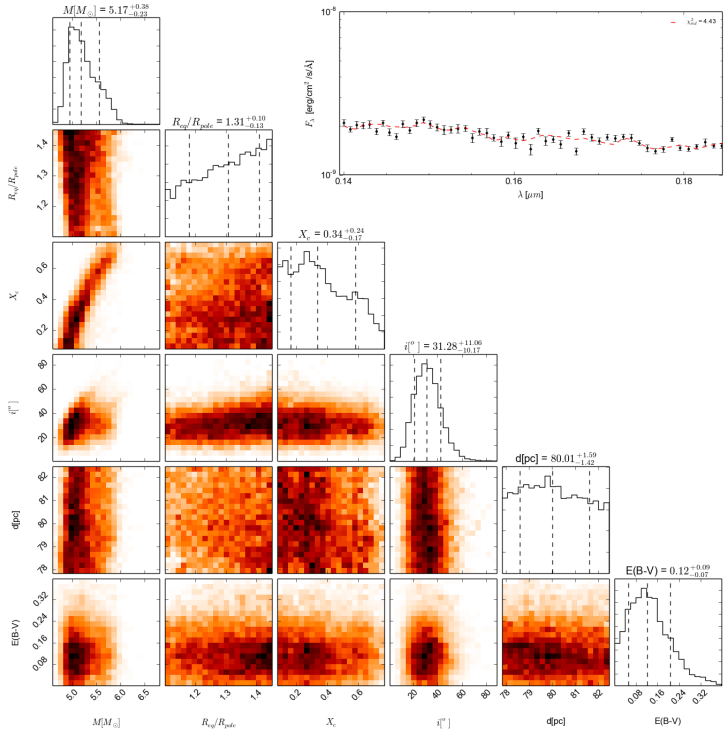

Figura 4.1: Saída do método obtida para a estrela α Columbae. O gráfico acima, à direita, mostra o espectro IUE original (pontos) com o melhor modelo em vermelho. Os gráficos na diagonal mostram a função densidade de probabilidade associada a cada parâmetro. Os mapas de cores mostram a correlação entre cada um dos parâmetros.

5.2 Implementação da rotina Python

A segunda etapa será desenvolver uma inferface de forma a permitir que a rotina PHYTON já existente seja rodada à partir do *web service*. Esta rotina utilizará os dados observacionais selecionados na etapa descrita na seção 5.1 e retornará os parâmetros estelares em uma forma gráfica (Fig. 4.1) juntamente com um arquivo de texto que conterá os melhores melhores parâmetros e com os respectivos erros.

Para isto, o aluno de IC precisará estudar como rodar rotinas PYTHON a partir de páginas *web*, tarefa que exigirá um estudo aprofundado tanto de *web programming* quanto da própria rotina PYTHON em si.

6 RESULTADOS ESPERADOS

Uma vez concluída, o *web service* será uma ferramenta muito útil para a comunidade de estrelas Be clássicas, por permitir obter de forma simples os parâmetros fundamentais da estrela Be a partir de dados observacionais de repositórios *online* e modelos fotosféricos estado-da-arte.

Para o aluno, tal projeto permitirá um estudo aprofundado de PHYTON, *web scripting* e dos protocolos básicos do VO.

REFERÊNCIAS

Secchi, A. 1866, Astronomische Nachrichten, 68, 63

Pringle, J. E. 1981, araa, 19, 137

Lee, R. W. 1991, Presented at the AIP Conference, Portland, ME, 23 Aug. 1991,

Wood, K., Bjorkman, K. S., & Bjorkman, J. E. 1997, apj, 477, 926

Quirrenbach, A., Bjorkman, K. S., Bjorkman, J. E., et al. 1997, apj, 479, 477

Porter, J. M. 1999, aap, 348, 512

Okazaki, A. T. 2001, pasj, 53, 119

Bjorkman, J. E., & Carciofi, A. C. 2005, Astronomical Polarimetry: Current Status and Future Directions, 343, 270

Tycner, C., Jones, C. E., Sigut, T. A. A., et al. 2008, apj, 689, 461

Tycner, C., Jones, C. E., Sigut, T. A. A., et al. 2008, apj, 689, 461

Carciofi, A. C., Okazaki, A. T., Le Bouquin, J.-B., et al. 2009, aap, 504, 915

Wheelwright, H. E., Bjorkman, J. E., Oudmaijer, R. D., et al. 2012, mnras, 423, L11

Rivinius, T., Carciofi, A.C., and Martayan, C.: 2013, *Astronomy and Astrophysics Review* **21**, 69.

Foreman-Mackey, D., Hogg, D. W., Lang, D., & Goodman, J. 2013, pasp, 125, 306

Faes, D. M. 2015, Universidade de São Paulo & Université Nice Sophia Antipolis

Klement, R., Carciofi, A. C., Rivinius, T., et al. 2015, arXiv:1510.01229

Appendix K

BeFaVOr Web Tutorial

Project Report: "Be-FaVOR: Be Stars - Facilities in VO Research. Uma ferramenta para a determinação de parâmetros de estrelas Be"

Release 1.0

Artur Alegre, Alex C. Carciofi e Bruno C. Mota

November 02, 2016

CONTENTS

ii

Project Report: "Be-FaVOR: Be Stars - Facilities in VO Research. Uma ferramenta para a determinação de parâmetros de estrelas Be", Release 1.0

O Observatório Astronômico Virtual (VO) é uma iniciativa internacional liderada pela *International Virtual Observatory Alliance* (IVOA), que visa integrar, através de ferramentas interoperacionais, diferentes bancos de dados e diferentes serviços no sentido de modelos, ferramentas de análise e outros.

Neste contexto, nosso trabalho visa disponibilizar uma ferramenta de análise *online* que proporcionará uma interface de integração entre o usuário e ferramentas desenvolvidas pelo grupo de pesquisa Beacon, coordenado pelo professor Dr. Alex C. Carciofi.

Esta ferramenta *online* irá permitir ao usuário estimar as propriedades fundamentais básicas de estrelas Be clássicas a partir de dados fotométricos. A base para esta ferramenta são os dados disponíveis em inúmeras bases de dados do VO, bem como os códigos HDUST de transferência radiativa e o código EMCEE de minimização de múltiplos parâmetros.

Project Report: "Be-FaVOR: Be Stars - Facilities in VO Research. Uma ferramenta para a determinação de parâmetros de estrelas Be", Release 1.0

CHAPTER

ONE

INTRODUÇÃO

Apesar de terem sido descobertas há 150 anos por Secchi 1866, estrelas Be continuam sendo verdadeiros enigmas. Estrelas Be clássicas são estrelas que apresentam a maior taxa de rotação entre as estrelas da Sequência Principal (Rivinius, Carciofi & Martayan (2013)). Hoje, há consenso na comunidade de que a alta taxa de rotação está na base do surgimento dos efeitos peculiares apresentados por estas estrelas.

Um dos problemas centrais no estudo de estrelas do tipo Be é a obtenção de parâmetros fundamentais da estrela, tais como massa, idade, taxa de rotação e inclinação. Suas características particulares tornam essa tarefa difícil: estrelas Be são achatadas em seus polos, apresentam efeito de escurecimento gravitacional e, quando vistas de ângulos diferentes, apresentam distribuições espectrais de energia (SED) com diferentes características. A característica mais marcante, entretanto, é a presença de um disco circunstelar que altera de forma significativa o espectro estelar.

Buscando uma solução para este problema, o presente projeto visa disponibilizar à comunidade uma ferramenta no formato de um *web service*, isto é, um serviço de Observatório Virtual, ligado à infraestrutura do BRAVO - *Brazilian Virtual Observatory*. O método a ser utilizado por esta ferramenta baseia-se no confronto entre grades de modelos fotosféricos que levam em consideração a rotação e espectros da missão IUE, retornando dados confiáveis com estimativa de erro robusta de parâmetros estelares de uma dada lista de estrelas.

Project Report: "Be-FaVOR: Be Stars - Facilities in VO Research. Uma ferramenta para a determinação de parâmetros de estrelas Be", Release 1.0

CHAPTER

TWO

DADOS OBSERVACIONAIS

2.1 Os dados do IUE

A missão *International Ultraviolet Explorer* (IUE) foi um projeto conjunto entre NASA, ESA e PPARC. Ainda hoje este projeto é entendido como um dos telescópios astronômicos mais produtivos de todos os tempos, ultrapassando as expectativas de seus objetivos originais, dentre estes, a obtenção de espectros de alta resolução de estrelas de todos os tipos espectrais para determinar suas características físicas e fazer repetidas observações de objetos com espectros variáveis.

Os arquivos de espectros do IUE podem ser acessados no sistema da ESA chamado IUE *Newly Extracted Spectra* (INES), cujo objetivo é fornecer à comunidade científica acesso aos espectros do IUE sem que se faça necessário um conhecimento técnico dos instrumentos. Para informações detalhadas sobre o sistema, veja http://sdc.cab.inta-csic.es/ines.

2.2 O *Web Service*

A ferramenta em desenvolvimento utilizará como *input* o nome de uma estrela para automaticamente baixar os dados do repositório *online* do INES e de outros serviços disponíveis e grafică-los de forma pré-derterminada. Desta maneira, não será necessário o usuário baixar os dados das estrelas que deseja estudar em seu computador, selecioná-los e, então, enviá-los de volta ao servidor para serem analisados; bastará apenas selecionar os espectros com os quais deseja trabalhar.

Para construir esta ferramenta, o projeto foi dividido em duas etapas:

1. Elaboração de uma rotina capaz de ler os dados observacionais diretamente através do servidor.

   Esta rotina é a responsável por fazer o *download* automático dos dados buscando no servidor pelo nome da estrela.

2. Implementação da rotina Python de determinação dos parâmetros estelares.

   Esta parte inclui a criação de uma interface que permita ao usuário executar as rotinas de interesse dentro de um ambiente de VO.

Este serviço será hospedado na *homepage* do grupo Beacon, ao lado de outro projeto que visamos integrar ao BRAVO, o BEATLAS (Faes et al. 2017 in prep.), ferramenta que colocará à disposição da comunidade cerca de 70.000 espectros sintéticos de estrelas Be.

Project Report: "Be-FaVOR: Be Stars - Facilities in VO Research. Uma ferramenta para a determinação de parâmetros de estrelas Be", Release 1.0

CHAPTER

THREE

FERRAMENTAS

Nesta seção, são descritas as rotinas Python criadas para leitura dos dados através do servidor: BeFaVOR-Web e TAKE-VIZIER-DATA. Esta última trata-se de uma rotina complementar para habilitar a primeira a buscar por múltiplas estrelas de uma vez.

3.1 BeFaVOR-Web

A rotina BeFaVOR-Web usa como *input* tanto o nome de uma única estrela quanto uma lista de estrelas para realizar uma busca por arquivos de espectros correspondentes no *database* do sistema INES, salvando-os na pasta definida. Em seguida, realiza-se, para a mesma estrela, uma busca no SIMBAD, através do qual obtemos os parâmetros: paralaxe, vsini e suas respectivas incertezas, além da referência bibliográfica para vsini. Também é verificado se a busca na plataforma IRSA-*Galactic DUST Reddening & Extinction* retorna algum valor de avermelhamento E(B-V) para aquela estrela. Caso positivo, o valor é salvo juntamente com os outros parâmetros em uma tabela na pasta definida.

3.1.1 Instalação

Para utilizar esta rotina em sua atual versão é preciso ter instalados os seguintes pacotes:

1. numpy
2. bs4
3. datetime
4. requests
5. selenium
6. astroquery
7. pyhdust
8. matplotlib
9. urllib
10. re
11. random
12. tafile

Os pacotes numerados de 1 a 8 podem ser instalados utilizando o gerenciador de pacotes **pip**, enquanto aqueles de 9 a 12 podem ser instalados pelo comando **apt-get install python3-pacote**.

Project Report: "Be-FaVOR: Be Stars - Facilities in VO Research. Uma ferramenta para a determinação de parâmetros de estrelas Be", Release 1.0

3.1.2 Executando a BeFaVOR-Web

Para rodar a rotina o usuário deve primeiro definir o *path* onde esta encontra-se instalada na tag **commum_folder**, bem como o *path* onde as tabelas serão salvas em **folder_tables**. Recomenda-se utilizar a versão mais atual disponível do Python.

Utilizando como exemplo o IPython 3.0, o código pode ser rodado seguindo os seguintes passos:

1. Abra o terminal e digite o comando: ipython3
2. Vá ao diretório em que a rotina encontra-se instalada;
3. No terminal, digite o comando: run BeFaV0r_web.py
4. A rotina perguntará se o usuário deseja buscar apenas um ou vários alvos. Digite '1' para buscar um único alvo ou 'more' para buscar múltiplos alvos;
5. Caso tenha digitado '1', a rotina perguntará o nome do alvo. Digite o nome da estrela desejada;
6. Caso tenha digitado 'more' a rotina executará a rotina complementar TAKE_VIZIER_DATA que baixará uma série de alvos de acordo com um catálogo pré-definido. Para mais detalhes, veja a descrição da rotina TAKE_VIZIER_DATA na sub-seção seguinte.

Se o usuário tiver buscado por um único alvo, além dos espectros do IUE salvos, a rotina criará um documento de texto com a seguinte estrutura de **linhas**:

1. Nome da estrela
2. Paralaxe
3. Incerteza da paralaxe
4. vsini
5. Incerteza do vsini
6. "Bump"
7. Referência bibliográfica do vsini
8. E(B-V)

"Bump" refere-se à presença de um espectro IUE que cobre a região conhecida como *bump* 2200 Angstron que é utiliza na determinação do valor de E(B-V). Caso retorne "*True*", existe este espectro e, caso retorne "*False*", significa que o espectro não cobre esta faixa espectral e, portanto, o valor é retirado do IRSA.

Se o usuário tiver buscado por múltiplos alvos, além dos espectros do IUE salvos, a rotina criará um documento de texto com uma estrutura de **colunas** pré-determinada pelo usuário. Por exemplo, caso o usuário selecione estrelas do *Bright Star Catalogue*, é possível gerar a seguinte estrutura:

1. Nome da estrela
2. Índice B-V
3. Índice U-B
4. Índice R-I
5. vsini
6. Incerteza B-V
7. Incerteza U-B
8. Incerteza vsini
9. Incerteza R-I

10. Data de observação
11. Tipo espectral

3.1.3 Funções da rotina BeFaVOR-Web

Segue a descrição das funções contidas na rotina BeFaVOR-Web, organizadas em ordem alfabética:

`BeFaVOr_web.`**`create_list_files`**(*list_name*, *folder*, *folder_table*)
Creates a list of the files inside a given folder.

Parameters

- **list_name** – list's name (string)
- **folder** – files' folder (string)

Returns creates a txt file, with the files' paths

`BeFaVOr_web.`**`create_txt_file`**(*data_list*, *file_name*)
Create a txt file.

Parameters

- **data_list** – list of data to be saved (array)
- **file_name** – txt file's name (string)

Returns txt file

`BeFaVOr_web.`**`find_regular_expression`**(*url*, *typ*, *atr*, *expr*)
Search for a specified expression inside a page code and lists all its ocurrences.

Parameters

- **url** – page url (string)
- **typ** – tag (string)
- **atr** – attribute (string)
- **expr** – expression (string)

Returns list of occurences

`BeFaVOr_web.`**`getTitle`**(*url*)
Gets the title of a certain webpage.

Parameters **url** – page url (string)

Returns page title

`BeFaVOr_web.`**`get_attribute`**(*url*, *atr*, *typ*)
Lists all text in a webpage that satisfacts a specified attribute.

Parameters

- **url** – page url (string)
- **atr** – attribute (string)
- **typ** – tag (string)

Returns text containing specified attribute

`BeFaVOr_web.`**`iue_submission`**(*star_name*)
Search in the IUE database for a certain star name.

Parameters **star_name** – name of the star (string)

Returns request of star name in IUE page

`BeFaVOr_web.`**`plot_gal`**(*ra_val*, *dec_val*, *folder_fig*)
Plot in "Galatic Coordinates" (i.e., Mollweide projection).

Parameters

- **ra_val** – right ascencion in RADIANS (float)
- **dec_val** – declination in RADIANS (float)
- **folder_fig** – name of the folder for the figure (string)

Returns saved images

`BeFaVOr_web.`**`read_simbad_coodr`**(*star_name*)
Query SIMBAD for the coordinates of a given star.

Parameters **star_name** – star's name (string)

Returns right ascencion and declination coordinates

`BeFaVOr_web.`**`read_simbad_data`**(*star_name*)
Query SIMBAD for a given star parallax, vsini, bump and references.

Parameters **star_name** – star's name (string)

Returns txt file with star's parallax, vsini, bump, the respective

errors and references for vsini and E(B-V)

`BeFaVOr_web.`**`read_txt`**(*list_name*, *folder*)
Read a given list of star names.

Parameters

- **list_name** – name o txt file containing the list (string)
- **folder** – list's folder (string)

Returns column of the list read

`BeFaVOr_web.`**`retrieve_ebmv_value`**(*star_name*)
Search the INES website for a specified star's E(B-V) value.

Parameters **star_name** – stars's name (string)

Returns E(B-V) value

`BeFaVOr_web.`**`selecting_data`**(*star_name*, *commum_folder*)
Search the INES website for a specified star.

Parameters

- **star_name** – name of the star (string)
- **commum_folder** – name of the folder where the routine is located

Returns request of the star name in INES page

`BeFaVOr_web.`**`show_page_code`**(*url*)
Shows the page code of a certain webpage.

Parameters **url** – page url (string)

Returns page code

BeFaVOr_web.**there_is_a_title**(*url*)
Prints the title of a certain webpage.

Parameters **url** – page url (string)

Returns page title

BeFaVOr_web.**untar**(*fname*)
Decompact a tar file.

Parameters **fname** – name o file to be decompacted (string)

Returns decompacted file

BeFaVOr_web.**unzip**(*zip_file*, *outdir*)
Unzip a given file into the specified output directory.

Parameters

- **zip_file** – name of file to be unziped (string)
- **outdir** – directory of the file (string)

Returns unziped file

3.2 TAKE-VIZIER-DATA

A rotina TAKE-VIZIER-DATA realiza uma busca por catálogos no VizieR. Em seguida, dentro de cada catálogo selecionado, é feita a seleção dos objetos de interesse através de um processo de filtragem por tipo espectral, classe de luminosidade e existência ou não de dados da missão IUE. Deste ponto em diante, a rotina segue os seguintes passos:

1. As estrelas selecionadas no VizieR são buscadas no arquivo do INES;
2. Os espectros daquelas encontradas são salvos no diretório definido;
3. Para cada estrela encontrada no INES, é criado um documento de texto onde são salvos os parâmetros retirados do SIMBAD e (opcional) os parâmetros obtidos dos catálogos lidos por meio do VIZIER.

Detalhes sobre as funções contidas nesta rotina podem ser vistos no anexo do capítulo 6.

Project Report: "Be-FaVOR: Be Stars - Facilities in VO Research. Uma ferramenta para a determinação de parâmetros de estrelas Be", Release 1.0

CHAPTER

FOUR

OUTRAS ATIVIDADES E PERSPECTIVAS

4.1 Atividades complementares

Ao longo do período de duração desta bolsa, além das tarefas diretamente relacionadas a este projeto, também foram realizadas atividades importantes para o desenvolvimento acadêmico, dentre elas destacamos:

1. Participação de reuniões semanais do grupo Beacon, onde são discutidos resultados recentes das pesquisas de seus membros, bem como artigos científicos relevantes para nossa linha de pesquisa;
2. Apresentação de resultados parciais deste projeto na reunião de grupo;
3. Participação de observações astronômicas tanto remotas quanto presenciais no Observatório Pico dos Dias para obtenção de dados polarimétricos e espectroscópicos.

4.2 Tarefas futuras

1. Incorporação das rotinas de leitura de dados em servidores desenvolvidas neste projeto com a rotina Python de determinação de parâmetros estelares que constitui parte do projeto de doutorado do aluno Bruno C. Mota.
2. Desenvolvimento e integração, na *homepage* do grupo Beacon, da interface que permitirá ao usuário executar as rotinas Python criadas ao longo ou anteriormente a este projeto em um ambiente de Observatório Virtual.

Project Report: "Be-FaVOR: Be Stars - Facilities in VO Research. Uma ferramenta para a determinação de parâmetros de estrelas Be", Release 1.0

CHAPTER

FIVE

CONCLUSÕES

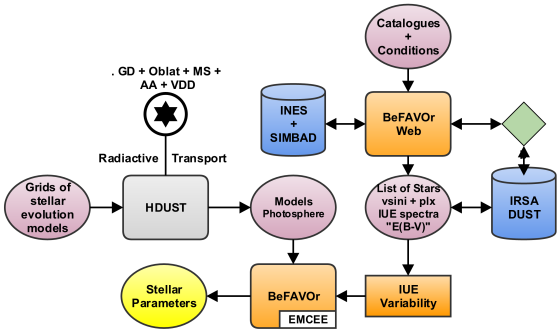

Figure 5.1: Fluxograma simplificado do método desenvolvido.

Na figura _fig1, mostramos uma representação simplificada do método que vem sendo desenvolvido. Neste projeto de iniciação, devenvolvemos o bloco *BeFaVOR web* representado na figura. Em resumo, o usuário necessita apenas selecionar catálogos de interesse, bem como os filtros adequados. A partir deste ponto, a rotina verifica se as estrelas selecionadas possuem dados IUE; caso positivo, dados de paralaxe e vsini são lidos e salvos automaticamente do SIMBAD, juntamente com os espectros do IUE (salvos da plataforma INES). Uma implementação adicional é a verificação da existência de uma região espectral que pode ser utilizada para se determinar o avermelhamento devido ao meio interestelar. Caso ela não exista, a rotina lê e salva uma estimativa do *web service* IRSA. Por fim, o usuário obtêm uma lista de estrelas, com seus respectivos dados de paralaxe, vsini, E(B-V) e incertezas. Estes dados são utilizados na rotina BeFaVOR de determinação dos parâmetros estelares, que está sendo desenvolvida pelo doutorando Bruno C. Mota.

Project Report: "Be-FaVOR: Be Stars - Facilities in VO Research. Uma ferramenta para a determinação de parâmetros de estrelas Be", Release 1.0

CHAPTER

SIX

ANEXOS

6.1 Anexo 1: Rotina BeFaVOr_web

```
# 1) Esta rotina deve ser rodada em ipython3

# ============================================================================
# Importing modules
import numpy as np
from urllib.request import urlopen
from urllib.error import HTTPError
from bs4 import BeautifulSoup
import sys
import re
import datetime
import random
import time
import requests
import math
from selenium import webdriver
from selenium.webdriver.support.ui import Select
import tarfile
from astroquery.simbad import Simbad
import csv
import os
from glob import glob
import pyhdust.phc as phc
import matplotlib.pyplot as plt
from selenium import webdriver
from selenium.webdriver.common.by import By
from selenium.webdriver.support.ui import WebDriverWait
from selenium.webdriver.support import expected_conditions as EC


# ============================================================================
def show_page_code(url):
    '''
    Shows the page code of a certain webpage.

    :param url: page url (string)
    :return: page code
    '''

    html = urlopen(url)
    bsObj = BeautifulSoup(html.read())
```

Project Report: "Be-FaVOR: Be Stars - Facilities in VO Research. Uma ferramenta para a determinação de parâmetros de estrelas Be", Release 1.0

```
    return bsObj


# ================================================================================
def getTitle(url):
    '''
    Gets the title of a certain webpage.

    :param url: page url (string)
    :return: page title
    '''

    try:
        html = urlopen(url)
    except HTTPError as e:
        print(e)
        return None
    try:
        bsObj = BeautifulSoup(html.read())
        title = bsObj.body.h1
    except AttributeError as e:
        return None
    return title


# ================================================================================
def there_is_a_title(url):
    '''
    Prints the title of a certain webpage.

    :param url: page url (string)
    :return: page title
    '''

    title = getTitle(url)
    if title is None:
        print("Title could not be found")
    else:
        print(title)
    return title


# ================================================================================
def example_try():

    while True:
        try:
            x = int(raw_input("Please enter a number: "))
            break
        except ValueError:
            print("Oops!  That was no valid number.  Try again...")
    return


# ================================================================================
def get_attribute(url, atr, typ):
    '''
    Lists all text in a webpage that satisfacts a specified attribute.
```

```
    :param url: page url (string)
    :param atr: attribute (string)
    :param typ: tag (string)
    :return: text containing specified attribute
    '''

    bsOBJ = show_page_code(url)
    namelist = bsOBJ.findAll(typ, {"class": atr})
    names = []
    for name in namelist:
        nome = name.get_text()
        names.append(nome)

    return names


# ================================================================================
def find_regular_expression(url, typ, atr, expr):
    '''
    Search for a specified expression inside a page code and lists all
    its ocurrences.

    :param url: page url (string)
    :param typ: tag (string)
    :param atr: attribute (string)
    :param expr: expression (string)
    :return: list of occurences
    '''

    html = urlopen(url)
    bsObj = BeautifulSoup(html)
    array = bsObj.findAll(typ, {atr: re.compile(expr)})
    for lista in array:
        print(lista["src"])
    return lista


# ================================================================================
random.seed(datetime.datetime.now())


def getLinks(articleUrl):
    html = urlopen("http://en.wikipedia.org" + articleUrl)
    bsObj = BeautifulSoup(html)
    return bsObj.find("div", {"id": "bodyContent"}).\
        findAll("a", href=re.compile("^(/wiki/)((?!:).)*$"))


# ================================================================================
def get_Link(articleUrl):
    links = getLinks("/wiki/Kevin_Bacon")
    while len(links) > 0:
        newArticle = links[random.randint(0, len(links) - 1)].attrs["href"]
        print(newArticle)
        links = getLinks(newArticle)


# ================================================================================
```

Project Report: "Be-FaVOR: Be Stars - Facilities in VO Research. Uma ferramenta para a determinação de parâmetros de estrelas Be", Release 1.0

```
def file_submission():
    files = {'uploadFile': open('../files/Python-logo.png', 'rb')}
    r = requests.post("http://pythonscraping.com/pages/processing2.php",
                      files=files)
    print(r.text)
    return


# ========================================================================
def simple_form():
    params = {'firstname': 'Ryan', 'lastname': 'Mitchell'}
    r = requests.post("http://pythonscraping.com/files/processing.php",
                      data=params)
    print(r.text)
    return


# ========================================================================
def file_submission2():
    files = {'uploadFile': open('../files/python.png', 'rb')}
    r = requests.post("http://pythonscraping.com/pages/processing2.php",
                      files=files)
    print(r.text)

    return


# ========================================================================
def iue_submission(star_name):
    '''
    Search in the IUE database for a certain star name.

    :param star_name: name of the star (string)
    :return: request of star name in IUE page
    '''

    ines_site = "http://sdc.cab.inta-csic.es/cgi-ines/IUEdbsMY"
    params = {'object': star_name}
    r = requests.post(ines_site, data=params)
    print(r.text)

    return r


# ========================================================================
def read_txt(list_name, folder):
    '''
    Read a given list of star names.

    :param list_name: name o txt file containing the list (string)
    :param folder: list's folder (string)
    :return: column of the list read
    '''

    list_name = folder + list_name

    cols = np.genfromtxt(list_name, unpack=True, comments='#',
                         delimiter='\t')
```

```
    return cols


# ============================================================================
def untar(fname):
    '''
    Decompact a tar file.

    :param fname: name o file to be decompacted (string)
    :return: decompacted file
    '''

    if (fname.endswith("tar.gz")):
        tar = tarfile.open(fname)
        tar.extractall()
        tar.close()
        print("Extracted in Current Directory")
    else:
        print("Not a tar.gz file: '%s '" % sys.argv[0])


# ============================================================================
def create_list_files(list_name, folder, folder_table):
    '''
    Creates a list of the files inside a given folder.

    :param list_name: list's name (string)
    :param folder: files' folder (string)
    :return: creates a txt file, with the files' paths
    '''

    a = open(folder_table + list_name + ".txt", "w")
    for path, subdirs, files in os.walk(folder):
        for filename in files:
            f = os.path.join(path, filename)
            a.write(str(f) + os.linesep)
    return


# ============================================================================
def create_txt_file(data_list, file_name):
    '''
    Create a txt file.

    :param data_list: list of data to be saved (array)
    :param file_name: txt file's name (string)
    :return: txt file
    '''

    with open(file_name, 'w') as f:
        writer = csv.writer(f, delimiter='\t')
        writer.writerows(zip(data_list))
    return


# ============================================================================
def read_simbad_data(star_name):
    '''
```

```
    Query SIMBAD for a given star parallax, vsini, bump and references.

    :param star_name: star's name (string)
    :return: txt file with star's parallax, vsini, bump, the respective
    errors and references for vsini and E(B-V)
    '''

    customSimbad = Simbad()
    # customSimbad.list_votable_fields() #  to list all avaiable fields
    customSimbad.get_votable_fields()
    customSimbad.add_votable_fields('plx', 'plx_error', 'rot')
    customSimbad.get_votable_fields()
    result_table = customSimbad.query_object(star_name)
    # star = result_table['MAIN_ID']
    star = np.copy(star_name)
    plx = result_table['PLX_VALUE'][0]
    plx_error = result_table['PLX_ERROR'][0]
    vsini = result_table['ROT_Vsini'][0]
    vsini_err = result_table['ROT_err'].item()
    rot_bibcode = result_table['ROT_bibcode']
    bump = True
    ebmv_ref = 0.0

    return star.item(), plx, plx_error, vsini, vsini_err, bump,\
        rot_bibcode.item(), ebmv_ref


# ============================================================================
def read_simbad_coodr(star_name):
    '''
    Query SIMBAD for the coordinates of a given star.

    :param star_name: star's name (string)
    :return: right ascencion and declination coordinates
    '''

    customSimbad = Simbad()
    customSimbad.get_votable_fields()
    result_table = customSimbad.query_object(star_name)

    ra = result_table['RA'][0]
    dec = result_table['DEC'][0]

    return ra, dec


# ============================================================================
def unzip(zip_file, outdir):
    '''
    Unzip a given file into the specified output directory.

    :param zip_file: name of file to be unziped (string)
    :param outdir: directory of the file (string)
    :return: unziped file
    '''

    import zipfile
    zf = zipfile.ZipFile(zip_file, "r")
```

```
    zf.extractall(outdir)
    return


# ============================================================================
def plot_gal(ra_val, dec_val, folder_fig):
    """
    Plot in "Galatic Coordinates" (i.e., Mollweide projection).

    :param ra_val: right ascencion in RADIANS (float)
    :param dec_val: declination in RADIANS (float)
    :param folder_fig: name of the folder for the figure (string)
    :return: saved images
    """

    fig = plt.figure()
    ax = fig.add_subplot(111, projection="mollweide")
    ax.set_xticklabels(['14h', '16h', '18h', '20h', '22h', '0h', '2h', '4h',
                        '6h', '8h', '10h'])

    for i in range(len(ra_val)):
        dec = dec_val[i].replace(' ', ':')
        ra = ra_val[i].replace(' ', ':')

        # list of floats (degrees fraction)
        dec = [phc.dec2degf(dec)]
        ra = [phc.ra2degf(ra)]

        # arrays of floats (radians)
        dec = np.array(dec) * np.pi / 180
        ra = np.array(ra) * np.pi / 180

        ax.scatter(ra, dec)
    plt.savefig(folder_fig + 'galatic_distribution.png')

    return


# ============================================================================
def selecting_data(star_name, commum_folder):
    '''
    Search the INES website for a specified star.

    :param star_name: name of the star (string)
    :param commum_folder: name of the folder where the routine is located
    :return: request of the star name in INES page
    '''

    from pyvirtualdisplay import Display
    display = Display(visible=0, size=(800, 600))
    display.start()

    # now Chrome will run in a virtual display.
    # you will not see the browser.

    # Creating the path
    a = star_name.split()
```

```
# short_star_name = a[0][0] + a[1][0:3]
short_star_name = a[0] + a[1]

# Starting the searching
if os.path.isdir(commum_folder + 'iue/' + short_star_name) is False:
    os.mkdir(commum_folder + 'iue/' + short_star_name)

    folder_data = commum_folder + 'iue/' + short_star_name

    # Define global Chrome properties
    options = webdriver.ChromeOptions()
    prefs = {"download.default_directory": folder_data}
    options.add_experimental_option("prefs", prefs)

    browser = webdriver.Chrome(chrome_options=options)
    # browser = webdriver.Firefox(firefox_profile=fp)

    # Define web source
    ines_site = "http://sdc.cab.inta-csic.es/cgi-ines/IUEdbsMY"

    # Openning it
    browser.get(ines_site)
    # browser.maximize_window()
    # time.sleep(3)

    # Selecting all data
    mySelect = Select(browser.find_element_by_name("limit"))
    mySelect.select_by_value("all")
    # time.sleep(3)

    # Selecting some stars
    browser.find_element_by_name("object").send_keys(star_name)
    browser.find_element_by_name(".submit").click()
    # time.sleep(3)

    # Taking the data
    browser.find_element_by_name("markRebin").click()
    browser.find_element_by_name(".submitNH").click()
    time.sleep(20)
    # browser.close()

    # Unzip files
    outdir = os.getcwd()
    # print(short_star_name)
    # new_path = outdir + '/iue/' + short_star_name + '/'
    os.chdir(folder_data)
    file_list = glob('*')
    if len(file_list) != 0:
        # print(file_list)
        fname = str(file_list[0])
        # print(fname)
        tar = tarfile.open(fname, "r:gz")
        tar.extractall()
        tar.close()
        os.system('rm *.gz')
    os.chdir(outdir)
    browser.close()
```

```
    return


# ============================================================================
def retrieve_ebmv_value(star_name):
    '''
    Search the INES website for a specified star's E(B-V) value.

    :param star_name: stars's name (string)
    :return: E(B-V) value
    '''

    from pyvirtualdisplay import Display
    display = Display(visible=0, size=(800, 600))
    display.start()

    # Define global Chrome properties
    browser = webdriver.Chrome()

    # Define web source
    irsa_site = "http://irsa.ipac.caltech.edu/applications/DUST/"

    # Openning it
    browser.get(irsa_site)
    # wait = WebDriverWait(browser, 180)
    # wait.until(EC.title_contains("title"))

    # Selecting some stars
    browser.find_element_by_name("locstr").send_keys(star_name)
    browser.find_element_by_class_name("tdsubmit").click()

    time.sleep(30)
    ebmv = browser.find_element_by_class_name("tdwhiteleft")
    ebmv = float(ebmv.text)
    browser.close()

    return ebmv

    return ebmv


# ============================================================================
def main():

    num_spa = 75
    print(num_spa * '=')
    print('\nBeFaVOr_Web\n')
    print(num_spa * '=')
# ----------------------------------------------------------------------------

    # Defining folders
    user = input('Who is using? (bmota or artur): ')
    commum_folder = '/home/' + user + '/Dropbox/Artur/BeFaVOr_web/'
    commum_folder_2 = '/home/' + user + '/Dropbox/Artur/BeFaVOr_web/'

    folder_tables = commum_folder + 'tables/'
    folder_tables_2 = commum_folder_2 + 'emcee/' + 'tables/'
```

```
    folder_figures = commum_folder + 'figures/'

    table_final = folder_tables + 'list.txt'
    table_final_2 = folder_tables_2 + 'list_final.txt'
# ----------------------------------------------------------------------------

    # Saving the input for the routine Befavour.py
    if os.path.isfile(table_final_2) is True:
        os.system('rm ' + table_final_2)

    if os.path.isfile(folder_figures) is False:
        os.system('rm -r ' + folder_figures)

    if os.path.isfile(folder_figures) is False:
        os.system('mkdir ' + folder_figures)

    if os.path.isfile(table_final) is True:
        os.system('rm ' + table_final)

    os.system('rm -r' + folder_tables)
    if os.path.isdir(commum_folder + 'tables/') is False:
        os.mkdir(commum_folder + 'tables/')
# ----------------------------------------------------------------------------

    # Would you like to run one or a list of stars?
    option = input('\nRun one or more stars: (1 or more) ')

    if option == '1':
        # Saving data from the INES database
        star = input('\nPlease, put the star name: ')
        print('\nSaving data from INES database...')
        selecting_data(star_name=star, commum_folder=commum_folder)

        # Saving SIMBAD stellar data to a table
        print('\nSaving data (plx, vsini) from SIMBAD database...')
        table_file = commum_folder + 'tables/' + star + '.txt'
        folder_tables = commum_folder + 'tables/'
        val = read_simbad_data(star_name=star)

        # Check if there are bump files
        folder_star = commum_folder + 'iue/' + star
        bump = glob(folder_star + 'L*')

        if len(bump) is 0:
            start_time = time.time()
            val = list(val)
            ebmv_bump = retrieve_ebmv_value(star_name=star)
            print(ebmv_bump)
            val[7] = ebmv_bump
            val[5] = False
            val = tuple(val)
            print("--- %s seconds ---" % (time.time() - start_time))

        # Saving the table
        create_txt_file(data_list=val, file_name=table_file)
# ----------------------------------------------------------------------------

    if option == 'more':
```

```
        cols = read_txt(list_name='selected_bn_stars.txt',
                        folder=commum_folder + 'tables_vizier/')

        cols_2 = read_txt(list_name='selected_bn_stars_compl.txt',
                          folder=commum_folder + 'tables_vizier/')

        cols_3 = read_txt(list_name='selected_be_stars.txt',
                          folder=commum_folder + 'tables_vizier/')

        cols_4 = read_txt(list_name='selected_be_bsc_stars.txt',
                          folder=commum_folder + 'tables_vizier/')

        # cols_5 = read_txt(list_name='selected_be_bsc_stars_compl.txt',
        #                   folder=commum_folder + 'tables_vizier/')

        stars = np.concatenate((cols[0], cols_2[0], cols_3[0],
                                cols_4[0]), axis=0)

        # stars = cols_3[0]

# ----------------------------------------------------------------------------

        for i in range(len(stars)):
            star = str(stars[i])
            star = "HD " + star[:-2]
            a = star.split()
            star_2 = a[0] + a[1]
            # Saving data from the INES database
            print(num_spa * '=')
            print('\nStar: %s' % star)
            print('\nSaving data from INES database... %d of %d' %
                  (i + 1, len(stars)))

            selecting_data(star_name=star, commum_folder=commum_folder)

            # Saving SIMBAD stellar data to a table
            print('\nSaving data from SIMBAD database... star: %s\n'
                  % (star))
            table_file = commum_folder + 'tables/' + star + '.txt'
            val = read_simbad_data(star_name=star)

            # Check if there are bump files
            folder_star = commum_folder + 'iue/' + star_2 + '/'

            bump = glob(folder_star + 'L*')
            # print(star_2)
            # print(folder_star)
            # print(bump)
            # print(len(bump))
            if len(bump) is 0:
                start_time = time.time()
                val = list(val)
                ebmv_bump = retrieve_ebmv_value(star_name=star)
                print(ebmv_bump)
                val[7] = ebmv_bump
                val[5] = False
                val = tuple(val)
                print("--- %s seconds ---" % (time.time() - start_time))
```

Project Report: "Be-FaVOR: Be Stars - Facilities in VO Research. Uma ferramenta para a determinação de parâmetros de estrelas Be", Release 1.0

```
                print(val)
            # nan and "--" Filters
            if math.isfinite(val[1]) is True and math.isfinite(val[2]) is True\
               and math.isfinite(val[3]) is True:

                if math.isfinite(val[3]) is True and\
                   math.isfinite(val[4]) is False:
                    val = list(val)
                    val[4] = 0.0
                    val = tuple(val)
                    create_txt_file(data_list=val, file_name=table_file)
                else:
                    create_txt_file(data_list=val, file_name=table_file)
            else:
                print('This Star was excluded!')
# ----------------------------------------------------------------------------

        # Plotting galatic distribution
        ra_val_arr = []
        dec_val_arr = []
        for i in range(len(stars)):
            star = str(stars[i])
            star = "HD " + star[:-2]
            ra, dec = read_simbad_coodr(star_name=star)
            ra_val_arr.append(ra)
            dec_val_arr.append(dec)

        plot_gal(ra_val=ra_val_arr, dec_val=dec_val_arr,
                 folder_fig=folder_figures)

# ----------------------------------------------------------------------------

    # Creating list of files
    create_list_files(list_name='list', folder=folder_tables,
                      folder_table=folder_tables)

    table_final = folder_tables + 'list.txt'
    table_final_2 = folder_tables_2 + 'list_final.txt'

    files = open(table_final)
    files = files.readlines()
    final_table = open(table_final_2, "a+")

    for i in range(len(files)):
        files_2 = open(files[i][:-1])

        lines = files_2.readlines()

        if len(lines) == 8:
            star = lines[0][:-1]
            a = star.split()

            if len(a) >= 2:
                short_star_name = a[0] + a[1]
            else:
                short_star_name = np.copy(a)

            final_table.writelines(('%s\t%s\t%s\t%s\t%s\t%s\n')
```

```
                                    % (short_star_name, lines[1][:-1],
                                       lines[2][:-1], lines[3][:-1],
                                       lines[4][:-1], lines[7][:-1],
                                       lines[5][:-1]))
    final_table.close()
    print(num_spa * '=')
    print('\nFinished\n')
    return


# ============================================================================
if __name__ == '__main__':
    main()
```

6.2 Anexo 2: Rotina TAKE-VIZIER-DATA

```
# ============================================================================
# !/usr/bin/env python
# -*- coding:utf-8 -*-

# Created by B. Mota 2016-02-16 to present...

# import packages

import matplotlib.pyplot as plt
import matplotlib as mpl
import matplotlib.font_manager as fm
import numpy as np
import pyhdust.phc as phc
from astroquery.vizier import Vizier
from astroquery.simbad import Simbad
import csv
import os
# import pyraf
mpl.rcParams.update({'font.size': 18})
mpl.rcParams['lines.linewidth'] = 2
font = fm.FontProperties(size=17)
mpl.rc('xtick', labelsize=17)
mpl.rc('ytick', labelsize=17)
fontsize_label = 18  # 'x-large'

__version__ = "0.0.1"
__author__ = "Bruno Mota"

# ============================================================================
# Parameters that must be defined
user = 'bruno'
num_spa = 75
commum_folder = '/home/' + user + '/Dropbox/Artur/BeFaVOr_web/' +\
    'tables_vizier/'
folder_fig = '/home/' + user + '/Dropbox/Artur/BeFaVOr_web/figures/'

if os.path.isdir(folder_fig) is False:
    os.mkdir(folder_fig)

print(num_spa * '=')
```

```
print('\nTake_VIZIER_data\n')
print(num_spa * '=')


# ============================================================================
def create_txt_file(a, b, c, d, e, f, g, h, i, j, l, file_name):
    '''
    Create a txt file.

    :param a: table's column (array)
    :param b: table's column (array)
    :param c: table's column (array)
    :param d: table's column (array)
    :param e: table's column (array)
    :param f: table's column (array)
    :param g: table's column (array)
    :param h: table's column (array)
    :param i: table's column (array)
    :param j: table's column (array)
    :param l: table's column (array)
    :param file_name: file's name (string)
    :return: txt file
    '''

    with open(file_name, 'w') as k:
        # file.write(('%s\t & \t %s \t & \t %s \t & \t %s \t & \t  %s \t &' +
        #                ' \t  %s \t & \t  %s   \n')
        writer = csv.writer(k, delimiter='\t')
        writer.writerows(zip(a, b, c, d, e, f, g, h, i, j, l))

    return


# ============================================================================
def create_txt_file_compl(a, b, c, d, e, f, g, h, file_name):
    '''
    Create a txt file.

    :param a: table's column (array)
    :param b: table's column (array)
    :param c: table's column (array)
    :param d: table's column (array)
    :param e: table's column (array)
    :param f: table's column (array)
    :param g: table's column (array)
    :param h: table's column (array)
    :param file_name: file's name (string)
    :return: txt file
    '''

    with open(file_name, 'w') as k:
        writer = csv.writer(k, delimiter='\t')
        writer.writerows(zip(a, b, c, d, e, f, g, h))

    return


# ============================================================================
```

```
def main():

    Vizier.ROW_LIMIT = -1  # VIZIER whole catalog
    cat = ['V/50', 'V/36B']
    catalogs = Vizier.get_catalogs(cat)
    catalog = catalogs[0]
    catalog_compl = catalogs[2]

    # Operating with the data
    data = catalog.as_array()
    data_compl = catalog_compl.as_array()

    # Print available data
    data.dtype
    data_compl.dtype

    # Filtering the SpType
    sptype = list(data['SpType'].data)
    sptype_compl = list(data_compl['SpType'].data)
    # indexes = np.where(conc_flux[0] > 0)

    indexes = []
    for i in range(len(sptype)):
        sptyp = sptype[i].decode('UTF-8')
        if len(sptyp) != 0:
            if sptyp[0] == 'B':
                if ('e' in sptyp) is False:
                    if ('IV' in sptyp) is False:
                        if ('IIII' in sptyp) is False:
                            if ('Hg' in sptyp) is False:
                                if ('Mn' in sptyp) is False:
                                    if ('n' in sptyp) is True:
                                        indexes.append(i)

    indexes_compl = []
    for i in range(len(sptype_compl)):
        sptyp_compl = sptype_compl[i].decode('UTF-8')
        if len(sptyp_compl) != 0:
            if sptyp_compl[0] == 'B':
                if ('e' in sptyp_compl) is False:
                    if ('IV' in sptyp_compl) is False:
                        if ('IIII' in sptyp_compl) is False:
                            if ('Hg' in sptyp_compl) is False:
                                if ('Mn' in sptyp_compl) is False:
                                    if ('n' in sptyp_compl) is True:
                                        if ('n' in sptyp_compl) is True:
                                            indexes_compl.append(i)

# ============================================================================
    # Selecting the data with the B stars
    selected_data = data[indexes]
    sptyp_selected = list(selected_data['SpType'])
    name_selected = selected_data['Name']
    hd_selected = selected_data['HD']
    plx = selected_data['Parallax']
    bmv = selected_data['B-V']
    err_bmv = selected_data['u_B-V']
    umb = selected_data['U-B']
```

```
    err_umb = selected_data['u_U-B']
    rmi = selected_data['R-I']
    vsini = selected_data['RotVel']
    err_vsini = selected_data['u_RotVel']
    companions = selected_data['MultCnt']

    selected_data_compl = data_compl[indexes_compl]
    sptyp_selected_compl = list(selected_data_compl['SpType'])
    hd_selected_compl = selected_data_compl['HD']
    plx_compl = selected_data_compl['Plx']
    bmv_compl = selected_data_compl['B-V']
    umb_compl = selected_data_compl['U-B']
    rmi_compl = selected_data_compl['R-I']
    vsini_compl = selected_data_compl['vsini']
    err_vsini_compl = selected_data_compl['u_vsini']


# ============================================================================
    # Checking if there are IUE data
    customSimbad = Simbad()
    customSimbad.TIMEOUT = 2000  # sets the timeout to 2000s

    # see which fields are currently set
    customSimbad.get_votable_fields()

    # To set other fields
    customSimbad.add_votable_fields('measurements')


# ============================================================================
    # Selecting the stars with IUE data
    data = data[indexes]
    obs_iue_date = []
    stars = []
    indexes = []
    print(num_spa * '=')
    print('\nselected stars: %d\n' % len(hd_selected))
    print(num_spa * '=')
    for i in range(len(hd_selected)):
        try:
            star = "HD " + str(hd_selected[i])
            result_table = customSimbad.query_object(star)
            obs_date = result_table['IUE_ObsDate']
            if len(obs_date.item()) != 0:
                print(num_spa * '-')
                print('\n' + star)
                print('%0.2f perc. concluded' % (100 * i / len(hd_selected)))
                print(obs_date)
                obs_iue_date.append(obs_date.item())
                stars.append(star)
                indexes.append(i)
        except:
            pass

    data_compl = data_compl[indexes_compl]
    obs_iue_date_compl = []
    stars_compl = []
    indexes_compl = []
```

```
    print('selected stars compl: %d' % len(hd_selected_compl))
    for i in range(len(hd_selected_compl)):
        try:
            star = "HD " + str(hd_selected_compl[i])
            result_table = customSimbad.query_object(star)
            obs_date = result_table['IUE_ObsDate']
            if len(obs_date.item()) != 0:
                print(num_spa * '-')
                print('\n' + star)
                print('%0.2f perc. concluded' % (100 * i / len(hd_selected)))
                print(obs_date)
                obs_iue_date_compl.append(obs_date.item())
                stars_compl.append(star)
                indexes_compl.append(i)
        except:
            pass

# ============================================================================
    # Selecting the data with the B stars in IUE database

    selected_data = data[indexes]
    sptyp_selected = list(selected_data['SpType'])
    name_selected = selected_data['Name']
    hd_selected = selected_data['HD']
    plx = selected_data['Parallax']
    bmv = selected_data['B-V']
    err_bmv = selected_data['u_B-V']
    umb = selected_data['U-B']
    err_umb = selected_data['u_U-B']
    rmi = selected_data['R-I']
    vsini = selected_data['RotVel']
    err_vsini = selected_data['u_RotVel']
    companions = selected_data['MultCnt']

    selected_data_compl = data_compl[indexes_compl]
    sptyp_selected_compl = list(selected_data_compl['SpType'])
    hd_selected_compl = selected_data_compl['HD']
    plx_compl = selected_data_compl['Plx']
    bmv_compl = selected_data_compl['B-V']
    umb_compl = selected_data_compl['U-B']
    rmi_compl = selected_data_compl['R-I']
    vsini_compl = selected_data_compl['vsini']
    err_vsini_compl = selected_data_compl['u_vsini']


# ============================================================================
    # Plotting correlations

    # Plot B-V vs U-B
    plt.clf()
    plt.scatter(bmv, umb, label='V/50', marker='o')
    plt.scatter(bmv_compl, umb_compl, label='V/36B', color='red', marker='o')
    plt.xlabel(r'(B-V) [mag]')
    plt.ylabel(r'(U-B) [mag]')
    plt.legend()
    plt.savefig(folder_fig + 'bmvVSumb.png')

# ----------------------------------------------------------------------------
```

```
    # Plot R-I vs U-B
    plt.clf()
    plt.scatter(rmi, umb, label='V/50', marker='o')
    plt.scatter(rmi_compl, umb_compl, label='V/36B', color='red', marker='o')
    plt.xlabel(r'(R-I) [mag]')
    plt.ylabel(r'(U-B) [mag]')
    plt.legend()
    plt.savefig(folder_fig + 'rmiVSumb.png')

# ------------------------------------------------------------------------------
    # Plot B-V vs R-I
    plt.clf()
    plt.scatter(bmv, rmi, label='V/50', marker='o')
    plt.scatter(bmv_compl, rmi_compl, label='V/36B', color='red', marker='o')
    plt.xlabel(r'(B-V) [mag]')
    plt.ylabel(r'(R-I) [mag]')
    plt.legend()
    plt.savefig(folder_fig + 'bmvVSrmi.png')

# ------------------------------------------------------------------------------
    # Plot B-V vs vsini
    plt.clf()
    plt.scatter(bmv, vsini, label='V/50', marker='o')
    plt.scatter(bmv_compl, vsini_compl, label='V/36B', color='red', marker='o')
    plt.xlabel(r'(B-V) [mag]')
    plt.ylabel(r'$v \sin i$ [km/s]')
    plt.legend()
    plt.savefig(folder_fig + 'bmvVSvsini.png')

# ==============================================================================

    create_txt_file(a=hd_selected, b=bmv, c=umb, d=rmi, e=vsini,
                    f=err_bmv, g=err_umb, h=err_vsini, i=companions.data,
                    j=obs_iue_date, l=sptyp_selected,
                    file_name=commum_folder + 'selected_stars.txt')

    create_txt_file_compl(a=hd_selected_compl, b=bmv_compl, c=umb_compl,
                          d=rmi_compl, e=vsini_compl, f=err_vsini_compl,
                          g=obs_iue_date_compl, h=sptyp_selected_compl,
                          file_name=commum_folder + 'selected_stars_compl.txt')

# ==============================================================================
    # example
    if False:
        R = np.array((data['Vc'] * 1e5) ** 2 /
                     10 ** data['logg'] / phc.Rsun.cgs)
        L = phc.sigma.cgs * np.array(data['Teff'], dtype=float)**4 * 4 *\
            np.pi * (R * phc.Rsun.cgs)**2 * phc.Lsun.cgs
        M = np.array((data['Vc'] * 1e5)**2 * (R * phc.Rsun.cgs) /
                     phc.G.cgs / phc.Msun.cgs)

# ==============================================================================
if __name__ == '__main__':
    main()
```

CHAPTER

SEVEN

REFERÊNCIAS E INDEX

7.1 Referências

Secchi, A.1866, Astronomische Nachrichten, 68, 63

Rivinius, T., Carciofi, A. C., & Martayan, C.2013, *Astronomy and Astrophysics Review*, 21, 69

Project Report: "Be-FaVOR: Be Stars - Facilities in VO Research. Uma ferramenta para a determinação de parâmetros de estrelas Be", Release 1.0

PYTHON MODULE INDEX

b

Project Report: "Be-FaVOR: Be Stars - Facilities in VO Research. Uma ferramenta para a determinação de parâmetros de estrelas Be", Release 1.0

INDEX

Appendix L

Article: Bayesian-MCMC inference of Fundamental Parameters of Westerlund 1

MNRAS **000**, 1–9 (2019) Preprint 26 May 2019 Compiled using MNRAS LATEX style file v3.0

Bayesian-MCMC inference of Fundamental Parameters of Westerlund 1
I. Stellar and Extinction parameters of single stars

M. Rubinho[1]★, B. C. Mota[1], D. M. Faes[1] and L. R. Rimulo[1]
[1]*Instituto de Astronomia, Geofísica e Ciências Atmosféricas, Universidade de São Paulo, Rua do Matão 1226, Cidade Universitária, 05508-900 São Paulo, SP, Brazil*

Accepted XXX. Received YYY; in original form ZZZ

ABSTRACT
There is a lack of information about the accurate stellar parameters of these stars. The deposition of chemically enriched material and his mechanical energy makes them crucial objects of study to understanding the stellar evolution. The young massive stellar cluster, Westerlund 1, is an unique laboratory to the study an comprehension of massive stars. We propose in this work a method of estimation and modeling of stellar fundamental parameters. Thus obtaining inferences regarding data not determined about Westerlund 1. Statistical analysis of a cluster allows a better understanding and validation of the method Describe the method *** Briefly show the results *** Conclusions ***

Key words: Stars: evolution – Stars: fundamental parameters – supergiants

1 INTRODUCTION

Massive stars ($> 20 M_{\odot}$) are known because of their influence in the dynamics and chemical evolution of the Galaxy (Zinnecker & Yorke 2007). It has been recognized that they play leading roles in shaping the interstellar medium (hereafter, ISM) and the galactic evolution. The main reasons are the deposition of chemically enriched material together with large quantities of mechanical energy (e.g. Massey 2003). These are some points that make them crucial objects to understanding the stellar evolution.

Even being of fundamental importance to understanding several processes in the Galaxy (e.g. Martins et al. 2005, Zinnecker & Yorke 2007, Tan et al. 2014), the formation and accurate stellar parameters are still incomplete. To accurately determine the intrinsic physical properties and evolution of these stars we need to establish the distances, ages and reddening of the clusters.

In this context, clustered star formation is the dominant mode of star formation in the Universe with about 80% of all stars originating in giant molecular clouds (Lada & Lada 2003). In the Galaxy, few massive clusters ($> 10^4$ M$_{\odot}$) are can be used to study these objects. For instance, we have the clusters: Arches (Figer et al. 2002), Quintuplet (Figer et al. 1999), Central cluster (Figer et al. 2004), and Westerlund 1 (Clark et al. 2005b). Among them, Westerlund 1 (hereafter Wd 1) is the most massive starburst cluster identified to-date in the Galaxy (Brandner et al. 2008; Clark et al. 2005b), being the first super star cluster discovered within the Galaxy (Westerlund 1961a). As such, its proximity allowed to study individual stars Clark et al. (2010). It has also a rich variety of other stellar types, including Wolf-Rayet stars (Clark et al. 2008; Skinner et al. 2006; Negueruela & Clark 2005), X-ray pulsar (Muno et al. 2006). These general features makes Wd 1 the perfect laboratory to study young massive stars.

In general, the physical properties of stars are not directly ascertainable. Besides this, the stellar parameters, extinction and geometrical parameters are coupled, which should, therefore, taken into account in any procedure used to infer these parameters. To deal with this issue, we used a Bayesian approach (section 2) to estimate the fundamental parameters of the massive stars of Wd 1.

The structure of the paper is as follows: the sections 2 and 3 show the adopted theoretical models and the Bayesian approach. We show the observational data are described in section 4. The results are shown in section 5. Finally, the discussions and conclusions are shown in sections 6 and 7.

2 THEORETICAL AND INFERENCE TOOLS

We adopted the Kurucz (Castelli & Kurucz 2003) atlas of model atmospheres [1] in our study. This atlas contains about 7 600 models of stellar spectra for a large range of metallicities, effective temperatures ($3\,500\,\mathrm{K} \leq T_{\mathrm{eff}} \leq 50\,000\,\mathrm{K}$), surface gravities ($0.0 \leq \log g \leq 5.0$) and stellar radius ($1\,\mathrm{R}_{\odot} \leq R_{\star} \leq 2\,500\,\mathrm{R}_{\odot}$). In our modeling, we adopted the solar metallicity and the remaining parameters were fixed to lie within described ranges.

To deal with the Bayes' approach, we used the modern Emcee

★ E-mail: esteemeuemail@gmail.com

[1] Available at http://kurucz.harvard.edu/grids.html;

Appendix M

Corner plots of the Sample of Stars

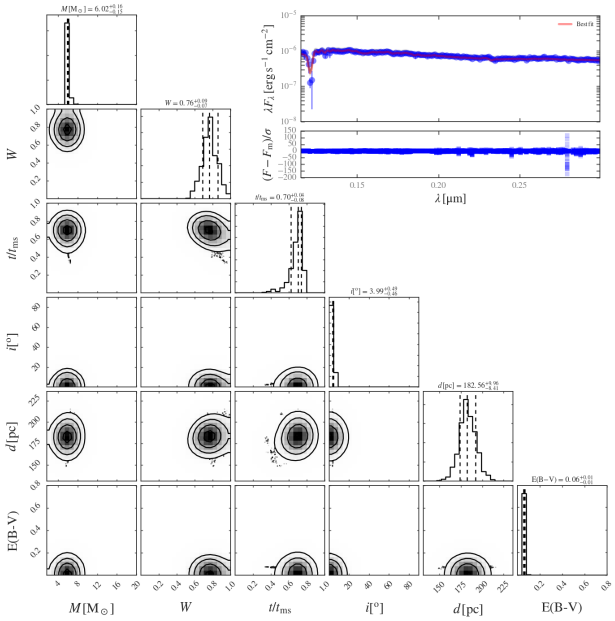

Figure 1: Corner plot of HD3369.

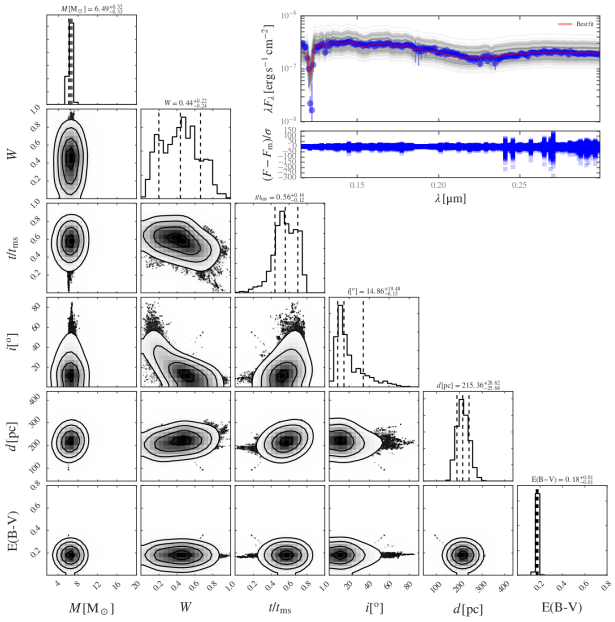

Figure 2: Corner plot of HD17543.

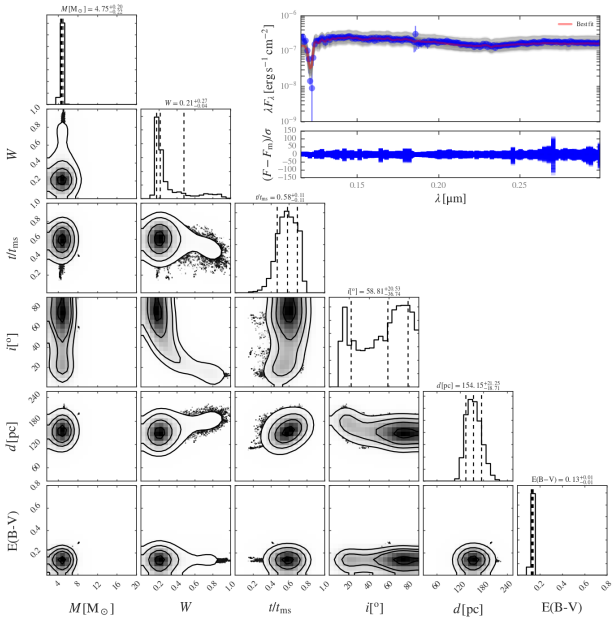

Figure 3: Corner plot of HD18537.

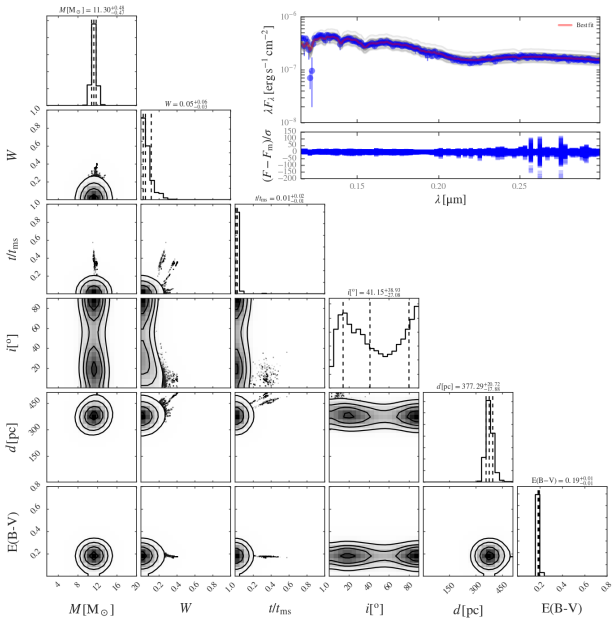

Figure 4: Corner plot of HD19374.

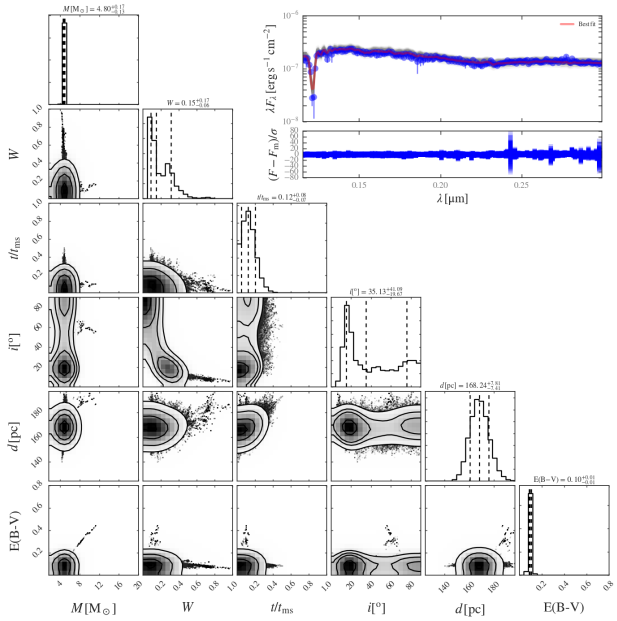

Figure 5: Corner plot of HD21278.

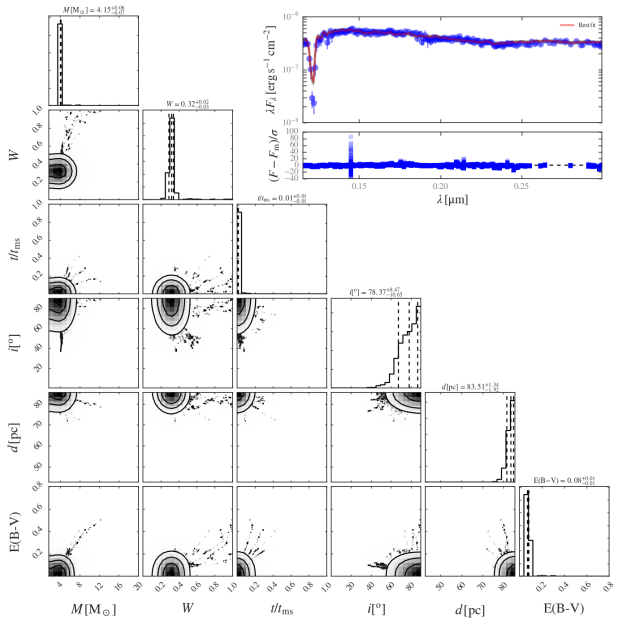

Figure 6: Corner plot of HD21364.

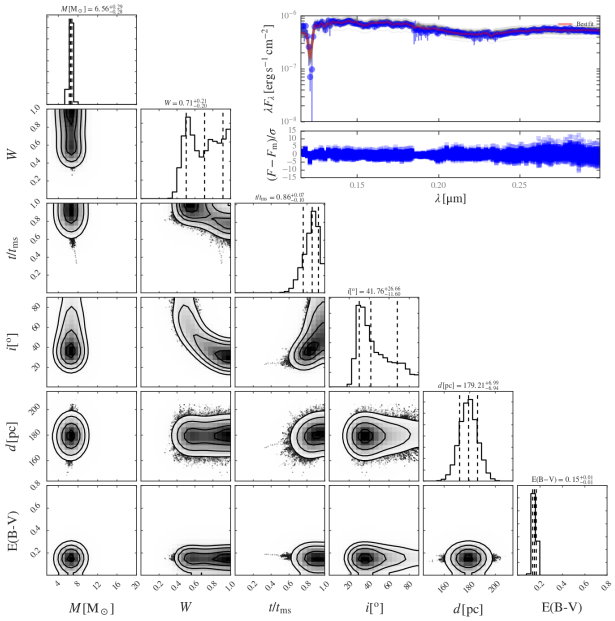

Figure 7: Corner plot of HD22192.

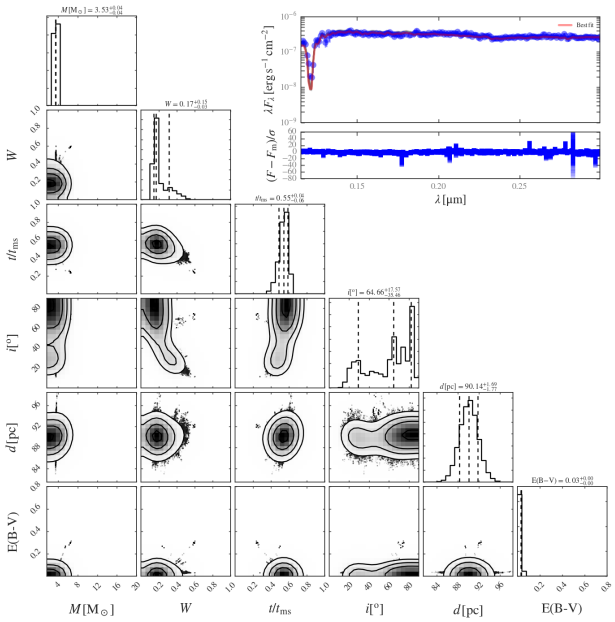

Figure 8: Corner plot of HD22203.

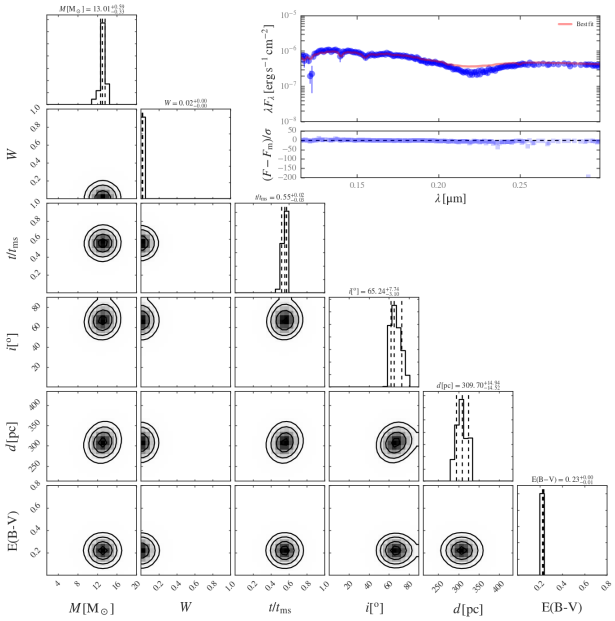

Figure 9: Corner plot of HD22951.

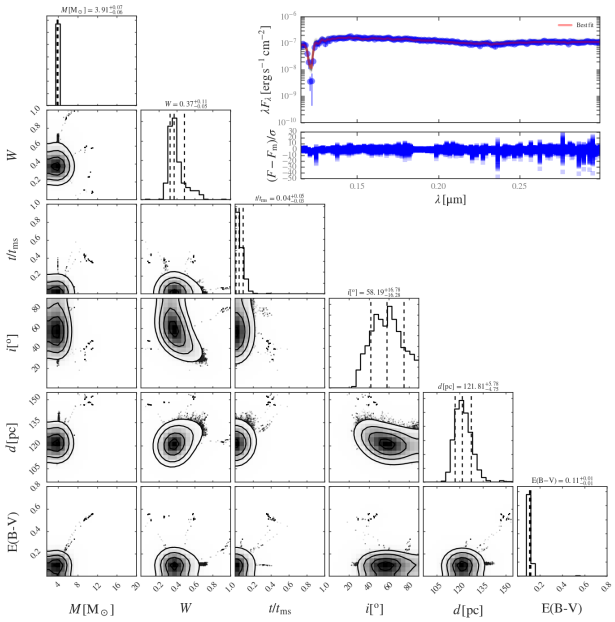

Figure 10: Corner plot of HD23324.

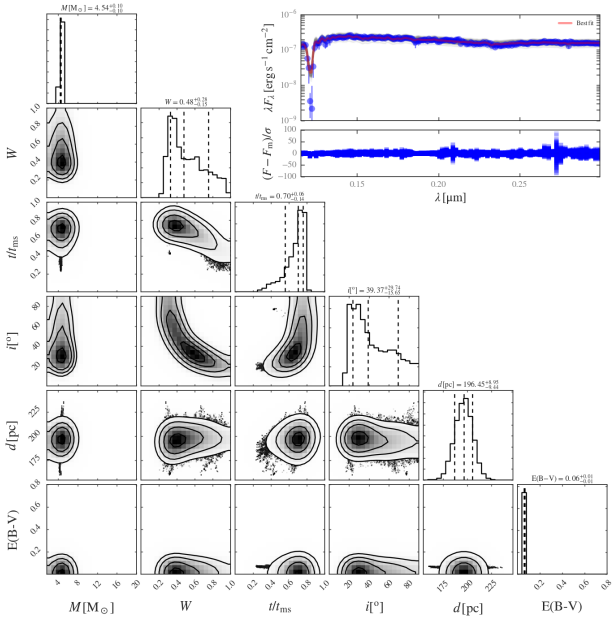

Figure 11: Corner plot of HD23363.

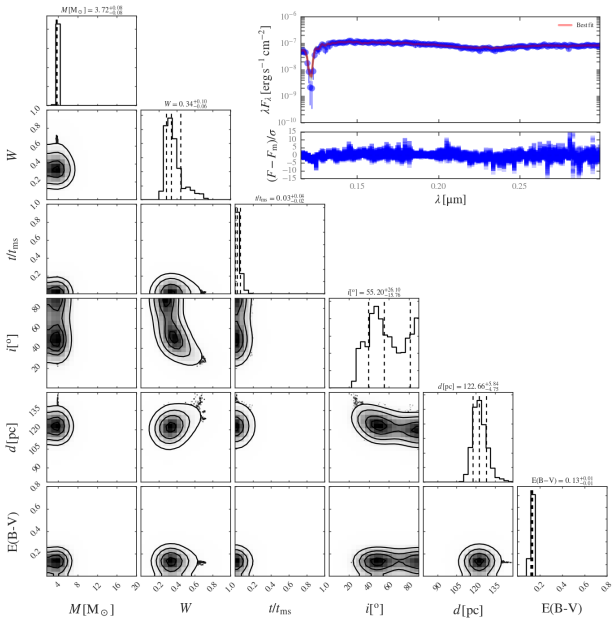

Figure 12: Corner plot of HD23432.

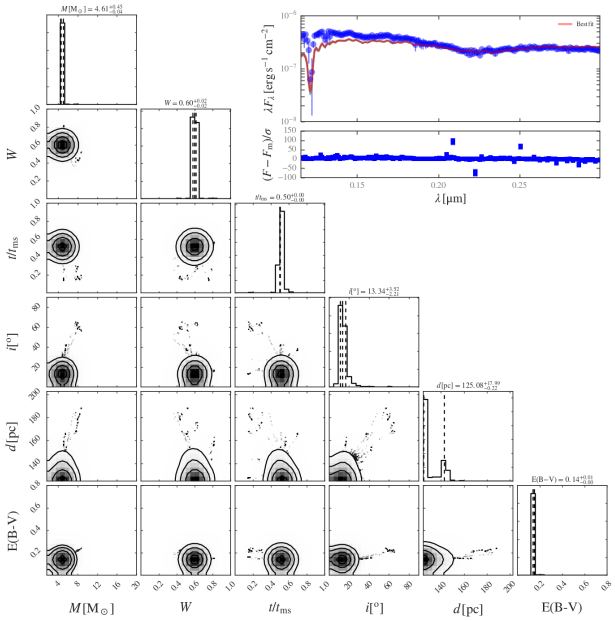

Figure 13: Corner plot of HD23466.

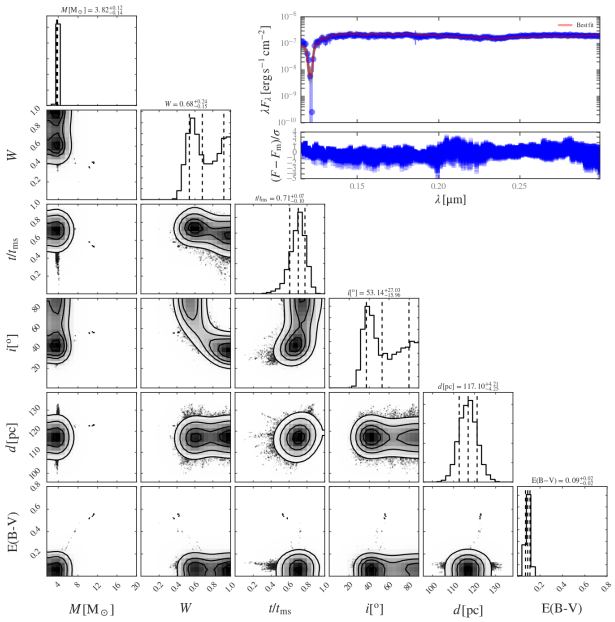

Figure 14: Corner plot of HD23862.

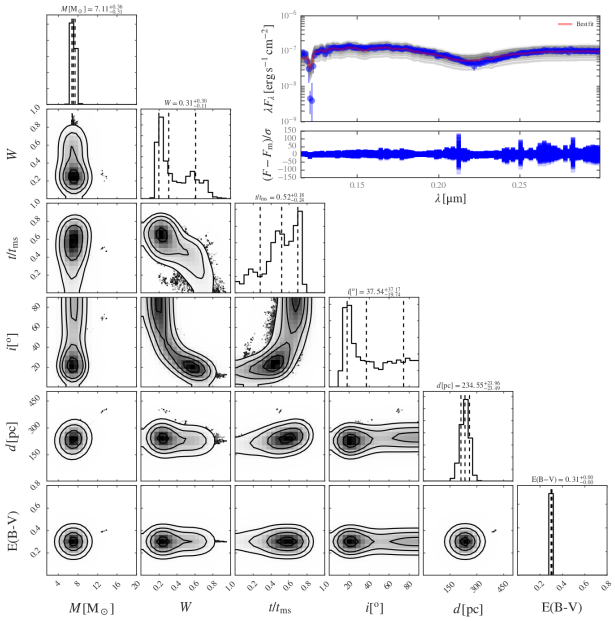

Figure 15: Corner plot of HD24263.

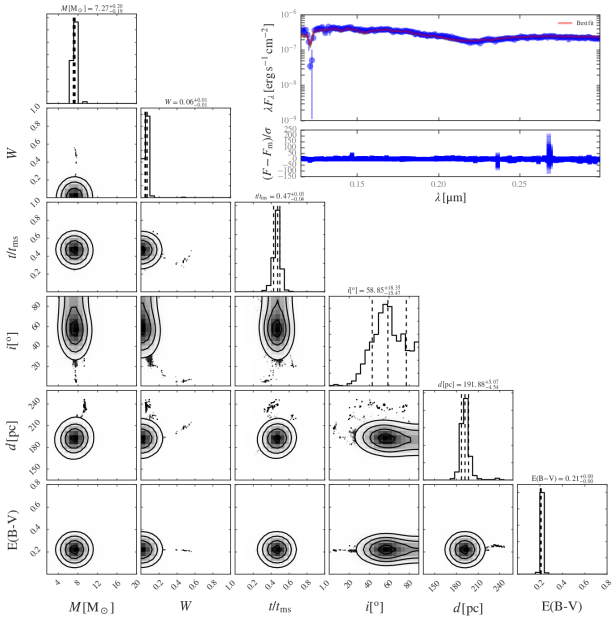

Figure 16: Corner plot of HD25558.

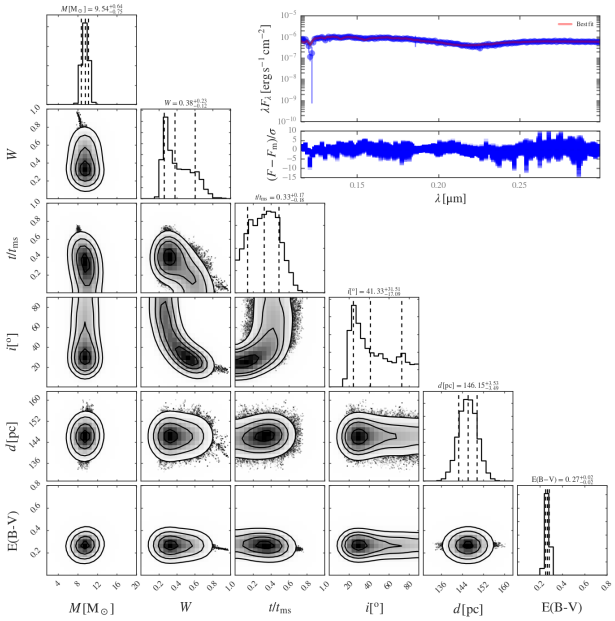

Figure 17: Corner plot of HD25940.

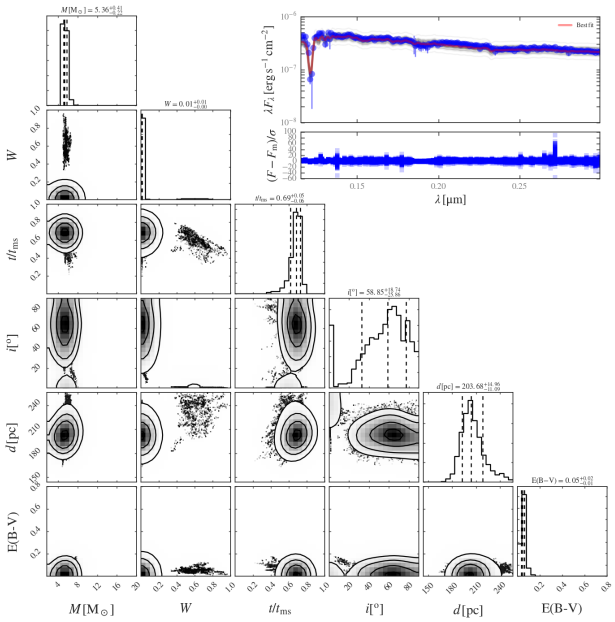

Figure 18: Corner plot of HD26326.

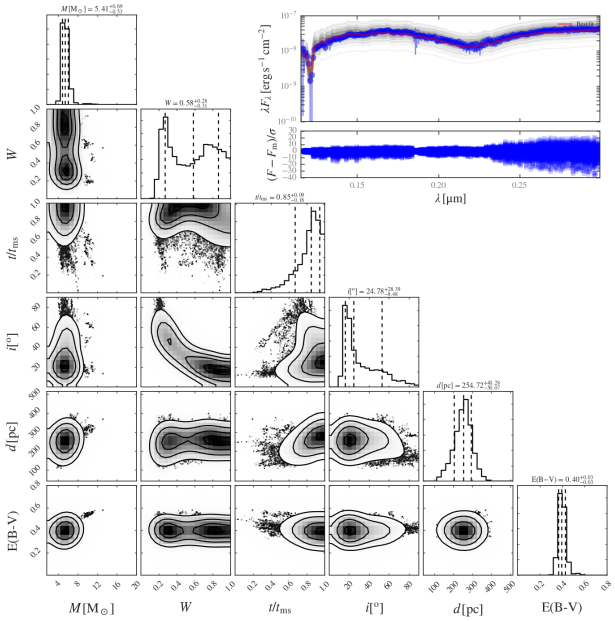

Figure 19: Corner plot of HD27778.

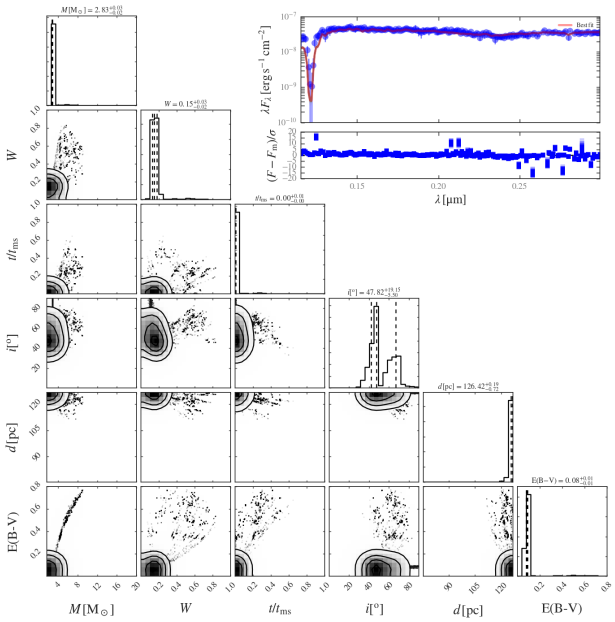

Figure 20: Corner plot of HD29365.

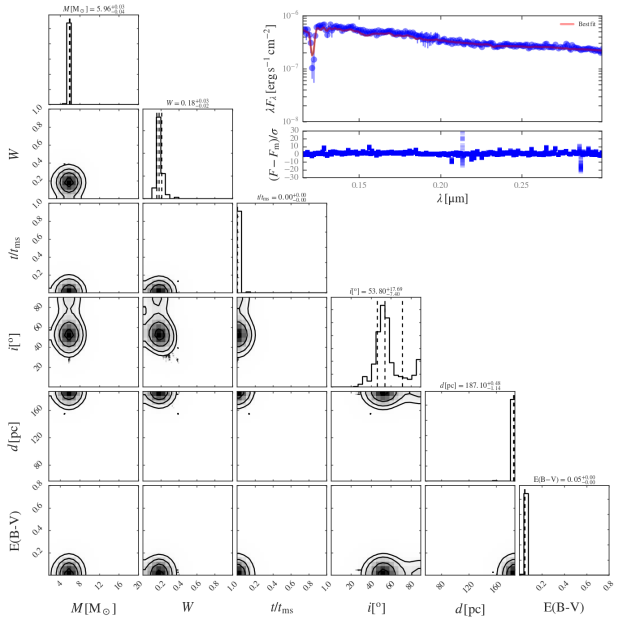

Figure 21: Corner plot of HD29763.

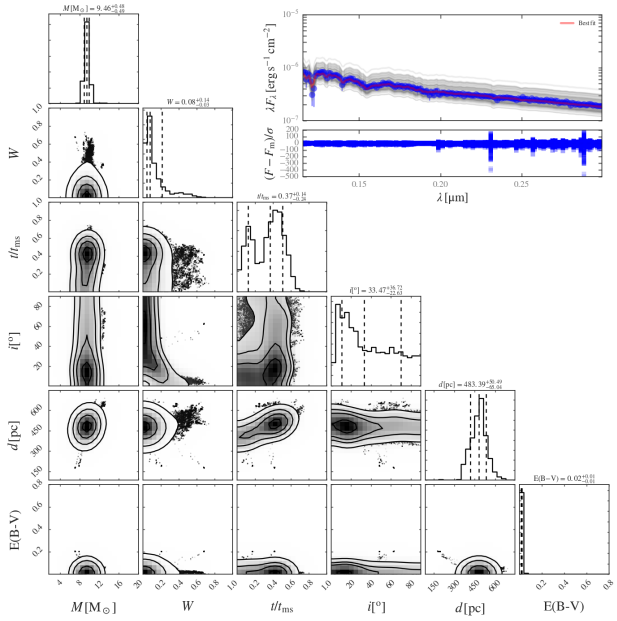

Figure 22: Corner plot of HD31726.

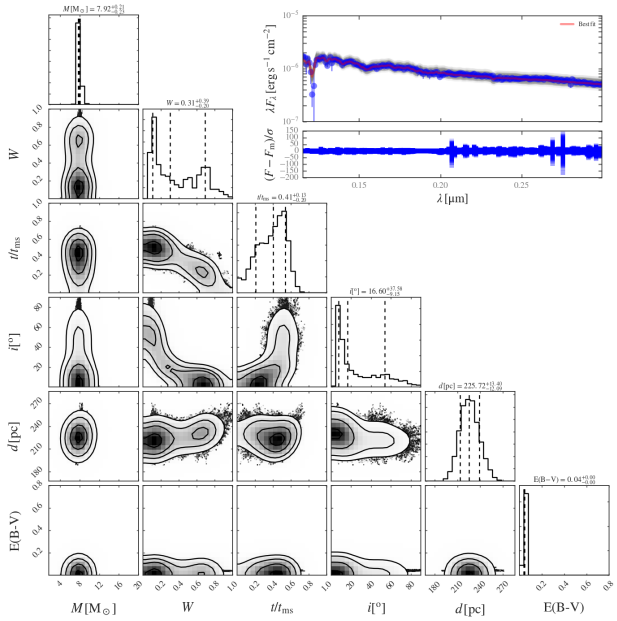

Figure 23: Corner plot of HD32249.

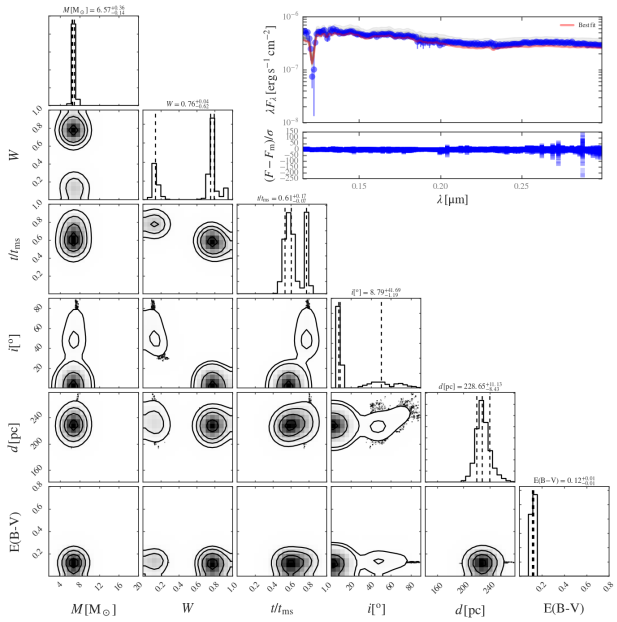

Figure 24: Corner plot of HD32343.

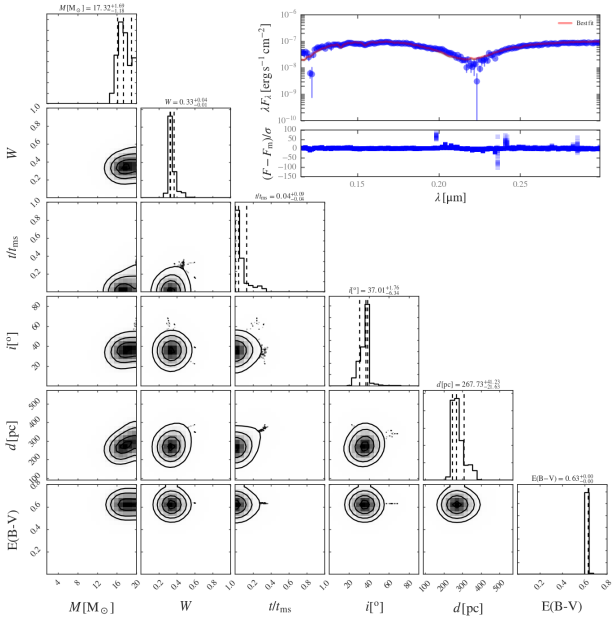

Figure 25: Corner plot of HD32991.

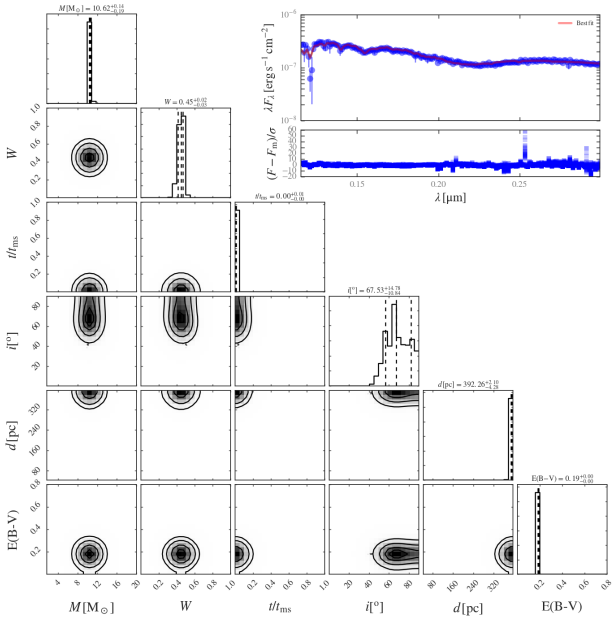

Figure 26: Corner plot of HD34748.

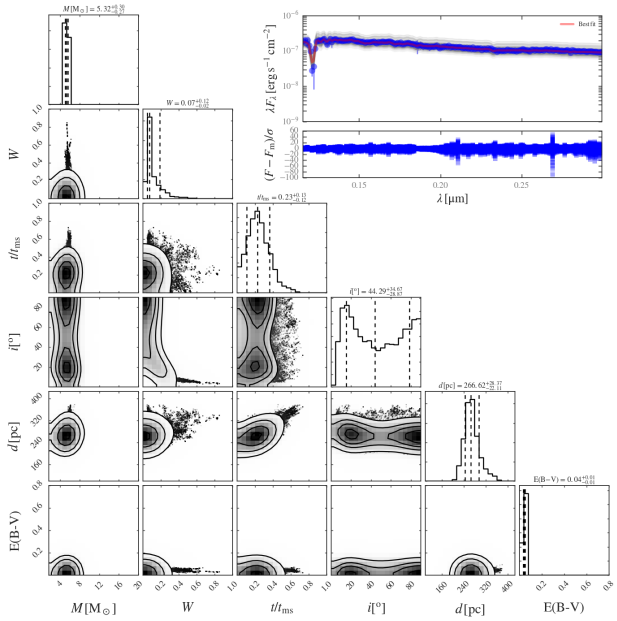

Figure 27: Corner plot of HD34798.

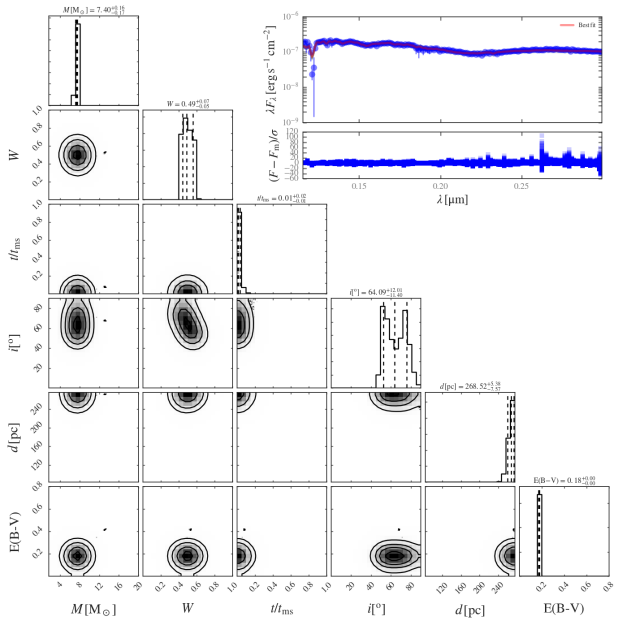

Figure 28: Corner plot of HD35532.

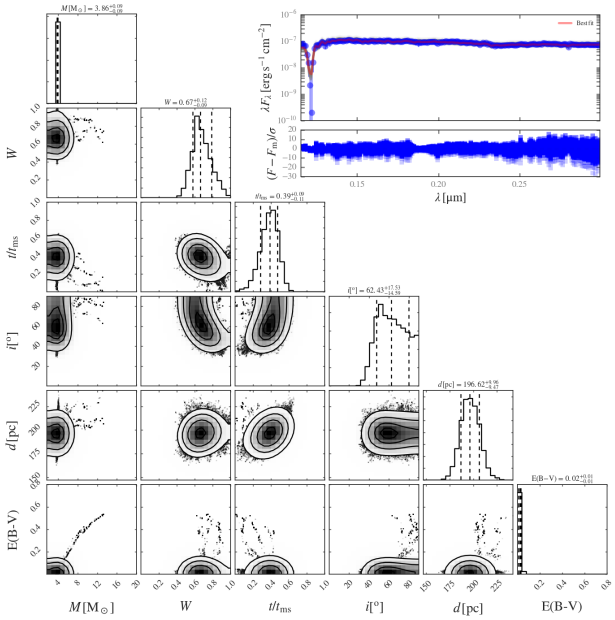

Figure 29: Corner plot of HD35580.

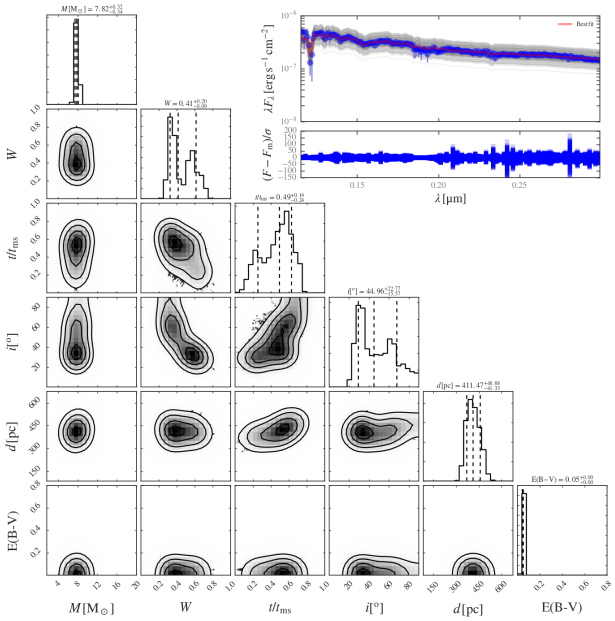

Figure 30: Corner plot of HD35588.

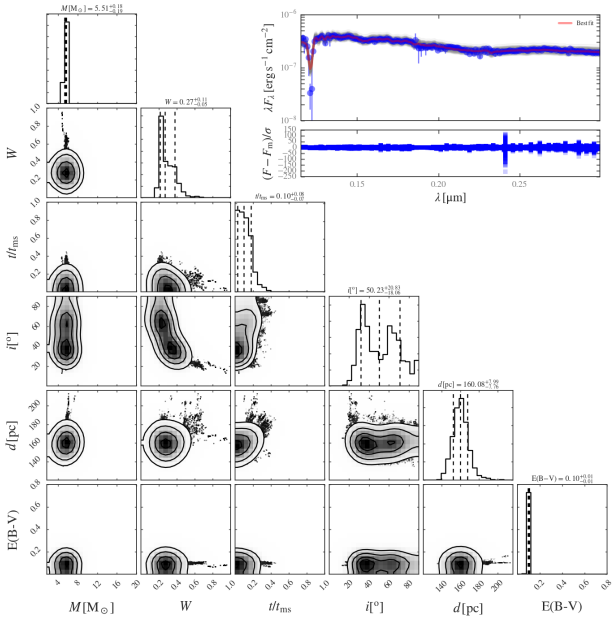

Figure 31: Corner plot of HD35671.

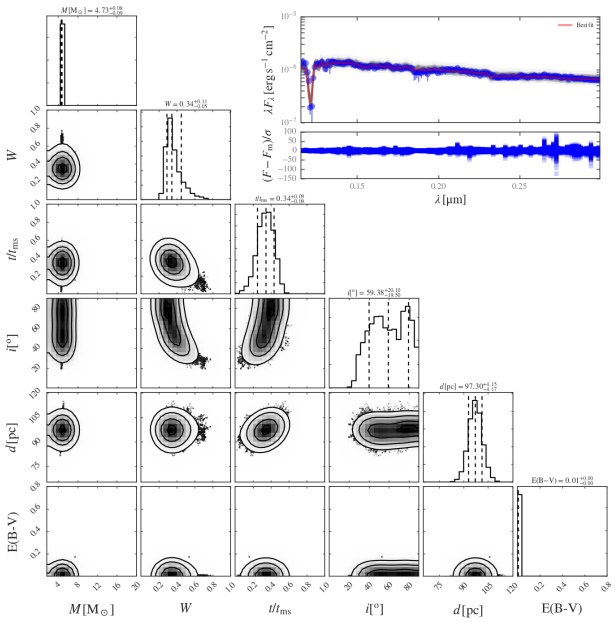

Figure 32: Corner plot of HD36267.

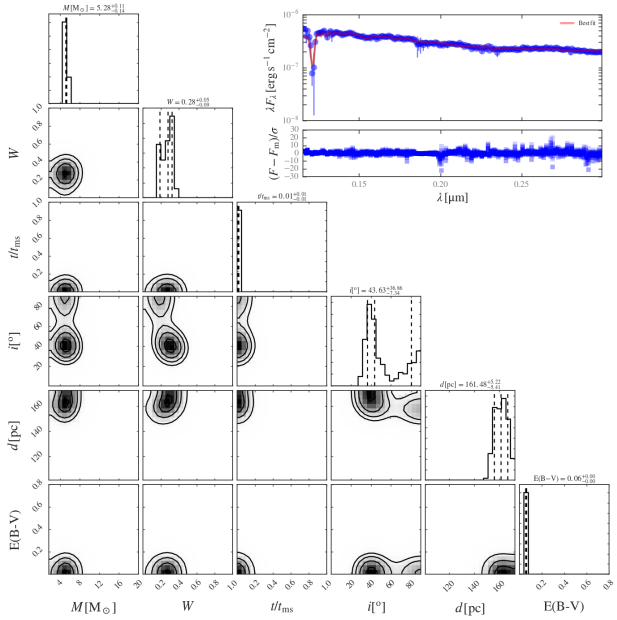

Figure 33: Corner plot of HD36653.

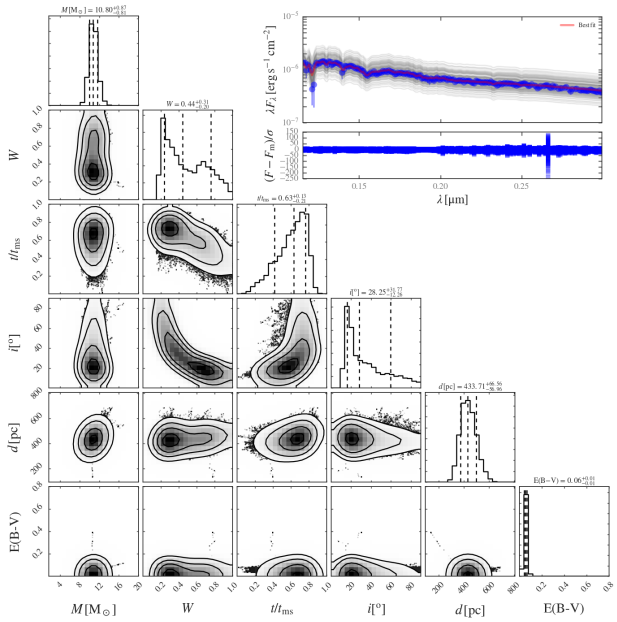

Figure 34: Corner plot of HD36695.

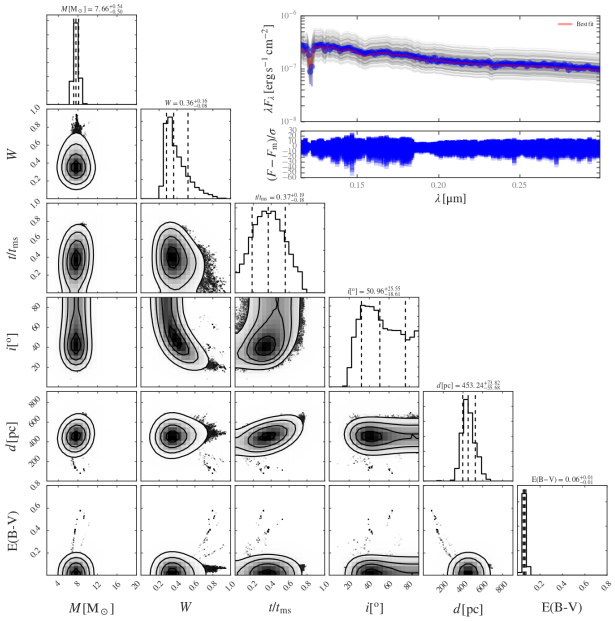

Figure 35: Corner plot of HD37017.

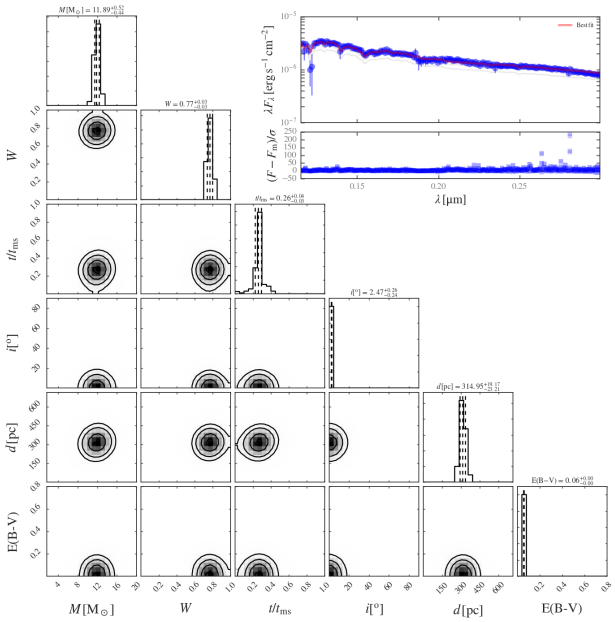

Figure 36: Corner plot of HD37018.

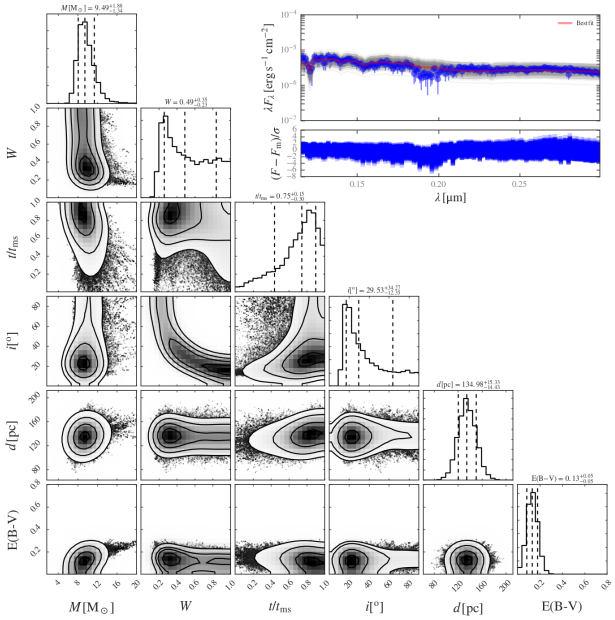

Figure 37: Corner plot of HD37202.

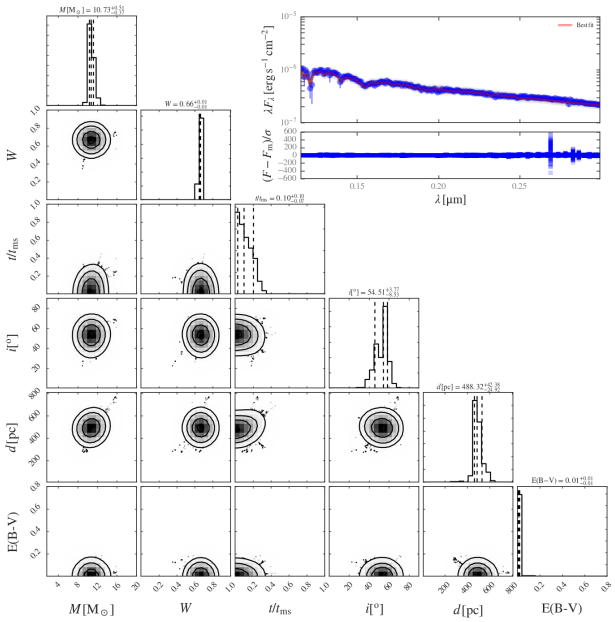

Figure 38: Corner plot of HD37303.

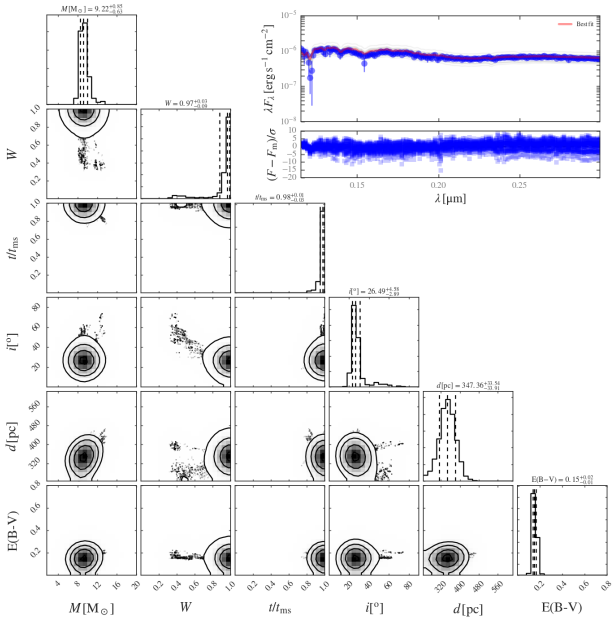

Figure 39: Corner plot of HD37490.

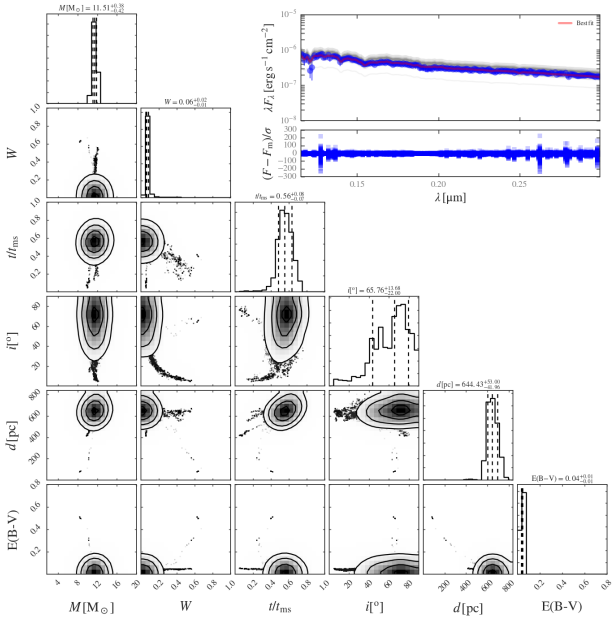

Figure 40: Corner plot of HD37744.

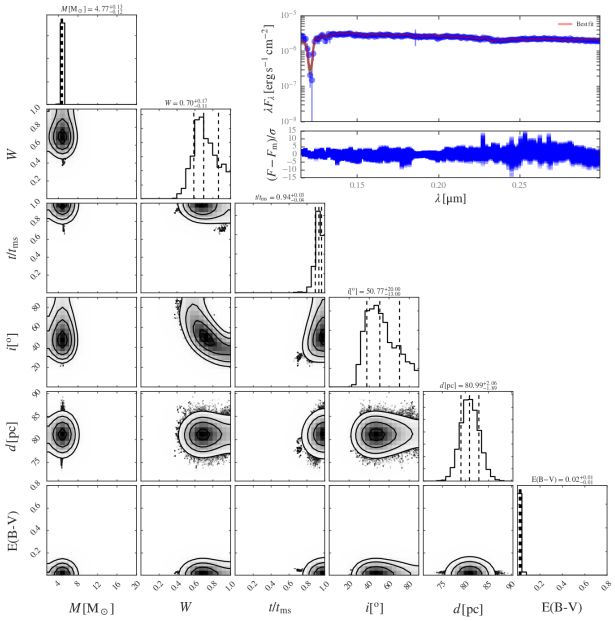

Figure 41: Corner plot of HD37795.

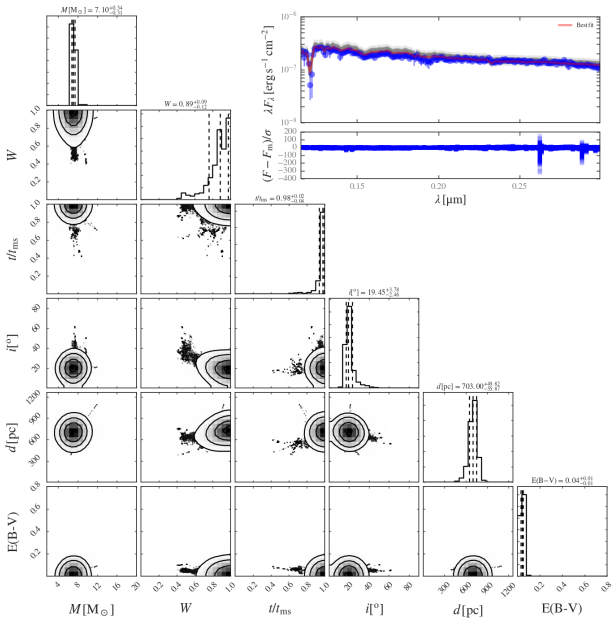

Figure 42: Corner plot of HD39698.

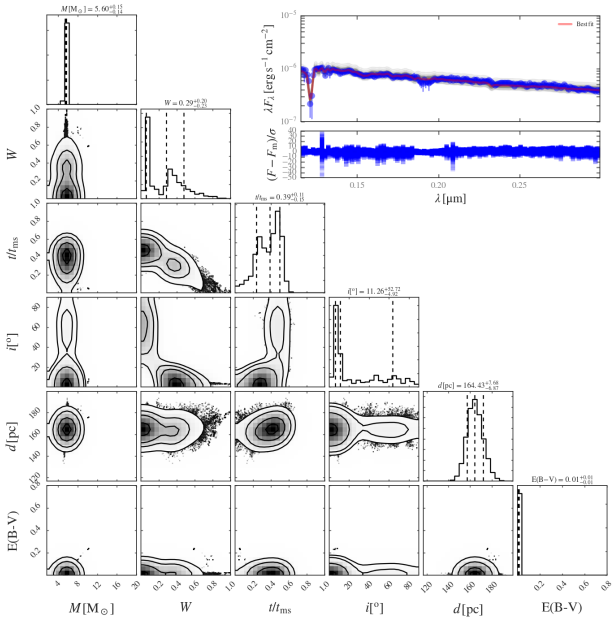

Figure 43: Corner plot of HD41753.

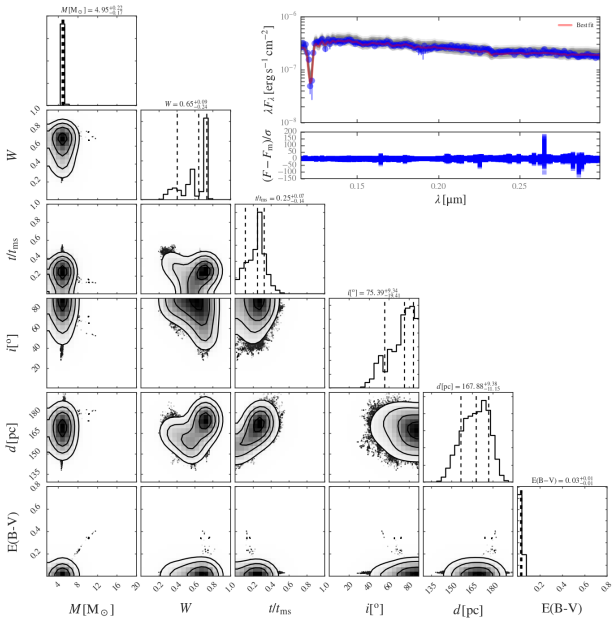

Figure 44: Corner plot of HD42545.

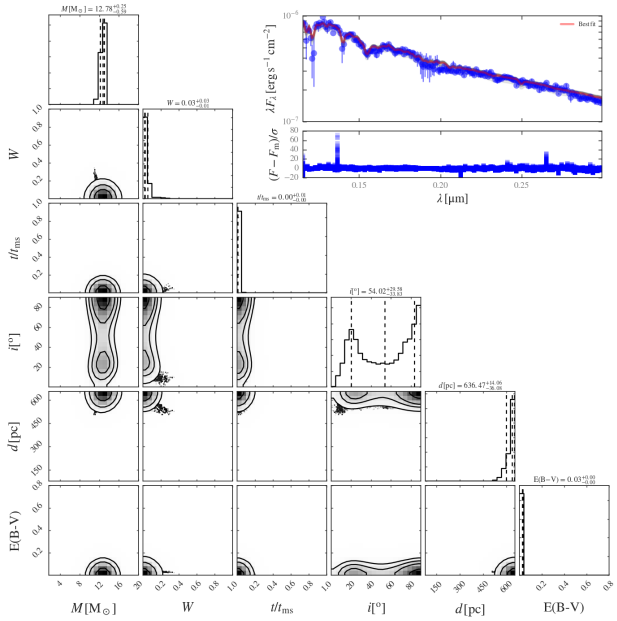

Figure 45: Corner plot of HD43112.

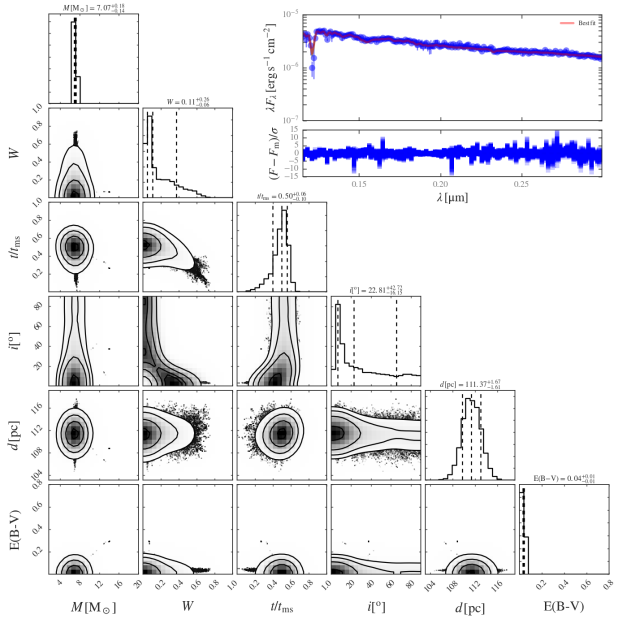

Figure 46: Corner plot of HD44402.

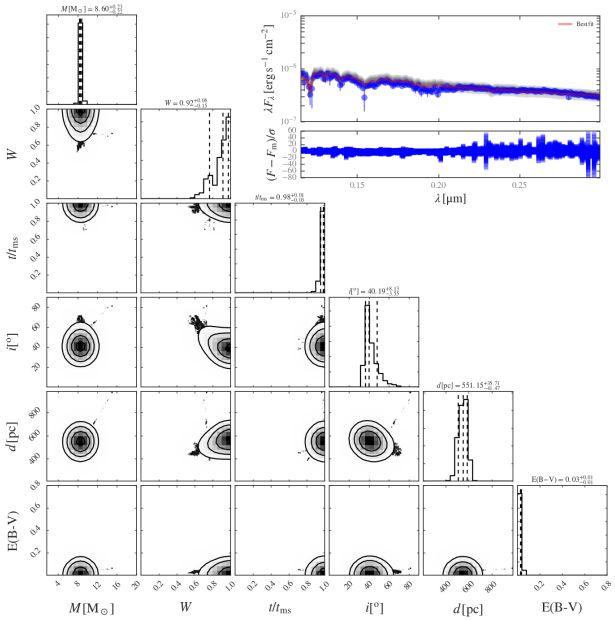

Figure 47: Corner plot of HD44506.

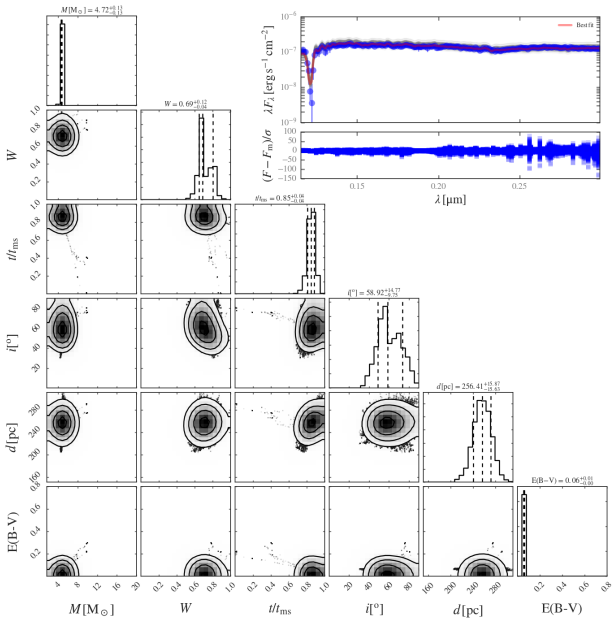

Figure 48: Corner plot of HD47054.

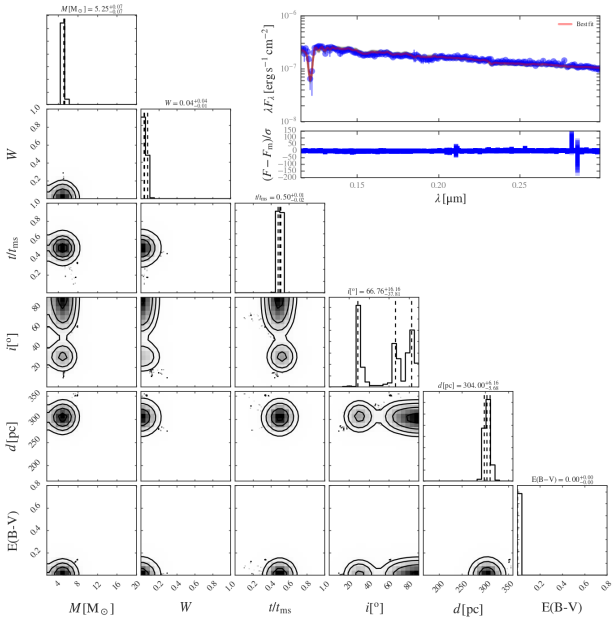

Figure 49: Corner plot of HD48977.

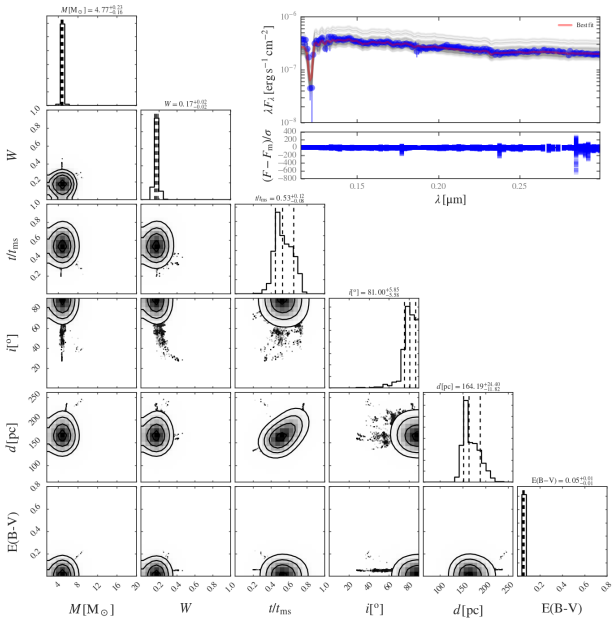

Figure 50: Corner plot of HD49662.

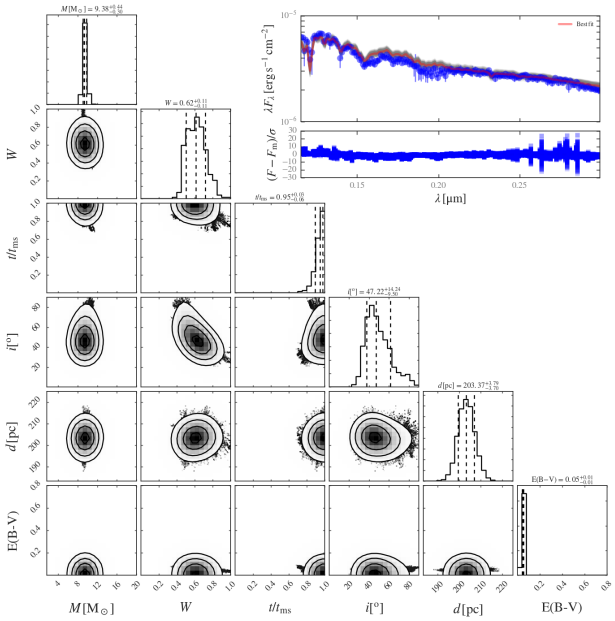

Figure 51: Corner plot of HD50013.

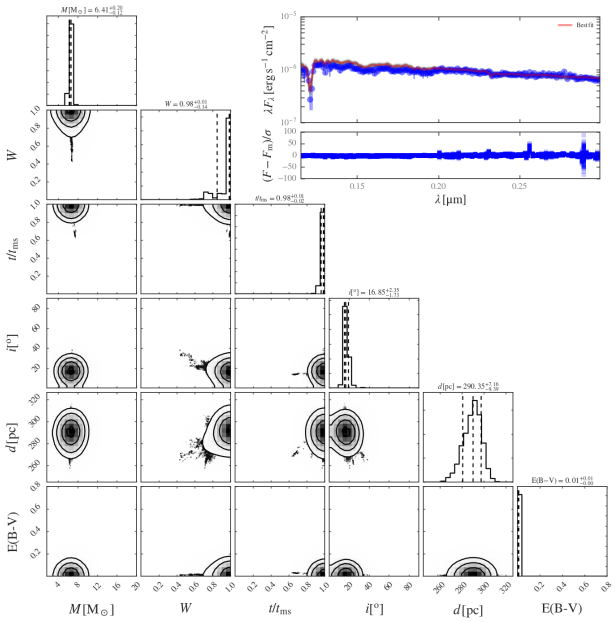

Figure 52: Corner plot of HD56139.

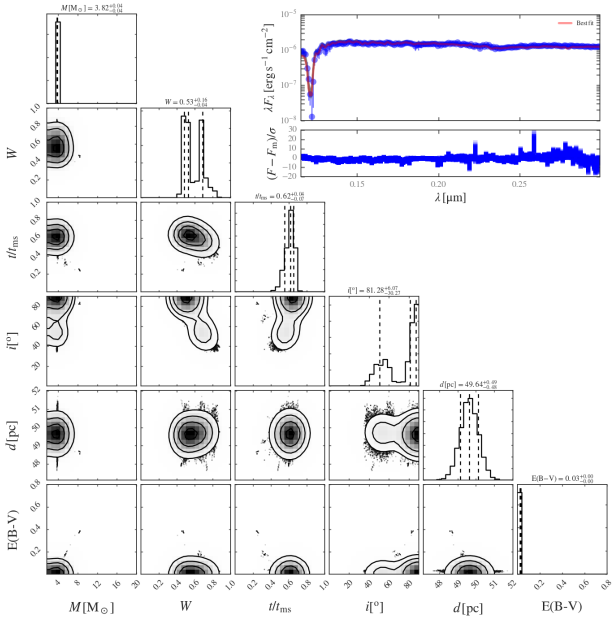

Figure 53: Corner plot of HD58715.

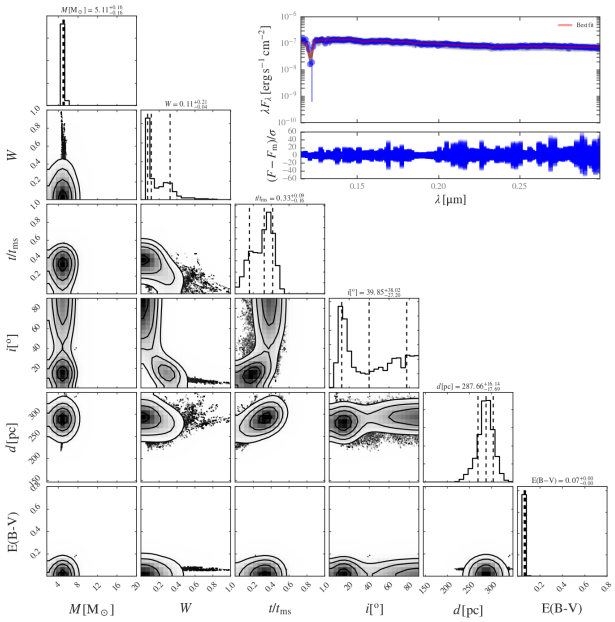

Figure 54: Corner plot of HD60098.

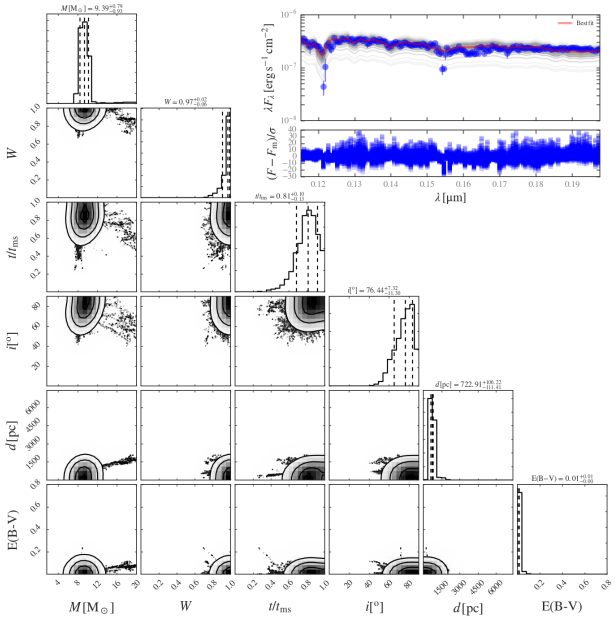

Figure 55: Corner plot of HD60848.

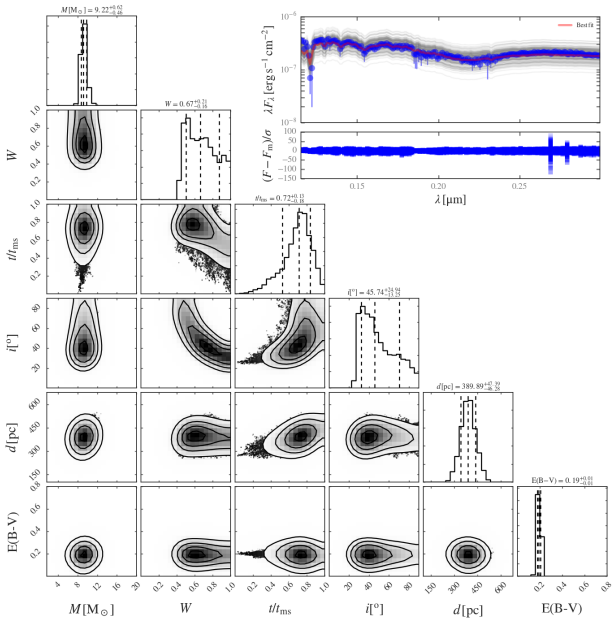

Figure 56: Corner plot of HD60855.

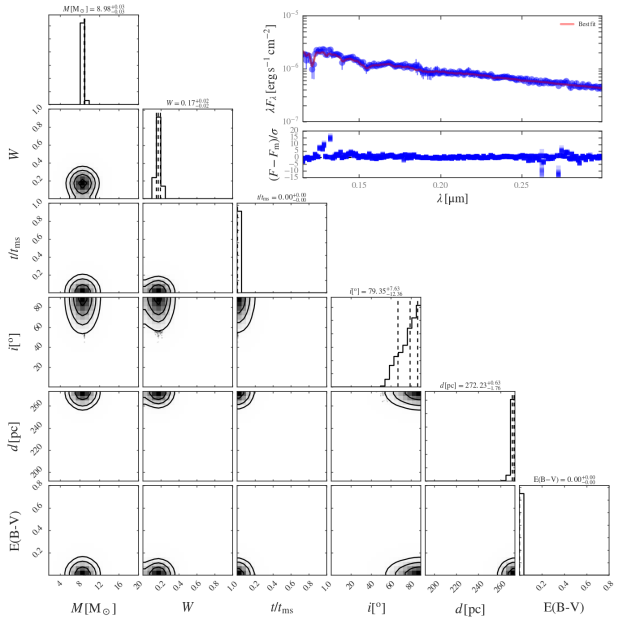

Figure 57: Corner plot of HD64740.

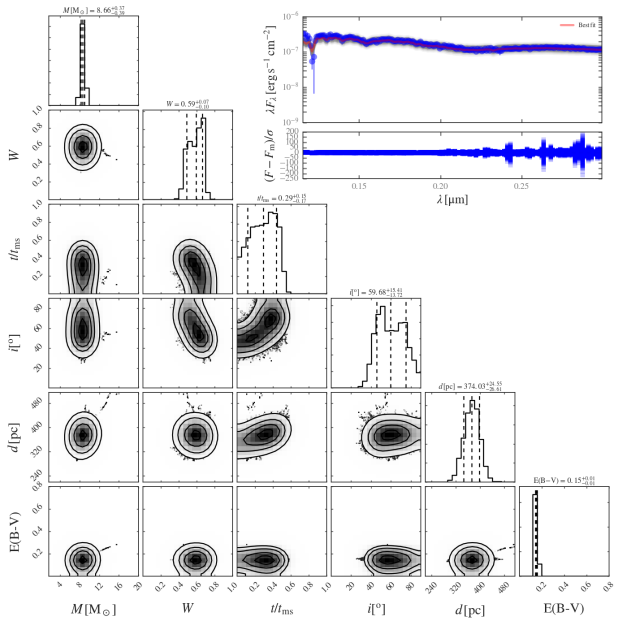

Figure 58: Corner plot of HD67536.

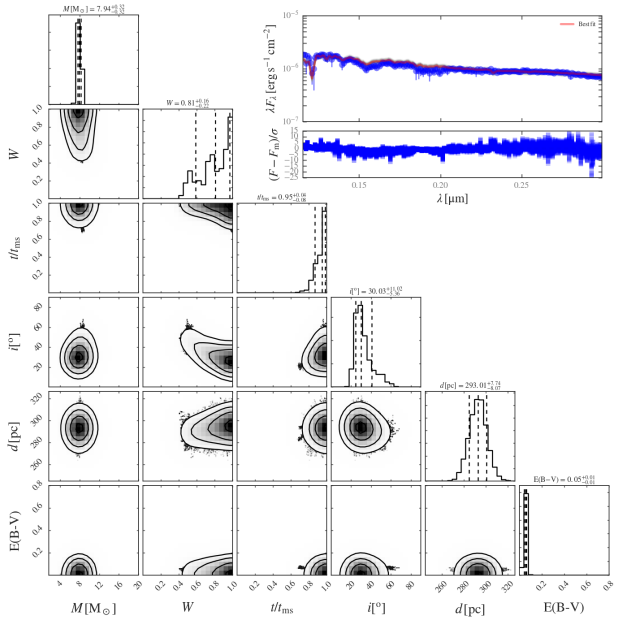

Figure 59: Corner plot of HD68980.

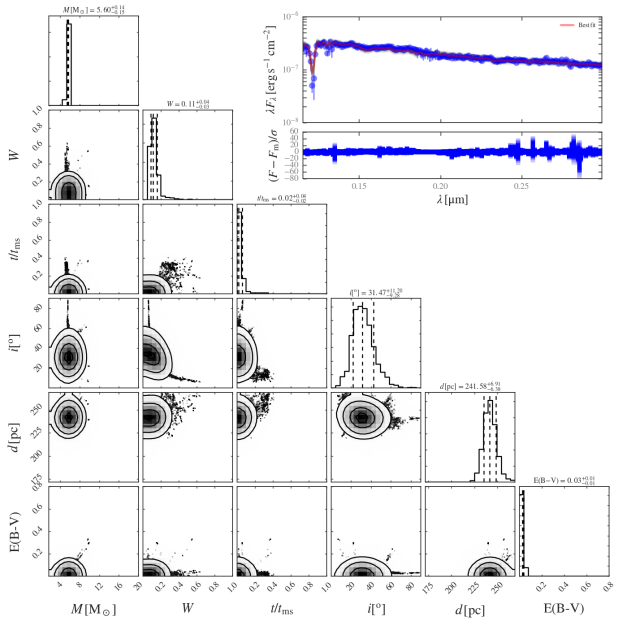

Figure 60: Corner plot of HD71459.

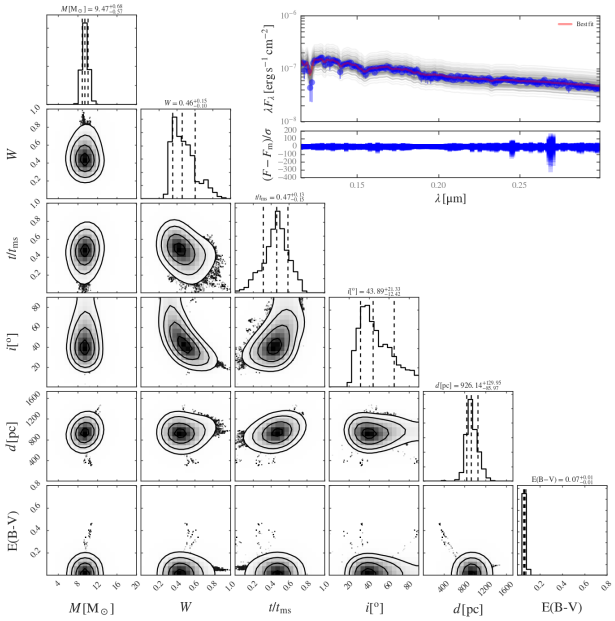

Figure 61: Corner plot of HD74234.

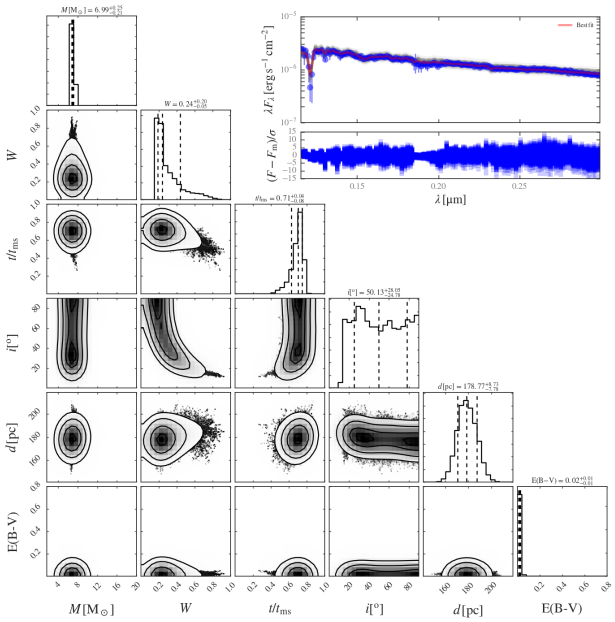

Figure 62: Corner plot of HD74280.

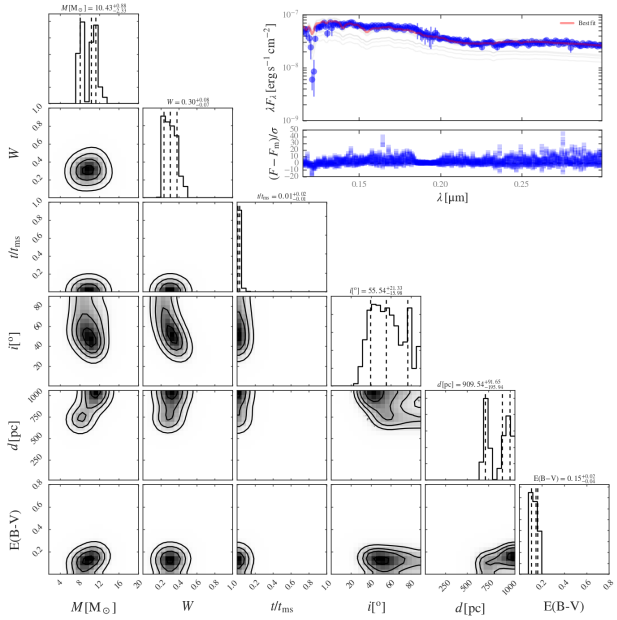

Figure 63: Corner plot of HD74319.

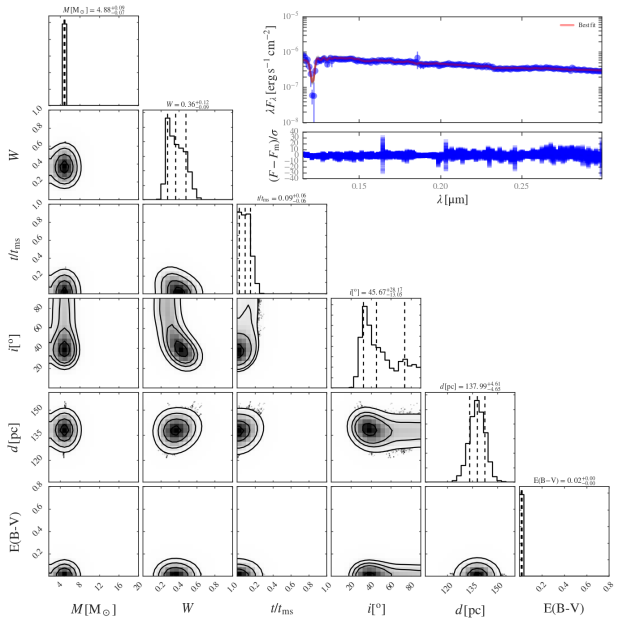

Figure 64: Corner plot of HD83754.

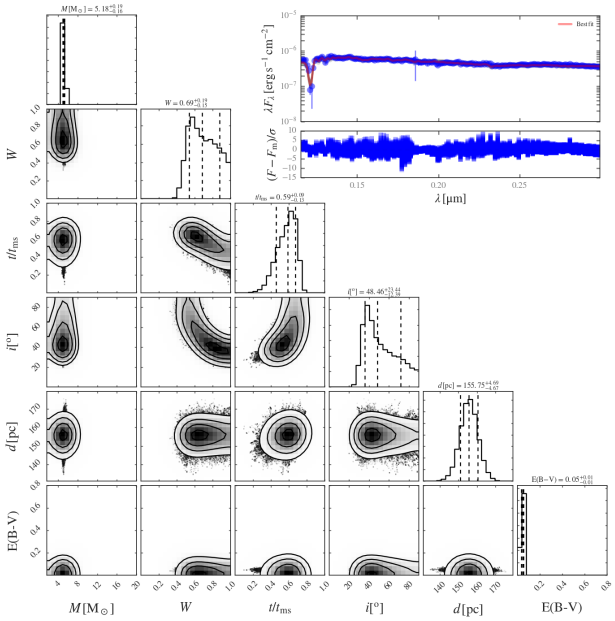

Figure 65: Corner plot of HD83953.

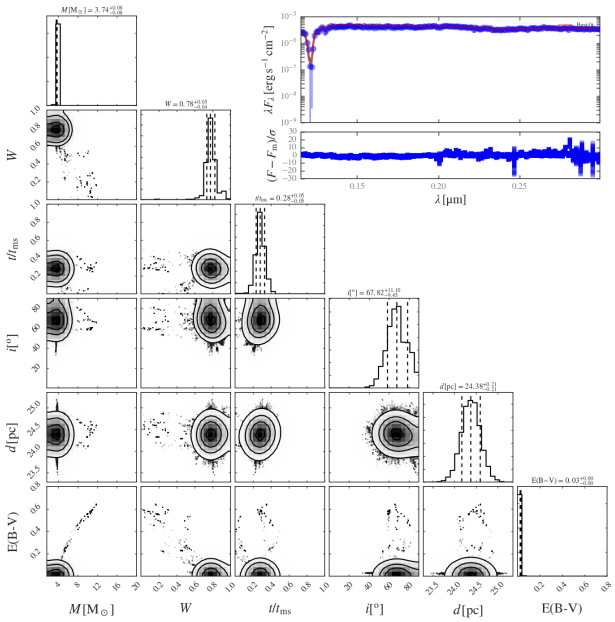

Figure 66: Corner plot of HD87901.

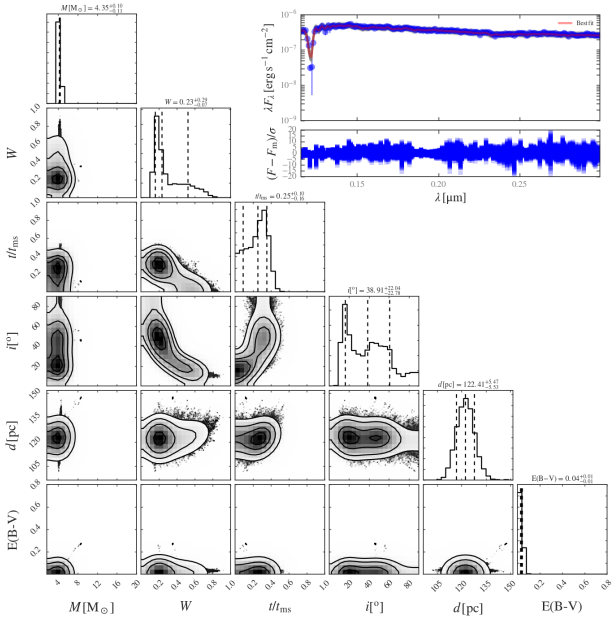

Figure 67: Corner plot of HD90994.

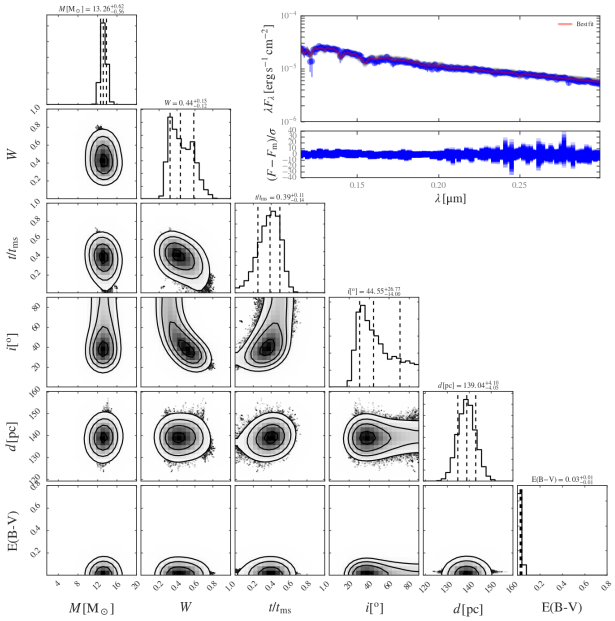

Figure 68: Corner plot of HD93030.

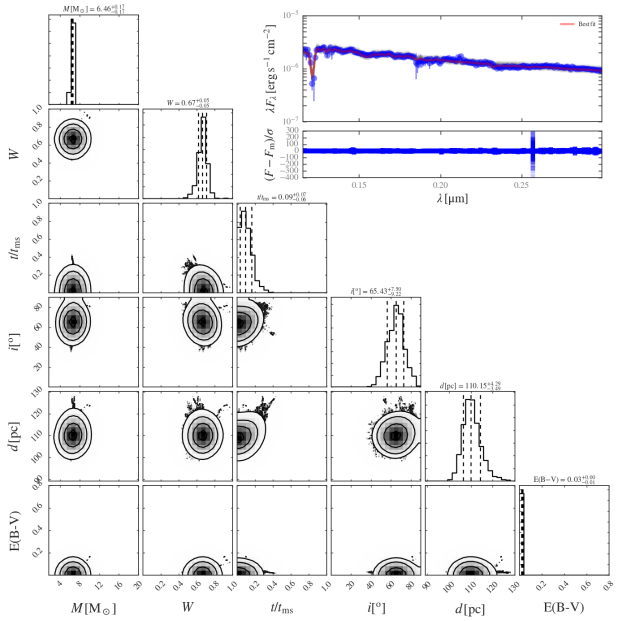

Figure 69: Corner plot of HD98718.

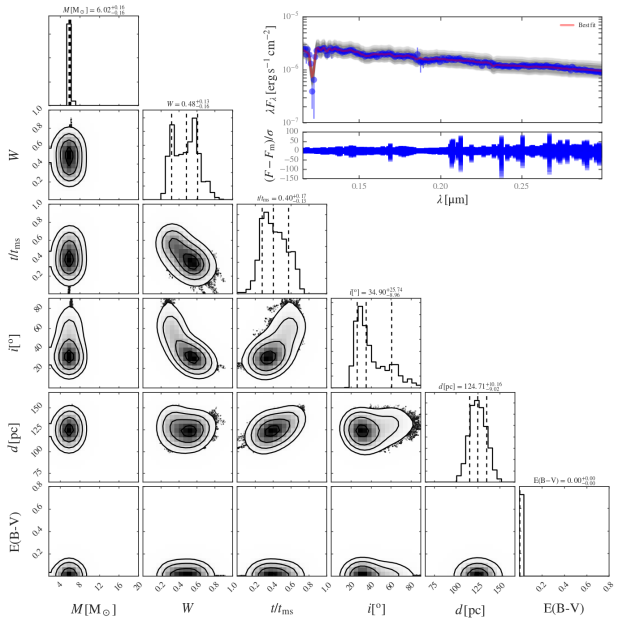

Figure 70: Corner plot of HD105937.

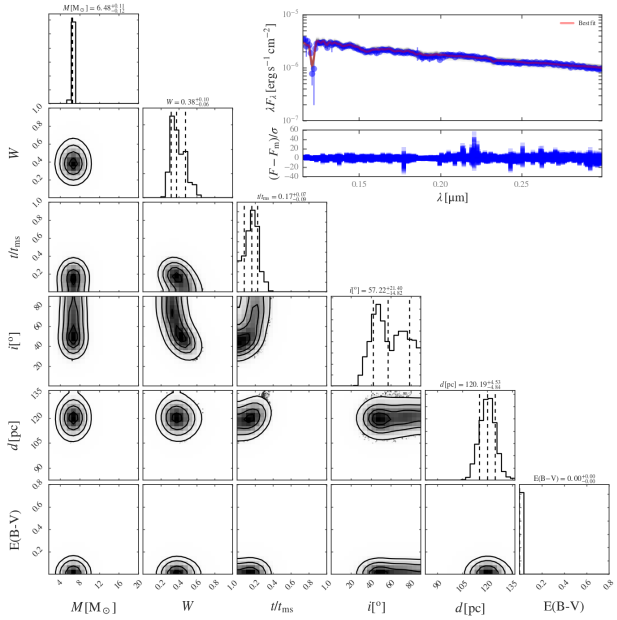

Figure 71: Corner plot of HD106983.

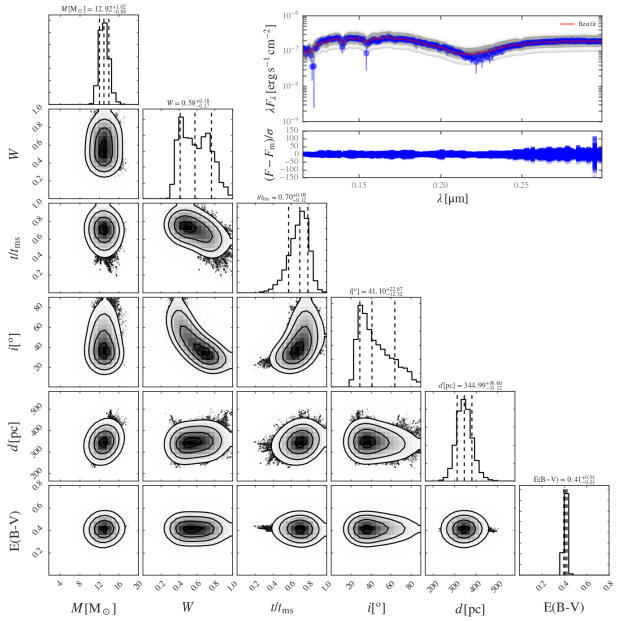

Figure 72: Corner plot of HD110432.

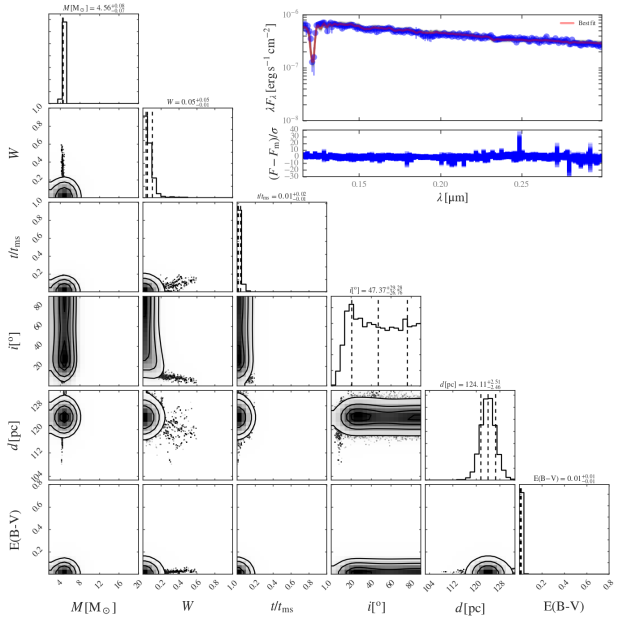

Figure 73: Corner plot of HD110956.

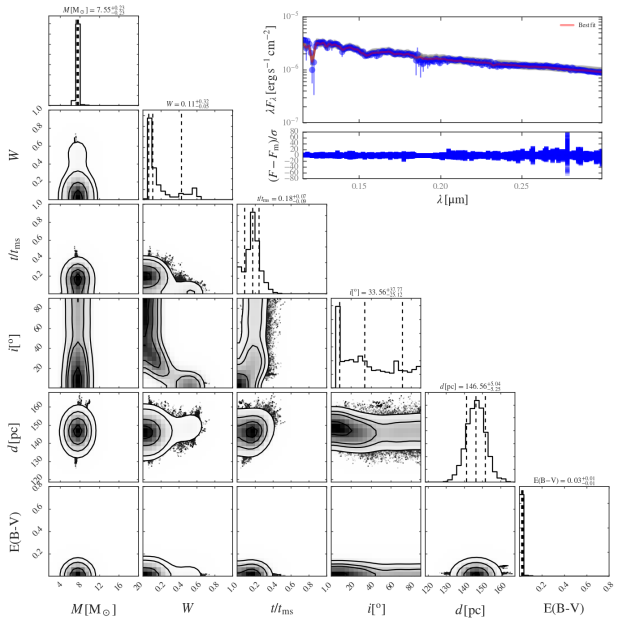

Figure 74: Corner plot of HD113791.

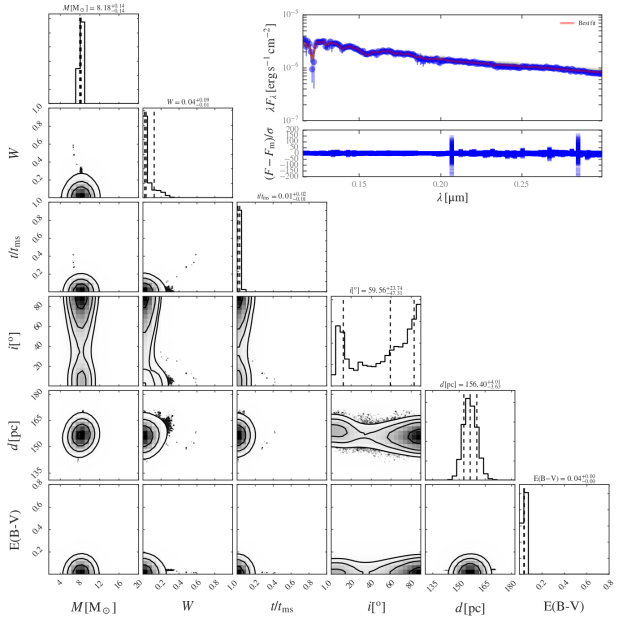

Figure 75: Corner plot of HD122980.

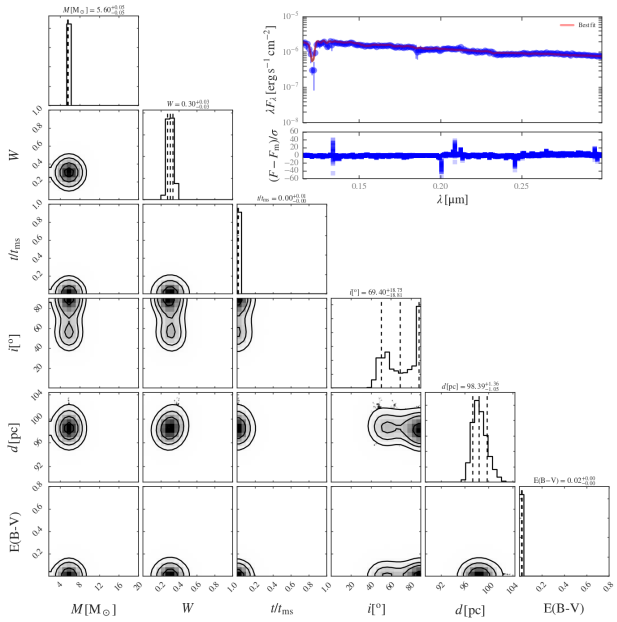

Figure 76: Corner plot of HD128345.

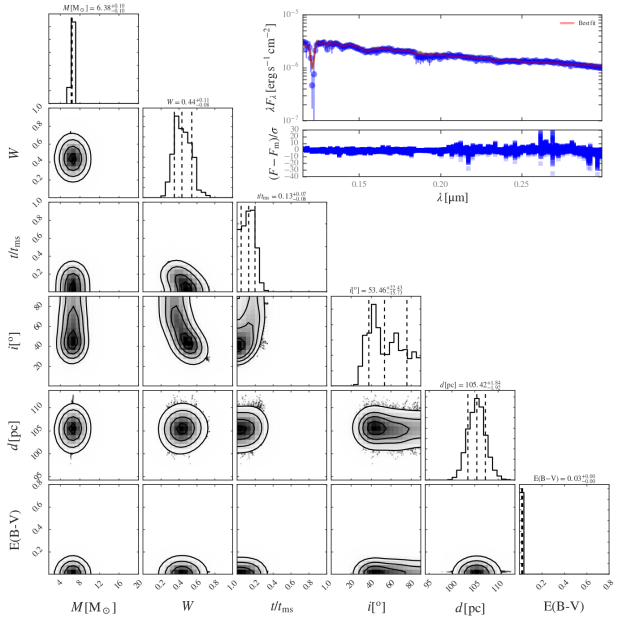

Figure 77: Corner plot of HD129116.

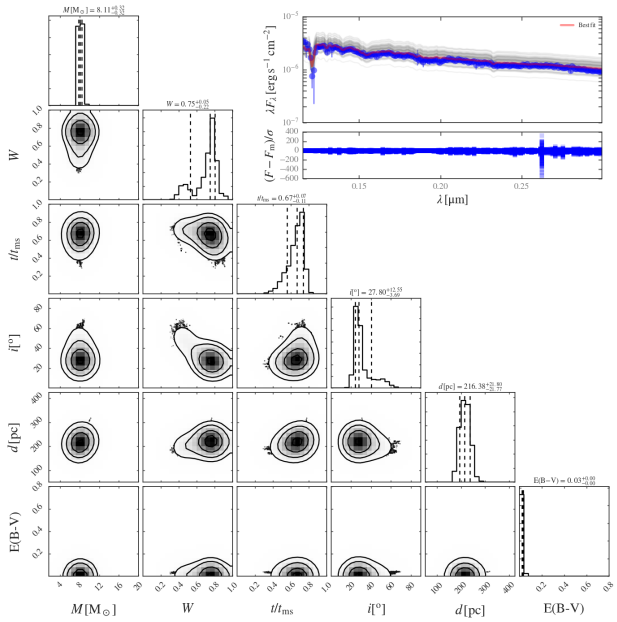

Figure 78: Corner plot of HD133955.

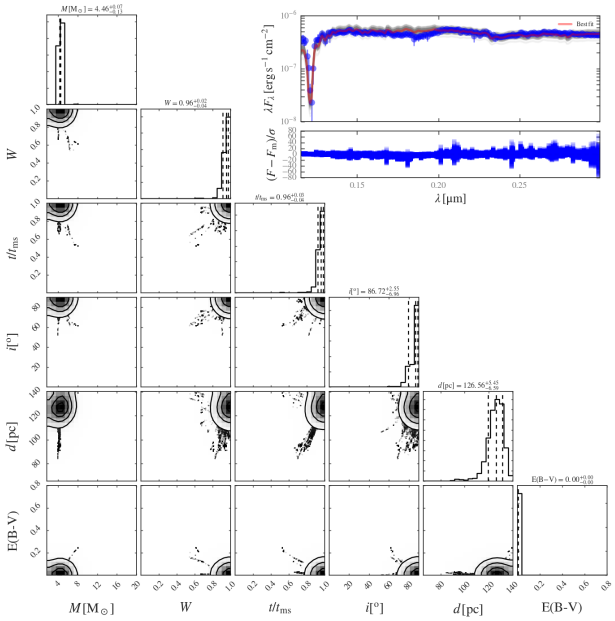

Figure 79: Corner plot of HD135734.

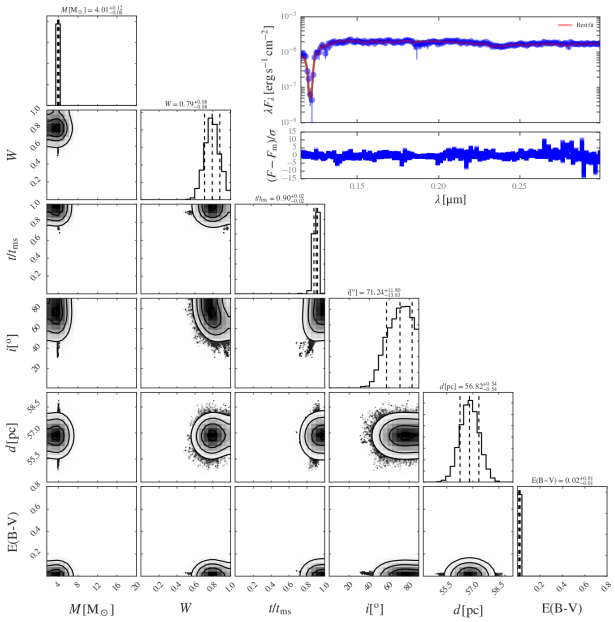

Figure 80: Corner plot of HD135742.

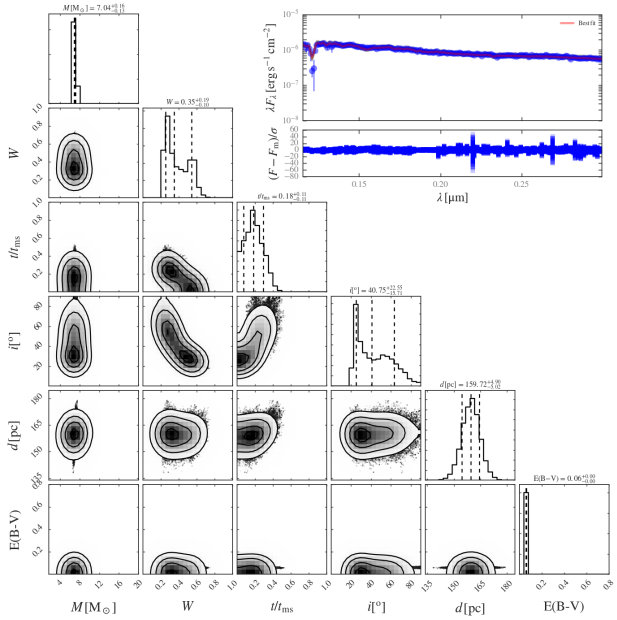

Figure 81: Corner plot of HD136664.

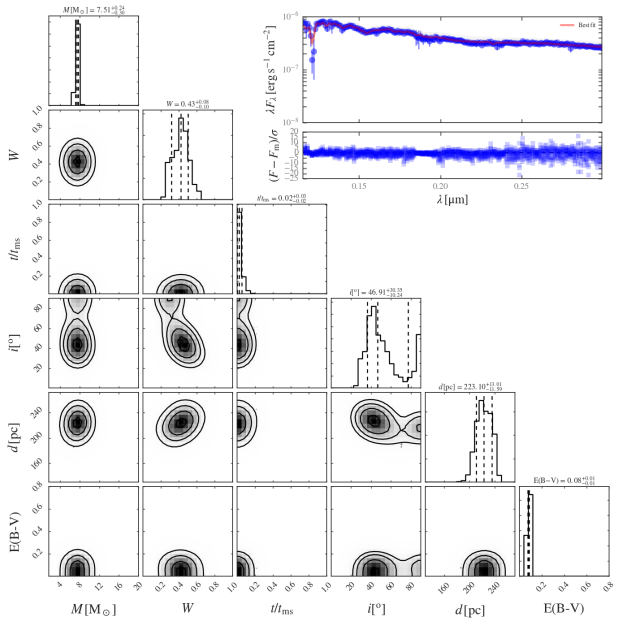

Figure 82: Corner plot of HD138485.

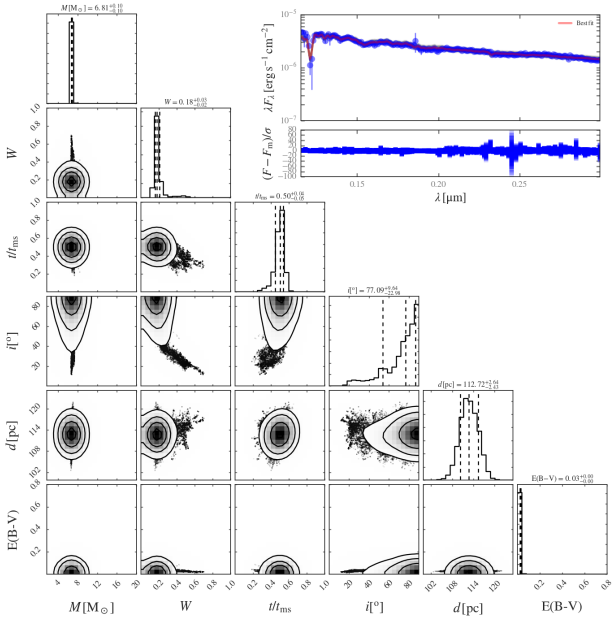

Figure 83: Corner plot of HD139365.

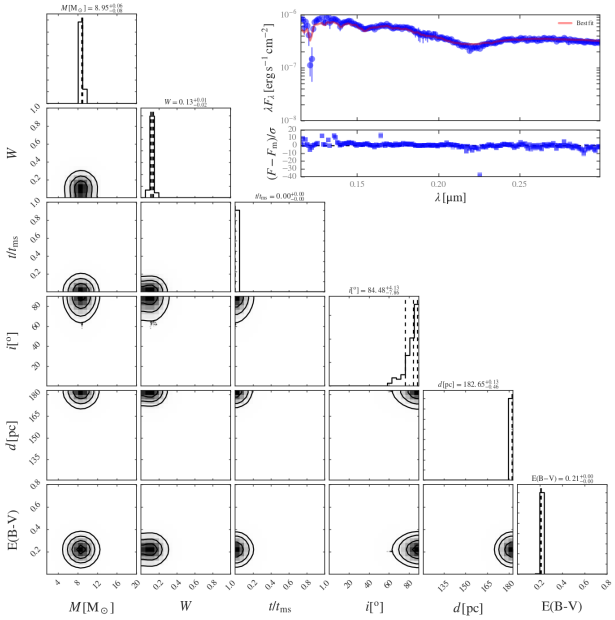

Figure 84: Corner plot of HD141637.

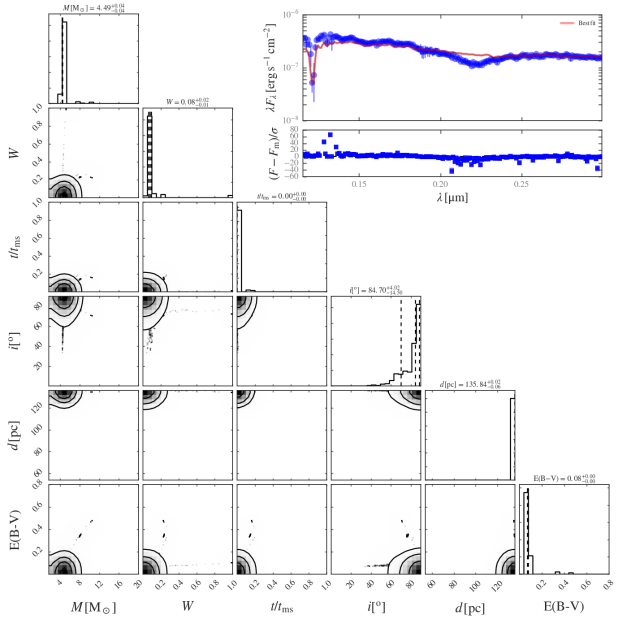

Figure 85: Corner plot of HD142096.

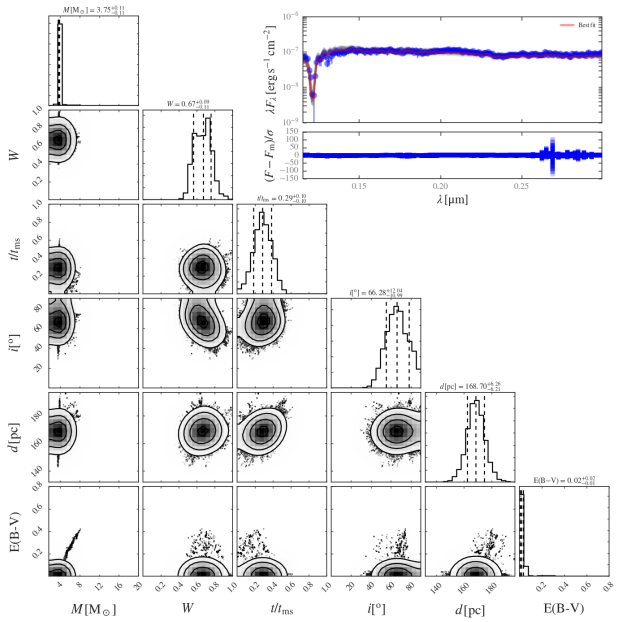

Figure 86: Corner plot of HD142926.

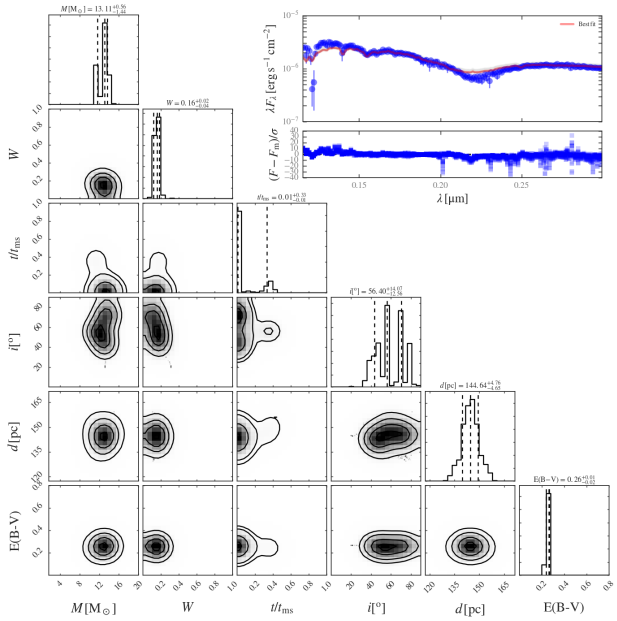

Figure 87: Corner plot of HD144470.

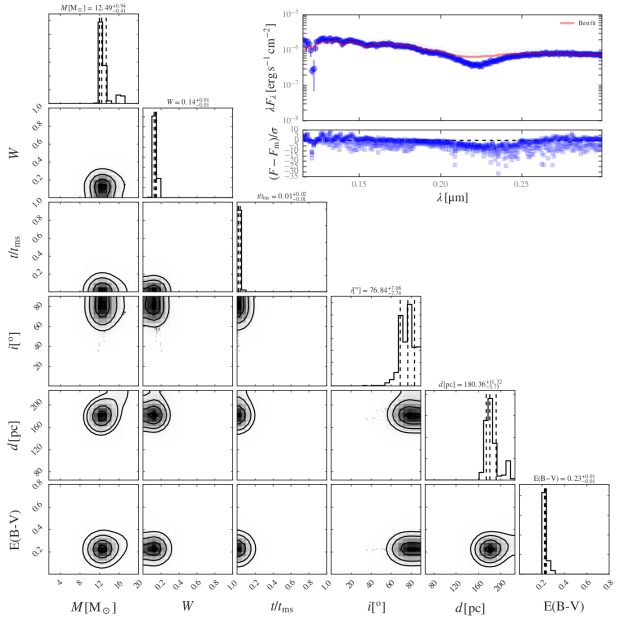

Figure 88: Corner plot of HD145502.

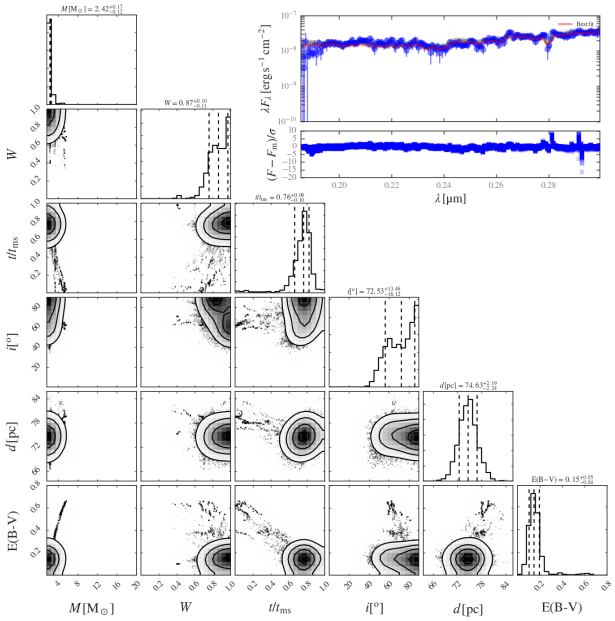

Figure 89: Corner plot of HD148283.

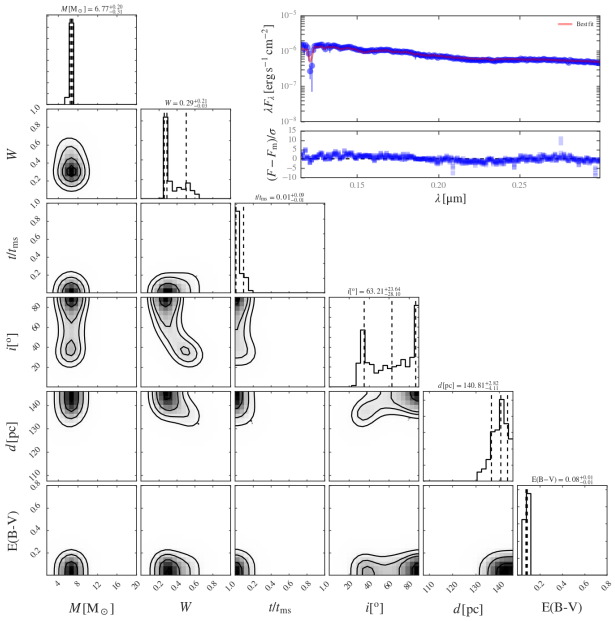

Figure 90: Corner plot of HD148605.

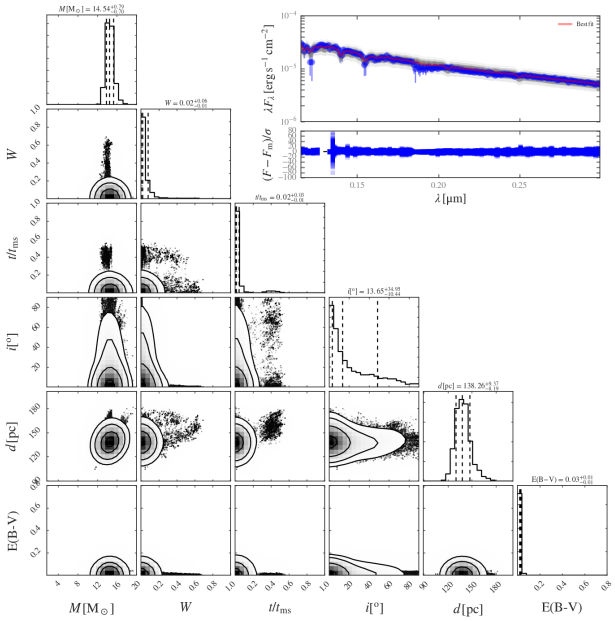

Figure 91: Corner plot of HD149438.

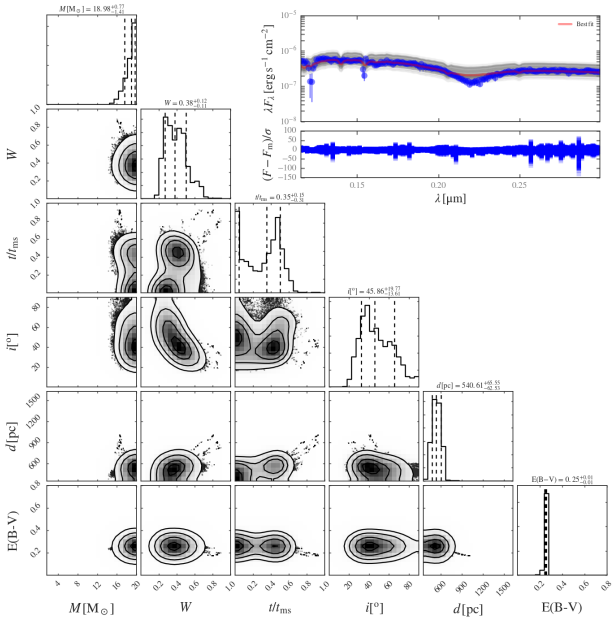

Figure 92: Corner plot of HD155806.

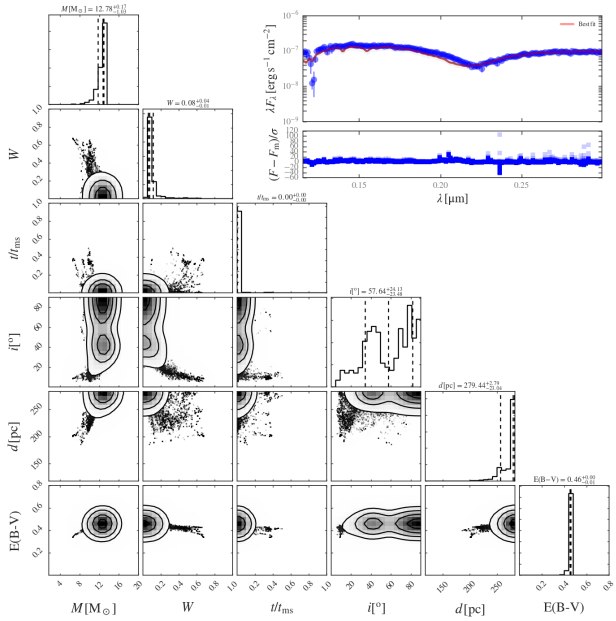

Figure 93: Corner plot of HD156247.

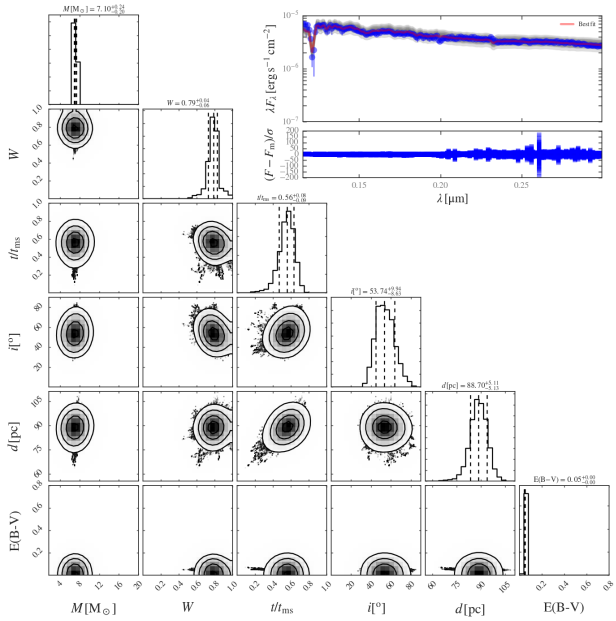

Figure 94: Corner plot of HD158427.

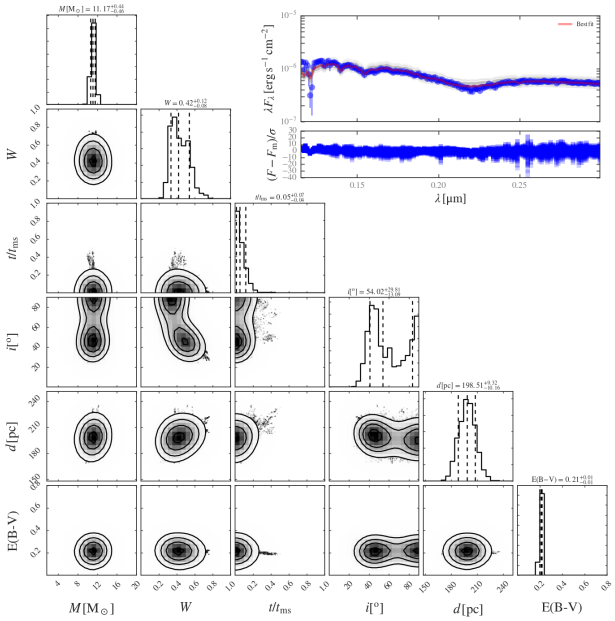

Figure 95: Corner plot of HD164284.

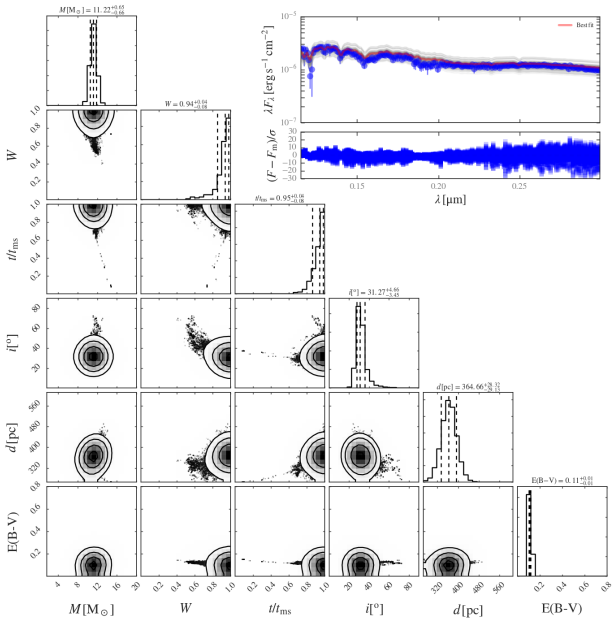

Figure 96: Corner plot of HD173948.

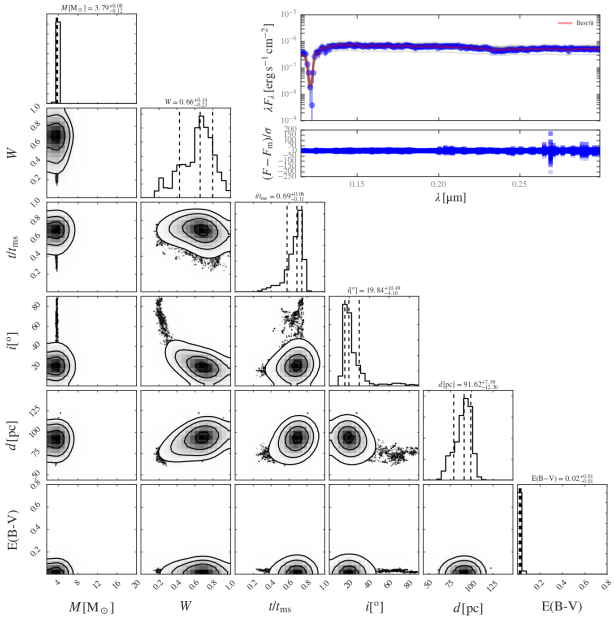

Figure 97: Corner plot of HD181454.

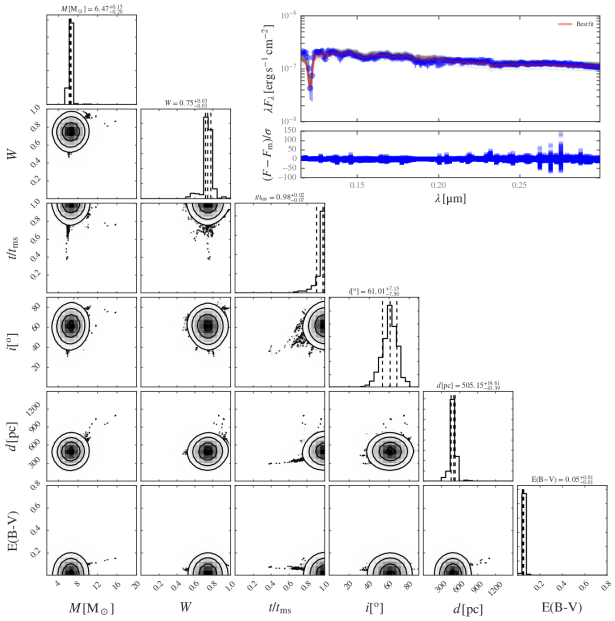

Figure 98: Corner plot of HD183362.

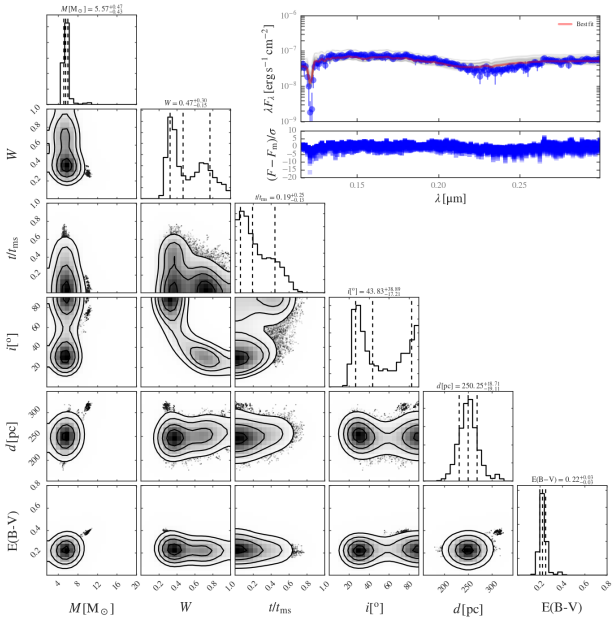

Figure 99: Corner plot of HD183656.

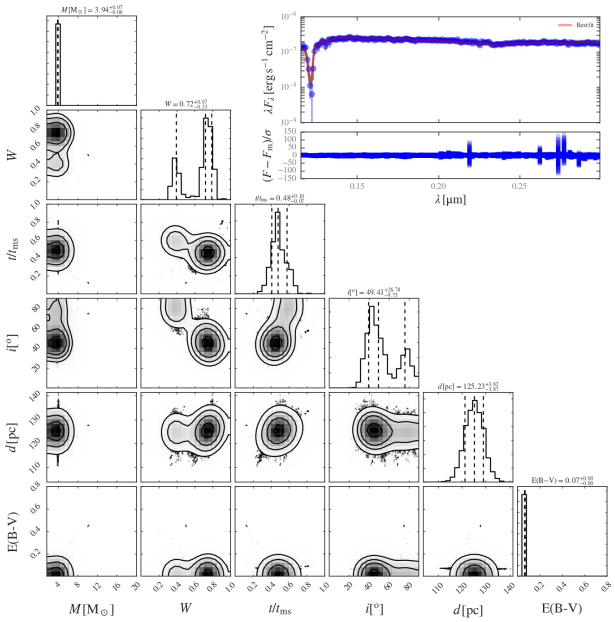

Figure 100: Corner plot of HD183914.

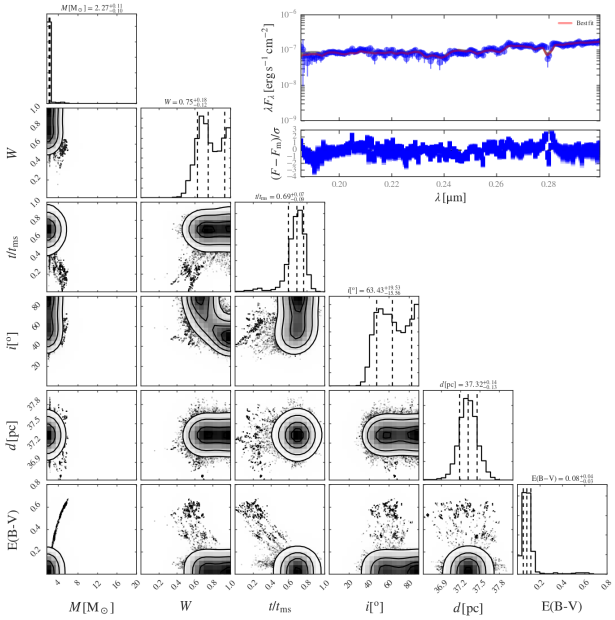

Figure 101: Corner plot of HD184006.

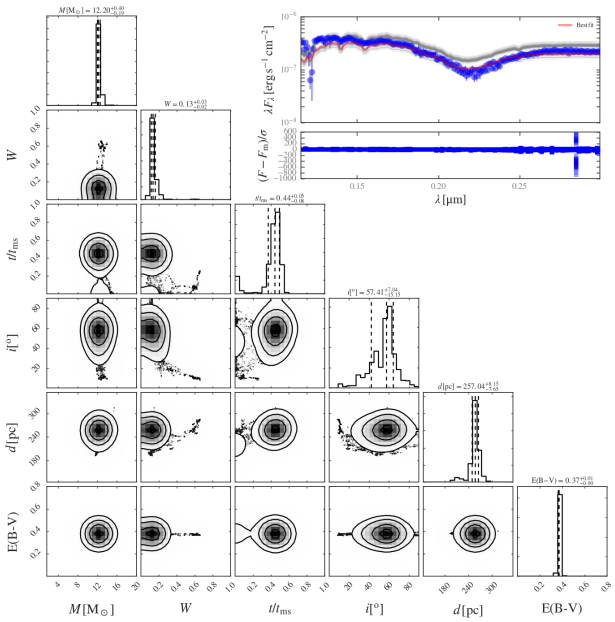

Figure 102: Corner plot of HD185507.

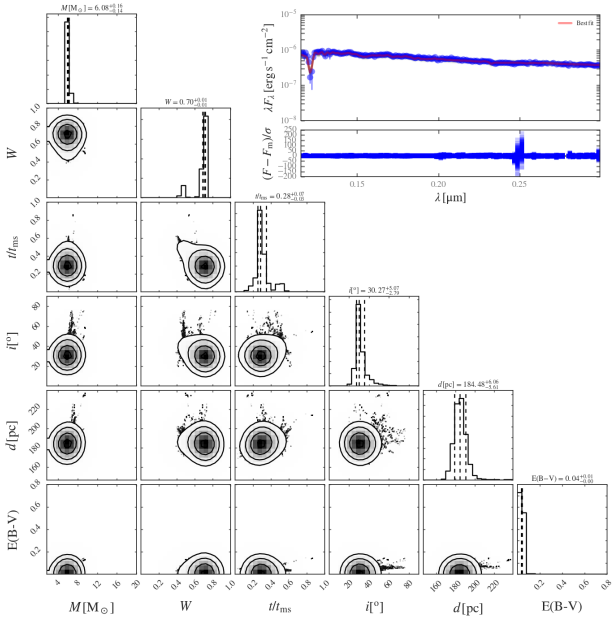

Figure 103: Corner plot of HD187811.

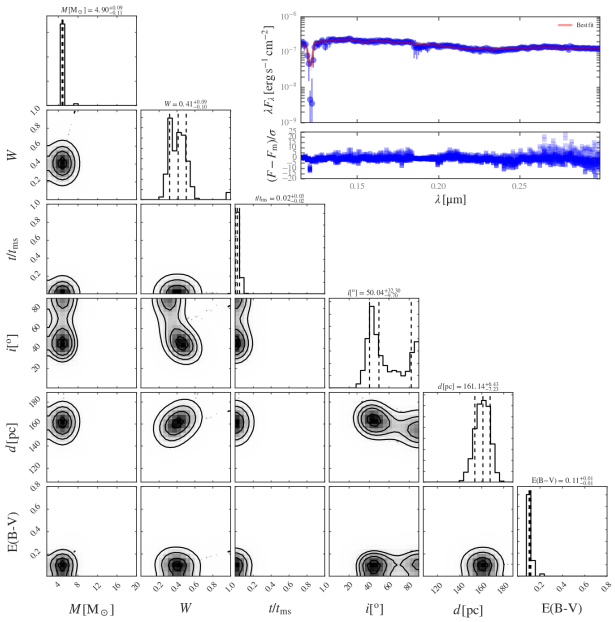

Figure 104: Corner plot of HD188293.

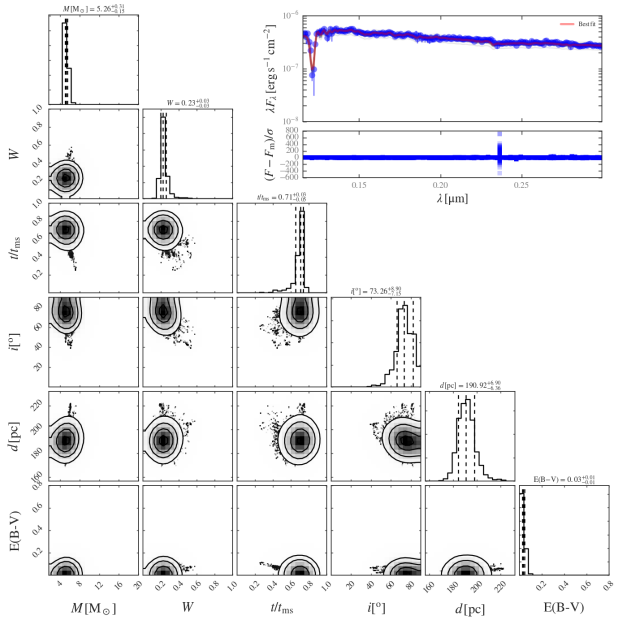

Figure 105: Corner plot of HD188665.

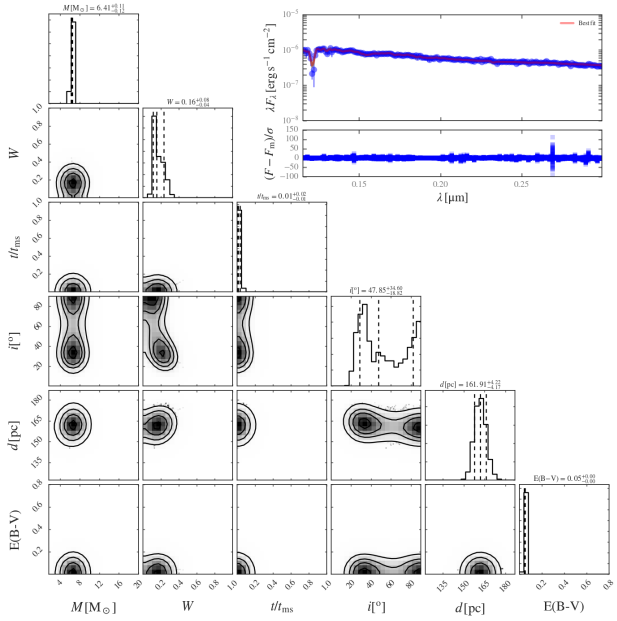

Figure 106: Corner plot of HD190993.

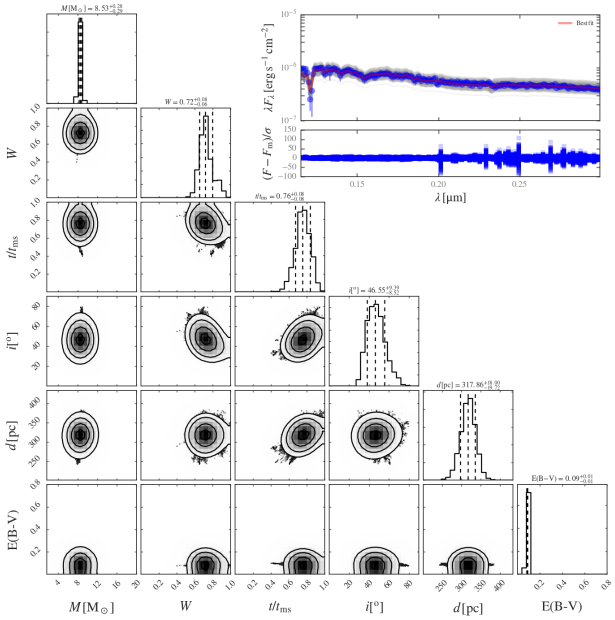

Figure 107: Corner plot of HD191610.

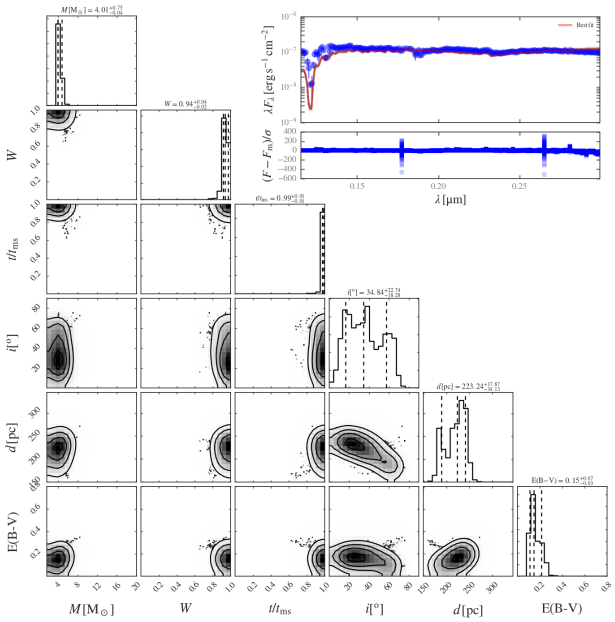

Figure 108: Corner plot of HD192044.

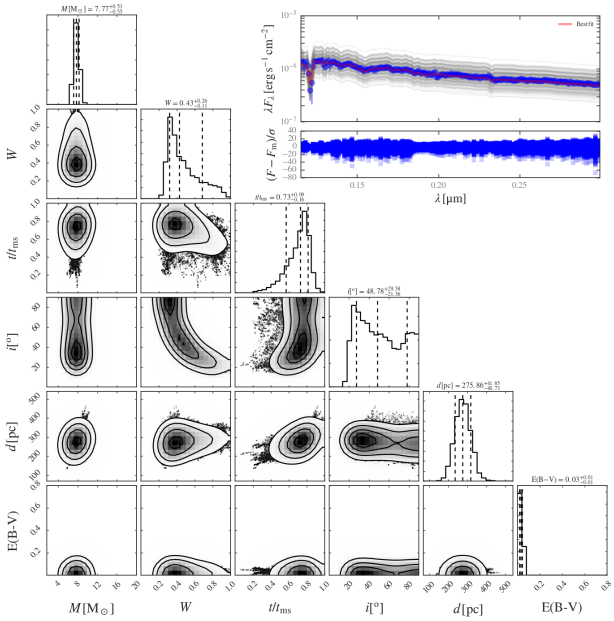

Figure 109: Corner plot of HD192685.

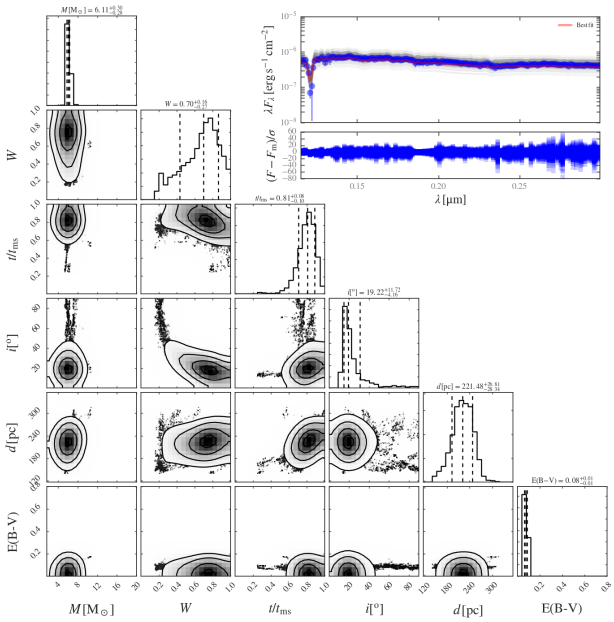

Figure 110: Corner plot of HD198183.

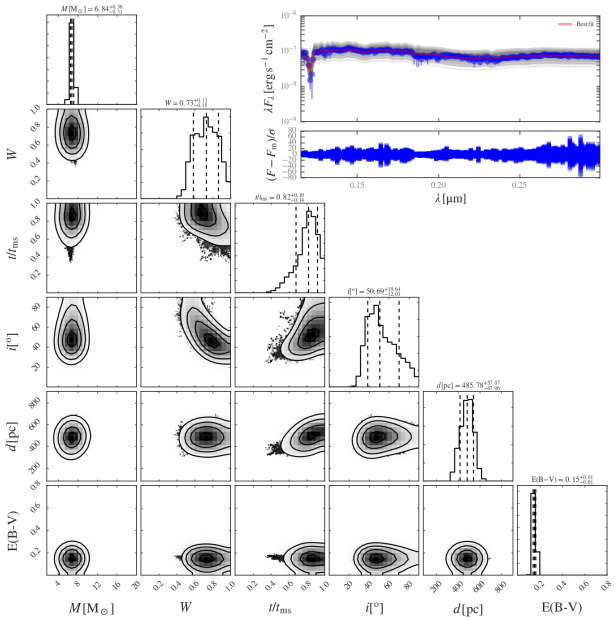

Figure 111: Corner plot of HD198625.

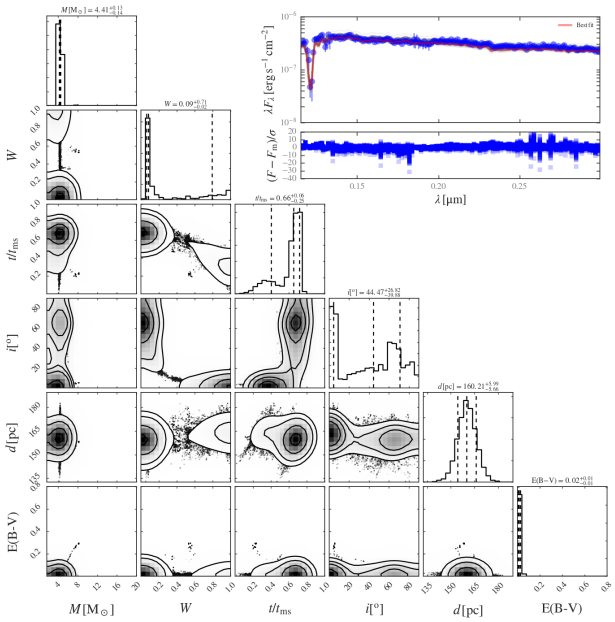

Figure 112: Corner plot of HD199081.

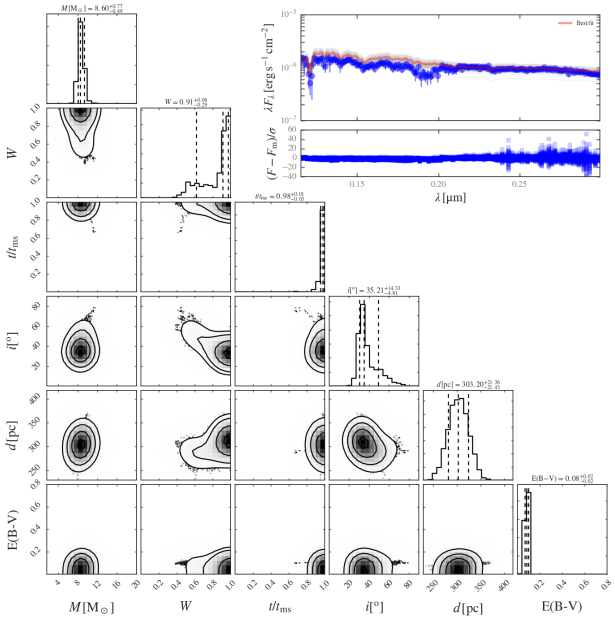

Figure 113: Corner plot of HD205637.

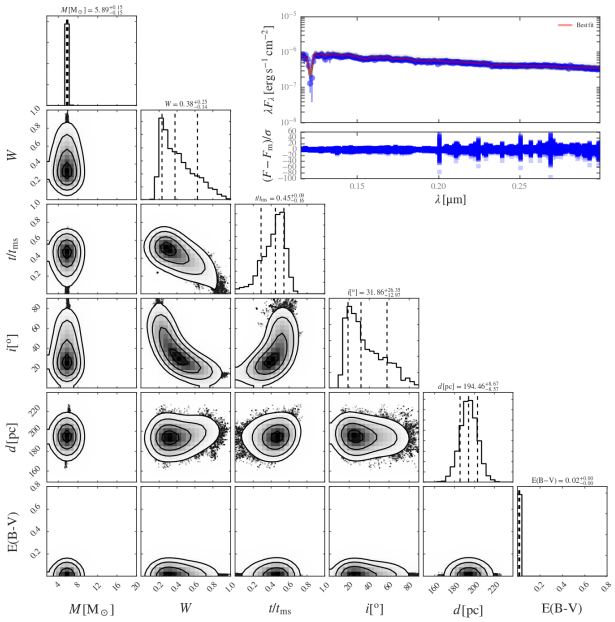

Figure 114: Corner plot of HD208057.

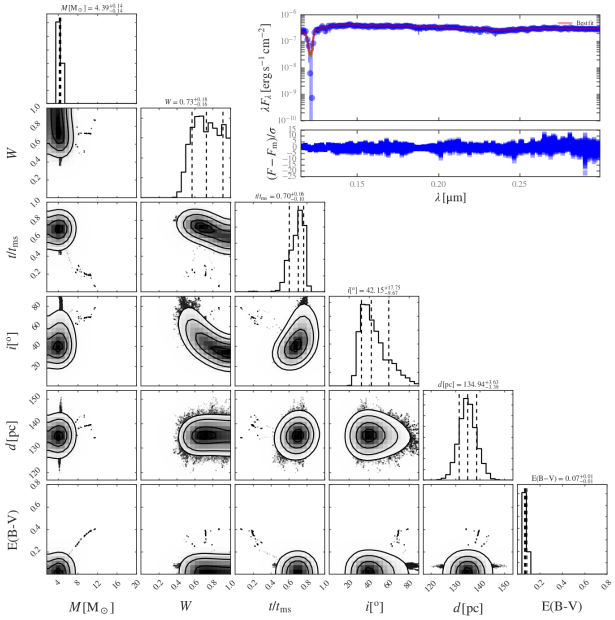

Figure 115: Corner plot of HD209409.

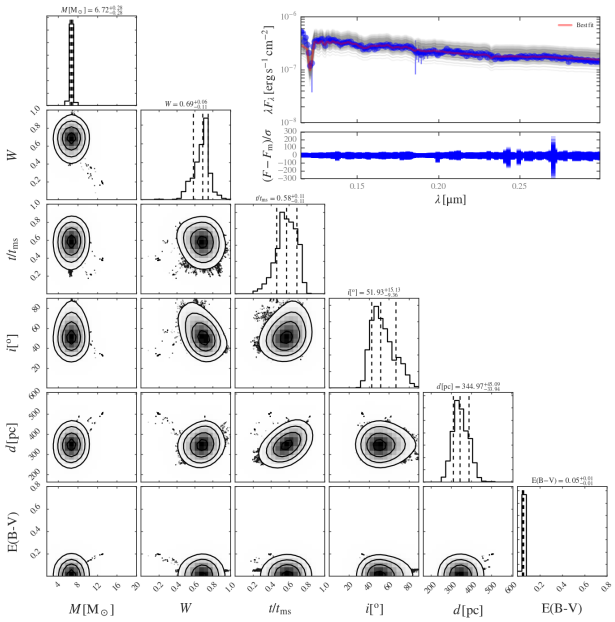

Figure 116: Corner plot of HD209522.

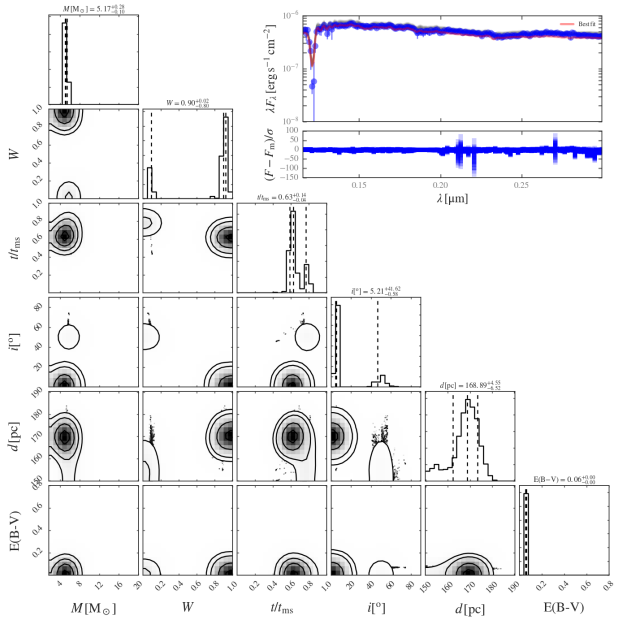

Figure 117: Corner plot of HD212120.

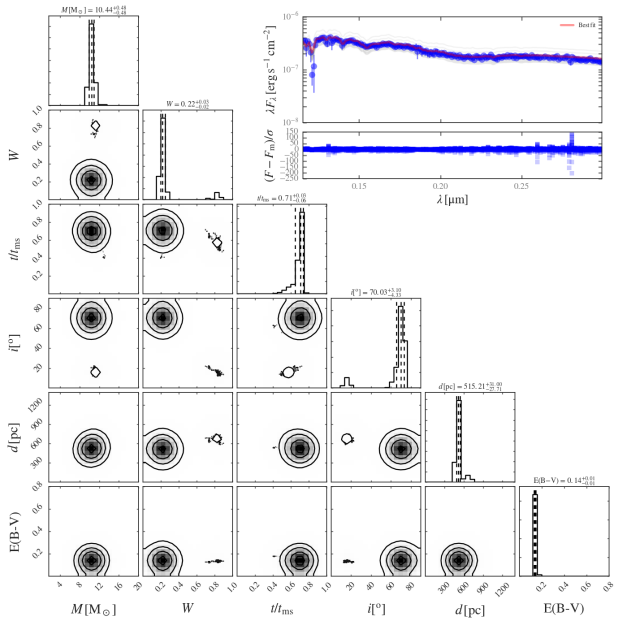

Figure 118: Corner plot of HD212978.

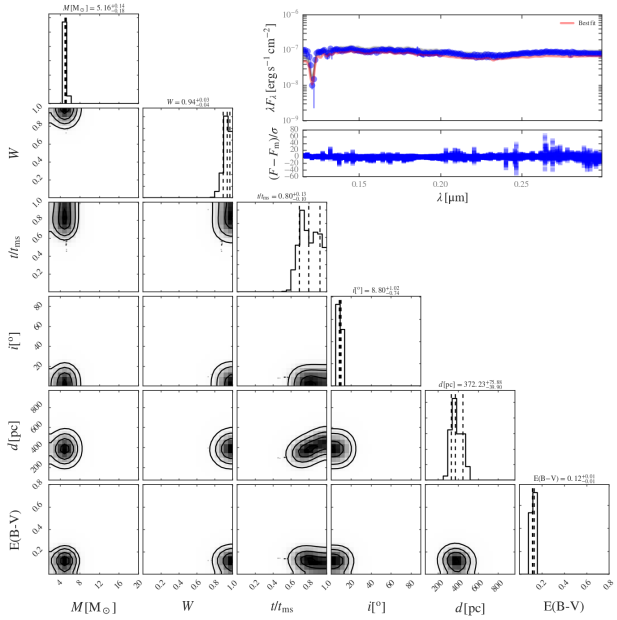

Figure 119: Corner plot of HD214240.

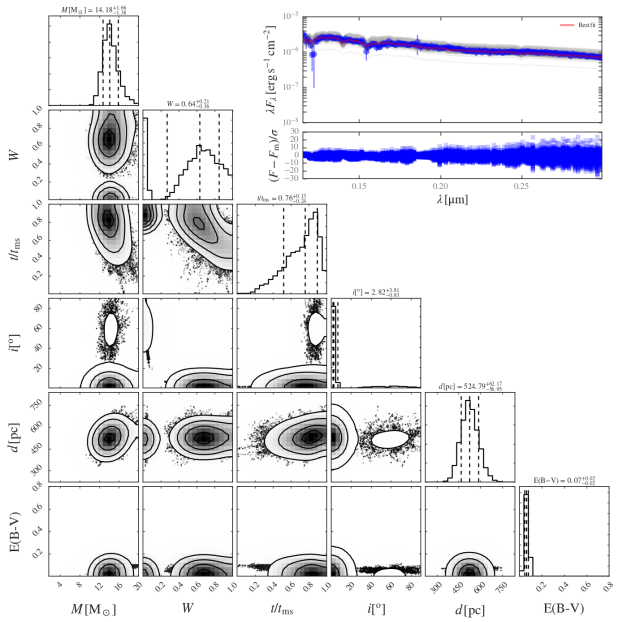

Figure 120: Corner plot of HD214680.

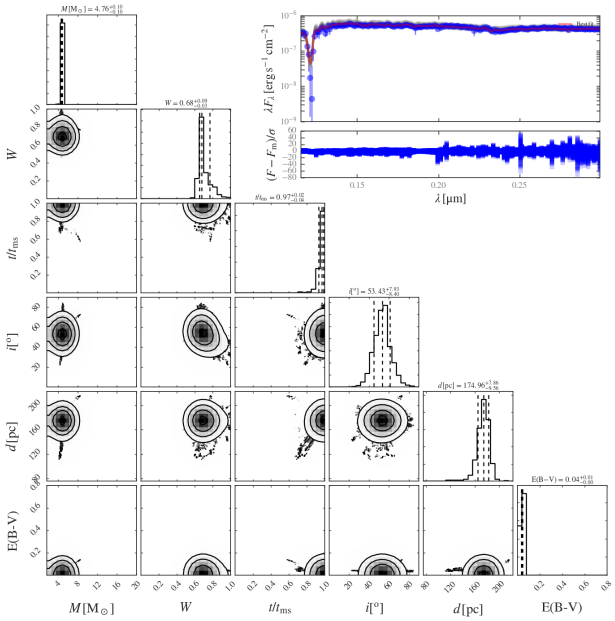

Figure 121: Corner plot of HD214748.

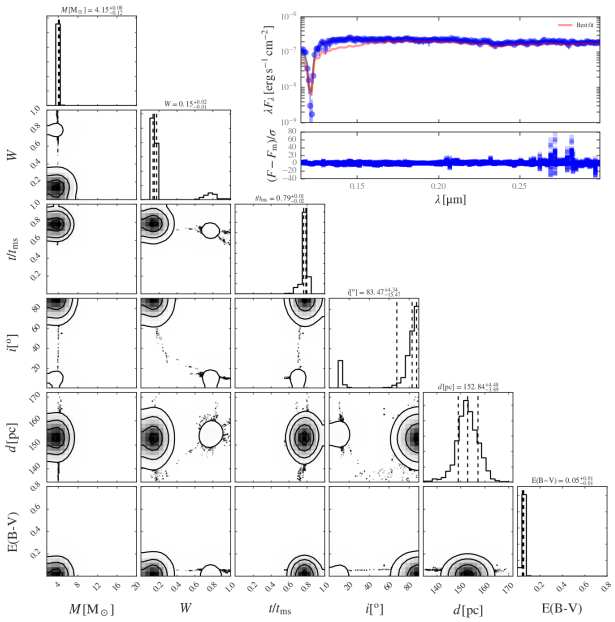

Figure 122: Corner plot of HD222173.

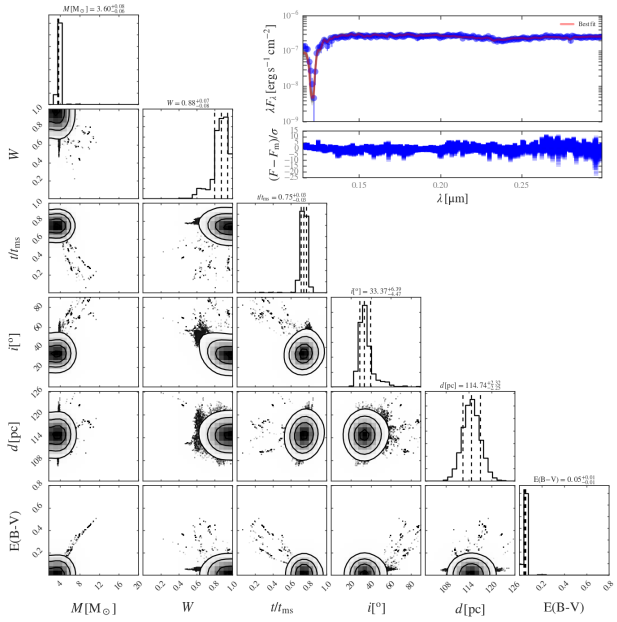

Figure 123: Corner plot of HD224686.